

Molecular dynamics investigation of viscoelastic properties of polymer melts

MOLECULAR DYNAMICS INVESTIGATION OF
VISCOELASTIC PROPERTIES OF POLYMER MELTS

By Oluseye Babafemi ADEYEMI,

*A Thesis Submitted to the School of Graduate Studies in the Partial
Fulfillment of the Requirements for the Degree Doctor of Philosophy*

McMaster University © Copyright by Oluseye Babafemi
ADEYEMI April 8, 2022

McMaster University

Doctor of Philosophy (2022)

Hamilton, Ontario (Chemical Engineering)

TITLE: Molecular dynamics investigation of viscoelastic properties of polymer melts

AUTHOR: Oluseye Babafemi ADEYEMI (McMaster University)

SUPERVISOR: Dr. Li Xi

NUMBER OF PAGES: xxi, 186

Abstract

Polymers and polymer mixtures play such important roles in our lives that it is hard to imagine life without them. Although a lot of progress has been made in the past few decades in our understanding of polymer dynamics and rheology using theoretical, computational, and experimental approaches, there are significant gaps in what is still left to be done. For example, polydispersity is the norm in industrially-produced polymers. However, a lot of the theories that have been propounded are predicated on monodisperse polymers. Most recently, molecular simulations have significantly improved our understanding of polymer dynamics by either validating theories or offering novel insights into their dynamics at the micro-structure level of detail. This thesis also uses molecular simulation to explore three different classes of polymer systems – monodisperse, polydisperse, and polymer-additive mixtures.

Two of the most significant theories of polymer dynamics are the Rouse model describing the dynamics of short and unentangled chains, and the tube and reptation model, which describes the motion of long, entangled chains. The reptation model predicts different dynamical regimes that are marked by distinct time scales and further introduced the concept of an entanglement length N_e – which signifies the length scale at which topological interactions between a test chain and surrounding matrix chains become significant. These distinct time scales have been investigated by various researchers but the reported values vary with different groups. Here, we devised a protocol for the accurate determination of these time scales. We also calculated N_e using these time scales and compared our results with those reported in the literature. Furthermore,

using Rouse mode analysis – a technique that resolves the coupled motion of monomers into distinct and uncoupled modes, we showed that the method can be used to determine N_e , with the values obtained closer to that using monomer displacement at longer time scales.

The computational calculation of the linear viscoelastic (LVE) properties of polymers is very expensive due to the long relaxation times associated with polymers. Using three different methods – Equilibrium molecular dynamics (EMD) via the Green-Kubo relation, non-equilibrium molecular dynamics (NEMD), and corrected Rouse Mode Analysis (cRMA), we determined the LVE properties of polymer melts for both unentangled and entangled chains and compared the uncertainty associated with each of them. Specifically, we demonstrate that the cRMA method, although applicable to only the shorter chains, yielded the lowest uncertainty. Compared to earlier reported results, we also show that, using shorter computational runs, the NEMD gives an acceptable level of accuracy in the calculation of the LVE properties.

Beyond methodology development, this thesis also studied the viscoelasticity of realistic polymer systems of practical interest, including polydisperse polymers and polymer-additive mixtures. We idealized a polydisperse system using a bidisperse model wherein we combined longer chains with shorter chains at different concentration levels. By investigating the individual motion of the different chains, we showed that the dynamics of the longer chains are sped up by the shorter chains, whereas the longer chains impeded the dynamics of the shorter chains, although the nature of the dynamics of the shorter chains was not altered. We also showed that the shorter chains reduce the extent of the

entanglement effect of the longer chains using an RMA approach. By using the individual LVE profiles of the long and short chains, we tested a semi-empirical mixing rule for predicting the stress relaxation modulus $G(t)$ of the bulk mixture. We found that a simple mixing rule works well when the shorter chains are the majority while the double reptation model – that assumes a simultaneous relaxation of both the test chains and surrounding matrix chains, does a better job of the prediction when the longer chains are the majority.

We further explored the effect of molecular structure of single-bead additives on the thermo-physical properties, such as the glass transition temperature and Young’s modulus on the polymer-additive mixture. By varying the dimensions of the molecular additive and over a range of concentration of the molecular additives, we found that smaller-sized additives are better able to reduce the glass transition temperature T_g and increase the Young’s modulus Y of the mixture due to the improved packing efficiency of the system. On the other hand, larger-sized particles are only marginally able to reduce the T_g . The LVE properties, specifically the zero-shear viscosity of the mixtures shows an opposite trend to the Y , where once again the smaller-sized particles better reduce the zero-shear viscosity. This essentially shows the decorrelation of traditional plasticization markers. A reduction in one property does not imply a reduction in another property and this varies with the dimensions and concentration of the additives.

We finally describe our various attempts at developing a multi-bead plasticizer model. For the models we have tried, we tuned the chain lengths of the beads and their interaction with the polymer. Detailed microstructure analysis

and viscoelasticity calculations reveal that they are either incompatible with the polymer, resulting in phase separation, or only marginally compatible over a very limited range.

Acknowledgements

This journey would have been impossible without the mentorship, guidance, and friendship I have received over the years from several people, few of whom I acknowledge below.

I am forever indebted to my advisor – Dr. Li Xi for the opportunity he afforded me to learn under his guidance. He has been instrumental in my development as a researcher. I have never ceased to be amazed at how he handled my unending questions. His patience, thoroughness, helpfulness, and approach to problem-solving have had a profound impact on my academic development. His avuncular supervision has indeed given me a rich foundation to build on. I am also grateful to Dr. Shiping Zhu – my co-advisor for the immensely helpful discussions we had on various topics. The regular meetings we had have helped my presentation skills and contributed in no small measure to the success of this program. I cannot thank Dr. Kari Dalnoki-Veress enough for serving on my committee. His unique insights on my research helped put this project on a sound footing. The polymer physics class he taught also helped break down some of the rather knotty concepts.

I am indebted to several members of the Xi research group – Naveen Vasudevan, Kushal Panchal, and Dr. Lu Zhu for their various help along the way. Dr. Dongyang Li deserves a special mention – his friendship, words of encouragement, and sound advice from time to time helped calm some nerves and quiet some fears I had along the way. My profound appreciation also goes to Dr. Adedapo Awolayo of the University of Calgary, I drew a lot of strength from

our conversations on myriads of issues – from research to writing and different opportunities in general.

I am grateful to my parents and siblings for their prayers and steadfast support through the years. Your love and care are forever treasured.

Lastly, I cannot thank my wife – Ànúolúwapò enough. The unwavering support, encouragement, and prayers she has consistently showered me with have made this journey a lot less burdensome than it could have otherwise been. I had my daughter – Tamilore during this program and her cries, smiles, giggles, and laughs surely added a lot of color to the final phase of this journey.

Contents

| | |
|---|------------|
| Abstract | iii |
| Acknowledgements | vii |
| 1 Introduction | 1 |
| 1.1 Background | 1 |
| 1.1.1 Monodisperse Polymers | 3 |
| 1.1.2 Polydispersity | 4 |
| 1.1.3 Plasticized Polymers | 5 |
| 1.2 Polymer Dynamics and Viscoelastic Properties | 5 |
| 1.2.1 Rouse Model | 6 |
| 1.2.2 Tube and Reptation Model | 8 |
| 1.2.3 Linear Viscoelasticity | 9 |
| 1.3 Coarse-Graining | 11 |
| 1.4 Dissertation Outline | 13 |
| References | 15 |
| 2 Methods for determining the entanglement strand length | 18 |
| 2.1 Introduction | 19 |
| 2.2 Simulation Details | 23 |

| | | |
|----------|---|-----------|
| 2.3 | Theory | 26 |
| 2.3.1 | Mean Square Displacement (MSD) | 26 |
| 2.3.2 | Rouse Mode Analysis (RMA) | 30 |
| 2.4 | Results | 32 |
| 2.4.1 | MSD | 32 |
| 2.4.2 | RMA | 41 |
| 2.5 | Discussion | 43 |
| 2.6 | Conclusions | 46 |
| | References | 47 |
| 3 | Methods for calculating linear viscoelastic properties | 52 |
| 4 | Viscoelastic properties of bidisperse polymer melts | 71 |
| 5 | Viscoelastic and thermo-mechanical properties of polymer-additive mix- tures | 89 |
| 5.1 | Introduction | 90 |
| 5.2 | Model and Methods | 93 |
| 5.3 | Results and Discussion | 98 |
| 5.3.1 | Glass Transition Temperature T_g | 98 |
| 5.3.2 | Young's Modulus | 103 |
| 5.3.3 | Linear Viscoelasticity | 106 |
| 5.3.4 | Voronoi Analysis | 114 |
| 5.3.5 | Rouse Mode Analysis | 117 |
| 5.3.6 | Mean Square Displacement | 122 |
| 5.4 | Conclusion | 127 |

| | |
|--|------------|
| References | 129 |
| 6 Polymer-plasticizer mixtures with more realistic plasticizer models | 137 |
| 6.1 Introduction | 138 |
| 6.2 Models and Methods | 142 |
| 6.2.1 Polymer Model and Simulation Procedure | 142 |
| 6.3 Results | 147 |
| 6.3.1 Phase Separation | 148 |
| 6.3.2 Temperature Effects | 168 |
| 6.3.3 Linear Viscoelasticity | 170 |
| 6.4 Discussion | 174 |
| 6.5 Conclusion | 175 |
| References | 177 |
| 7 Conclusions and Contributions | 183 |

List of Figures

| | | |
|-----|--|----|
| 2.1 | Schematic of a polymer chain confined in a tube by surrounding matrix chains. The tube step length is a and the dashed line in the middle of the tube segments represents the primitive path of the chain. ^{2,10} | 20 |
| 2.2 | Schematic of the mean square displacement of internal monomers of entangled chains plotted as a function of time. The five distinct timescales and their corresponding values and are shown. | 28 |
| 2.3 | Mean square displacement of internal monomers $g_1(t)$ of $N = 500$. The vertical lines are chosen based on visual inspection and indicate the region over which the initial regression is carried out. | 33 |
| 2.4 | Scaling law exponents of the monomer mean square displacement $g_1(t)$ plotted against time for $N = 500$ [(a), (c), and (e) are obtained from large blocks to determine the ranges for the 1.0, 0.5, and 0.25 scaling exponents respectively, (b), (d), and (f) are the more refined plots for exponents obtained by using smaller blocks for the regression]. The horizontal lines are included as a guide to the eye to indicate the scaling law. | 35 |

| | | |
|-----|---|----|
| 2.5 | Scaling law exponents of the monomer mean square displacement $g_1(t)$ plotted against time for $N = 500$ [(g) and (i) are obtained from large blocks to determine the ranges for the 0.5, and 1.0 scaling exponents respectively, (h) and (j) are the more refined plots for exponents obtained by using smaller blocks for the regression]. | 36 |
| 2.6 | Mean square displacement of internal monomers $g_1(t)$ of chains $N = 200, 350$ and 500 . The three curves overlap until $t \sim \mathcal{O}(10^4)$ before they separate. Vertical offsets have been added to the $N = 200$ and $N = 350$ for clarity. | 39 |
| 2.7 | Mean square displacement of the center of mass of the chains $g_{31}(t)$ of chains $N = 200, 350$, and 500 . The intermediate scaling shows a power law of $t^{\sim 0.6}$ | 40 |
| 2.8 | Scaling law exponents for center of mass mean square displacement ($g_3(t)$ plotted against time for $N = 500$ [(a) is obtained from large blocks to determine the ranges for the 0.5 scaling exponents (b) is the more refined plots for the exponents obtained by using smaller blocks for the regression]. The horizontal lines are included as a guide to the eye to indicate the scaling law. | 41 |
| 2.9 | Rouse mode analysis with stretched exponential fitting – stretching parameter β_p of $N = 200, 350$, and 500 | 42 |

| | | |
|-----|---|-----|
| 5.1 | Glass transition temperature T_g of pure and additive polymer melt $N = 100$ determined from the dependence of the specific volume on temperature. Vertical offsets are added to the $\phi = 0.01$ and 0.1 curves by a factor of 1.25 and 0.77 respectively to make the plot clearer. | 99 |
| 5.2 | Change in glass transition temperature ΔT_g for additive concentration from 1% to 30% of various additive sizes. Error bars represent standard error over 3 independent samples and are smaller than marker sizes. | 100 |
| 5.3 | Temperature dependence of the specific volume for a Lennard-Jones liquid at a pressure of 2.0 showing a jump singularity. . . . | 101 |
| 5.4 | Young's modulus Y for pure polymer and some selected mixtures. The linear portion of the strain used for the calculation was 2% of the overall strain. | 104 |
| 5.5 | Change in Young's Modulus $\Delta Y(Y - Y_0)$ for plasticizer concentration from 1% to 30% of various additive sizes. The error bars represent standard error over 100 independent configurations and are smaller than the markers. | 105 |
| 5.6 | Young's modulus and glass transition temperature for various bead sizes at an additive concentration $\phi_B = 0.01$ | 107 |
| 5.7 | Stress relaxation modulus $G(t)$ at $\phi_B = 0.05$ | 109 |
| 5.8 | Zero-shear viscosity η_0 and Young's modulus Y for various bead sizes at an additive concentration $\phi_B = 0.05$ | 111 |
| 5.9 | G' for polymer-additive mixture at an additive concentration of $\phi_B = 0.05$ | 113 |

| | | |
|------|---|-----|
| 5.10 | G'' for polymer-additive mixture at an additive concentration of $\phi_B = 0.05$ | 113 |
| 5.11 | Probability density function of normalized Voronoi volume of (a) polymer beads at $\sigma_B = 0.5$ (b) additive beads at $\sigma_B = 0.5$ (c) polymer beads at $\sigma_B = 1.0$ (d) additive beads at $\sigma_B = 1.0$ for selected concentration. Each Voronoi volume (V_f) is normalized by that of its enclosed particle (V_p) | 116 |
| 5.12 | Probability density function of Voronoi volume at $\phi_B = 0.05$ for various bead sizes. | 117 |
| 5.13 | Rouse Mode Analysis of the polymer-additive mixture at $\phi_B = 0.05$ for various bead sizes. | 120 |
| 5.14 | Mean square displacement of (a) the polymer chains, (b) the plasticizer additives at $T = 0.4$ | 124 |
| 5.15 | Mean square displacement $g_3(t)$ of the polymer in the polymer-additive mixture at $T = 1.0$ | 126 |
| 6.1 | Chemical structure of Bis(2-ethylhexylphthalate) DEHP | 144 |
| 6.2 | Generic Plasticizer Model | 144 |
| 6.3 | Visualization of a well-mixed polymer-plasticizer mixture prior to phase separation. The blue beads the polymer beads. The red and yellow beads make up the plasticizer beads. The yellow beads serve as attractive anchor points to enhance miscibility with the blue polymer beads. | 149 |

| | | |
|-----|--|-----|
| 6.4 | Time-dependent coordination number showing the evolution of the microstructure at $\epsilon = 0.3, 1.2,$ and 4.0 . These plots are typical for our systems and indicate the structure has reached a steady state. | 152 |
| 6.5 | Model A. Phase separation and compatibility between the polymer and plasticizer beads at 100 TUs. The blue B and red R beads are the polymer and plasticizer beads respectively. The yellow beads (Y) are part of plasticizer beads and are tuned to make the plasticizer chain more attractive to the polymer chain. The figures are the ϵ interaction between the B and Y beads (a) $\epsilon = 0.3$ (phase separation), (b) $\epsilon = 1.2$ (phase separation), and (c) $\epsilon = 4.0$ (compatibility). | 153 |
| 6.6 | Model C. Phase separation and microphase separation between the polymer and plasticizer beads at 100 TUs. The blue B and red R beads are the polymer and plasticizer beads respectively. The yellow beads Y are part of plasticizer beads and are tuned to make the plasticizer chain more attractive to the polymer chain. The figures are the ϵ interaction between the B and Y beads (a) $\epsilon = 0.3$ (phase separation), (b) $\epsilon = 1.2$ (phase separation), and (c) $\epsilon = 4.0$ (microphase separation). | 153 |
| 6.7 | Radial distribution function $g(r)$ of model A, $R - Y - R - Y - R$. The figures are the ϵ interaction between the B and Y beads at (a) $\epsilon = 0.3$ (phase separation), (b) $\epsilon = 1.2$ (phase separation), and (c) $\epsilon = 4.0$ (compatibility) | 154 |

| | | |
|------|---|-----|
| 6.8 | Radial distribution function $g(r)$ of model C, $R - R - R - Y - R - Y - R - R - R$. The figures are the ϵ interaction between the B and Y beads at (a) $\epsilon = 0.3$ (phase separation), (b) $\epsilon = 1.2$ (phase separation), and (c) $\epsilon = 4.0$ (microphase separation). | 155 |
| 6.9 | Model D. Phase separation and compatibility between the polymer and plasticizer beads at 100 TUs. The blue B and red R beads are the polymer and plasticizer beads respectively. The yellow beads (Y) are part of plasticizer beads and are tuned to make the plasticizer chain more attractive to the polymer chain. The figures are the ϵ interaction between the B and Y beads showing (a) $\epsilon = 0.1$ (phase separation), (b) $\epsilon = 3.0$ (compatibility), and (c) $\epsilon = 5.0$ (compatibility). | 158 |
| 6.10 | Model F. Phase separation and microphase separation between the polymer and plasticizer beads at 100 TUs. The blue B and red R beads are the polymer and plasticizer beads respectively. The yellow beads Y are part of plasticizer beads and are tuned to make the plasticizer chain more attractive to the polymer chain. The figures are the ϵ interaction between the B and Y beads (a) $\epsilon = 0.1$ (phase separation), (b) $\epsilon = 3.0$ (microphase separation), and (c) $\epsilon = 5.0$ (microphase separation). | 158 |
| 6.11 | Radial distribution function for model D. The figures are the ϵ interaction between the B and Y beads (a) $\epsilon = 0.1$ (phase separation), (b) $\epsilon = 3.0$ (compatibility), and (c) $\epsilon = 5.0$ (compatibility) . . . | 159 |

| | | |
|------|--|-----|
| 6.12 | Radial distribution function for model F. The figures are the ϵ interaction between the (B) and (Y) beads (a) $\epsilon = 0.1$ (phase separation), (b) $\epsilon = 3.0$ (microphase separation), and (c) $\epsilon = 5.0$ (microphase separation) | 160 |
| 6.13 | Model G. Phase separation, microphase separation, and compatibility between the polymer and plasticizer beads. The blue B and red R beads are the polymer and plasticizer beads respectively. The yellow beads (Y) are part of plasticizer beads and are tuned to make the plasticizer chain more attractive to the polymer chain. The figures are the ϵ interaction between the B and Y beads (a) $\epsilon = 0.1$ (phase separation), (b) $\epsilon = 2.0$ (microphase separation), and (c) $\epsilon = 5.0$ (compatibility). | 162 |
| 6.14 | Model I. Phase separation and microphase separation between the polymer and plasticizer beads. The blue B and red R beads are the polymer and plasticizer beads respectively. The yellow beads (Y) are part of plasticizer beads and are tuned to make the plasticizer chain more attractive to the polymer chain. The figures are the ϵ interaction between the B and Y beads (a) $\epsilon = 0.3$ (phase separation), (b) $\epsilon = 2.0$ (microphase separation), and (c) $\epsilon = 4.0$ (microphase separation). | 162 |
| 6.15 | Radial distribution function for model G. The figures are the ϵ interaction between the B and Y beads (a) $\epsilon = 0.1$ (phase separation), (b) $\epsilon = 2.0$ (microphase separation), and (c) $\epsilon = 5.0$ (compatibility) | 163 |

| | | |
|------|--|-----|
| 6.16 | Radial distribution function for model I. The figures are the ϵ interaction between the (B) and (Y) beads (a) $\epsilon = 0.3$ (phase separation) (b) $\epsilon = 2.0$ (microphase separation), and (c) $\epsilon = 4.0$ (microphase separation) | 164 |
| 6.17 | Phase separation and compatibility between the polymer and plasticizer beads of model J. The blue <i>B</i> and red <i>R</i> beads are the polymer and plasticizer beads respectively. The yellow beads <i>Y</i> are part of plasticizer beads and are tuned to make the plasticizer chain more attractive to the polymer chain. The figures are the ϵ interaction between the <i>B</i> and <i>Y</i> beads (a) $\epsilon = 0.1$ (phase separation), (b) $\epsilon = 1.0$ (phase separation), and (c) $\epsilon = 5.0$ (compatibility). | 165 |
| 6.18 | Radial distribution function for model J. The figures are the ϵ interaction between the (B) and (Y) beads (a) $\epsilon = 0.1$ (phase separation), (b) $\epsilon = 1.0$ (phase separation), and (c) $\epsilon = 5.0$ (compatibility) | 166 |
| 6.19 | Summary of the phase separation of the various models. We used ϵ values of 0.1, 0.3, 0.5, 1.0, 1.2, 1.5, 2.0, 3.0, 4.0, and 5.0. Red represents the phase separation region, yellow the microphase separation, and green represents regions where the plasticizer and polymer are compatible. | 167 |
| 6.20 | Radial distribution function $g(r)$ for model A at different temperatures. The ϵ interaction was kept at 1.5 between the <i>B</i> and <i>Y</i> beads (a) $T = 0.4$, (b) $T = 0.8$ (c) $T = 1.0$, and (d) $T = 1.2$ | 169 |

6.21 Stress relaxation modulus $G(t)$ and zero-shear viscosity η_0 for models A, G, and J at a temperature of 1.0. The pure polymer and polymer mixed with a short chain additive N_s equal in length to the plasticizer length are included as references. 173

List of Tables

| | | |
|-----|--|-----|
| 2.1 | Time for the intersection of the different fitting lines to the power regimes extracted from the pure $N = 200$, $N = 350$, $N = 500$ melt MSD curve. | 38 |
| 2.2 | The characteristic times τ_0 , τ_e , τ_R , and τ_d for the pure $N = 200$, $N = 350$, $N = 500$ melt MSD curve. | 38 |
| 2.3 | N_e calculated from the different equations of MSD given in eq. (2.25)–eq. (2.27) and from RMA | 38 |
| 5.1 | Detailed compositions of polymer-plasticizer systems simulated at various plasticizer mass fractions. σ_B , m_B , M_B , and M_A are the plasticizer size, mass of each plasticizer particle, total mass of the plasticizer, and total mass of the polymer chains respectively. The length of the polymer chain was kept constant at $N = 100$ | 97 |
| 6.1 | Multi-bead model configuration of the form (R) n –(Y) k –(R) m –(Y) k –(R) n where n and m are the leg and torso length respectively | 145 |

Chapter 1

Introduction

1.1 Background

Polymer is a broad term that encompasses materials such as plastics, thermosets, and elastomers. With over 350 million tons of plastic produced in 2018¹ and a North American per capita consumption of some polymers like polyethylene, polypropylene, and polyvinyl chloride of about 65kg/person, polymers have become the bedrock of the world's current technological innovation and contempt. They have important applications in virtually all industries – implantable pacemakers in the health sector, aircraft wings in transportation, piping in construction, etc...The primary reasons why polymers are so popular are due to their exceptional properties; light weight, high flexibility, the ease with which they can be customized and their longevity² – which ironically is also the bane of their existence.

Although a lot of progress has been made in our understanding of the response of polymers to flows, there are still some gaps in our understanding

of some observed features. For example the nature of entanglements have not been completely resolved; the entanglement length N_e , which is one of the important concepts in the tube and reptation model³⁻⁵ of polymer dynamics, still varies with the method of determination.^{6,7} The wide range of spatial and time scales inherent in these polymer materials, which are largely responsible for their excellent features, do not make their analysis any easier when compared with smaller molecules. For example, water is made up of small molecules and is homogeneous on length scales of $\mathcal{O}(1\text{\AA})$ whereas for a polymer, due to the connectivity of several monomers making up the polymer chain, there are different length scales spanning – a single bond $\mathcal{O}(1\text{\AA})$, persistence length $\mathcal{O}(10\text{\AA})$, entanglement length⁸ $\mathcal{O}(100\text{\AA})$ to the whole chain segment – which can be several thousands more than the smallest length scale. These different length scales fluctuate on timescales that span the order of picoseconds for the bond length to minutes for the whole chain segment.^{9,10} These different time and length scales contribute to the dynamics and stress relaxation processes observed in polymer melts in a non-trivial manner and should be accounted for. In this thesis, we focus on the dynamics and viscoelasticity of three polymer systems – monodisperse, polydisperse, and plasticized polymers. We apply molecular dynamics (MD) methods to these three systems. Our simulations reveal how different molecular parameters affect some of the observed viscoelastic features.

This chapter lays the foundation for this thesis. It introduces our foci for these 3 systems as well as the main theoretical underpinnings of polymer dynamics. We then discuss the archetypal aspects of the linear viscoelasticity of

polymers. We briefly cover the coarse-grained model of the polymer chain that we used throughout the thesis and finish off by giving an outline for the subsequent chapters.

1.1.1 Monodisperse Polymers

Monodisperse polymers consist of chains of uniform length. A lot of theoretical^{4,11} and molecular simulation^{9,12,13} work have focused on monodisperse polymers to understand how polymers behave under different conditions. One of the most consequential theories of polymer dynamics - the tube and reptation model (discussed in section 1.2.2), that describes the dynamics of long entangled polymer chains, predicted different dynamical regimes that are distinctly marked by unique power law time scales. These scales have been verified in several molecular simulation studies..^{6,12,14,15} In this thesis, we use monodisperse polymers to devise a protocol for the reliable estimation of these time scales. Another significant outcome of the tube model is the concept of entanglement length, where the topological restrictions due to the long length of the polymer chain are rather dominant. Although our long term goal was to study the viscoelasticity of polydisperse polymers and polymer mixtures, this part of the thesis research focused on monodisperse polymers to get a few "tools" ready. Specifically, we attempt to extract the entanglement length from our monodisperse systems. We use these results throughout the rest of the thesis. Since we discuss the linear viscoelasticity rather extensively too, we compare different methods for computing the linear viscoelastic properties in MD simulation using our monodisperse systems.

1.1.2 Polydispersity

Regardless of the polymerization technique employed in the production process, polydispersity is inevitable in industrially produced polymers.^{16,17} The theories of polymer dynamics on monodisperse linear polymers are more established. Here, we use MD to explore how the different chains affect each other's dynamics in a mixture. We idealize a polydisperse system with a bidisperse system containing two different chain lengths – one short chain and one long chain. The main framework for discussing the dynamics of the chains is based on their lengths and are the Rouse model for short, unentangled melts (discussed in section 1.2.1) and the tube and reptation model for longer, entangled chains (discussed in section 1.2.2). The viscoelastic properties of interest are also discussed in section 1.2.3. More specifically, our objectives here are three-fold:

- Quantify the effect a long chain has on the dynamics of the short chain and vice-versa. Since the dynamics of a polymer chain is strongly affected by the chain length, we varied the chain lengths to span the 2 dominant regimes of polymer dynamics – unentangled and entangled regimes.
- Evaluate the extent to which topological constraints of the longer chains are affected by the presence of the shorter chains.
- Use the viscoelastic profiles of the individual components of the bidisperse system to predict the bulk viscoelasticity of the mixture using a semi-empirical mixing rule.

1.1.3 Plasticized Polymers

Pure polymers are rarely used by themselves in their pure form. They are usually blended with some other additives to yield intermediate products that can be subsequently processed into other suitable forms like powder, flakes, pellets or granules. These additives include colorants, fillers, stabilizers, anti-oxidants, flame retardants, plasticizers, and other polymers to produce blends or alloys. Of these additives, plasticizers account for more than one-third of all the global additives market.^{18,19} Primarily, plasticizers are employed to enhance the processability, flexibility, or distensibility of the polymer. They reduce the glass transition temperature T_g of the polymer material as well as their mechanical properties. Despite their huge importance, the mechanisms by which plasticizers work are not yet fully understood.²⁰ We use MD to investigate the molecular factors affecting the viscoelasticity of plasticized polymers. For the model employed, prior work has shown that the plasticization effect depends strongly on the concentration and molecular sizes of the plasticizers.²¹⁻²³ Specifically, we focus on how the molecular structure of the plasticizers affect the linear viscoelastic properties.

1.2 Polymer Dynamics and Viscoelastic Properties

The dynamics and viscoelastic properties of polymer melts are very important in several fields such as biology and the plastic industry. They govern flow behavior during polymer processing. The dynamics of polymer melts are generally classified based on the polymer chain lengths: short, unentangled chains and long, entangled chains. For short, unentangled melts, their dynamics and

viscoelasticity are well described by the Rouse model wherein the diffusion coefficient D scales as N^{-1} and viscosity $\eta \sim N$. When the chains are sufficiently long and topological interactions between the chains are significant, i.e., entangled, the tube model and reptation mode of relaxation typically describes the dynamics and stress relaxation. Here, $D \sim N^{-2}$ and $\eta \sim N^3$. Several experimental studies^{10,24} however report $\eta \sim N^{3.4}$. The quantitative discrepancies have been attributed to the presence of other relaxation mechanisms other than reptation.

1.2.1 Rouse Model

The Rouse model²⁵ is the simplest model describing the dynamics of a polymer chain. The model assumes a Gaussian chain and represents the chain as a bead-spring model consisting of N beads and $N - 1$ springs and considers all the other surrounding chains as a continuous viscous medium. Each bead experiences a frictional force proportional to its velocity. The dynamics of each bead on the test chain can be described by the inertia-less Langevin equation. The equation of motion of the i -th bead can then be written as

$$\zeta \frac{d\vec{r}_i}{dt} = H_s [(\vec{r}_{i+1} - \vec{r}_i) - (\vec{r}_i - \vec{r}_{i-1})] + \vec{f}_i^r \quad (1.1)$$

where ζ is the monomeric friction coefficient, $H_s = 3k_B T/b^2$ (k_b is the Boltzmann constant, T is the temperature, and b is the bond length) is the spring constant, \vec{r}_i is the position of the i -th bead, and \vec{f}_i^r is the random force exerted

on the i -th bead satisfying

$$\langle \vec{f}_i^r(t) \vec{f}_j^r(t') \rangle = 2\zeta k_B T \delta_{ij} \delta(t - t') \vec{\delta} \quad (1.2)$$

where $\delta(t)$ is the Dirac delta function, δ_{ij} is the Kronecker delta, and $\vec{\delta}$ is the identity tensor. The Rouse model does not explicitly account for interactions such as excluded volume and hydrodynamic interaction except that due to the chain connectivity. It further assumes all the other interactions can be subsumed into the friction coefficient. Despite the crude approximations, the model has been found to adequately describe the dynamics of unentangled polymer melts.⁵ Equation 1.1 can be solved by projecting the original bead coordinates \vec{r}_i to a set of mutually orthogonal coordinates known as Rouse modes or normal coordinates \vec{X}_p ($p = 0, 1, \dots, N - 1$).

$$\vec{X}_p \equiv \sqrt{\frac{2}{N}} \sum_{n=1}^N \vec{r}_n(t) \cos\left(\frac{(i - 1/2)p\pi}{N}\right) \quad (1.3)$$

$(p = 0, 1, 2, \dots, N - 1)$

The $p = 0$ mode describes the motion of the center of mass of the chain and the other modes ($1 \leq p \leq N - 1$) describe the internal relaxations of sub-chains, or "blobs", of the size of N/p beads. Each of the transformed coordinate or Rouse mode \vec{X}_p follows Langevin dynamics with its own friction coefficient and random force. Importantly, relaxation of different modes is mutually independent. The autocorrelation function (ACF) of each $p > 1$ mode decays exponentially

$$\langle \vec{X}_p(t) \vec{X}_p(0) \rangle = \langle \vec{X}_p^2 \rangle \exp\left(-\frac{t}{\tau_p}\right) \quad (1.4)$$

with its own relaxation time τ_p given by

$$\tau_p^{-1} = \frac{12k_B T}{\zeta b^2} \sin^2 \left(\frac{p\pi}{2N} \right) \quad (1.5)$$

where b^2 is the mean-square bond (spring) length. For leading modes with $p \lesssim N/5$, which describes the motions of larger segments with $N/p \gtrsim 5$ beads, eq. (5.20) can be approximated by²⁵

$$\tau_p = \frac{\zeta b^2}{3\pi^2 k_B T} \left(\frac{N}{p} \right)^2. \quad (1.6)$$

and the relaxation modulus $G(t)$ is given by

$$G(t) = \frac{\rho k_B T}{N} \sum_p \exp(-2tp^2/\tau_R) \quad (1.7)$$

1.2.2 Tube and Reptation Model

When a chain exceeds a critical length – called the entanglement length N_e , the Rouse model alone is no longer sufficient to describe its dynamics. The tube model of Edwards³ and the reptation theory by Gennes,⁴ which were subsequently refined by Doi et al.⁵ are used. In this model, topological constraints due to some other chains restrict the motion of a *test chain* along a tube and prevents any lateral excursion of the chain beyond the tube diameter. The axis of this tube is known as the primitive chain and has the same end-to-end distance as the polymer chain. The chain can still wriggle within the confines of the tube but the longer, time-dependent curvilinear diffusive motion of the primitive chain only occurs longitudinally in the tube. This chain motion is referred to

as reptation. The associated curvilinear diffusion coefficient D can be estimated from Einstein's relation

$$D = \frac{kT}{N\zeta} \quad (1.8)$$

where N is the length of the chain and ζ is the chain's monomeric friction coefficient. The time τ_d it takes for the primitive chain to fully *reptate* out of the tube can be estimated²⁶ from

$$\tau_d = \frac{\langle L \rangle^2}{D} \quad (1.9)$$

where L is the length of the primitive chain. The full derivation with the prefactor is⁵

$$\tau_d = \frac{1}{\pi^2} \frac{\zeta N^3 b^4}{k_B T a^2} \quad (1.10)$$

where a is the tube's diameter and b is the bond length between the beads of the chain. The fraction of the tube still occupied by the chain $\psi(t)$ at any time t is

$$\psi(t) = \frac{8}{\pi^2} \sum_{p:odd} \frac{1}{p^2} \exp\left(\frac{-p^2 t}{\tau_d}\right) \quad (1.11)$$

and is proportional to the stress. The $G(t)$ then becomes

$$G(t) = G_N^0 \psi(t) \quad (1.12)$$

where G_N^0 is the plateau modulus.

1.2.3 Linear Viscoelasticity

The linear viscoelasticity of polymeric fluids is usually described based on their response in simple flow fields. The material functions obtained depends on the

flow field used. We describe the steady shear flows and the small amplitude oscillatory motion below.

Steady Shear Flow In steady shear flows also known as planar Couette flow, the polymer particles are free to rotate and there is an extensive vorticity developed in the flow field. The velocity profile is

$$v_x = \dot{\gamma}y \quad (1.13)$$

where $\dot{\gamma}y$ is the shear rate. The equations describing the flow field are

$$\tau_{yx} = -\eta \frac{dv_x}{dy} \quad (1.14)$$

$$\tau_{xx} - \tau_{yy} = -\psi_1 \left(\frac{dv_x}{dy} \right)^2 \quad (1.15)$$

$$\tau_{yy} - \tau_{zz} = -\psi_2 \left(\frac{dv_x}{dy} \right)^2 \quad (1.16)$$

where τ_{ii} is the normal stress and $\tau_{ij}(i \neq j)$ is the shear stress, η is the non-Newtonian viscosity and is dependent on shear rate, ψ_1 and ψ_2 are the first and second normal stress coefficients respectively.

Small Amplitude Oscillatory Shear This is the classical method for determining the viscoelastic response of a fluid. The fluid is subjected to a sinusoidal strain of

$$\gamma(t) = \gamma_0 \sin(\omega t) \quad (1.17)$$

The velocity profile developed in the flow will be nearly linear if the amplitude of the flow is small and fluid is highly viscous.²⁷ Shear stress is then given as

$$\sigma(t) = \gamma_0(G'(\omega) \sin(\omega t) + G''(\omega) \cos(\omega t)) \quad (1.18)$$

G' and G'' give the storage and loss moduli of the fluid respectively, similarly interpreted as a measure of the elastic and viscous content of the fluid. Alternatively, G' and G'' can be obtained from the Fourier integral of $G(t)$

$$G' = \omega \int_0^{\infty} G(t) \sin(\omega t) \quad (1.19)$$

$$G'' = \omega \int_0^{\infty} G(t) \cos(\omega t) \quad (1.20)$$

1.3 Coarse-Graining

In this work, we focus on flexible linear polymers. As mentioned in the earlier sections, owing to the different and extensive time and length scales in polymers, a full atom simulation that specifies the interactions between all the atoms in a real polymer system is prohibitive for determining the rheological properties of a polymer. As mentioned earlier, the time scale of bond fluctuation is of $\mathcal{O}(10^{-13})$ s or even much shorter whereas the stress relaxation phenomena can be observed on $\mathcal{O}(10^2)$ s!^{9,10} Using the most sophisticated parallel computers

available, the time required to completely capture the different observable phenomena is on the order of years. This makes a full-atom simulation of highly entangled chains almost impossible to perform in a conventional sense although there have been several multi-scale approaches²⁸ that attempt to bridge these length and time divides. The implication of these scales for computer simulation is very severe. However, since we are not interested in a specific polymer material but in the general features of the rheological characteristics of our systems and how different molecular parameters affect the bulk properties, we ignore the local chemical details of the monomer and use a coarse-grained model for our studies.

For the pure melt, bidisperse, and plasticized systems, we use a bead-spring model to represent the polymer chains where the beads, representing the monomers, are bonded by finitely extensible and non-linear (FENE) springs. The interaction between the bonded beads is given by

$$U_{\text{FENE}}(r) = -\frac{1}{2}KR_0^2 \ln \left[1 - \left(\frac{r}{R_0} \right)^2 \right] + 4\epsilon \left[\left(\frac{\sigma}{r} \right)^{12} - \left(\frac{\sigma}{r} \right)^6 + \frac{1}{4} \right] \quad (1.21)$$

where r is the distance between the beads and σ and ϵ are the standard Lennard-Jones (LJ) length and energy parameters respectively. The first term of the equation is an attractive potential which models FENE springs between closest neighbors along the chain and has a maximum bond length $R_0 = 1.5\sigma$, while the second term models the excluded-volume repulsion between beads and included at $r \leq 2^{1/6}\sigma$. The spring constant $K = 30\sigma/\epsilon$ allows a reasonable

integration time step and prevents chains from crossing each other.¹² The interaction between non-bonding beads is modeled using the standard LJ potential

$$U_{\text{LJ}}(r) = 4\epsilon \left[\left(\frac{\sigma}{r} \right)^{12} - \left(\frac{\sigma}{r} \right)^6 \right]. \quad (1.22)$$

We truncate the potential at $r = 2.5\sigma$ and shifted by a constant to ensure continuity at the cutoff.

1.4 Dissertation Outline

The motif of this thesis is on the dynamics and rheology of polymers and polymer mixtures. We start in chapter 2 by focusing on a reliable protocol for extracting the different relaxation timescales of flexible, entangled linear polymer chain and also discuss a method for the determination of the entanglement length N_e of the chains using Rouse mode analysis. In chapter 3, we compare different methods of computing linear viscoelasticity from molecular dynamics simulation, with emphasis on the computational resource requirement and discuss the challenges inherent in the application of these methods. In chapter 4, the dynamics and rheology of a bidisperse polymer melt consisting of long chains well in the entangled regime and a short chain spanning unentangled to mildly entangled regime, in different weight fractions are studied in detail. Furthermore, we investigate a mixing rule based on the double reptation model for describing the linear viscoelastic properties of the bidisperse mixture using the relaxation profiles of the monodisperse constituent. We further investigate the molecular parameters affecting the design of polymer-plasticizer mixture using

a single-bead plasticizer model, again focusing on the dynamics and rheology of the mixture as well as the broad factors affecting plasticization in chapter 5. We describe our various attempts at developing a multi-bead plasticizer model in chapter 6, detailing the broad factors affecting plasticizer compatibility with polymers. We conclude the thesis in chapter 7 where we give a summary of the thesis and the main contributions.

References

- [1] European-Plastics. *An analysis of European plastics production, demand and waste data*. Tech. rep. 2019, 1–33.
- [2] L. Xi. Molecular simulation for predicting the rheological properties of polymer melts. *Molecular Simulation* 45(14-15) (2019), 1242–1264.
- [3] S. F. Edwards. Statistical mechanics with topological constraints: I. *Proceedings of the Physical Society (1958-1967)* 91(3) (1967), 513.
- [4] P.-G. de Gennes. Reptation of a polymer chain in the presence of fixed obstacles. *The journal of chemical physics* 55(2) (1971), 572–579.
- [5] M. Doi and S. F. Edwards. *The theory of polymer dynamics*. Vol. 73. oxford university press, 1988.
- [6] M. Pütz, K. Kremer, and G. S. Grest. What is the entanglement length in a polymer melt? *Europhysics Letters* 49(6) (Mar. 2000), 735–741. ISSN: 02955075.
- [7] J.-X. Hou. Note: Determine entanglement length through monomer mean-square displacement. *The Journal of chemical physics* 146(2) (2017), 026101.
- [8] T. McLeish. Tube theory of entangled polymer dynamics. *Advances in physics* 51(6) (2002), 1379–1527.
- [9] K. Binder. *Monte Carlo and molecular dynamics simulations in polymer science*. Oxford University Press, 1995.
- [10] J. D. Ferry. *Viscoelastic properties of polymers*. John Wiley & Sons, 1980.

- [11] M. Doi et al. Dynamics of polymers in polydisperse melts. *Macromolecules* 20(8) (1987), 1900–1906.
- [12] K. Kremer and G. S. Grest. Dynamics of entangled linear polymer melts: A molecular-dynamics simulation. *The Journal of Chemical Physics* 92(8) (1990), 5057–5086.
- [13] M. Kröger, W. Loose, and S. Hess. Rheology and structural changes of polymer melts via nonequilibrium molecular dynamics. *Journal of rheology* 37(6) (1993), 1057–1079.
- [14] Z. Wang, A. E. Likhtman, and R. G. Larson. Segmental dynamics in entangled linear polymer melts. *Macromolecules* 45(8) (2012), 3557–3570. ISSN: 00249297.
- [15] H. P. Hsu and K. Kremer. Static and dynamic properties of large polymer melts in equilibrium. *Journal of Chemical Physics* 144(15) (2016), 154907. ISSN: 00219606.
- [16] J. M. Dealy, D. J. Read, and R. G. Larson. *Structure and rheology of molten polymers: from structure to flow behavior and back again*. Carl Hanser Verlag GmbH Co KG, 2018.
- [17] S. Zhu and A. Hamielec. Polymerization kinetic modeling and macromolecular reaction engineering (2012).
- [18] R. Pfaendner. How will additives shape the future of plastics? *Polymer degradation and stability* 91(9) (2006), 2249–2256.
- [19] M. Rahman and C. S. Brazel. The plasticizer market: an assessment of traditional plasticizers and research trends to meet new challenges. *Progress in polymer science* 29(12) (2004), 1223–1248.

- [20] D. Li et al. An atomistic evaluation of the compatibility and plasticization efficacy of phthalates in poly (vinyl chloride). *Macromolecules* 51(18) (2018), 6997–7012.
- [21] R. A. Riggleman, J. F. Douglas, and J. J. de Pablo. Tuning polymer melt fragility with antiplasticizer additives. *The Journal of chemical physics* 126(23) (2007), 234903.
- [22] R. A. Riggleman, J. F. Douglas, and J. J. de Pablo. Antiplasticization and the elastic properties of glass-forming polymer liquids. *Soft Matter* 6(2) (2010), 292–304.
- [23] K. Panchal. The Effects of Molecular Structure and Design on the Plasticizer Performance Through Coarse-Grained Molecular Simulation. Master's thesis. 2018.
- [24] W. W. Graessley. Polymer chain dimensions and the dependence of viscoelastic properties on concentration, molecular weight and solvent power. *Polymer* 21(3) (1980), 258–262.
- [25] P. E. Rouse Jr. A theory of the linear viscoelastic properties of dilute solutions of coiling polymers. *The Journal of Chemical Physics* 21(7) (1953), 1272–1280.
- [26] M. Rubinstein, R. H. Colby, et al. *Polymer physics*. Vol. 23. Oxford university press New York, 2003.
- [27] R. B. Bird, R. C. Armstrong, and O. Hassager. Dynamics of polymeric liquids. Vol. 1: Fluid mechanics (1987).
- [28] K. Kremer and F. Müller-Plathe. Multiscale problems in polymer science: simulation approaches. *MRS bulletin* 26(3) (2001), 205–210.

Chapter 2

Methods for determining the entanglement strand length

This chapter focuses on two methods – Mean square displacement (MSD) and Rouse mode analysis (RMA) for determining the entanglement length N_e of flexible Kremer-Grest (KG) bead spring model. The (MSD) method is the established method in the literature for extracting N_e . However, it is rather difficult to extract the relevant timescales of interest. Here, we seek to standardize the MSD method for the first time, establish a reliable protocol for calculating N_e , and propose a new approach to extract N_e using (RMA). We conclude by comparing the results from these two approaches.

I carried out the research, including setting up the model, carrying out the simulations, and analyzing the data. I also wrote the initial draft. Li Xi made extensive recommendations, edits, and supervised the whole research.

This chapter is under preparation for future publication.

2.1 Introduction

The entanglement length N_e is one of the fundamental parameters of the tube model.¹ For a long entangled chain, it describes the length scale at which the effects of the topological constraints on the dynamics of a test chain due to matrix chains become noticeable –i.e., a change over from the Rouse dynamics of short sub-segments of an entangled chain to reptation dynamics of the whole chain. It is also the number of monomers contained in the tube diameter.² The tube step length a relates the Kuhn length of the chain b to N_e ,

$$N_e = \frac{a^2}{b^2} \quad (2.1)$$

There are several approaches²⁻⁹ used in the literature to calculate N_e in molecular simulations. The mean squared displacement (MSD) of a monomer, commonly referred to as $g_1(t)$ is a convenient method that tracks the time-dependent trajectory of the individual monomers of a chain. One of the predictions of the reptation model is the slowing down of chain dynamics at intermediate time and length scales, and an eventual diffusive motion after a sufficiently long time when the chain has completely *reptated* out of its tube. This slowing down has been attributed to the presence of entanglements as a result of the *intermolecular* interaction between a test chain and neighboring chains. The surrounding matrix chains form a tube and restricts the motion of the test chain into a longitudinal diffusive motion in the tube. A schematic of the tube model is shown in fig. 2.1. There are distinct time scales associated with these dynamics. The intersection of the fitting lines of these different dynamical regimes occurs near the characteristic relaxation times. This is subsequently used to determine N_e . This

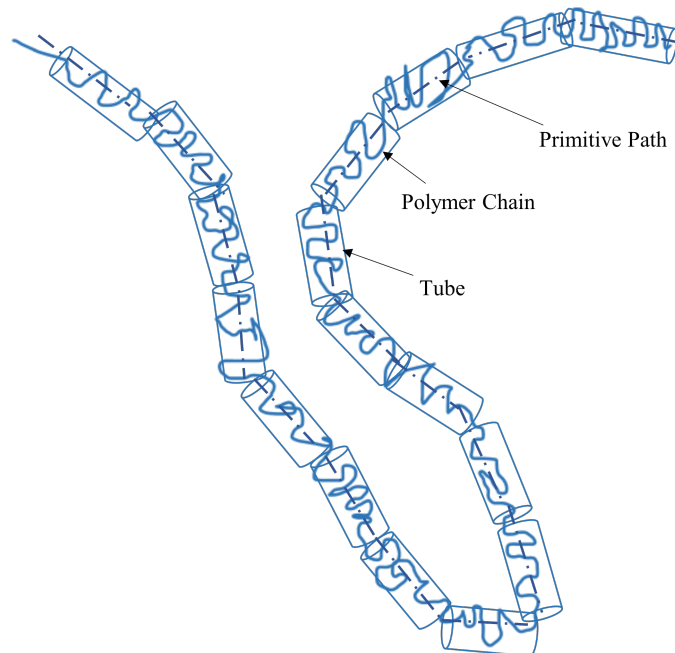


FIGURE 2.1: Schematic of a polymer chain confined in a tube by surrounding matrix chains. The tube step length is a and the dashed line in the middle of the tube segments represents the primitive path of the chain.^{2,10}

was the approach used by Kremer et al.³ and several other authors.^{4,7,8,11,12} For the same fully flexible polymer model, several authors have reported different values using the MSD approach. Kremer et al.³ and Pütz et al.⁴ both reported N_e values close to 32, while Wang et al.⁷ obtained a value of 50. However, Likhtman et al.⁵ argued that the intersection of the fitting lines to the different dynamical regimes does not occur at the characteristic relaxation time of the entanglement strand as done by the previous authors. Rather, the intersection time occurs at a time t^* near the relaxation time. Still, Hou² showed that there is an additional missing prefactor of $\pi/2$ that comes from the Gaussian distribution of the tube's segment displacement and obtained a value of $N_e = 85$. Nevertheless, the MSD method suffers from the fragility of the regression technique or fitting process.

The number of data points used in the fitting procedure can significantly affect the calculated characteristic times at the intersection points and consequently the value of N_e .

In rubber elasticity theory,^{13,14} the presence of cross-links in polymer networks shows up in the stress relaxation modulus $G(t)$ where it relaxes to a finite value G_e in form of a plateau. Entangled polymers are also conceptualized as consisting of temporary cross-links and this is also marked by a prolonged plateau modulus in the $G(t)$ that depends on the chain length. Unlike the cross-linked polymer however, the $G(t)$ eventually decays to zero given sufficient time. The relationship between N_e and G_N^0 is given as,^{5,8,10}

$$G_N^0 = \frac{4}{5} \nu k_B T / N_e \quad (2.2)$$

where ν is the monomer number density of the polymer chains, k_B is the Boltzmann constant, and T is the temperature. In principle, it is possible to calculate N_e from the plateau modulus according to eq. (2.2). However, in MD simulations, the $G(t)$ is notoriously difficult to calculate due to the fluctuations intrinsic to small scale systems that dominate the $G(t)$ signal. By pre-averaging the stress tensor to improve the signal-noise ratio, Hsu et al.⁸ used this method to calculate N_e for semi-flexible KG chains with comparable results with other methods.

Another method commonly used relies on the primitive path (PP) of the polymer chain. As shown in fig. 2.1, the PP is the shortest path between the two ends of the original chain and lies along the axis of the tube. It is obtained by

fixing both ends of the chain and contracting the chain into a contour while preserving the non-crossability constraints with the other chains.^{15,16} The Primitive Path Analysis (PPA) method was first developed by Everaers et al.^{17,18} In this approach, an energy minimization run is carried out where the non-bonded repulsive interactions between contiguous chain beads are turned off while chain ends are fixed in space. This permits the chains to contract to their PP length under the action of their own spring forces and also due to the topological constraints imposed by the surrounding chains.^{16,19} The resulting primitive path is still a random walk at larger scales and can be mapped to freely jointed chains to calculate the entanglement parameters. Other authors have used different protocols for shrinking the chains to obtain the primitive path. The Z1 algorithm of Kröger²⁰ and the CReTA code developed by Tzoumanekas et al.²¹ use a geometric minimization approach to shrink the contour lengths of the chains while their ends are fixed and the topological constraints imposed by the surrounding chains are preserved. The resulting PPs are tensionless lines and the points of contact between the lines signify the entanglement points. However, the N_e obtained from these two approaches differ by a factor of 2 which Everaers¹⁸ have explained by appealing to the phantom network model of rubber elasticity. Indeed, these different results for N_e from the various PPA methods greatly underscore how important it is to define the underlying assumptions or models when reporting N_e values. Some of the criticisms of the PPA model include; the artificial contraction of the chains which destroys the original melt structure of the chain, since real chains do not shrink¹⁹ and the need to extrapolate the results to an infinite long chain.²

In this work, our goals are two-fold: (i) to standardize the MSD approach for determining the intersection of the timescales, and (ii) to explore the Rouse Mode Analysis (RMA) method for calculating N_e . Given how sensitive the MSD approach is to the regression technique, it is tempting to avoid this difficulty by using the RMA method. For the first time, we attempt to use the RMA to calculate N_e . The large uncertainties inherent in the MSD are significantly reduced. The applicability of Rouse modes to unentangled melts is well established in the literature.^{3,22,23} For entangled chains, Rouse modes can still be applied by using a stretched exponential to capture the chain relaxation^{24–26} as further discussed in the later sections. We proceeded by discussing the chain model and numerical methods used (section 2.2). We then followed with a discussion on the relevant theories of the MSD and RMA methods. We demonstrate our procedure for the extraction of the relevant timescales and the extraction of N_e in both methods in section 2.4.

2.2 Simulation Details

We use the KG bead-spring model³ where each chain consists of N beads bonded by finitely extensible non-linear elastic (FENE) springs.²⁷ The potential between bonded beads is

$$U_{\text{FENE}}(r) = -\frac{1}{2}KR_0^2 \ln \left[1 - \left(\frac{r}{R_0} \right)^2 \right] + 4\epsilon \left[\left(\frac{\sigma}{r} \right)^{12} - \left(\frac{\sigma}{r} \right)^6 + \frac{1}{4} \right] \quad (2.3)$$

where r is the distance between the beads and σ and ϵ are the standard Lennard-Jones (LJ) length and energy parameters. The first term of the equation represents an attractive potential which models FENE springs between nearest neighbors along the chain with a maximum bond length $R_0 = 1.5\sigma$, while the second term models the excluded-volume repulsion between beads and the term is only included at $r \leq 2^{1/6}\sigma$. The spring constant $K = 30\sigma/\epsilon$ is chosen to allow a reasonable integration time step while preventing chains from crossing each other.³ The interaction between non-bonding beads is modeled by the standard LJ potential

$$U_{\text{LJ}}(r) = 4\epsilon \left[\left(\frac{\sigma}{r}\right)^{12} - \left(\frac{\sigma}{r}\right)^6 \right]. \quad (2.4)$$

The potential is truncated at $r = 2.5\sigma$ and shifted by a constant to ensure continuity at the cutoff. Hereinafter, all results will be reported in reduced LJ units in which length, energy, time, and temperature are scaled by σ , ϵ , $\tau = \sqrt{m\sigma^2/\epsilon}$, and ϵ/k_{B} (k_{B} is the Boltzmann constant), respectively. A constant time step of 0.01 (in LJ time units or TUs) is used for all simulation.

We used chain lengths $N = 200, 350$, and 500 . Each system contains $50,000$ beads except for $N = 350$ with $56,000$ beads. The beads were placed in a cubic box with periodic boundary conditions at a constant bead density of 0.85 . All the simulations were carried out using the Large-scale Atomic/Molecular Massively Parallel Simulator (LAMMPS) package.²⁸ The initial configuration was generated by randomly placing the specified number and types of chains in the simulation cell. Generation of the individual chains follows a procedure that is

analogous to a self-avoiding walk in a continuum space, which prevents back-folding of successive bonds but still leaves a large number of bead overlaps. A dissipative particle dynamics (DPD) push-off method,²⁹ originally proposed by Sliozberg et al.³⁰ was then used to obtain an equilibrated structure for production runs. During the DPD run, interaction between non-bonding beads was replaced by a soft repulsive potential of the form of

$$U_{\text{DPD}}(r) = \begin{cases} \frac{A_{\text{DPD}}}{2} r_c \left(1 - \frac{r}{r_c}\right) & r < r_c \\ 0 & r \geq r_c \end{cases}. \quad (2.5)$$

DPD simulation was run at $T = 1.0$ using a cut-off distance $r_c = 1.0$. The potential was initially low with $A_{\text{DPD}} = 25$. At the beginning, restriction was imposed on the maximum distance each bead can move within one time step which gradually increases from 0.001 to 0.1 over 15 TUs. The restriction was then removed and the simulation was run for another 100 TUs. This was subsequently followed by a gradual ramp of A_{DPD} to 1000 over 5.5 TUs. The DPD potential was then replaced with the standard LJ potential and MD in an NVT ensemble was performed for additional 500 TUs during which a random velocity distribution was reassigned to all beads every 0.5 TUs. Equilibration quality was examined through the mean square internal displacement (MSID)

$$\langle R^2(n) \rangle \equiv \langle |\vec{r}_j - \vec{r}_i|^2 \rangle \quad (2.6)$$

which measures the square distance between the i -th and j -th monomeric unit of the same chain, averaged over all ij -pairs with the same index separation

$n \equiv |j - i|$. Auhl et al.³¹ showed that, compared with the radial distribution function, end-to-end distance and radius of gyration, MSID better captures chain deformation at intermediate scales which does not fully relax until the whole chain is equilibrated.

For each cell composition, three random initial configurations were independently generated and each underwent the above equilibration procedure before its production run. The production run of each configuration lasted for a total of 3×10^6 TUs for $N = 200$ and $N = 350$ cases and 6×10^6 TUs for the $N = 500$ case. Results reported in this study were averages over these three trajectories from independent initial configurations unless specified otherwise. Error bars report the standard error between the independent runs.

2.3 Theory

2.3.1 Mean Square Displacement (MSD)

The dynamics of an entangled polymer melt can be studied using the mean-squared displacement (MSD) of a monomer, $g_1(t)$ of a polymer chain

$$g_1(t) = \frac{1}{n_c N} \sum_{i=1}^{n_c} \sum_{j=1}^N [\vec{r}_{ij}(t) - \vec{r}_{ij}(0)]^2 \quad (2.7)$$

or the MSD of the center of mass, $g_3(t)$ of an individual chain averaged over the total number of chains present in the system

$$g_3(t) \equiv \frac{1}{n_c} \sum_{i=1}^{n_c} [\vec{r}_{i,c.m.}(t) - \vec{r}_{i,c.m.}(0)]^2 \quad (2.8)$$

where

$$\vec{r}_{i,c.m.}(t) \equiv \frac{1}{N_i} \sum_{j=1}^{N_i} \vec{r}_{ij}(t), \quad (2.9)$$

n_c is the number of chains, N_i is the length of the i -th chain, $\vec{r}_{ij}(t)$ is the position of the j -th monomer of the i -th chain, and $\vec{r}_{i,c.m.}(t)$ is the position of the center of mass of the i -th chain.

According to the reptation model^{1,4,32} there are four distinct power law regimes associated with the monomer motion $g_1(t)$ in an entangled melt at times $t > \tau_0$ (τ_0 is the characteristic time required for a monomer to move an order of its size). The different power law time scaling for $g_1(t)$ and $g_3(t)$ are theoretically predicted to be,

$$g_1(t) = \begin{cases} 6b^2(Wt) & t \leq \tau_0 \\ 2\sqrt{\frac{3}{\pi}}b^2(Wt)^{1/2} & \tau_0 \leq t \leq \tau_e \\ \beta\left(\frac{4}{3\pi}\right)^{1/4}ab(Wt)^{1/4} & \tau_e \leq t < \tau_R \\ \beta\sqrt{\frac{2}{N}}ab(Wt)^{1/2} & \tau_R \leq t \leq \tau_d \\ 2\frac{a^2}{N^2}Wt^1 & t \geq \tau_d \end{cases} \quad (2.10)$$

and

$$g_3(t) = \begin{cases} 6\frac{b^2}{N}Wt & t \leq \tau_e \\ \beta\frac{a^2}{N}(Wt)^{1/2} & \tau_e \leq t \leq \tau_R \\ 2\frac{a^2}{N^2}Wt^1 & t \geq \tau_R \end{cases} \quad (2.11)$$

where b is the bond length, $W = \frac{k_B T}{\zeta b^2}$ is the Rouse monomer diffusion rate, β

is a prefactor included as a result of the Gaussian nature of the segment displacement along the tube⁹ and a is the step length of the tube.^{1,4,7} Also, τ_e is

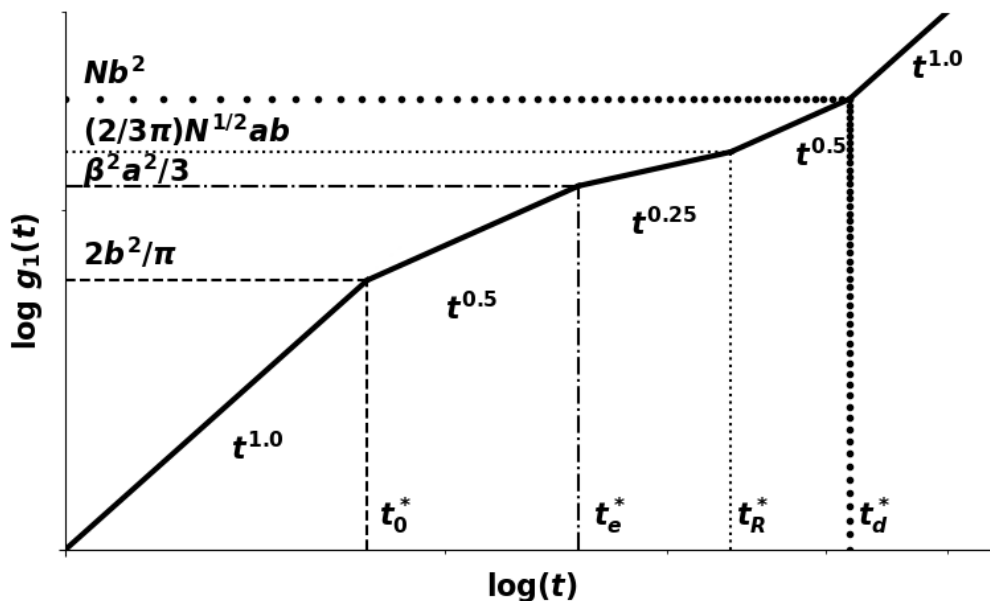


FIGURE 2.2: Schematic of the mean square displacement of internal monomers of entangled chains plotted as a function of time. The five distinct timescales and their corresponding values and are shown.

the entanglement time or the Rouse relaxation time of N_e monomers, τ_R , the Rouse time for the whole chain and τ_d is the time required for the chain to completely leave its tube. These characteristic timescales associated with the segmental dynamics of the chain were believed to occur at the intersection of these different power law regimes.^{1,3,8} However, Likhtman et al.⁵ showed that the relaxation times do not occur at the points of intersection, but rather at times close to the relaxation times. Figure 2.2 shows a schematic of these power law regimes. The relationship between the intersection times and the characteristic relaxation times are obtained by solving for t between two intersecting lines.

This results in

$$t_0^* = \pi\tau_0 \quad (2.12)$$

$$t_e^* = \frac{\pi}{9}\tau_e \quad (2.13)$$

$$t_R^* = \pi\tau_R \quad (2.14)$$

$$t_d^* = \frac{\pi^2}{2}\tau_d \quad (2.15)$$

At very early times $t < \tau_0$, past the timescale where deterministic short-time motion is no longer in effect, the monomer is completely oblivious of and unaffected by the presence of the other monomers and moves in a diffusive manner. When $\tau_0 < t < \tau_e$, the monomer slows down due to the connectivity to the other monomers. The monomer only meanders within the tube and does not feel the topological constraints imposed by the surrounding chains yet, resulting in a $t^{1/2}$ scaling. When $\tau_e < t < \tau_R$ however, the topological constraints due to the tube restrict the motion of the monomer or chain segment to a 1-dimensional diffusive motion along its contour. After a sufficiently long time $t > \tau_d$ the motion of the chain segments again becomes diffusive. Alternatively, the center of mass of the chain $g_3(t)$ can be studied. There are 3 distinct power law regions here – a diffusive motion when $t \leq \tau_e$, a $t^{1/2}$ scaling when $\tau_e \leq t \leq \tau_R$, and a diffusive motion past τ_R .

2.3.2 Rouse Mode Analysis (RMA)

The Rouse model treats the probe chain as a Gaussian chain and considers all its surrounding chains as a continuous viscous medium – i.e., a mean-field approach. Dynamics of each bead on the probe chain is described by the inertialess Langevin equation.¹⁵ For example, the equation of motion for the i -th bead is written as

$$\zeta \frac{d\vec{r}_i}{dt} = H_s [(\vec{r}_{i+1} - \vec{r}_i) - (\vec{r}_i - \vec{r}_{i-1})] + \vec{f}_i^r \quad (2.16)$$

where ζ is the monomeric friction coefficient, H_s is the spring constant, \vec{r}_i is the position of the i -th bead, and \vec{f}_i^r is the random force exerted on the i -th bead satisfying

$$\langle \vec{f}_i^r(t) \vec{f}_j^r(t') \rangle = 2\zeta k_B T \delta_{ij} \delta(t - t') \vec{\delta} \quad (2.17)$$

where $\delta(t)$ is the Dirac delta function, δ_{ij} is the Kronecker delta, and $\vec{\delta}$ is the identity tensor. Equation (2.16) shows that position coordinates of neighboring beads are coupled in their dynamics through spring forces. The RMA projects the original bead coordinates \vec{r}_i to a set of mutually orthogonal coordinates known as Rouse modes or normal coordinates \vec{X}_p ($p = 0, 1, \dots, N - 1$). We adopt the original form of projection by Rouse²²

$$\vec{X}_p \equiv \sqrt{\frac{2}{N}} \sum_{n=1}^N \vec{r}_n(t) \cos\left(\frac{(i - 1/2)p\pi}{N}\right) \quad (2.18)$$

$(p = 0, 1, 2, \dots, N - 1)$

which is widely used in the literature.^{23–25,33,34} The $p = 0$ mode describes the motion of the center of mass of the chain and the other modes ($1 \leq p \leq N - 1$) describe the internal relaxations of sub-chains, or "blobs", of the size of N/p

beads. Each of the transformed coordinate or Rouse mode \vec{X}_p follows Langevin dynamics with its own friction coefficient and random force. Importantly, relaxation of different modes is mutually independent. The autocorrelation function (ACF) of each $p > 1$ mode decays exponentially

$$\langle \vec{X}_p(t) \vec{X}_p(0) \rangle = \langle \vec{X}_p^2 \rangle \exp\left(-\frac{t}{\tau_p}\right) \quad (2.19)$$

with its own relaxation time τ_p given by

$$\tau_{p,Rouse}^{-1} = \frac{12k_B T}{\zeta b^2} \sin^2\left(\frac{p\pi}{2N}\right) \quad (2.20)$$

where b^2 is the mean-square bond (spring) length. For leading modes with $p \lesssim N/5$, which describes the motions of larger segments with $N/p \gtrsim 5$ beads, eq. (2.20) can be approximated by²²

$$\tau_{p,Rouse} = \frac{\zeta b^2}{3\pi^2 k_B T} \left(\frac{N}{p}\right)^2. \quad (2.21)$$

The Rouse model is commonly used to describe the dynamics of unentangled polymer melts. With increasing chain length, topological constraints set in and relaxation dynamics changes. For entangled chains, we may still project the coordinates to \vec{X}_p using eq. (2.18) but the ACFs no longer follow simple exponential decay. A stretched exponential is often used instead^{25,34–37}

$$\langle \vec{X}_p(t) \vec{X}_p(0) \rangle = \langle \vec{X}_p^2 \rangle \exp\left[-\left(\frac{t}{\tau_p^*}\right)^{\beta_p}\right] \quad (2.22)$$

where τ_p^* and β_p are the time scale and exponent (stretching parameter) for the p -th mode. The relaxation time of a stretched exponential can be defined as

$$\tau_p \equiv \int_0^\infty \exp \left[- \left(\frac{t}{\tau_p^*} \right)^{\beta_p} \right] dt = \left(\frac{\tau_p^*}{\beta_p} \right) \Gamma \left(\frac{1}{\beta_p} \right) \quad (2.23)$$

where $\Gamma(x)$ is the gamma function. Note that at the simple exponential limit, i.e., $\beta_p \rightarrow 1$, the two time scales are the same $\tau_p = \tau_p^*$. In the reptation model, the longest relaxation time is

$$\tau_{p,rept} = \frac{N^2 b^2}{p^2} \frac{\zeta}{\pi^2 k_B T} \frac{N}{N_e} \quad (2.24)$$

2.4 Results

2.4.1 MSD

We show a representative monomeric MSD curve for our $N=500$ system in fig. 2.3. Variation in the curve slope is clearly distinguishable with transitions identified at approximately $3, 2.8 \times 10^3, 5.5 \times 10^5$, and 4.5×10^6 TUs corresponding to τ_0, τ_e, τ_R , and τ_d respectively. We now describe the procedure of precisely identifying these transition time scales. Our multi-step approach is as follows:

1. We divide the MSD curve into large blocks by visual inspection as shown in fig. 2.3. Each individual block is large enough that it would contain the scaling power of interest and possibly overlap with a neighboring scaling power.

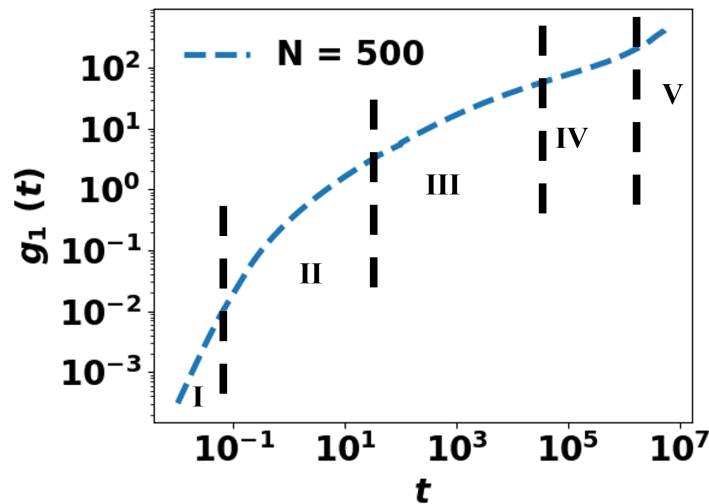


FIGURE 2.3: Mean square displacement of internal monomers $g_1(t)$ of $N = 500$. The vertical lines are chosen based on visual inspection and indicate the region over which the initial regression is carried out.

2. We perform a block-wise curve fitting with overlapping blocks using a select number of points over the entire block size. The number of data points selected for the regression is large and the obtained slope will be smeared due to the size. However, a plot of the power law exponent against time would indicate the time regime where the slope falls onto the expected scaling-law exponent. By overlapping blocks, we mean that we perform regression on elements 1 – 100, 5 – 105, 10 – 110, ... 900 – 1000. The main goal here is to *roughly* identify the region where the slope may lie.
3. We then zero in into the time regime identified in step 2 above and use a fewer number of data points for the regression – five data points. This time, the blocks do not overlap as in step 2 above. This ideally results in a plateau that indicates the start and end points of the scaling law.

4. We carry out another regression using only the start and end points identified in step 3 and force the regression to take the intended slope.
5. We repeat steps 1 – 4 for all the power laws we want to determine. The fitting lines are extended such that they intersect. This intersection point signifies the timescale of interest.

Starting with the first power law scaling t^1 , fig. 2.4a shows the results of a block-wise curve fitting with overlapping blocks – i.e. (steps 1 & 2) on $g_1(t)$ for $N = 500$. Here the number of points over which the regression was done is 50. The number was chosen because of the relatively short time between this power law regime and the next. We observe that the time over which the t^1 scaling was observed was somewhere between ~ 0.2 and 0.4 . We then zoom into this result by carrying out a non-overlapping regression (step 3) over a smaller number of data points (5 in this case) as shown in fig. 2.4b. The start and end points for the t^1 scaling is at $t = 0.3$ and $t = 0.8$ respectively. Using these values, we then carry out another regression and extended the fitting lines to intersect with the neighboring fitting lines (steps 4 and 5). Figure 2.4c and Figure 2.4e also show the results of a block-wise curve fitting with overlapping blocks using 100 data points for the same $N = 500$ chain (Step 1 & 2) for the first $t^{1/2}$ and $t^{1/4}$ scaling. This results in an apparent plateau at time $(1.5 \times 10^1 - 3.0 \times 10^1)$ in fig. 2.4c. This further decreased to a plateau at 0.525 and briefly at 0.5 before falling off. Since we are interested in the 0.5 scaling, we zoom into the time region between 3.5×10^1 and 4.0×10^1 and do a non-overlapping regression in these time regime (Step 3). This is done since there is a huge correlation between successive data points in the previous step. The results are shown in fig. 2.4d.

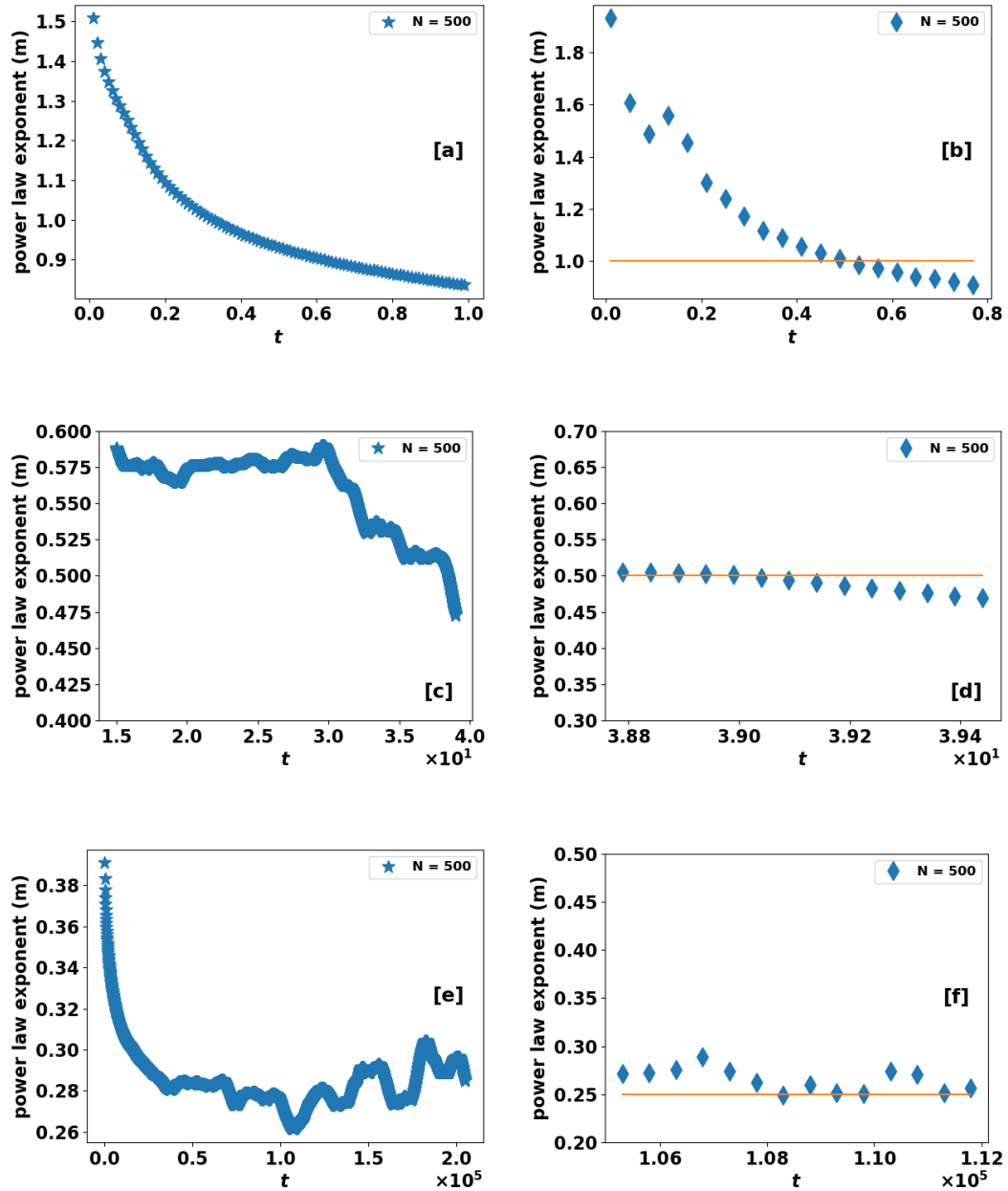


FIGURE 2.4: Scaling law exponents of the monomer mean square displacement $g_1(t)$ plotted against time for $N = 500$ [(a), (c), and (e) are obtained from large blocks to determine the ranges for the 1.0, 0.5, and 0.25 scaling exponents respectively, (b), (d), and (f) are the more refined plots for exponents obtained by using smaller blocks for the regression]. The horizontal lines are included as a guide to the eye to indicate the scaling law.

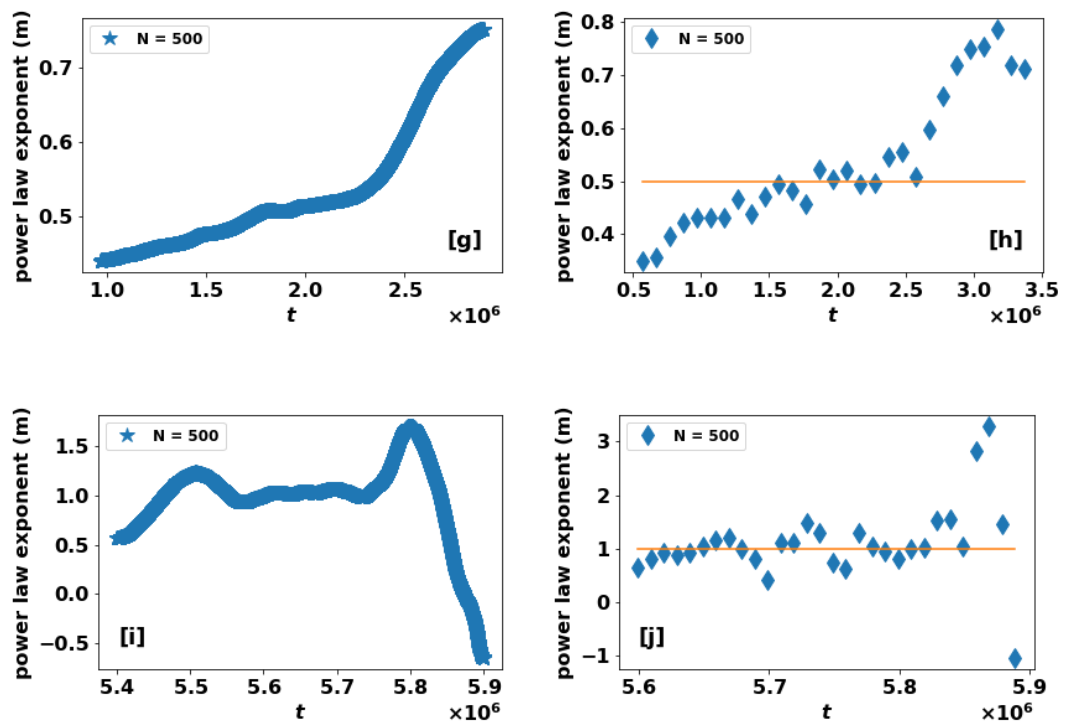


FIGURE 2.5: Scaling law exponents of the monomer mean square displacement $g_1(t)$ plotted against time for $N = 500$ [(g) and (i) are obtained from large blocks to determine the ranges for the 0.5, and 1.0 scaling exponents respectively, (h) and (j) are the more refined plots for exponents obtained by using smaller blocks for the regression].

The 0.5 scaling is now more clearly defined. Some minor fluctuations are to be expected in the values. The 0.5 scaling then begins to taper off at later times. The start and end points for the actual regression are $t = 38.71$ and $t = 39.0$. Figure 2.4e similarly shows the results for the 0.25 scaling where there are more peaks and dips in the results. The 0.25 scaling is a direct prediction of the reptation model where the chain is only allowed to move along the contour path of the tube due to the topological restrictions imposed by the rest of the matrix chains. The minimum dip at 0.25 occurs over a rather short time range because of the relatively short time the chain spends in the tube constriction before increasing to the Rouse scaling of 0.5. The more refined scaling is shown in fig. 2.4e where we clearly observe the 0.25 scaling with minor fluctuations. We use $t = 108200$ and $t = 108800$ as the start and end points for the regression and force the 0.25 slope through these points. Finally, fig. 2.5a and fig. 2.5c show the block-wise curve fitting with overlapping blocks for the later $t^{1/2}$ and t^1 scaling where the expected plateaus are more pronounced. Figure 2.5b and fig. 2.5d show the refined results. The start and end points used for the regression are $t = 1292200$ and $t = 2890300$ for the 0.5 slope. For the final 1.0 slope, we used $t = 5734600$ and $t = 5838100$ for the regression.

We repeat the process for the other time scales and show the final results of the intersection of the different scaling laws in fig. 2.6 for the chains $N = 200$, $N = 350$, and $N = 500$. As expected, we observe the expected t^1 scaling at early times, a transition to $t^{1/2}$ which describes the Rouse dynamics of the strand between entanglements, then a more restricted $t^{1/4}$ scaling. For the $N = 200$ chain however, we were also unable to see the $t^{1/4}$ scaling but $t^{0.35}$. The later

TABLE 2.1: Time for the intersection of the different fitting lines to the power regimes extracted from the pure $N = 200$, $N = 350$, $N = 500$ melt MSD curve.

| N | t_0^* | t_e^* | t_R^* | t_d^* |
|-----|---------|--------------------|--------------------|--------------------|
| 200 | 3.23 | 1.28×10^3 | 5.05×10^4 | 3.86×10^5 |
| 350 | 3.20 | 3.43×10^3 | 1.66×10^5 | 1.74×10^6 |
| 500 | 3.31 | 3.14×10^3 | 5.88×10^5 | 4.36×10^6 |

TABLE 2.2: The characteristic times τ_0 , τ_e , τ_R , and τ_d for the pure $N = 200$, $N = 350$, $N = 500$ melt MSD curve.

| N | τ_0 | τ_e | τ_R | τ_d |
|-----|----------|--------------------|--------------------|--------------------|
| 200 | 1.03 | 3.67×10^3 | 1.61×10^4 | 7.82×10^4 |
| 350 | 1.02 | 9.83×10^3 | 5.28×10^4 | 3.53×10^5 |
| 500 | 1.05 | 9.00×10^3 | 1.87×10^5 | 8.84×10^5 |

$t^{1/2}$ and t^1 scaling are also clearly shown. The results of the intersection and the corresponding characteristic relaxation times for all the chains studied are given in Table 2.1 and table 2.2 respectively.

Since $\tau_e = \tau_0 N_e^2$, $\tau_R = \tau_0 N^2$, and $\tau_d = \tau_0 N^3 / 3N_e$, the calculation of N_e can be done using the ratio of any two of these relaxation times.

$$N_e' = \left(\frac{\tau_e}{\tau_0}\right)^{1/2} \equiv 3\left(\frac{t_e^*}{t_0^*}\right)^{1/2} \quad (2.25)$$

TABLE 2.3: N_e calculated from the different equations of MSD given in eq. (2.25)–eq. (2.27) and from RMA

| N | $N_e' = \left(\frac{\tau_e}{\tau_0}\right)^{1/2}$ | $N_e'' = N\left(\frac{\tau_e}{\tau_R}\right)^{1/2}$ | $N_e''' = 3N\left(\frac{\tau_R}{\tau_d}\right)$ | $N_e^R = 3N\frac{\tau_{p,Rouse}}{\tau_{p, rept}}$ |
|-----|---|---|---|---|
| 200 | 58 | 96 | 123 | 236 |
| 350 | 98 | 151 | 157 | 203 |
| 500 | 92 | 110 | 318 | 213 |

$$N_e'' = N \left(\frac{\tau_e}{\tau_R} \right)^{1/2} \equiv 3N \left(\frac{t_e^*}{t_R^*} \right)^{1/2} \quad (2.26)$$

$$N_e''' = 3N \frac{\tau_R}{\tau_d} \equiv \frac{3\pi N}{2} \left(\frac{t_R^*}{t_d^*} \right) \quad (2.27)$$

Using eq. (2.25), eq. (2.26), and eq. (2.27), N_e is 92, 110, and 318 respectively for

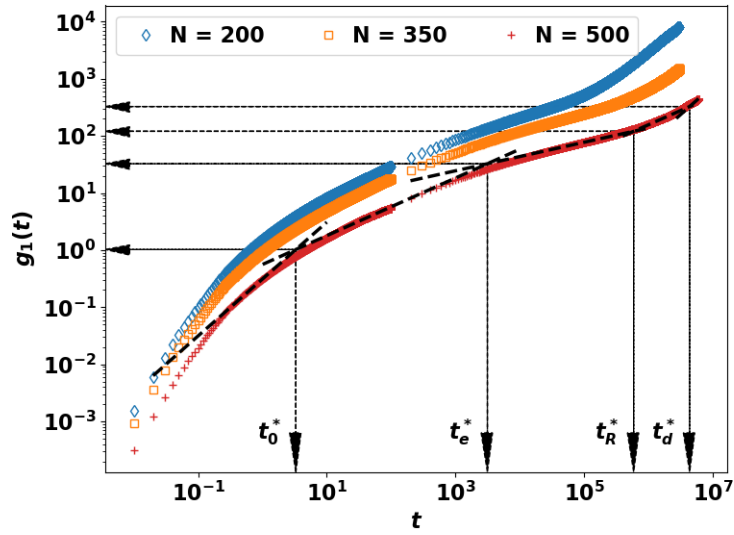


FIGURE 2.6: Mean square displacement of internal monomers $g_1(t)$ of chains $N = 200, 350$ and 500 . The three curves overlap until $t \sim \mathcal{O}(10^4)$ before they separate. Vertical offsets have been added to the $N = 200$ and $N = 350$ for clarity.

$N = 500$. While N_e' and N_e'' are close (a factor difference of ~ 1.2), the value obtained from eq. (2.27) represents a two-fold increase from that obtained using eq. (2.25). The most refined estimate obtained from PPA of flexible chains using the standard bead model-spring model is 85 ± 7 ,^{6,38} which is the same order of magnitude as that obtained using eq. (2.25). The difference between N_e''' and the other values could be due to insufficient statistics at the long-time regime.

Other authors^{11,12} have however ascribed the difference between N_e' and N_e'' to the dilation of the tube. In their calculation of N_e for semi-flexible KG chains

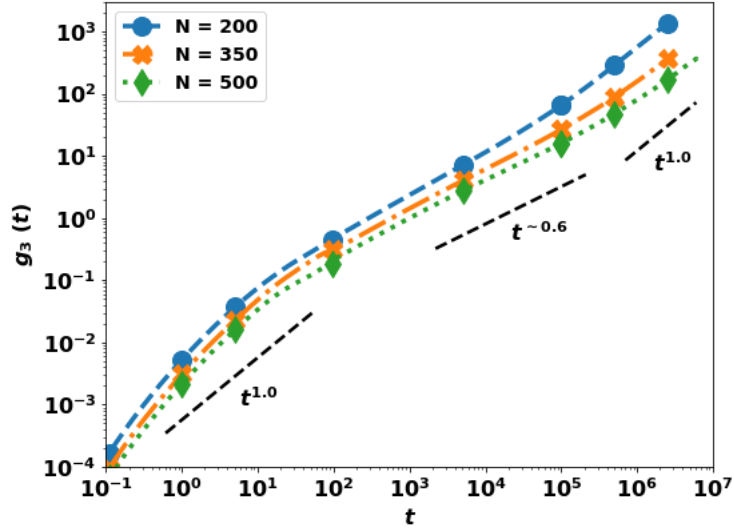


FIGURE 2.7: Mean square displacement of the center of mass of the chains $g_{31}(t)$ of chains $N = 200, 350,$ and 500 . The intermediate scaling shows a power law of $t^{-0.6}$.

with $N = 200$ using values from the first ($g_1(t) \propto t^{1/2}$ and $g_1(t) \propto t^{1/4}$) and second crossover points ($g_1(t) \propto t^{1/4}$ and $g_1(t) \propto t^{1/2}$), Zhou et al.¹¹ reported an increase of ~ 2 between N_e' and N_e'' values. For the same semi-flexible model but with a longer chain length of $N = 350$, Wang et al.¹² obtained an increase of ~ 1.5 . As far as we know, N_e calculation using τ_R and τ_d (corresponding to N_e''') for fully flexible chains has not been reported in the literature. This is perhaps due to the long time required to get to this regime in simulations.

The MSD of the center of mass of the chains is shown in fig. 2.7. At the early and later times, there is a clear $t^{1.0}$ scaling. However, we observed a $t^{0.6}$ scaling in the intermediate time regime around $t \sim \mathcal{O}(10^4)$ instead of the $t^{0.5}$ predicted

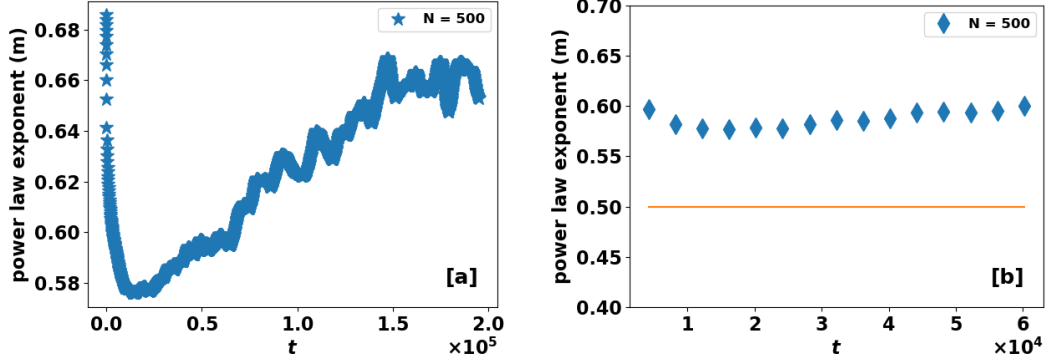


FIGURE 2.8: Scaling law exponents for center of mass mean square displacement ($g_3(t)$) plotted against time for $N = 500$ [(a) is obtained from large blocks to determine the ranges for the 0.5 scaling exponents (b) is the more refined plots for the exponents obtained by using smaller blocks for the regression]. The horizontal lines are included as a guide to the eye to indicate the scaling law.

by the reptation theory. Figure 2.8a and fig. 2.8b show the coarse and refined slopes of $g_3(t)$. Consequently, using the $g_3(t)$ for extracting the timescales may introduce some ambiguities in the results.

2.4.2 RMA

Dependence of relaxation time of individual Rouse modes $\tau_{p, rept}$, as calculated from eq. (2.23), on the segment size N/p is shown in fig. 2.9. Rouse model predicts (eq. (2.21)) $\tau_p/(N/p)^2$ to be constant for all modes. However, it has been found that Rouse prediction is accurate for $N/p \gtrsim 5$ which is indeed observed in our simulation. Departure from the plateau is found at smaller scales ($N/p \lesssim 5$), where the relaxation times of all chain lengths overlap. Entanglement causes a sudden slowdown in the dynamics, which shows as a surge in $\tau_p/(N/p)^2$ starting at $N/p \sim \mathcal{O}(10)$. At the long-segment (small- p) limit, another, much

higher, plateau is reached. This conforms with the tube model prediction¹ of eq. (2.24)

$$\tau_{p, rept} \sim \left(\frac{N}{N_e} \right) \left(\frac{N}{p} \right)^2.$$

A raised right-end plateau is also discernible in the $N = 200$ and $N = 350$ case. For the $N = 500$ case, we observe some fluctuations in the expected plateau at the right end. We extract N_e from the ratio of the 2 plateaus i.e. Equation (2.21)

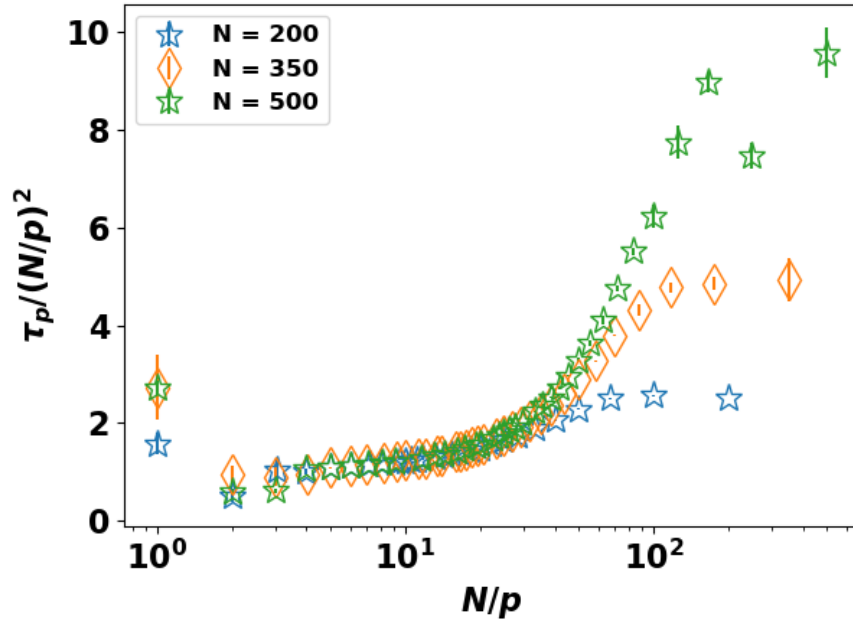


FIGURE 2.9: Rouse mode analysis with stretched exponential fitting – stretching parameter β_p of $N = 200, 350,$ and 500 .

to Equation (2.24).

$$N_e^R = 3N \frac{\tau_{p, Rouse}}{\tau_{p, rept}} \quad (2.28)$$

For $N = 200, 350$, and 500 , $N_e^R = 236, 203$, and 213 respectively. The results are included in table 2.3. The results for $N = 200$ suggests that the entanglement strand is at the same order of the chain length. For $N = 350$ however, the result is a factor of $\sim 2.1, 1.34$ and 1.29 higher than the prediction for N_e', N_e'', N_e''' from the MSD analysis. Similarly, for $N = 500$, however, N_e^R exceeds N_e' and N_e'' by a factor of 2.3 and 1.95 . There is some level of agreement between N_e^R and N_e''' . This is not too surprising because both methods rely on the relaxation time at the long time limit. For a more accurate comparison of these methods, a much longer chain, far greater than the entanglement length would need to be used.

2.5 Discussion

There have been several molecular dynamics studies reporting the different power law regimes^{2-4,7,8,12,34} described in section 2.3.1 as a validation of the reptation picture of polymer dynamics. The transition times between the different timescales are determined by a power-law fit of the simulation data which is very susceptible to the number of data points selected for the fitting. There is also the latent dilemma of whether the characteristic entanglement time scaling of $t^{1/4}$ can be clearly observed. For the regime between τ_e and τ_R , Kopf et al.³⁴ reported a transition of $t^{0.46}$ to $t^{0.37}$ for fully flexible KG chains with $N = 150$. For other studies, the scaling reported is usually a value that puts the expected $t^{1/4}$ scaling within the uncertainty limits. Departure from this exponent is normally rationalized as due to the finite chain length studied and the short length of the $t^{1/4}$ scaling which is not necessarily larger than the crossover regions with neighboring regimes (where smooth transitions between slopes are observed).

There is also a wide variability in the reported characteristic timescales. For example, using a fully flexible KG model and a chain length $N = 200$, Kremer et al.³ reported $\tau_e = 1800$ and a power law exponent of 0.28 ± 0.03 in that regime which is within the expected 0.25 limit. For longer chains of $N = 700$ and 10000 of the same KG model, Pütz et al.⁴ clearly observed the $t^{1/4}$ scaling but reported $\tau_e = 1420$ and 1100 respectively for both chains. Similarly, using the same fully flexible KG chain model but a chain length $N = 1000$, Wang et al.⁷ results showed a clear $t^{1/4}$ scaling but a $\tau_e \approx 2950$. This clearly demonstrates the lack of robustness inherent in the MSD approach.

Regression produces a considerable statistical error during the determination of these characteristic time scales. In particular, the calculated values are sensitive to the start and end point included in the regression, both of which are chosen somewhat arbitrarily. Here, we have described a multi-step approach for the MSD method that attempts to standardize the regression protocol. However, as shown in the previous sections our results are not conclusive yet. For N'_e the value of 98 and 92 obtained from $N = 350$ and 500 are within the same order of magnitude. However, the values are about a factor of 2 larger than that obtained from $N = 200$. N''_e are much closer in values with a ~ 1.5 -factor difference between the shortest ($N=200$) and longest chain ($N=500$). On the other hand, N'''_e showed the most variance, with $N = 200$ and $N = 500$ differing by a factor of ~ 2.5 . This is a major drawback as the values should converge asymptotically to a value in an ideal scenario. Given that the $t^{0.25}$ scaling is not observed in the $N = 200$ case, this could be a possible extenuating reason.

Although we have attempted a procedure for the reliable and repeatable extraction of these timescales, some lingering questions remain. There is a wide variability in the N_e values (ranging from 58 to 318) we have obtained using the different characteristic timescales. There are several factors that can affect the outcomes of the extracted timescales. Firstly, the finite chain length used for the determination. By our N_e estimates, the number of entanglements for our longest chain $N = 500$ would be ~ 9 at best and ~ 1 using $N_e = 318$. Even for the longest chain we have simulated $N = 500$, the duration of the $t^{1/4}$ scaling is extremely short, indicating that the chains we have used are only weakly or marginally entangled. As such the entanglement effects may not be strong enough to ensure consistent values. A validation of our approach would require much longer chains.

Furthermore, the pre-factors used in the tube model have not been rigorously determined although they have been widely used. They rest on the premise that the tube is Gaussian and that the short time monomer motion and the segmental motion within the tube are Rouse-like.^{1,4} However, our work²⁶ revealed a departure from Rouse dynamics at short length and time scales. This makes comparison using the different timescales rather iffy. More generally, the sampling density and the block size used for the regression are other factors that could introduce variance.

The RMA values are more consistent. For all the chains we have studied, N_e has the same order of magnitude. The difficulties associated with the MSD approach – including regression uncertainties, are easily sidestepped. However, there is a dip in the $\tau_p / (N/p)^2$ vs N/p for the $N=500$ chain for reasons unclear

at this time. Compared to the N_e estimates of 85 in the literature,^{2,6} the RMA values are much higher. The RMA values uses characteristic time at long times (whole chain relaxation) and intermediate times (Rouse time) suggesting that, perhaps the tube's diameter is not constant across these different timescales. Here as well, longer chains would be needed to validate this approach.

2.6 Conclusions

Using a fully flexible KG model, we have studied and compared two methods for determining the entanglement length N_e – the mean square displacement (MSD) and Rouse mode analysis (RMA) methods. The chain lengths studied were $N = 200, 350,$ and 500 . For the MSD method, we developed a protocol for fitting the lines to the MSD of the internal monomers $g_1(t)$ curve since the values obtained depend greatly on the regression procedure. The intersection of the fitting lines to the different dynamical regime gives times that are closely related to the characteristic relaxation times of $\tau_0, \tau_e, \tau_R,$ and τ_d . These are time scales of different stages of stress relaxation process of entangled chains. We subsequently used these values to calculate N_e . The N_e values obtained depend on the pair of characteristic times (τ_0 & τ_e, τ_e & $\tau_R,$ and τ_R & τ_d) used, with the τ_R & τ_d times giving high N_e values compared to the other two pairs. We further calculated τ_R and τ_d using RMA. The RMA offers a more robust and less sensitive method for calculating N_e . While there are some numerical differences in the MSD, we found a remarkable consistency in the RMA approach for all the chains we have studied.

References

- [1] M. Doi and S. F. Edwards. *The theory of polymer dynamics*. Vol. 73. oxford university press, 1988.
- [2] J.-X. Hou. Determine mesh size through monomer mean-square displacement. *Polymers* 11(9) (2019), 1405.
- [3] K. Kremer and G. S. Grest. Dynamics of entangled linear polymer melts: A molecular-dynamics simulation. *The Journal of Chemical Physics* 92(8) (1990), 5057–5086.
- [4] M. Pütz, K. Kremer, and G. S. Grest. What is the entanglement length in a polymer melt? *Europhysics Letters* 49(6) (Mar. 2000), 735–741. ISSN: 02955075.
- [5] A. E. Likhtman and T. C. McLeish. Quantitative theory for linear dynamics of linear entangled polymers. *Macromolecules* 35(16) (2002), 6332–6343.
- [6] R. S. Hoy, K. Foteinopoulou, and M. Kröger. Topological analysis of polymeric melts: Chain-length effects and fast-converging estimators for entanglement length. *Physical Review E* 80(3) (2009), 031803.
- [7] Z. Wang, A. E. Likhtman, and R. G. Larson. Segmental dynamics in entangled linear polymer melts. *Macromolecules* 45(8) (2012), 3557–3570. ISSN: 00249297.
- [8] H. P. Hsu and K. Kremer. Static and dynamic properties of large polymer melts in equilibrium. *Journal of Chemical Physics* 144(15) (2016), 154907. ISSN: 00219606.

- [9] J.-X. Hou. Note: Determine entanglement length through monomer mean-square displacement. *The Journal of chemical physics* 146(2) (2017), 026101.
- [10] R. Larson et al. Definitions of entanglement spacing and time constants in the tube model. *Journal of Rheology* 47(3) (2003), 809–818.
- [11] Q. Zhou and R. G. Larson. Direct calculation of the tube potential confining entangled polymers. *Macromolecules* 39(19) (2006), 6737–6743.
- [12] Z. Wang and R. G. Larson. Constraint release in entangled binary blends of linear polymers: A molecular dynamics study. *Macromolecules* 41(13) (2008), 4945–4960.
- [13] J. D. Ferry. *Viscoelastic properties of polymers*. John Wiley & Sons, 1980.
- [14] M. Rubinstein, R. H. Colby, et al. *Polymer physics*. Vol. 23. Oxford university press New York, 2003.
- [15] M. Doi et al. Dynamics of polymers in polydisperse melts. *Macromolecules* 20(8) (1987), 1900–1906.
- [16] L. Xi. Molecular simulation for predicting the rheological properties of polymer melts. *Molecular Simulation* 45(14-15) (2019), 1242–1264.
- [17] R. Everaers et al. Rheology and microscopic topology of entangled polymeric liquids. *Science* 303(5659) (2004), 823–826.
- [18] R. Everaers. Topological versus rheological entanglement length in primitive-path analysis protocols, tube models, and slip-link models. *Physical Review E* 86(2) (2012), 022801.

- [19] J. M. Dealy, D. J. Read, and R. G. Larson. *Structure and rheology of molten polymers: from structure to flow behavior and back again*. Carl Hanser Verlag GmbH Co KG, 2018.
- [20] M. Kröger. Shortest multiple disconnected path for the analysis of entanglements in two-and three-dimensional polymeric systems. *Computer physics communications* 168(3) (2005), 209–232.
- [21] C. Tzoumanekas and D. N. Theodorou. Topological analysis of linear polymer melts: a statistical approach. *Macromolecules* 39(13) (2006), 4592–4604.
- [22] P. E. Rouse Jr. A theory of the linear viscoelastic properties of dilute solutions of coiling polymers. *The Journal of Chemical Physics* 21(7) (1953), 1272–1280.
- [23] M. Vladkov and J.-L. Barrat. Linear and nonlinear viscoelasticity of a model unentangled polymer melt: molecular dynamics and rouse modes analysis. *Macromolecular theory and simulations* 15(3) (2006), 252–262.
- [24] J. T. Kalathi et al. Rouse mode analysis of chain relaxation in polymer nanocomposites. *Soft matter* 11(20) (2015), 4123–4132.
- [25] J. S. Shaffer. Effects of chain topology on polymer dynamics: Configurational relaxation in polymer melts. *The Journal of chemical physics* 103(2) (1995), 761–772.
- [26] O. Adeyemi, S. Zhu, and L. Xi. Dynamics and stress relaxation of bidisperse polymer melts with unentangled and moderately entangled chains. *Physics of Fluids* 33(6) (2021), 063105.

- [27] R. B. Bird et al. *Dynamics of polymeric liquids*. 2nd. Vol. 2. New York: Wiley, 1987.
- [28] S. Plimpton. *Fast parallel algorithms for short-range molecular dynamics*. Tech. rep. Sandia National Labs., Albuquerque, NM (United States), 1993.
- [29] S. Zhang and L. Xi. Effects of precursor topology on polymer networks simulated with molecular dynamics. *Polymer* 116 (2017), 143–152.
- [30] Y. R. Sliozberg and J. W. Andzelm. Fast protocol for equilibration of entangled and branched polymer chains. *Chemical Physics Letters* 523 (2012), 139–143.
- [31] R. Auhl et al. Equilibration of long chain polymer melts in computer simulations. *The Journal of chemical physics* 119(24) (2003), 12718–12728.
- [32] P.-G. de Gennes. Reptation of a polymer chain in the presence of fixed obstacles. *The journal of chemical physics* 55(2) (1971), 572–579.
- [33] P. H. Verdier. Monte Carlo Studies of Lattice-Model Polymer Chains. I. Correlation Functions in the Statistical-Bead Model. *The Journal of Chemical Physics* 45(6) (1966), 2118–2121.
- [34] A. Kopf, B. Dünweg, and W. Paul. Dynamics of polymer "isotope" mixtures: Molecular dynamics simulation and Rouse model analysis. *Journal of Chemical Physics* 107(17) (1997), 6945–6955. ISSN: 00219606.
- [35] J. Padding and W. J. Briels. Uncrossability constraints in mesoscopic polymer melt simulations: non-Rouse behavior of C₁₂₀H₂₄₂. *The Journal of Chemical Physics* 115(6) (2001), 2846–2859.

- [36] Y. Li, M. Kröger, and W. K. Liu. Nanoparticle effect on the dynamics of polymer chains and their entanglement network. *Physical review letters* 109(11) (2012), 118001.
- [37] J. T. Kalathi et al. Rouse mode analysis of chain relaxation in homopolymer melts. *Macromolecules* 47(19) (2014), 6925–6931. ISSN: 15205835.
- [38] J.-X. Hou et al. Stress relaxation in entangled polymer melts. *Physical review letters* 105(6) (2010), 068301.

Chapter 3

Methods for calculating linear viscoelastic properties

The theme of this thesis is on the dynamics and linear viscoelasticity of pure polymers and plasticized polymers. The computational calculation of the linear viscoelastic (LVE) properties of polymers is very expensive due to the long relaxation times associated with polymers. In this chapter, we focus on three classical methods for determining the linear viscoelasticity of polymer melts in molecular dynamics simulations; equilibrium molecular dynamics (EMD), Non-EMD, and Rouse mode analysis, with emphasis on the computational resource requirement and discuss the challenges inherent in the application of these methods. The length of the polymer chains we have used ranged from unentangled to entangled polymers. We compared the results from the three methods. We find that the uncertainty from these methods are comparable.

I was responsible for the setting up the model, carrying out all the simulations, analyzing the data, and the preparation of the initial draft. The research

was conducted under the supervision of Li Xi and Shiping Zhu who also provided feedback on the draft. This chapter has been submitted for publication.

Equilibrium and non-equilibrium molecular dynamics approaches for the linear viscoelasticity of polymer melts

Oluseye Adeyemi,¹ Shiping Zhu (朱世平),¹ and Li Xi (奚力)^{1,2, a)}

¹⁾*Department of Chemical Engineering, McMaster University, Hamilton, Ontario L8S 4L7, Canada*

²⁾*School of Computational Science and Engineering, McMaster University, Hamilton, Ontario L8S 4K1, Canada*

Viscoelastic properties of polymer melts are particularly challenging to compute due to the intrinsic stress fluctuations in molecular dynamics (MD). We compared equilibrium and non-equilibrium MD approaches for extracting the storage (G') and loss moduli (G'') over a wide frequency range from a bead-spring chain model, in both unentangled and entangled regimes. We found that, with properly chosen data processing and noise reduction procedures, different methods render quantitatively equivalent results. In equilibrium MD (EMD), applying the Green-Kubo relation with a multi-tau correlator method for noise filtering generates smooth stress relaxation modulus profiles, from which accurate G' and G'' can be obtained. For unentangled chains, combining the Rouse model with a short-time correction provides a convenient option that circumvents the stress fluctuation challenge altogether. For non-equilibrium MD (NEMD), we found that combining a stress pre-averaging treatment with discrete Fourier transform analysis reliably computes G' and G'' with much shorter simulation length than previously reported. Comparing the efficiency and statistical accuracy of these methods, we concluded that EMD is both reliable and efficient, and is suitable when the whole spectrum of linear viscoelastic properties is desired, whereas NEMD offers flexibility when only some frequency ranges are of interest.

I. INTRODUCTION

The linear viscoelastic (LVE) properties of polymers provide unique insights into their structure and also govern the flow behavior during processing. These properties are usually measured by a small displacement of the polymer molecules from their equilibrium positions, thereby ensuring that the response is still in the linear regime. Experimentally, LVE properties are determined by a small amplitude oscillatory shear (SAOS) experiment^{1,2}, which provides the storage (G') and loss (G'') moduli of the material over a frequency spectrum. The accessible frequency ranges are either limited by the equipment capabilities or the degradation of the polymers at high shear rates or temperatures. The high-shear rate challenge is typically mitigated by the temperature superposition technique.

Owing to the range of time and length scales involved, computing the viscoelastic properties of polymers in molecular dynamics (MD) simulations still remains a formidable task. Indeed, for long-chain polymers, it remains unrealistic to capture the whole spectrum of linear viscoelasticity using fully atomistic molecular models. Even for highly coarse-grained models, accurate determination of viscoelastic properties in MD must still overcome the challenges of long relaxation times and strong stress fluctuations. In particular, for highly-entangled polymers, MD must be combined with high-level polymer dynamics models for quantitative prediction³.

Regardless of the model being used, extraction of viscoelastic properties from MD simulations is an essential step. This can be achieved with either equilibrium or non-equilibrium MD (EMD and NEMD) simulation. The EMD approach samples the spontaneous stress fluctuations in the thermodynamic ensemble of the system. The shear stress relaxation modulus $G(t)$, from which linear viscoelastic material functions are calculated, is related to the time autocorrelation function (TACF) of the stress tensor through the Green-Kubo (GK) relation⁴. The NEMD approach, on the other hand, models the flow condition of rheological measurement from which the corresponding material function is directly computed⁵.

Take shear viscosity, which is the most computed rheological property in the literature, for example. Since the EMD approach simulates equilibrium conditions, it can only provide the zero-shear viscosity as a temporal integral of the relaxation modulus

$$\eta_0 \equiv \lim_{\dot{\gamma} \rightarrow 0} \eta = \int_0^{\infty} G(t) dt \quad (1)$$

(where $\dot{\gamma}$ is the shear rate). By contrast, the NEMD approach simulates the steady shear flow condition and calculates the viscosity by dividing the steady-state shear stress by the shear rate. For simple liquids such as the Lennard-Jones (LJ) fluid, shear viscosity values from EMD and NEMD approaches agree well^{6,7}. Although there was a general perception that the EMD approach is prone to large statistical uncertainty due to intense stress fluctuations in molecular systems and difficult convergence of the integral in eq. (1), it has been shown that reliable results are attainable with careful selection of the integration limits and data processing procedure^{7,8}. For polymers, viscosity is in general a function of shear

^{a)}corresponding author, E-mail: xili@mcmaster.ca; Web: <https://www.xiresearch.org>

rate, but a Newtonian plateau exists at the small $\dot{\gamma}$ limit. Extrapolation of the $\eta(\dot{\gamma})$ profile from NEMD to the $\dot{\gamma} = 0$ limit again agrees well with the EMD value from eq. (1)^{9–13}.

The focus of this study is on the full spectrum of linear viscoelastic properties as reflected in the frequency (ω)-dependent $G'(\omega)$ and $G''(\omega)$ profiles. Compared with shear viscosity, the computational cost for obtaining G' and G'' is significantly higher (in both EMD and NEMD) as viscoelastic responses at a wide range of frequencies are now required. The EMD approach again relies on the GK relation and was first reported by Sen et al.¹², followed by a number of later developments^{14,15}. Many more studies reported the EMD results of $G(t)$ but did not convert it to $G'(\omega)$ and $G''(\omega)$ ^{16–20}. The NEMD approach simulates the sinusoidal oscillatory shear flow (modeling the SAOS condition) and obtains G' and G'' from the time-dependent shear stress signal. Those efforts date back to earlier studies by Cifre et al.²¹ and Vladkov and Barrat¹³, and NEMD results of G' and G'' were also reported more recently by Karim et al.²².

Information on the comparison between these two approaches is rather limited. For the bead-spring chain or Kremer-Grest (KG) model²³ of very short chain length ($N = 10$ and 20), Vladkov and Barrat¹³ conducted a comparative study between EMD and NEMD approaches for polymer viscoelasticity. Direct comparison between the GK and NEMD approaches, however, was only reported for the zero-shear viscosity. The study did not report the G' and G'' results from the GK relation because it was not able to extract statistically meaningful results buried under strong noises. It instead proposed a corrected Rouse mode analysis (cRMA) approach which brings in MD data to fill in the short-time dynamics missing in the Rouse model. The method is fundamentally still an EMD approach but its viability relies on the accuracy of the Rouse model which is designed only for unentangled polymers. For the short chains studied, good agreement was found between G' and G'' results from cRMA and NEMD. More recently, Karim et al.^{22,24} compared NEMD results of G' and G'' , for $N = 20$ and 80 , from several sources with the GK results of Sen et al.¹². Good agreement is generally found in the frequency range tested by NEMD (typically fewer than three decades) with discrepancy sometimes observed at the low frequency (long-time) limit where statistical uncertainty is highest in both methods.

The purpose of this study is to determine which method is better for the accurate calculation of G' and G'' over a wide frequency range. Many researchers seem to prefer NEMD because of the general belief that EMD is more affected by strong stress fluctuations. Indeed, the large noise-to-signal ratio in the long-time tail of $G(t)$ obtained from the GK relation has sometimes caused erroneous conclusions in previous studies³. It takes extremely long EMD simulations to effectively reduce the statistical uncertainty in $G(t)$. For shear viscosity calculation, it is widely accepted that NEMD requires substantially

less computational cost for satisfactory accuracy^{3,6,7,25}. We note that this advantage does not straightforwardly translate to $G'(\omega)$ and $G''(\omega)$ calculation because NEMD must be separately performed for each frequency level of interest, while the EMD approach allows the calculation of the whole spectrum with one long simulation run.

In this study, we directly compare the accuracy and efficiency of EMD and NEMD approaches for computing $G'(\omega)$ and $G''(\omega)$ profiles. This is the first time these two approaches are compared with identical molecular models, which will allow us to identify the discrepancies, if any, that are attributed solely to the difference in the methodology for computing viscoelastic properties. In addition to evaluating the quantitative equivalence between their results, efficiency, in terms of which method provides statistically more accurate results with limited computational resources, is also a key consideration. For EMD, our primary focus is on the GK approach, but we also include the cRMA approach for completeness. Methods are evaluated in monodisperse melts of KG chains with $N = 25$ to 350 , covering both unentangled and (moderately) entangled regimes. To our knowledge, NEMD calculation of G' and G'' has not been previously reported for entangled polymers. Both categories of methods are strongly influenced by statistical errors due to stress fluctuations in MD simulation. We have experimented with various noise reduction techniques and present the best procedure that we find for each method. This allows us to compare the methods on an equal footing – i.e., each method is evaluated at its optimal settings. Therefore, in addition to guiding the choice of method for computing viscoelastic properties, the study also aims to demonstrate the best practice in each approach.

II. METHODS

A. Simulation Details

We model the polymer chains using the classical Kremer-Grest (KG) bead-spring chain model²³. Consecutive beads in a polymer chain interact with the finitely extensible non-linear elastic (FENE) springs potential

$$U_{\text{FENE}}(r) = -\frac{1}{2}KR_0^2 \ln \left[1 - \left(\frac{r}{R_0} \right)^2 \right] + 4\epsilon \left[\left(\frac{\sigma}{r} \right)^{12} - \left(\frac{\sigma}{r} \right)^6 + \frac{1}{4} \right] \quad (2)$$

where r represents the distance between the beads, and σ and ϵ are the LJ length and energy parameters. The first term of the equation models an attractive potential due to the entropic interaction between the polymer segments, which diverges at a maximum bond length $R_0 = 1.5\sigma$. The second term represents the repulsive force between beads and is only included at distances $r \leq 2^{\frac{1}{6}}\sigma$. The spring force $K = 30\epsilon/\sigma^2$ allows the use of

a large integration timestep and also prevents the bonds from cutting through each other. The interaction potential between the non-bonded beads is modeled by the standard Lennard Jones (LJ) potential

$$U_{\text{LJ}}(r) = 4\epsilon \left(\left(\frac{\sigma}{r} \right)^{12} - \left(\frac{\sigma}{r} \right)^6 \right) \quad (3)$$

for which a cutoff of 2.5σ is used and a vertical offset is added to ensure continuity at the cutoff. All the results are reported in reduced LJ units and length, energy, time, and temperature values are scaled by, σ , ϵ , $\tau = \sqrt{m\sigma^2/\epsilon}$, and ϵ/k_B (k_B is the Boltzmann constant) respectively. The chain lengths studied range from the unentangled $N = 25$ and 50 to marginally entangled $N = 100$ and moderately entangled $N = 350$ cases²⁰. The $N = 350$ case contains a total of 56000 beads in the simulation box while all other cases contain 50000 beads in each simulation box. All simulations were performed at a constant bead density of $0.85 \sigma^{-3}$. The temperature of the simulations was maintained at $1\epsilon/k_B$ with Nosé-Hoover chains. All the simulations were carried out using the Large-scale Atomic/Molecular Massively Parallel Simulator (LAMMPS) package²⁶. The equation of motion was integrated using the velocity Verlet algorithm with a time step of $\Delta t = 0.01$ (in LJ time units or TUs).

Initial configurations were generated by randomly placing the specified number and types of chains in a cell following a self-avoiding walk conformation statistics. The structures were further equilibrated using a modified dissipative particle dynamics (DPD) push-off step²⁷ during which a soft repulsive potential

$$U_{\text{DPD}}(r) = \begin{cases} \frac{A_{\text{DPD}}}{2} r_c \left(1 - \frac{r}{r_c} \right), & (r < r_c) \\ 0, & (r \geq r_c) \end{cases} \quad (4)$$

was used to replace the LJ potential (eq. (3)) between the non-bonded beads. DPD equilibration was performed at $T = 1.0$ and used a cut-off distance $r_c = 1.0$. The DPD potential was initially kept low at $A_{\text{DPD}} = 25$. At the beginning, we restricted the maximum distance that each bead can move in a single time step and gradually increased it from 0.001 to 0.1 over 15TUs. After the restriction was removed, we further ran the DPD simulation for another 100TUs, following which A_{DPD} was gradually ramped up to 100 over 5TUs. Finally, we replaced the DPD potential with the standard LJ potential (eq. (3)) and performed MD simulation in an NVT ensemble for another 500TUs during which a random velocity distribution was assigned to all the beads every 0.5TUs. Mean square internal displacement of the chains, which is a sensitive indicator of unrelaxed chain conformations²⁸, was examined to ensure the convergence of the equilibration procedure – see Adeyemi et al.²⁰.

B. Equilibrium Molecular Dynamics (EMD) or Green-Kubo (GK) Approach

The GK relation relates the shear stress relaxation modulus $G(t)$ to the TACF of shear stress fluctuations

$$G(t) = \frac{V}{k_B T} \langle \sigma_{xy}(t) \sigma_{xy}(0) \rangle \quad (5)$$

where V is the volume of the system, T is the temperature and σ_{xy} is an off-diagonal stress component. The major challenge in using this approach is the intense fluctuations of the stress TACF which is particularly severe at the terminal (large t) regime. One strategy for the reduction of fluctuation is by pre-filtering the stress signal with moving average before the TACF is calculated^{18,29}. Alternatively, moving average may be applied directly to the $G(t)$ profile¹². The window size for moving average must be carefully selected to prevent the data from being overly smeared. Lee and Kremer¹⁵ found that $G(t)$ calculated from the filtered $\sigma_{xy}(t)$ signal is artificially reduced at the short-time end, but argued that, with properly-chosen window size, the long-time behavior of $G(t)$ is unaffected. Nevertheless, using a fixed window size in the moving average approach is intrinsically limited because not only are the fluctuations coming from various frequencies, but the uncertainty in $G(t)$ also grows with the time lag t due to the diminishing number of independent segments for averaging in a fixed-length time series. For this reason, strong fluctuations at the long-time limit of $G(t)$ cannot be effectively tamed with moving average^{15,29,30} which is often a cause of erroneous results³.

A more delicate multi-tau correlator method, proposed by Ramírez et al.³¹, was used in this study. From our practical experience, the method generates adequately smooth $G(t)$ profile across nearly the whole range of time lag except at the very long time end where the relaxation modulus has nearly vanished. The idea is to filter the stress signal $\sigma_{xy}(t)$ and calculate its TACF on the fly with a multi-level hierarchical data structure. Each level contains p data points. Level 0 stores the most recent p points from the time series, from which TACF for time at $t = 0\Delta t, 1\Delta t \dots, (p-1)\Delta t$, is calculated and also stored. At level l ($l \geq 1$), each data entry is the average between m data points from level $l-1$ and the most recent p block averages (each covers m^l data points in the original time series) are stored. Correspondingly, the TACF stored at each level also covers longer time lag than the previous one. Effectively, this method filters $\sigma_{xy}(t)$ with progressively larger window size for the TACF calculation at longer time lags. We used $m = 2$ and $p = 16$ as recommended by Ramírez et al.³¹.

The equivalence between shear stress components of different directions in an isotropic fluid is also leveraged to reduce statistical error. Average over TACFs of those equivalent components is expected to have lower uncertainty than that of a single component σ_{xy} ³². The par-

ticular form used in this study

$$G(t) = \frac{V}{5k_B T} [\langle \sigma_{xy}(t)\sigma_{xy}(0) \rangle + \langle \sigma_{yz}(t)\sigma_{yz}(0) \rangle + \langle \sigma_{zx}(t)\sigma_{zx}(0) \rangle] + \frac{V}{30k_B T} [\langle N_{xy}(t)N_{xy}(0) \rangle + \langle N_{xz}(t)N_{xz}(0) \rangle + \langle N_{yz}(t)N_{yz}(0) \rangle] \quad (6)$$

where

$$N_{\alpha\beta} = \sigma_{\alpha\alpha} - \sigma_{\beta\beta} \quad (7)$$

($\alpha, \beta = x, y, z$) is the same as that used in Ramírez et al.³¹.

Combining these measures allowed us to produce an adequately smooth $G(t)$ for the computation of the dynamic moduli G' and G'' through

$$G' = \omega \int_0^\infty G(t) \sin(\omega t) dt \quad (8)$$

and

$$G'' = \omega \int_0^\infty G(t) \cos(\omega t) dt. \quad (9)$$

Numerical evaluation of eq. (8) and eq. (9) is not as straightforward as it may appear, because the multi-tau correlator method returns $G(t)$ on a non-uniform grid: the spacing between consecutive points increases with time lag t . Likhtman et al.¹⁴ fitted the $G(t)$ profile to a series of Maxwell modes, from which the integrals were evaluated analytically. The Maxwell modes approximate $G(t)$ with the superposition of exponential decay functions, which thus cannot capture oscillations in the profile. We used a different approach and approximated $G(t)$ with piecewise linear functions and integrated each piece analytically. With sufficient resolution, this treatment retains all the variations in the $G(t)$ profile while also avoiding nonlinear regression. Details of our method are given in Appendix A.

As listed in table I, multiple separate EMD simulation runs were performed for each case and the average of those independent runs was reported. The duration of each independent simulation run matches that of the corresponding chain length in Likhtman et al.¹⁴

The EMD approach is particularly appealing because one simulation run contains the information for the whole LVE profile. Meanwhile, if information is desired outside the linear regime, NEMD would be the only viable approach.

C. Non-Equilibrium Molecular Dynamics (NEMD) Approach

The NEMD technique measures the system's unsteady response to an induced perturbation. Unlike the EMD

TABLE I: EMD simulation parameters, including the duration of each independent simulation and number of independent simulations used. The maximum stress relaxation time τ_{\max} is defined as the time when the obtained $G(t)$ (fig. 1) decays to 10^{-3} .

| N | Simulation Duration (TUs) | Num. Runs | τ_{\max} (TUs) |
|-----|---------------------------|-----------|---------------------|
| 25 | 5×10^5 | 5 | 1.065×10^3 |
| 50 | 5×10^5 | 5 | 2.949×10^3 |
| 100 | 1×10^6 | 5 | 1.835×10^4 |
| 350 | 3×10^6 | 3 | 4.614×10^5 |

method, this approach mimics a real experimental setup by imposing the corresponding flow condition on the simulation box. In the determination of G' and G'' , the deformation is SAOS. The SLLOD equations of motion were used, which imposes a time-dependent velocity profile across the domain³³. The imposed velocity corresponds to a sinusoidal strain of

$$\gamma(\omega) = \gamma_0 \sin(\omega t) \quad (10)$$

where γ_0 is the amplitude of the oscillation and ω is the angular frequency. At the start of the simulation, an initial mean velocity profile that matches the instantaneous box deformation rate of the moment is imposed on all beads for the quick convergence of the flow condition. In general, for a viscoelastic sample, the stress response $\sigma(t)$ oscillates with the same frequency as the strain input

$$\sigma(t) = \sigma_0 \sin(\omega t + \delta). \quad (11)$$

There is, however, a phase angle shift δ which varies between 0 and $\pi/2$ (purely elastic and purely viscous limits, respectively). The stress can be further decomposed into two orthogonal functions

$$\sigma(t) = \gamma_0 [G'(\omega) \sin(\omega t) + G''(\omega) \cos(\omega t)] \quad (12)$$

such that one of them is in sync with the imposed strain (eq. (10)) and the other has a $\pi/2$ phase lead. Equation (12) above is easily seen from the trigonometric expansion of eq. (11) using

$$\sin(\omega t + \delta) = \cos \delta \sin(\omega t) + \sin \delta \cos(\omega t). \quad (13)$$

Comparing eq. (11), eq. (12), and eq. (13), we get

$$G' = \frac{\sigma_0}{\gamma_0} \cos \delta \quad (14)$$

$$G'' = \frac{\sigma_0}{\gamma_0} \sin \delta. \quad (15)$$

Data processing for the NEMD method can also present significant challenges as the obtained $\sigma(t)$ time series is again loaded with strong noises. Previous studies often used least-square fitting of the NEMD stress output to obtain G' and G'' in eq. (12)^{21,34}. In Appendix B,

we show that, in the absence of noise, a simple discrete Fourier transform (DFT) of the sinusoidal time series

$$s(t) \equiv \frac{\sigma(t)}{\gamma_0} \quad (16)$$

only has two non-zero modes

$$\hat{s}_{\pm k_\omega} = \frac{1}{2} (G'' \mp iG') \quad (17)$$

where $\hat{\cdot}$ denotes Fourier modes and k_ω is the wavenumber corresponding to the imposed frequency ω : i.e.,

$$k_\omega = N_{\text{cycle}} \quad (18)$$

is the number of complete oscillatory cycles in the simulation run. Stress fluctuations from simulation will show up in a wide range of frequencies, but the signal at the $\pm k_\omega$ modes will still be the dominant ones and their imaginary and real parts are related to G' and G'' , respectively. In practice, we additionally performed a noise-filtering step by pre-averaging the $\sigma(t)$ signal before the DFT analysis. The $\sigma(t)$ time series was divided into small blocks, each of which covers 1/100 of an oscillatory cycle. The average of each block was used to compute $s(t)$ – the input of DFT. Since the block size and oscillatory cycle differ by two orders of magnitude, this step is designed to smoothen the signal without interfering with the primary Fourier modes. Applying DFT directly on the NEMD stress output without pre-averaging, according to our tests, will give nearly identical G' and G'' at high frequencies. At low frequencies, however, its results contain strong, seemingly random, statistical errors.

We performed NEMD for 50 frequency levels spanning four decades of ω (from 10^{-4} to 1). Simulation at each frequency level contains $N_{\text{cycle}} = 25$ complete cycles. In total, 9.16×10^8 MD time steps were used for the entire spectrum. The number of time steps spent at each frequency level increases $\propto 1/\omega$. For comparison, $N_{\text{cycle}} = 100$ to 200 was often used in previous studies^{21,34}. As we will show in this study, with the noise reduction procedure described above, $N_{\text{cycle}} = 25$ was sufficient to generate statistically robust results. Shortening of individual NEMD runs partially contributed to our ability to cover a wider frequency range and longer chains than previous studies (which did not go over three decades and did not attempt entangled chains).

Finally, as shown in table I, each EMD run of the $N = 350$ long-chain case costs 3×10^8 time steps. The total cost of three independent EMD runs at $N = 350$, which were used in obtaining its $G(t)$, is comparable to the combined cost of all NEMD runs at different frequencies (one run at each frequency). This arrangement allows us to directly compare these two methods at the same computational cost for this particular chain length.

D. Corrected Rouse Mode Analysis (cRMA)

The Rouse model describes the dynamics of an unentangled polymer melt without the topological constraints

imposed by other surrounding chains. It describes the relaxation of the polymer melt with a mean-field approach in which effects of surrounding chains on the dynamics of the probe chain are coarse grained as a continuous viscous medium. The equations of motions for the chain beads can be simplified by projecting the original bead coordinates to a set of mutually orthogonal coordinates known as the Rouse modes^{35,36}

$$\vec{X}_p \equiv \begin{cases} \sqrt{\frac{1}{N}} \sum_{n=1}^N \vec{r}_i(t) & (p=0) \\ \sqrt{\frac{2}{N}} \sum_{n=1}^N \vec{r}_i(t) \cos\left(\frac{(i-1/2)p\pi}{N}\right) & (p=1, 2, \dots) \end{cases} \quad (19)$$

where \vec{r}_i denotes the original bead position in Cartesian coordinates and i and p are the indices for the beads and Rouse modes, respectively. The $p=0$ mode is proportional to the center of mass coordinates of the chain. Higher modes, $1 < p \leq N-1$, describe the internal relaxation of sub-chain segments of the size of N/p beads. Orthogonality of Rouse modes means that their relaxation dynamics are independent from one another. Specifically, the TACF of the p -th mode

$$\langle \vec{X}_p(t) \vec{X}_p(0) \rangle = \langle \vec{X}_p^2 \rangle \exp\left(-\frac{t}{\tau_p}\right) \quad (20)$$

does not depend on any other mode. Its relaxation time scale τ_p is related to the relaxation time of the first mode τ_1 (same as the Rouse time τ_R) through $\tau_p = \tau_1/p^2$. In practice, τ_p can be obtained by fitting the TACF of the corresponding Rouse mode from EMD to eq. (20). Once τ_p is known, the $G(t)$ can be calculated by

$$G^{\text{Rouse}}(t) = \frac{\nu k_B T}{N} \sum_{p=1}^N \exp\left(-\frac{2t}{\tau_p}\right) \quad (21)$$

where ν is the number density of the beads.

Computation of Rouse modes from eq. (19) only requires bead positions \vec{r}_i whose fluctuations during an EMD simulation are negligibly small when compared with stress fluctuations. As such, obtaining $G(t)$ from the Rouse modes using eq. (21) is expected to produce much lower statistical uncertainty, implying that accurate results can be obtained with shorter runs. In this study, the same EMD data set from Sec. IIB was used for computing Rouse modes.

Vladkov and Barrat¹³ tested this idea and noted that, for their very short ($N = 10$ and 20) chains, G' from RMA is very close to the NEMD results, while G'' from RMA is substantially lower than NEMD. This deficit was attributed to the non-bonded interactions between beads which are mostly excluded in the mean-field approximation of the surrounding chains. Effects of those interactions are felt at time scales shorter than the internal relaxation times of the polymer conformation τ_p . It is

thus possible to extract their contributions directly from the short-time limit of the stress TACF, where statistical accuracy is the highest. Vladkov and Barrat¹³ proposed to fit the short time part of the $G(t)$ profile from the GK relation eq. (5) using

$$G^{\text{early}}(t) = A \exp\left(-\frac{t}{\tau_A}\right) \cos(\Omega t) + B \exp\left(-\frac{t}{\tau_B}\right) \quad (22)$$

where A , B , τ_A , τ_B , and Ω are fitting parameters.

The full $G(t)$ expression for the cRMA approach is then

$$G(t) = \begin{cases} G^{\text{early}}(t) & t \leq \tau^* \\ G^{\text{Rouse}}(t) & t > \tau^* \end{cases} \quad (23)$$

with $G^{\text{early}}(t)$ and $G^{\text{Rouse}}(t)$ given by eq. (22) and eq. (21), respectively. The cut-off time $\tau^* = 0.44$ was empirically chosen in this study so that $G^{\text{early}}(t)$ and $G^{\text{Rouse}}(t)$ connect continuously. It also sets the upper bound of the GK $G(t)$ data used for parameterizing eq. (22). To obtain G' and G'' , the integrals of eq. (8) and eq. (9) were correspondingly evaluated as summations of two segments. The first segment integrates from $t = 0$ to τ^* using $G^{\text{early}}(t)$. For both unentangled ($N = 25$ and 50) cases, the obtained $\tau_A \approx \tau_B \approx 0.1$ are much smaller than τ^* – $G^{\text{early}}(t)$ is vanishingly small at $t > \tau^*$. We thus approximately used integration from 0 to ∞ instead which can be evaluated analytically to give¹³

$$G'^{\text{early}} = \frac{A}{2} \left(\frac{\omega(\omega + \Omega)\tau_A^2}{1 + (\omega + \Omega)^2\tau_A^2} + \frac{\omega(\omega - \Omega)\tau_A^2}{1 + (\omega - \Omega)^2\tau_A^2} \right) + B \frac{\omega^2\tau_B^2}{1 + \omega^2\tau_B^2} \quad (24)$$

$$G''^{\text{early}} = \frac{A\omega\tau_A}{2} \left(\frac{1}{1 + (\omega + \Omega)^2\tau_A^2} + \frac{1}{1 + (\omega - \Omega)^2\tau_A^2} \right) + B \frac{\omega\tau_B}{1 + \omega^2\tau_B^2}. \quad (25)$$

The second segment integrates from τ^* to ∞ using $G^{\text{Rouse}}(t)$, which is evaluated numerically using the procedure of Appendix A.

III. RESULTS AND DISCUSSION

In this section, we first present the simulation outputs and data processing for each of the EMD (GK), NEMD, and cRMA approaches (Sec. III A to III C). G' and G'' from these approaches are then compared in Sec. III D. Uncertainty and computational cost considerations are discussed in Sec. III E.

A. EMD Results

The $G(t)$ profiles from EMD using the GK relation are shown in fig. 1. It can be seen that the hierarchical averaging in the multi-tau correlator method has effectively

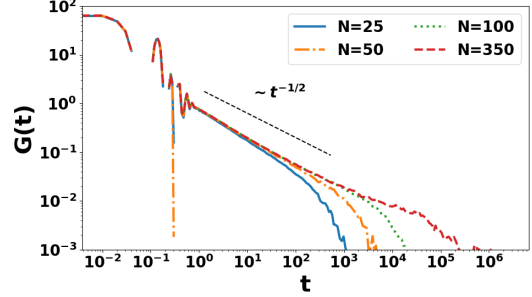


FIG. 1: Shear stress relaxation modulus $G(t)$ of varying chain length using EMD results and the GK relation.

erased noise in the $G(t)$ for nearly the whole time range of interest. At early times, the curves all collapse on one another. The wild oscillations at early times come from bond fluctuations and the curves appear broken because negative values are not shown in the logarithmic scale. This is followed in all cases by a $t^{-1/2}$ scaling regime as predicted by the Rouse model. The curves separate at later times. The shorter chains ($N = 25$ and 50) decay exponentially after their respective Rouse times. For longer chains, however, the relaxation is prolonged as a result of entanglement. Departure from the Rouse relaxation is most visible for the longest $N = 350$ case. (Departure from the $t^{-1/2}$ Rouse scaling for the $N = 350$ case was confirmed in our earlier study²⁰). At $N = 350$, the chains are not yet deeply entangled and thus $G(t)$ does not develop a full-fledged stress plateau which is not expected until $N \gg N_e$ ^{18,37}.

B. NEMD Results

For a sinusoidal strain deformation that is small enough to still be in the linear regime, it is expected that the resulting stress is equally sinusoidal and oscillates with the same frequency as the strain but with a phase shift reflecting the viscoelasticity of the material. The first thing to check is thus whether the resulting stress is indeed oscillating with the same frequency. Figures 2a to 2d show the stress and strain time series for different frequencies for the longest chain $N = 350$. It can be seen that the stress indeed oscillates at the same frequency as the strain with a notable phase lead. Despite the pre-averaging treatment mentioned in Sec. II C, the resulting stress signal still contains substantial noise. As frequency decreases, the stress magnitude is lower and the noise-to-stress ratio is higher.

To demonstrate the effectiveness of DFT in extracting the dominant mode for G' and G'' , we take the lowest frequency ($\omega = 1.2068 \times 10^{-4}$) case in fig. 2d as an example, where the noise level appears comparable to the ampli-

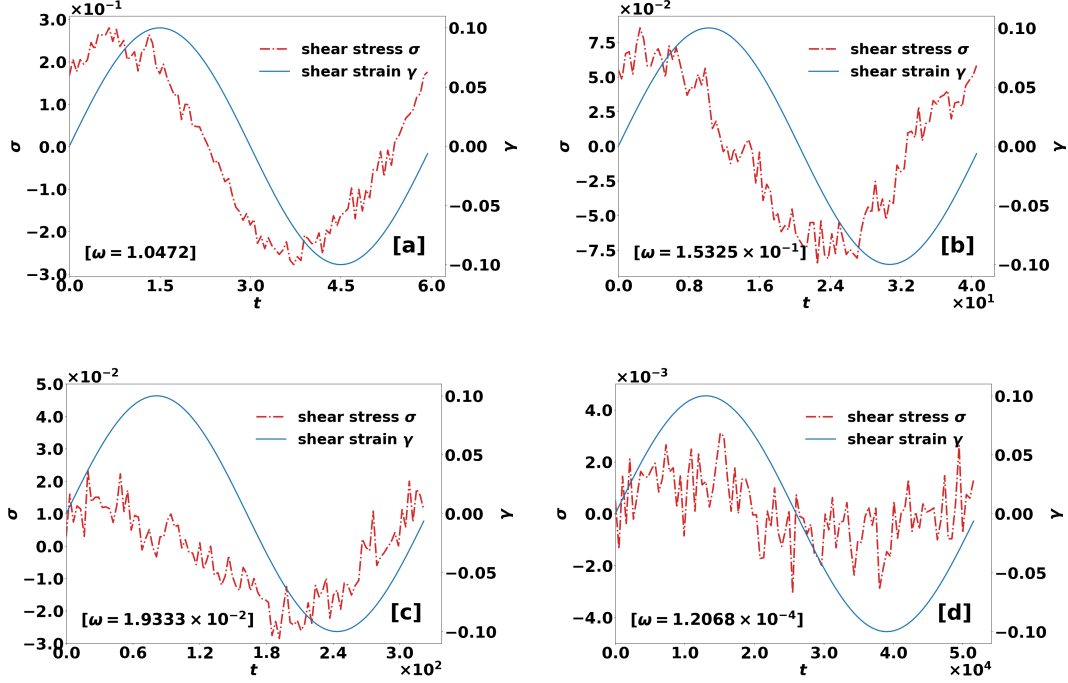


FIG. 2: Stress-strain time series of a typical converged cycle at each frequency for $N = 350$ (a) $\omega = 1.0472$ (b) $\omega = 1.5325 \times 10^{-1}$ (c) $\omega = 1.9333 \times 10^{-2}$ (d) $\omega = 1.2068 \times 10^{-4}$ (all using $\gamma_0 = 0.1$). The stress signal at each frequency has been pre-averaged over a window size of $1/100$ of the cycle.

tude of the primary oscillation. Figure 3 shows the power spectrum of its stress time series (all 25 cycles included in the statistics), as defined by

$$P_k = |\tilde{c}_k|^2 \quad (26)$$

for the leading wavenumbers. Here, P_k is the power associated with the k -th mode and \tilde{c}_k is its complex Fourier coefficient. Since the whole time series contains 25 cycles, the primary mode is expected at $k = 25$. The power magnitude at $k = 25$ is indeed distinctly higher than the rest of the spectrum (despite the large noise seen in fig. 2d). Its real and imaginary parts are used to calculate G'' and G' respectively, according to eq. (17). An equally high peak is expected at the $(N_t - 25)$ -th mode. (N_t is the total number of points in the time series). Its Fourier coefficient is simply the complex conjugate of the $k = 25$ mode.

Data in fig. 3 come from 25 cycles with a maximum strain amplitude $\gamma_0 = 0.1$. The γ_0 value was chosen based on previous studies which reported that 0.1 falls well within the linear regime where the complex moduli do not depend on the strain magnitude^{13,21}. Our chosen $N_{\text{cycle}} = 25$ is, however, substantially lower than those

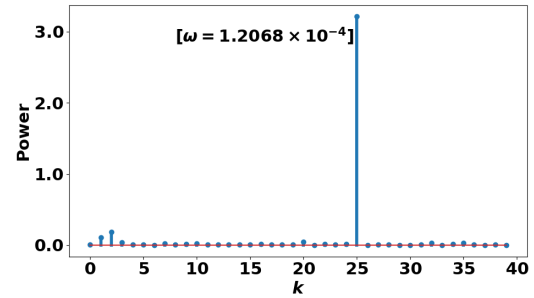


FIG. 3: Power spectrum of the stress signal for input frequency $\omega = 1.2068 \times 10^{-4}$. The first 40 modes are shown.

same previous studies (which used 100 to 200 cycles). To justify this choice, we divide the whole time series into individual cycles. Applying DFT to each cycle renders its own G' and G'' values. Figure 4 shows these single-

cycle G' and G'' values for extended 100-cycle simulation runs. For $\gamma_0 = 0.1$, at low frequency (fig. 4a), results from all cycles fluctuate around common mean values, but at high frequency (fig. 4b), the results do not converge statistically until a transient period is passed. The transient period seems to depend on both frequency and chain length. The particular case in fig. 4b shows a transient period lasting for ~ 20 cycles but transient periods as long as ~ 40 cycles were observed in other cases. As such, when reporting data from these high-frequency cases, the transient period must be discarded and the following 25 cycles in the converged regime should be used.

The computational overhead introduced by those extra transient cycles is small since they only affect the least expensive, high-frequency regime. However, the fact that, starting from the equilibrium state, it requires a number of cycles for the system to converge to steady oscillation suggests that perturbation to the equilibrium is substantial –i.e., the oscillatory shear may no longer belong to the linear regime. Since the linear and non-linear regimes are separated based on the Weissenberg number $Wi \equiv \tau_{\text{relax}}\gamma_0\omega$ (τ_{relax} is the polymer relaxation time), transition to the non-linear regime occurs at lower γ_0 for higher ω . Indeed, for the same frequency and chain length, if we reduce γ_0 to 0.01 (fig. 4c), the transient period is no longer observed. This effect of strain magnitude will be further discussed below when we compare G' and G'' results.

Figure 5 shows the effects of N_{cycle} on the normalized uncertainty in the results. The uncertainty of, e.g., $N_{\text{cycle}} = 10$, was estimated by the standard error of the 10 individual measurements coming from each cycle, which was then normalized by the overall measurement from all 10 cycles combined. There is an initial rapid decrease in uncertainty at the small N_{cycle} end but as more cycles are included in the statistics, the marginal gain of increasing the simulation length diminishes. Figure 5 only shows the $N = 350$ case but the observation is similar for other chain lengths. In all cases, the uncertainty becomes reasonably small for $N_{\text{cycle}} \geq 25$. We have repeated the analysis with larger block size –i.e. instead of using single cycles, we used every two or every five cycles as an individual measurement and still arrived at the same conclusion.

C. cRMA Results

The cRMA approach is only applicable to shorter unentangled chains. Figure 6 shows the TACFs of the first 3 modes for $N = 25$ and 50 calculated using eq. (20) from EMD runs. The profiles are normalized with $\langle \mathbf{X}_p^2 \rangle$ and thus all start at 1 at the $t = 0$ limit, which is not shown in fig. 6 due to the logarithmic scale used. Smooth exponential decay can be readily seen in all profiles. One may note that the $p = 1$ mode of $N = 25$ nearly overlaps with the $p = 2$ mode of $N = 50$. This is because the $p = 2$ mode describes the relaxation of a sub-chain

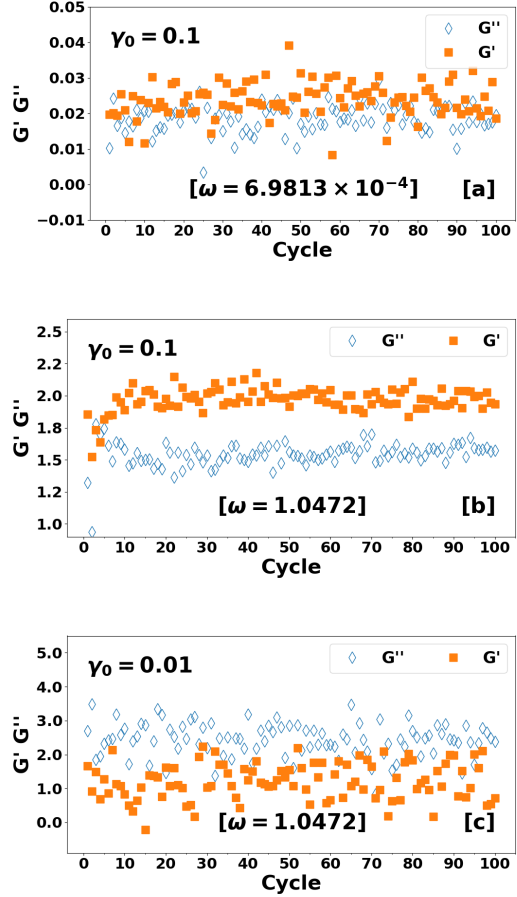


FIG. 4: G' and G'' calculated from individual cycles for $N = 350$: (a) $\gamma_0 = 0.1$ and $\omega = 6.9813 \times 10^{-4}$; (b) $\gamma_0 = 0.1$ and $\omega = 1.0472$; (c) $\gamma_0 = 0.01$ and $\omega = 1.0472$.

segment with half of the total chain length, which, in the case of $N = 50$, happens to be 25 monomers. Fitting the TACF profiles to eq. (20) yields the relaxation times for the modes τ_p . For the same chain length, the Rouse model prediction of $\tau_p = \tau_1/p^2$ is approximately held: e.g., for $N = 50$, $\tau_1 = 2906.25$, $\tau_2 = 761.03$, and $\tau_3 = 325.78$.

The obtained τ_p values were used to compute the Rouse-model prediction $G^{\text{Rouse}}(t)$ per eq. (21) which is then plotted in fig. 7 along with the GK result. It is clear that the Rouse model accurately captures the GK result for over three decades. Discrepancy is noted at $t \gtrsim \mathcal{O}(10^4)$ where the stress has nearly vanished and the GK result is laden with noise. At the short-time end

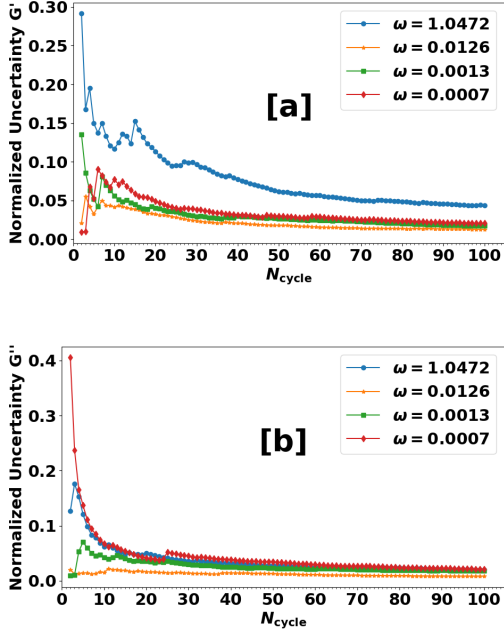


FIG. 5: Uncertainty of (a) G' and (b) G'' with increasing number of cycles included in the time series, normalized by the estimated G' and G'' values ($N = 350$).

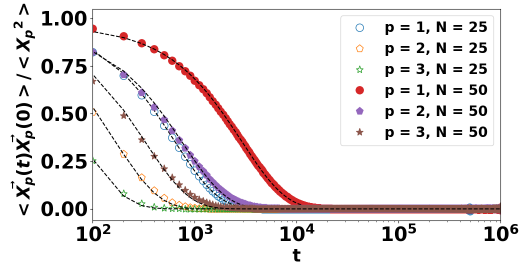


FIG. 6: Relaxation of $p = 1, 2,$ and 3 Rouse modes for $N = 25$ (filled markers) and $N = 50$ (empty markers). Lines represent fitted regression lines using the simple exponential relaxation function of eq. (20).

($t \lesssim \mathcal{O}(1)$), $G^{\text{Rouse}}(t)$ is significantly lower than the GK $G(t)$ profile. This deficit is attributed to the bead-bead non-bonded interactions not fully captured by the Rouse model and will result in an underestimate of G'' especially at the high frequency regime¹³. A correction is introduced by fitting the short-time part of $G(t)$ to

eq. (22). The resulting $G^{\text{early}}(t)$ captures the short-time $G(t)$ profile well (fig. 7b) but decays quickly after $t \approx 0.4$. Calculation of G' and G'' in the cRMA approach combines $G^{\text{early}}(t)$ and $G^{\text{Rouse}}(t)$ according to the procedure in Sec. IID.

D. Comparison of Methods

We turn now to the comparison of the computed G' and G'' profiles. We first show the results of the shorter chains $N = 25$ and 50 in fig. 8a and fig. 8b. Since both types of chains are well within the unentangled regime²⁰, a rubbery plateau does not exist in the G' profile. We further observe the Rouse scaling $-G' \propto \omega^2$ and $G'' \propto \omega$ at the terminal (low ω) frequencies for both chains. The G'' values are greater than the G' values at all frequencies. For $N = 25$ in fig. 8a, all three methods (EMD/GK, NEMD, cRMA) give nearly equivalent results for intermediate and high frequencies (10^{-3} and above) for both G' and G'' . The agreement is equally good at the low frequency end for G'' , but for G' , strong fluctuations are found in both the EMD/GK and NEMD results. The high noise-to-signal ratio is most likely due to the low magnitude of G' in that regime, which reflects the quick relaxation of the $N = 25$ chains. For $N = 50$ in fig. 8b, the results are very similar to $N = 25$ except that fluctuations in G' at the low- ω end appear smaller especially in the NEMD case.

Of the three methods, cRMA is least affected by simulation noise and uncertainty. This does not come as much of a surprise because the cRMA method is based on particle coordinates from the EMD simulation and avoids the intrinsically noisy stress calculation, with the only exception of the short-time stress correlation used in the correction term. Comparison with the EMD/GK and NEMD results shows that cRMA also produces reliable results for linear viscoelastic properties. However, its usage is limited to strictly unentangled polymers.

Unless otherwise noted, NEMD results here and below used a standard strain amplitude of $\gamma_0 = 0.1$, except in the high frequency regime ($\omega \geq 7.2222 \times 10^{-2}$) where $\gamma_0 = 0.01$ was used. This is because the standard $\gamma_0 = 0.1$ would yield unreliable results at higher frequencies. Figure 9 shows the comparison between these two strain amplitudes in the $N = 50$ case as an example. The standard $\gamma_0 = 0.1$ is accurate for frequency up to $\omega = 0.2244$, after which unnatural kinks are found in both profiles, with G' and G'' being respectively over- and under-estimated compared with EMD results. Similar behaviors are found in all other chain lengths studied. Reducing γ_0 to 0.01 produces results that not only extend smoothly from the $\gamma_0 = 0.1$ results of lower frequency, but also agree well with EMD results. This corroborates our earlier discussion that for $\gamma_0 = 0.1$, the flow is no longer in the linear regime at high frequency.

Figure 10 shows G' and G'' for the longest chain species $N = 350$ studied. Different from the shorter unentangled

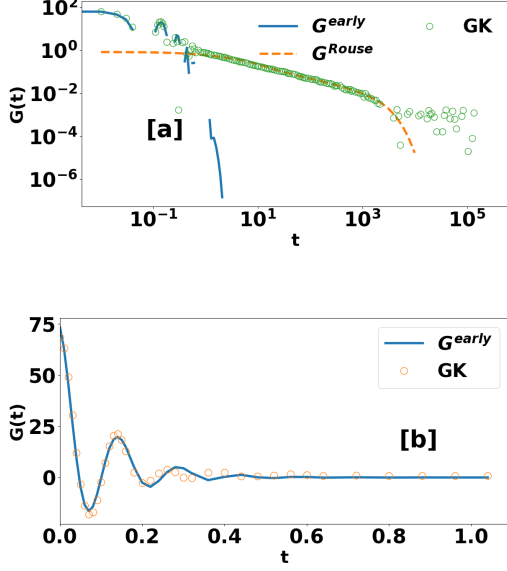


FIG. 7: Relaxation modulus from the Rouse model $G^{\text{Rouse}}(t)$ compared with that from the Green-Kubo relation $G(t)$ (both using EMD data for $N = 50$); $G^{\text{early}}(t)$ is a fit to the short-time part of $G(t)$: (a) full view; (b) enlarged view of the short-time regime.

chains in fig. 8, the entangled chains display crossovers between the G' and G'' profiles. Two crossovers are observed in the frequency range studied. The first crossover at $\omega \sim \mathcal{O}(10^{-6})$ is at the same order of magnitude as $1/\tau_d$ – the disentanglement time $\tau_d = 1.74 \times 10^6$ was determined from the monomer mean square displacement (MSD) curve for the same $N = 350$ chains in Adeyemi et al.²⁰. Crossover at $\omega \sim 1/\tau_d$ was also commonly found in experimental systems.³⁸ The second crossover, as also expected from experiments, should appear at $\omega \sim 1/\tau_e$. In our simulation, the corresponding crossover is found at $\omega \sim 2 \times 10^{-3}$, whereas τ_e is 3.43×10^3 as determined, again, from MSD²⁰ – i.e., $1/\tau_e \approx 3 \times 10^{-4}$. The two values differ by a factor of 6 to 7. We note that the difference of this magnitude is not uncommon even between τ_e values measured from different experimental techniques³⁹. In addition, since $N = 350$ is not long enough for the chains to be fully entangled – as reflected by the lack of a fully developed stress plateau, quantitative discrepancies with characteristics of fully entangled polymers in experiments are expected.

Likhtman et al.¹⁴ also reported the first crossover between $\omega = 10^{-6}$ and 10^{-5} . Their G' and G'' profiles appear smoother than ours in the terminal regime. This can be attributed to their use of Maxwell modes for fitting the

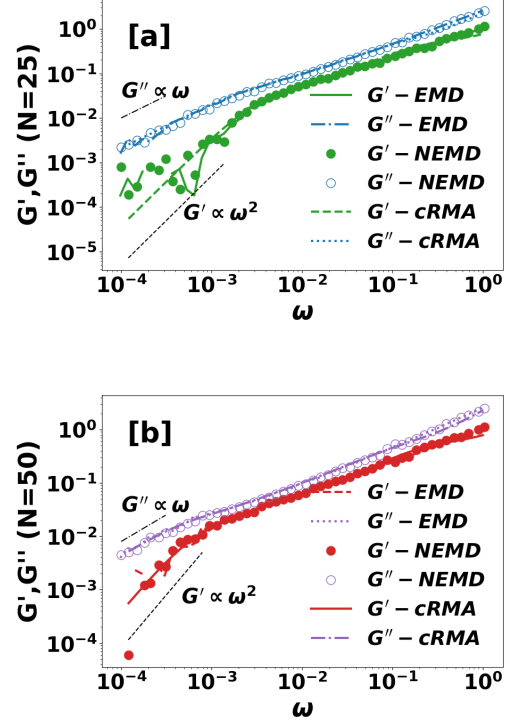


FIG. 8: G' and G'' using EMD/GK, NEMD, and cRMA methods for (a) $N = 25$ and (b) $N = 50$ ($\gamma_0 = 0.01$ is used for $\omega \geq 7.2222 \times 10^{-2}$ and $\gamma_0 = 0.1$ used for lower ω).

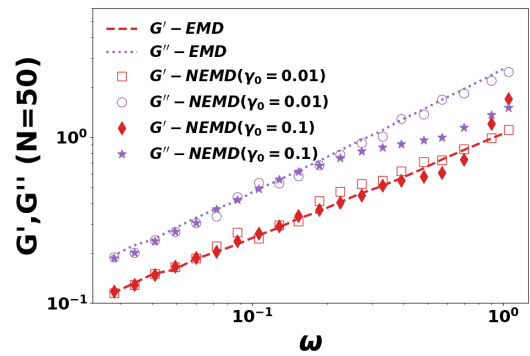


FIG. 9: Effects of strain amplitudes on the NEMD results in the high frequency regime ($N = 50$).

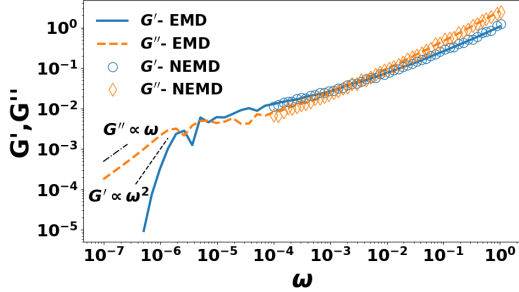


FIG. 10: G' and G'' using EMD/GK and NEMD for $N = 350$.

$G(t)$ profile which inherently cannot capture the oscillations in the $G(t)$ profile – either the short-time oscillation caused by bond fluctuations or the long-time oscillation caused by statistical uncertainty. Our fitting used piecewise linear functions (Appendix A), which preserves all oscillations in the relaxation modulus. We may as well obtain smooth terminal-regime profiles if we filter the $G(t)$ profile at the long-time limit before its conversion to G' and G'' . Likhtman et al.¹⁴, however, were not able to identify the second crossover, the one corresponding to $1/\tau_e$, unless the system density is significantly raised. Finally, we again note the excellent agreement between EMD and NEMD results in fig. 10. Both methods predict the second crossover at the same position, although our NEMD did not cover sufficiently low frequency to reach the first crossover.

Figures 11 and 12 show the G' and G'' results for all chain lengths. For G' , the curves all collapse on themselves at higher frequencies. At lower frequencies, the magnitude of G' increases with increasing chain length. Entanglement effects are clearly noticeable in the $N = 350$ case, where the profile decays with a lower slope at $\omega \lesssim \mathcal{O}(10^{-3})$. It, however, falls short of developing a fully flat plateau. The slower decay allows the G' profile to intersect the G'' profile in that frequency range (fig. 10). In comparison, the unentangled species ($N = 25$ and 50) decays at faster rates as they approach the terminal regime. Signs for entanglement cannot be clearly identified from the G'' profiles (fig. 12).

In all cases, NEMD and EMD/GK results are in excellent agreement for the frequency range covered by our NEMD simulations, which provides mutual validation between these two methods. For NEMD, it is clear that, with a proper data processing procedure, one can obtain reliable results with much fewer cycles (25 in this study) than previous reports. For EMD, its application using the GK relation has been plagued by the strong statistical noise. Likhtman et al.¹⁴ has showed that the multi-tau correlator method can effectively suppress the noise and render smooth $G(t)$ profiles. Its success, however,

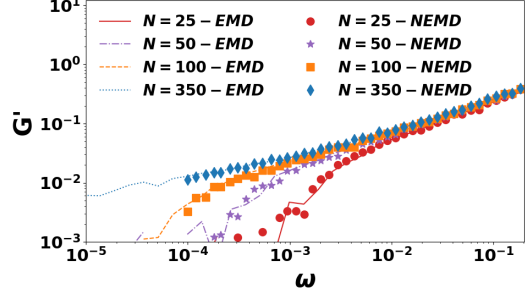


FIG. 11: G' for $N = 25, 50, 100$ and 350 chains using EMD/GK and NEMD.

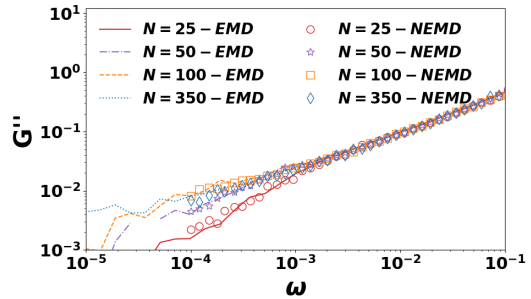


FIG. 12: G'' for $N = 25, 50, 100$ and 350 chains using EMD/GK and NEMD.

builds on the aggressive filtering, using extended averaging windows, at the long-time end of the TACF. The effects of such filtering on the quantitative accuracy of the results were not known, until our direct comparison with NEMD establishes its validity.

With G' and G'' , we can calculate the complex modulus

$$G^* \equiv \sqrt{G'^2 + G''^2}$$

and then the complex viscosity

$$\eta^* \equiv \frac{G^*}{\omega}$$

to test the validity of the Cox-Merz rule. The steady shear viscosity η was obtained by running the NEMD simulation of steady shear flow at different shear rates $\dot{\gamma}$. For each $\dot{\gamma}$, the first 10^5 TUs of the shear stress time series was discarded and the following 1.5×10^5 was averaged to be used in the shear viscosity calculation. Uncertainty was estimated by dividing the retained part into three blocks of equal length and the standard error of viscosity values from those blocks are reported.

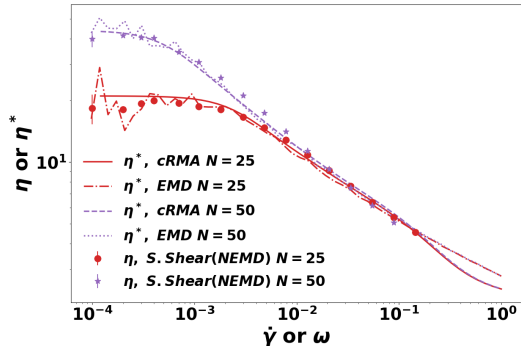


FIG. 13: Comparison of the complex viscosity $\eta^*(\omega)$, from EMD/GK and cRMA approaches, with the shear viscosity $\eta(\dot{\gamma})$, from NEMD of steady shear flow conditions ($N = 25$ and $N = 50$). Error bars are shown for the latter but only when they are larger than the marker size.

Figure 13 plots the steady shear viscosity $\eta(\dot{\gamma})$ in comparison with $\eta^*(\omega)$ for the unentangled chain species. Only EMD/GK and cRMA results are plotted for η^* . The NEMD/SAOS results are very close to EMD/GK (as reflected in their numerically equivalent G' and G'' results) and thus omitted for clarity. The viscosity profiles show typical behaviors of polymer melts, including a Newtonian plateau at the low shear end and shear-thinning at higher shear rates. It is clear that $\eta(\dot{\gamma})$ stays close to $\eta^*(\omega)$ for the entire range tested, indicating the general applicability of the Cox-Merz rule to the KG model chains. Both EMD/GK and NEMD/steady shear are subject to larger statistical uncertainty at the low ω or $\dot{\gamma}$ end, while the cRMA approach gives smooth and accurate results for unentangled chains.

E. Discussion: Accuracy and Cost

Results presented so far have established that, with proper noise reduction and data processing procedures, both EMD and NEMD give quantitatively reliable results for G' and G'' . The question now becomes which method should one choose for obtaining the most accurate results with limited computational resources.

Figure 14 shows the statistical uncertainty in the G' and G'' values calculated from all three methods using our standard simulation lengths reported in Sec. II. For EMD/GK and cRMA, uncertainty is straightforwardly estimated from the standard error of results from independent trajectories. As shown in table I, three to five independent EMD runs were performed for each case. For NEMD/SAOS, the 25-cycle time series used for each frequency was divided into five equal blocks (with five cycles

in each). Each block of time series undergoes the DFT analysis to obtain its own G' and G'' values and the uncertainty is reported as the standard error between single-block results. The reported uncertainty magnitudes in fig. 14 are all normalized by the corresponding G' or G'' values – i.e., they are reported as relative errors.

Accuracy of G' and G'' results must be discussed in the frequency range of relevance, which varies with chain length. We define the maximum stress relaxation time τ_{\max} as the time for $G(t)$ to first drop to 10^{-3} (see fig. 1) and listed the timescale in table I for different chain lengths. We note that for $N = 350$, τ_{\max} is much longer than its Rouse time $\tau_R = 1.66 \times 10^5$ (as determined from MSD²⁰) due to entanglement effects, whereas for $N = 25$ and 50 , τ_{\max} is very close to their respective τ_R (which can be estimated from the τ_R of the $N = 350$ case using $\tau_R \propto N^2$). The standard EMD simulation length chosen for each independent run is one to two orders of magnitude longer than τ_{\max} to ensure that the stress TACF has multiple independent segments to average over for the longest time scale of interest. We then mark $\omega_{\min} \equiv 1/\tau_{\max}$ as the minimum frequency of interest for each chain length in fig. 14.

For unentangled cases ($N = 25$ and 50), cRMA is clearly more accurate than both other methods, especially at the low-frequency end, where both EMD/GK and NEMD suffer from strong fluctuations, the statistical error from cRMA is well below 1%.

Between EMD/GK and NEMD, there is notable difference in the frequency dependence of uncertainty. The GK relation relies on the stress TACF to calculate $G(t)$. For EMD simulation of a given duration, there are more shorter independent segments to average over than longer ones. As a result, at $\omega \gtrsim 10^{-2}$, its error is rather low – no more than a few percent, while each EMD case see its largest error at the low frequency end. Uncertainty from NEMD is less dependent on frequency and fluctuates more or less in the 10^{-2} to 10^{-1} range. In fig. 14a and fig. 14b, the error does seem to grow above 10% at the low frequency end, but that is likely due to the frequency dropping below ω_{\min} , where the complex modulus magnitudes are vanishingly small and no longer of significant interest. It appears that for NEMD, the uncertainty depends mostly on the number of cycles included in the statistics which was set to be the same at different frequencies.

To compare the efficiency between EMD and NEMD, we first look at the $N = 350$ case (fig. 14d), where the simulation cost, measured in terms of the total number of MD time steps used in the statistics (all three independent runs for EMD and 25 cycles at all frequencies for NEMD), is controlled to be nearly the same. From fig. 14d, the statistical errors from both methods are comparable in a wide frequency range of $10^{-4} \lesssim \omega \lesssim 10^{-1}$. The advantage of EMD is clear at $\omega \gtrsim 10^{-1}$, where its error drops below 1%, but NEMD remains acceptable at below 10%. The higher error from NEMD at high frequency is attributed to the declining effectiveness of the

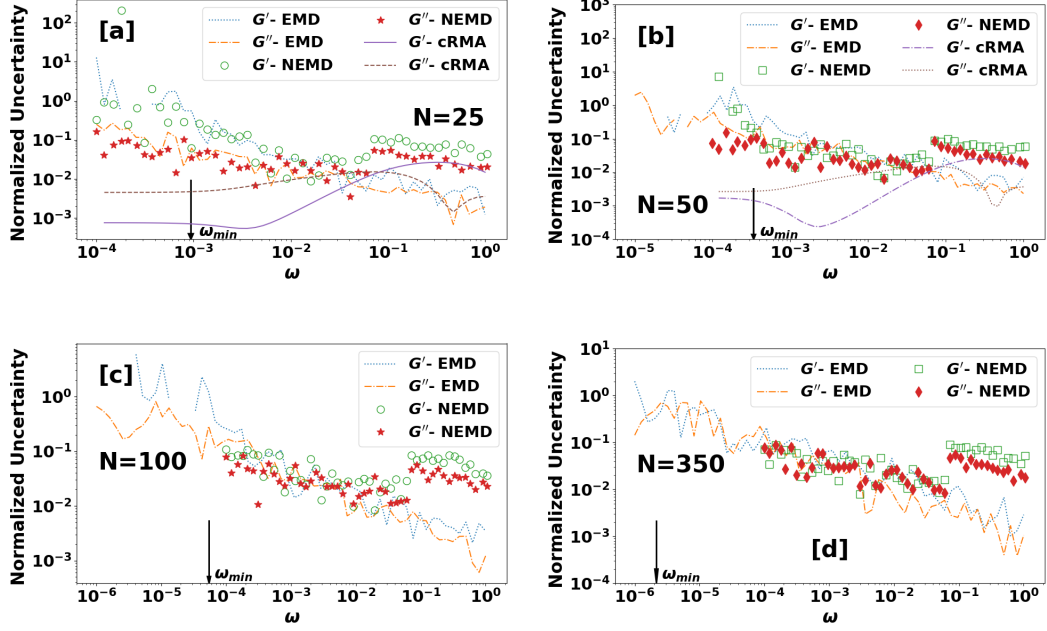


FIG. 14: Uncertainty of G' and G'' from EMD/GK, NEMD, and (for unentangled chains only) cRMA normalized by the estimated G' and G'' values: (a) $N = 25$, (b) $N = 50$, (c) $N = 100$, and (d) $N = 350$.

pre-averaging step applied to the stress signal. To avoid contamination of stress signal at the imposed frequency, we set the pre-averaging block size to 1/100 of the oscillation period. As the imposed frequency increases, the block size diminishes and becomes less effective at noise removal. One may easily improve the accuracy at high frequencies by running more cycles, which would not introduce substantial extra cost due to the shorter periods there. Per fig. 5, increasing to 100 cycles is estimated to reduce the error in G' by half. (Although fig. 5 used a block size of 1 cycle for error estimation – versus 5 cycles used in fig. 14, we have confirmed that the dependence of error on N_{cycle} is not sensitive to the block size.)

Limitation of NEMD is more obvious at the low frequency end. The frequency range swept by NEMD in this study goes down to 10^{-4} , which leaves nearly two decades of lower frequencies that are still of interest (i.e., $> \omega_{\min}$) uncovered. By contrast, the same set of EMD data can be used to generate G' and G'' of any frequency without additional computational cost. Of course, for limited EMD simulation length, statistical uncertainty increases with decreasing frequency, but as far as results in fig. 14d are concerned, the error remains at $\sim 10\%$ for most of the $\omega \sim \mathcal{O}(10^{-5})$ decade. To capture the same decade using NEMD, the computational cost would be 10 times as high as that of the $\mathcal{O}(10^{-4})$ decade – i.e.,

the overall NEMD simulation cost must increase by an order of magnitude. Based on fig. 5, one may propose to accept slightly higher uncertainty and run the lowest frequencies with fewer cycles, which nonetheless would still require significantly higher computational cost.

The conclusion is similar at $N = 100$ (fig. 14c), where the lowest frequency swept by NEMD is closer to ω_{\min} . NEMD also shows similar uncertainty level as EMD except at $\omega \gtrsim 10^{-1}$ where the advantage of EMD is clear. Note that this equivalence in performance between these two methods is built on substantially higher computational cost in NEMD. Recall that the total computational cost of NEMD in this study does not change with chain length. For $N = 100$, the cost of EMD (table I) is only one third that of NEMD. This, however, does not mean that EMD is three times better – everything else the same, increasing the data size by a factor of three would lead to a factor of $\sqrt{3}$ reduction in the uncertainty, which is not big compared with fluctuations between data points in fig. 14c. The advantage of EMD is smaller for shorter chains ($N = 25$ and 50 in fig. 14a and fig. 14b). In both cases, NEMD offers similar statistical accuracy as EMD except, again, at the high-frequency end. The total cost of NEMD is higher by nearly one order of magnitude, but part of the low frequency data fall below ω_{\min} . If we only count NEMD runs at $\omega \geq \omega_{\min}$, the total computa-

tional cost would be comparable to EMD at $N = 25$.

Our analysis shows that, contrary to many's belief, EMD using the GK relation and multi-tau correlator method not only provides accurate results for linear viscoelastic properties, it also appears to be more efficient in some cases, especially for longer chains where the need of covering lower frequencies puts higher burden on NEMD. For EMD, in theory, meaningful results at all frequencies can be generated with a single run that covers the longest relaxation time. In practice, EMD is equally constrained by the limited simulation duration in the long-time (low-frequency) end of the spectrum. Figure 15 shows the variation of the normalized statistical error of EMD if we shorten the duration of each independent run to 1/10, 1/3, and 2/3 of the standard duration (table I). It is clear that as the simulation gets shorter, accuracy at lower frequencies is first affected. For example, with a 10-fold increase in simulation length, the error in G' reduces by a factor of 3 to 5 (fig. 15a), which is comparable to the factor of $\sqrt{10}$ expected.

The advantage of EMD is that information on different frequencies is contained in the same time series, whereas NEMD would require a new simulation even for a slightly different frequency. Although EMD seems more susceptible to statistical noise, which is easier to remove in NEMD because the frequency of the primary signal is known *a priori*, this weakness is partially lessened by the success of the multi-tau correlator method. The net outcome is thus a small advantage in favor of EMD when computing the complete spectrum of linear viscoelasticity is the goal. The real advantage of NEMD lies in its flexibility. For example, one may easily save half of the computational cost by dropping every other frequency level covered. It would also be preferred when only a certain frequency range is of interest or lower accuracy is permissible at certain frequencies. The latter is because it allows the user to independently adjust the accuracy at different levels by changing the number of cycles used.

IV. CONCLUSIONS

In this study, we compared equilibrium and non-equilibrium MD approaches for computing the linear viscoelastic properties of polymer melts, using a KG bead-spring chain model with chain lengths that range from the unentangled ($N = 25$ and 50) to the marginally and moderately entangled ($N = 100$ and $N = 350$) regimes. For EMD, the primary focus was on the Green-Kubo (GK) approach, but, for unentangled chains, we also tested a corrected Rouse mode analysis approach in which short-time GK results were introduced to supplement the stress relaxation modulus calculation from the Rouse model. We showed that with proper data processing and noise reduction procedures, all these approaches produced quantitatively equivalent results for G' and G'' . For EMD with the GK relation, the multi-

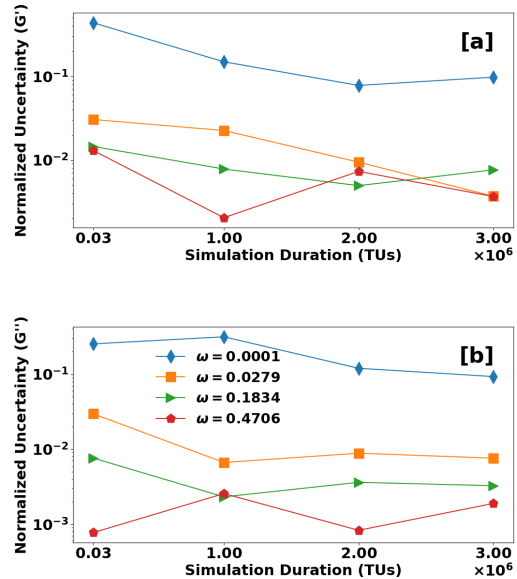


FIG. 15: Dependence of normalized uncertainty in EMD/GK results on the duration of each independent simulation run (out of three used in the statistics of $N = 350$): (a) G' and (b) G'' . The longest run shown in the figure (with 3×10^6 TUs) is the standard duration used in the study.

tau correlator method effectively removes the noise while preserving the quantitatively accurate relaxation dynamics. Numerical integration of the Fourier integrals with the relaxation modulus $G(t)$ approximated by a piecewise linear function faithfully converts the results to complex moduli. For NEMD, we applied DFT to extract G' and G'' from the pre-averaged stress signal and showed that 25 cycles at each frequency is sufficient to obtain statistically meaningful results. The simulation length is much shorter than previously reported in the literature which significantly reduces the computational expense needed to obtain a representative spectrum. In addition, we found that the strain amplitude of the imposed oscillatory shear must be carefully chosen for different frequency levels to avoid non-linear effects.

Comparing the statistical uncertainty of these methods, we found that, despite the common perception that the EMD/GK approach is more strongly influenced by stress fluctuations, it offers at least equally accurate and, sometimes, more accurate results than NEMD when the same total simulation time is used. The advantage of NEMD is its flexibility especially when only a limited frequency range is of interest. The cRMA method relies on the accuracy of the Rouse model but, at least for

the KG model in the unentangled regime, it offers highly accurate results.

Appendix A: Numerical Evaluation of the Fourier Integral

Assume we are given $G(t)$ values at a series of discrete points: G_1, G_2, \dots , and G_k , where G_k represents the value of $G(t)$ at the k -th temporal grid point t_k . The data points do not have to be equally spaced apart. Indeed, in this study, the discretized $G(t)$ points came from the multi-tau correlator method, which by construction uses a non-uniform temporal grid and its spacing increases with t . We used the multi-tau correlator output series of G_k without modification.

Note that evaluating eqs. (8) and (9) is equivalent to performing the Fourier integral

$$I \equiv \int_0^\infty G(t) \exp(-i\omega t) dt. \quad (\text{A1})$$

For its numerical evaluation, we follow the method in Luyben⁴⁰ and divide the integral into sub-integrals of individual grid intervals – i.e., $\Delta t_k \equiv t_k - t_{k-1}$. Equation (A1) is then written as the summation of sub-integrals I_k :

$$I = \sum_{k=1}^N \left(\int_{t_{k-1}}^{t_k} G(t) \exp(-i\omega t) dt \right) \equiv \sum_{k=1}^N I_k \quad (\text{A2})$$

We now approximate $G(t)$ in each interval t_{k-1} to t_k with a linear function (higher order polynomials can be used to improve the accuracy):

$$\begin{aligned} G(t) &\approx \phi_k(t) \\ &= \alpha_{0k} + \alpha_{1k}(t - t_{k-1}) \quad \text{for } t_{k-1} < t < t_k \end{aligned} \quad (\text{A3})$$

where α_{1k} is the slope of the line over the k -th interval

$$\alpha_{1k} = \frac{G_k - G_{k-1}}{\Delta t_k} \quad (\text{A4})$$

and α_{0k} is the value of ϕ_k at the beginning of the interval

$$\alpha_{0k} = G_{k-1}. \quad (\text{A5})$$

The constants α_{0k} and α_{1k} change with each interval. Inserting eq. (A3) into eq. (A2) gives

$$I_k \approx \int_{t_{k-1}}^{t_k} [\alpha_{0k} + \alpha_{1k}(t - t_{k-1})] \exp(-i\omega t) dt \quad (\text{A6})$$

which can be evaluated analytically. Integrating eq. (A6) by parts and substituting α_{0k} and α_{1k} by eq. (A4) and

eq. (A5) give

$$\begin{aligned} I_k &\approx \frac{G_{k-1}}{i\omega} (\exp(-i\omega t_{k-1}) - \exp(-i\omega t_k)) \\ &\quad - \frac{G_k - G_{k-1}}{\Delta t_k} \frac{\Delta t_k}{i\omega} \exp(-i\omega t_k) \\ &\quad + \frac{G_k - G_{k-1}}{\Delta t_k \omega^2} (\exp(-i\omega t_k) - \exp(-i\omega t_{k-1})) \\ &= G_k \left(-\frac{\exp(-i\omega t_k)}{i\omega} + \frac{\exp(-i\omega t_k) - \exp(-i\omega t_{k-1})}{\omega^2 \Delta t_k} \right) \\ &\quad + G_{k-1} \left(\frac{\exp(-i\omega t_{k-1})}{i\omega} - \frac{\exp(-i\omega t_k) - \exp(-i\omega t_{k-1})}{\omega^2 \Delta t_k} \right). \end{aligned} \quad (\text{A7})$$

Extracting $\exp(-i\omega t_{k-1})$ and noting that $\Delta t_k = t_k - t_{k-1}$, we obtain

$$\begin{aligned} I_k &\approx \exp(-i\omega t_{k-1}) \left\{ G_k \left(\frac{\exp(-i\omega \Delta t_k) - 1}{\omega^2 \Delta t_k} - \frac{\exp(-i\omega \Delta t_k)}{i\omega} \right) \right. \\ &\quad \left. - G_{k-1} \left(\frac{\exp(-i\omega \Delta t_k) - 1}{\omega^2 \Delta t_k} - \frac{1}{i\omega} \right) \right\}. \end{aligned} \quad (\text{A8})$$

Finally, the full integral is given as

$$\begin{aligned} \int_0^\infty G(t) \exp(-i\omega t) dt &\approx \\ \sum_{k=1}^N \exp(-i\omega t_{k-1}) &\left\{ G_k \left(\frac{\exp(-i\omega \Delta t_k) - 1}{\omega^2 \Delta t_k} - \frac{\exp(-i\omega \Delta t_k)}{i\omega} \right) \right. \\ &\quad \left. - G_{k-1} \left(\frac{\exp(-i\omega \Delta t_k) - 1}{\omega^2 \Delta t_k} - \frac{1}{i\omega} \right) \right\}. \end{aligned} \quad (\text{A9})$$

Appendix B: Data Processing for the Stress Output from Small Amplitude Oscillatory Shear (SAOS) in NEMD

The SAOS output (eq. (12)) can be rewritten as

$$s(t) = \frac{\sigma(t)}{\gamma_0} = G'(\omega) \sin(\omega t) + G''(\omega) \cos(\omega t). \quad (\text{B1})$$

Assume that the total NEMD run covers N_{cycle} whole oscillatory cycles with a combined temporal duration of T_{run} , and $s(t)$ is stored on N_t grid points with equal spacing Δt . The time mark at each grid point is

$$t_j = j \Delta t = \frac{j T_{\text{run}}}{N_t} \quad (\text{B2})$$

and

$$\begin{aligned} s_j \equiv s(t_j) &= G' \sin \left(\frac{\omega j T_{\text{run}}}{N_t} \right) + G'' \cos \left(\frac{\omega j T_{\text{run}}}{N_t} \right) \\ (j = 0, 1, \dots, N_t - 1). \end{aligned} \quad (\text{B3})$$

(Note: the $j = N_t$ point is not included because we assign $s_{N_t} = s_0$ to enforce the periodicity of the time series.) The discrete Fourier transform (DFT) of the series is

$$\begin{aligned}
\hat{s}_k &= \frac{1}{N_t} \sum_{j=0}^{N_t-1} s_j \exp\left(-\frac{2\pi i k j}{N_t}\right) \\
&= \frac{1}{N_t} \sum_{j=0}^{N_t-1} \left(G' \sin\left(\frac{\omega j T_{\text{run}}}{N_t}\right) + G'' \cos\left(\frac{\omega j T_{\text{run}}}{N_t}\right) \right) \\
&\quad \left(\cos\left(-\frac{2\pi k j}{N_t}\right) + i \sin\left(-\frac{2\pi k j}{N_t}\right) \right) \\
&= \frac{1}{N_t} \sum_{j=0}^{N_t-1} \left(G' \sin\left(\frac{2\pi k_\omega j}{N_t}\right) + G'' \cos\left(\frac{2\pi k_\omega j}{N_t}\right) \right) \\
&\quad \left(\cos\left(-\frac{2\pi k j}{N_t}\right) + i \sin\left(-\frac{2\pi k j}{N_t}\right) \right) \\
&= \frac{1}{N_t} \left(\sum_{j=0}^{N_t-1} G' \sin\left(\frac{2\pi k_\omega j}{N_t}\right) \cos\left(-\frac{2\pi k j}{N_t}\right) \right. \\
&\quad \left. + \sum_{j=0}^{N_t-1} G'' \cos\left(\frac{2\pi k_\omega j}{N_t}\right) \cos\left(-\frac{2\pi k j}{N_t}\right) \right. \\
&\quad \left. + i \left(\sum_{j=0}^{N_t-1} G' \sin\left(\frac{2\pi k_\omega j}{N_t}\right) \sin\left(-\frac{2\pi k j}{N_t}\right) \right) \right. \\
&\quad \left. + \sum_{j=0}^{N_t-1} G'' \cos\left(\frac{2\pi k_\omega j}{N_t}\right) \sin\left(-\frac{2\pi k j}{N_t}\right) \right)
\end{aligned} \tag{B4}$$

where

$$k_\omega \equiv \frac{\omega T_{\text{run}}}{2\pi} = \frac{T_{\text{run}}}{T_{\text{cycle}}} = N_{\text{cycle}} \tag{B5}$$

i.e., the total number of oscillatory cycles in the run (note that $\omega/2\pi$ equals the frequency of oscillation – i.e., the reciprocal of the cycle period T_{cycle}). Due to the orthogonality of sine and cosine functions, for the typical situation of $0 < k_\omega \ll N_t$, eq. (B4) is non-zero only for $k = k_\omega$ and $k = N_t - k_\omega$. The latter is equivalent to $k = -k_\omega$ due to the 2π -periodicity of these functions. The non-zero modes are complex conjugates

$$\hat{s}_{\pm k_\omega} = \frac{1}{2} (G'' \mp iG') \tag{B6}$$

containing G' and G'' in their imaginary and real parts, respectively.

ACKNOWLEDGMENTS

The authors acknowledge the financial support from the Natural Sciences and Engineering Research Council of Canada (NSERC) Discovery Grants program (No. RGPIN-2014-04903 and No. RGPIN-2020-06774)

and the allocation of computing resources awarded by Compute/Calcul Canada. S.Z. thanks the Canada Research Chairs (CRC) program (No. 950-229035). This work is made possible by the facilities of the Shared Hierarchical Academic Research Computing Network (SHARCNET: www.sharcnet.ca).

DATA AVAILABILITY

The data that support the findings of this study are available from the corresponding author upon reasonable request.

- ¹John D Ferry. *Viscoelastic properties of polymers*. John Wiley & Sons, 1980.
- ²Robert Byron Bird, Robert Calvin Armstrong, and Ole Hassager. *Dynamics of polymeric liquids*. vol. 1: Fluid mechanics. 1987.
- ³Li Xi. Molecular simulation for predicting the rheological properties of polymer melts. *Molecular Simulation*, 45(14-15):1242–1264, 2019.
- ⁴Denis J Evans and Gary P Morriss. *Statistical mechanics of nonequilibrium liquids*. ANU Press, 2007.
- ⁵Peter T Cummings and Denis J Evans. Nonequilibrium molecular dynamics approaches to transport properties and non-newtonian fluid rheology. *Industrial & engineering chemistry research*, 31(5):1237–1252, 1992.
- ⁶Berk Hess. Determining the shear viscosity of model liquids from molecular dynamics simulations. *The Journal of chemical physics*, 116(1):209–217, 2002.
- ⁷Ting Chen, Berend Smit, and Alexis T Bell. Are pressure fluctuation-based equilibrium methods really worse than nonequilibrium methods for calculating viscosities? *The Journal of chemical physics*, 131(24):246101, 2009.
- ⁸Yong Zhang, Akihito Otani, and Edward J Maginn. Reliable viscosity calculation from equilibrium molecular dynamics simulations: A time decomposition method. *Journal of chemical theory and computation*, 11(8):3537–3546, 2015.
- ⁹Martin Kröger and Siegfried Hess. Rheological evidence for a dynamical crossover in polymer melts via nonequilibrium molecular dynamics. *Physical review letters*, 85(5):1128, 2000.
- ¹⁰Zhengfang Xu, Juan J de Pablo, and Sangtae Kim. Transport properties of polymer melts from nonequilibrium molecular dynamics. *The Journal of chemical physics*, 102(14):5836–5844, 1995.
- ¹¹Zhengfang Xu, Rajesh Khare, Juan J de Pablo, and Sangtae Kim. On the calculation of transport properties of polymer melts from nonequilibrium molecular dynamics. *The Journal of chemical physics*, 106(19):8285–8286, 1997.
- ¹²Suchira Sen, Sanat K Kumar, and Pawel Keblinski. Viscoelastic properties of polymer melts from equilibrium molecular dynamics simulations. *Macromolecules*, 38(3):650–653, 2005.
- ¹³Mihail Vladkov and Jean-Louis Barrat. Linear and nonlinear viscoelasticity of a model unentangled polymer melt: molecular dynamics and rouse modes analysis. *Macromolecular theory and simulations*, 15(3):252–262, 2006.
- ¹⁴Alexei E Likhtman, Sathish K Sukumaran, and Jorge Ramirez. Linear viscoelasticity from molecular dynamics simulation of entangled polymers. *Macromolecules*, 40(18):6748–6757, 2007.
- ¹⁵Won Bo Lee and Kurt Kremer. Entangled polymer melts: relation between plateau modulus and stress autocorrelation function. *Macromolecules*, 42(16):6270–6276, 2009.
- ¹⁶Qiang Zhou and Ronald G Larson. Direct calculation of the tube potential confining entangled polymers. *Macromolecules*, 39(19):6737–6743, 2006.
- ¹⁷Ji-Xuan Hou, Carsten Svaneborg, Ralf Everaers, and Gary S Grest. Stress relaxation in entangled polymer melts. *Physical review letters*, 105(6):068301, 2010.

- ¹⁸Hsiao-Ping Hsu and Kurt Kremer. Static and dynamic properties of large polymer melts in equilibrium. *The Journal of Chemical Physics*, 144(15):154907, 2016.
- ¹⁹Brandon L Peters, K Michael Salerno, Ting Ge, Dvora Perahia, and Gary S Grest. Viscoelastic response of dispersed entangled polymer melts. *Macromolecules*, 53(19):8400–8405, 2020.
- ²⁰Oluseye Adeyemi, Shiping Zhu, and Li Xi. Dynamics and stress relaxation of bidisperse polymer melts with unentangled and moderately entangled chains. *Physics of Fluids*, 33(6):063105, 2021.
- ²¹José Gines Hernández Cifre, Siegfried Hess, and Martin Kröger. Linear viscoelastic behavior of unentangled polymer melts via non-equilibrium molecular dynamics. *Macromolecular theory and simulations*, 13(9):748–753, 2004.
- ²²Mir Karim, Tsutomu Indei, Jay D Schieber, and Rajesh Khare. Determination of linear viscoelastic properties of an entangled polymer melt by probe rheology simulations. *Physical Review E*, 93(1):012501, 2016.
- ²³Kurt Kremer and Gary S Grest. Dynamics of entangled linear polymer melts: A molecular-dynamics simulation. *The Journal of Chemical Physics*, 92(8):5057–5086, 1990.
- ²⁴Mir Karim, Swapnil C Kohale, Tsutomu Indei, Jay D Schieber, and Rajesh Khare. Determination of viscoelastic properties by analysis of probe-particle motion in molecular simulations. *Physical Review E*, 86(5):051501, 2012.
- ²⁵Maurizio Mondello and Gary S Grest. Viscosity calculations of n-alkanes by equilibrium molecular dynamics. *The Journal of chemical physics*, 106(22):9327–9336, 1997.
- ²⁶Steve Plimpton. Fast parallel algorithms for short-range molecular dynamics. *Journal of computational physics*, 117(1):1–19, 1995.
- ²⁷Yelena R Sliozberg and Jan W Andzelm. Fast protocol for equilibration of entangled and branched polymer chains. *Chemical Physics Letters*, 523:139–143, 2012.
- ²⁸Rolf Auhl, Ralf Everaers, Gary S Grest, Kurt Kremer, and Steven J Plimpton. Equilibration of long chain polymer melts in computer simulations. *The Journal of chemical physics*, 119(24):12718–12728, 2003.
- ²⁹Mohammad Masoori and Michael L Greenfield. Reducing noise in computed correlation functions using techniques from signal processing. *Molecular Simulation*, 43(18):1485–1495, 2017.
- ³⁰JT Padding and Willem J Briels. Time and length scales of polymer melts studied by coarse-grained molecular dynamics simulations. *The Journal of chemical physics*, 117(2):925–943, 2002.
- ³¹Jorge Ramírez, Sathish K Sukumaran, Bart Vorselaars, and Alexei E Likhtman. Efficient on the fly calculation of time correlation functions in computer simulations. *The Journal of chemical physics*, 133(15):154103, 2010.
- ³²Peter J Daivis and Denis J Evans. Comparison of constant pressure and constant volume nonequilibrium simulations of sheared model decane. *The Journal of chemical physics*, 100(1):541–547, 1994.
- ³³Denis J Evans and GP Morriss. Nonlinear-response theory for steady planar couette flow. *Physical Review A*, 30(3):1528, 1984.
- ³⁴Huan-Chang Tseng, Jiann-Shing Wu, and Rong-Yeu Chang. Linear viscoelasticity and thermorheological simplicity of n-hexadecane fluids under oscillatory shear via non-equilibrium molecular dynamics simulations. *Physical Chemistry Chemical Physics*, 12(16):4051–4065, 2010.
- ³⁵Prince E Rouse Jr. A theory of the linear viscoelastic properties of dilute solutions of coiling polymers. *The Journal of Chemical Physics*, 21(7):1272–1280, 1953.
- ³⁶A. Kopf, B. Dünweg, and W. Paul. Dynamics of polymer "isotope" mixtures: Molecular dynamics simulation and Rouse model analysis. *Journal of Chemical Physics*, 107(17):6945–6955, 1997. ISSN 00219606. doi:10.1063/1.474934. URL <https://doi.org/10.1063/1.474934>.
- ³⁷Alexei E Likhtman and Sathish K Sukumaran. Comment on "entangled polymer melts: Relation between plateau modulus and stress autocorrelation function". *Macromolecules*, 43(8):3980–3983, 2010.
- ³⁸Michael Rubinstein, Ralph H Colby, et al. *Polymer physics*, volume 23. Oxford university press New York, 2003.
- ³⁹Chen-Yang Liu, Roland Keunings, and Christian Bailly. Direct rheological evidence of monomer density reequilibration for entangled polymer melts. *Macromolecules*, 40(8):2946–2954, 2007.
- ⁴⁰William L Luyben. *Process Modeling, Simulation, and Control for Chical Engineers*. McGraw-Hill, Inc., 1973.

Chapter 4

Viscoelastic properties of bidisperse polymer melts

In this chapter, we focus on bidisperse polymer melts in which a moderately entangled polymer chain was mixed with shorter chains ranging from unentangled melt to weakly entangled melt. We investigated the dynamics of the different components by tracking their mean square displacement. The shorter chains accelerate the dynamics of the longer chains while the dynamics of the shorter chains are inhibited by the longer chains. A Rouse Mode Analysis was further carried out on the systems investigated and we saw that the shorter chains lessen the effects of entanglements on longer chains. By investigating a mixing rule for evaluating the stress relaxation of the mixture, it was observed that when the longer entangled chains are in the majority, the double reptation model predicts the stress relaxation of the system with remarkable accuracy. On the other hand, when the shorter chains are in the majority, a simple mixing rule was better at the prediction.

I was responsible for the model setup, performing all simulations, data analysis, and the preparation of the initial draft. Drs. Xi and Zhu supervised the research, revised the manuscript, and finalized the paper.

This chapter is published in its final form as "Oluseye Adeyemi, Shiping Zhu, and Li Xi, "Dynamics and stress relaxation of bidisperse polymer melts with unentangled and moderately entangled chains", *Physics of Fluids* 33, 063105 (2021)".

The version of record is provided by the publisher at <https://doi.org/10.1063/5.0053790>.
Copyright (c) 2021 The Authors".

Dynamics and stress relaxation of bidisperse polymer melts with unentangled and moderately entangled chains

Cite as: Phys. Fluids **33**, 063105 (2021); doi: 10.1063/5.0053790

Submitted: 11 April 2021 · Accepted: 25 May 2021 ·

Published Online: 23 June 2021



View Online



Export Citation



CrossMark

Oluseye Adeyemi,  Shiping Zhu (朱世平),  and Li Xi (奚力) 

AFFILIATIONS

Department of Chemical Engineering, McMaster University, Hamilton, Ontario L8S 4L7, Canada

Note: This paper is part of the special topic, Celebration of Robert Byron Bird (1924–2020).

^{a)} Author to whom correspondence should be addressed: xili@mcmaster.ca. URL: <https://www.xiresearch.org>

ABSTRACT

Polydispersity is inevitable in industrially produced polymers. Established theories of polymer dynamics and rheology, however, were mostly built on monodisperse linear polymers. Dynamics of polydisperse polymers is yet to be fully explored—specifically how chains of different lengths affect the dynamics of one another in a mixture. This study explored the dynamics of bidisperse polymer melts using molecular dynamics and a bead–spring chain model. Binary mixtures between a moderately entangled long-chain species and an unentangled or marginally entangled short-chain species were investigated. We found that adding short chains can significantly accelerate the dynamics of the long chains by substantially lessening their extent of entanglement. Meanwhile, although introducing long chains also hinders the motion of the short chains, it does not qualitatively alter the nature of their dynamics—unentangled short chains still follow classical Rouse dynamics even in a matrix containing entangled chains. Detailed Rouse mode analysis was used to reveal the effects of entanglement at chain segments of different scales. Stress relaxation following a step shear strain was also studied, and semi-empirical mixing rules that predict the linear viscoelasticity of polydisperse polymers based on that of monodisperse systems were evaluated with simulation results.

Published under an exclusive license by AIP Publishing. <https://doi.org/10.1063/5.0053790>

I. INTRODUCTION

The rheology of polymeric materials depends on their molecular structure. This dependence has been exploited in practical applications for improving melt processability and in characterizing their molecular weight distributions (MWD).¹ The reliability of these applications requires robust molecular theories capable of relating the rheological properties and chain relaxation dynamics to the underlying molecular makeup.

For melts of short unentangled chains, their dynamics and viscoelasticity are well described by the Rouse model.^{2–4} When the chains are sufficiently long and topological constraints between the chains are significant, i.e., entangled chains, the tube model and reptation concept pioneered by Edwards⁵ and de Gennes⁶ and further refined by Doi and Edwards⁴ have been used with considerable success. Quantitative discrepancies between experimental results and the initial tube model have been attributed to the presence of additional relaxation mechanisms other than reptation.⁷ Additional relaxation mechanisms such as contour length fluctuation (CLF),⁴ which describes the retraction and expansion of the contour length, and constraint release (CR),^{8,9}

which accounts for the loss of entanglements due to the relaxation of other chains, have improved the quantitative prediction.

These theories have largely been predicated on monodisperse samples. Industrial polymers are polydisperse, and extension of these theories to polydisperse samples requires the understanding of the interplay between the relaxation dynamics of chains with different lengths. Semi-empirical mixing rules, which weigh the contributions of different chain lengths present in the polydisperse samples, are often used. The double reptation model tries to capture the effects of polydispersity naturally. Implicit in applying the double reptation model to polydisperse polymers is the assumption that the relaxation dynamics of each constituent chain length is not altered by the presence of other chains. Various studies have shown that this is not the case.^{10–13} Experimentally, it is difficult to generate, e.g., strictly bidisperse samples to study the mutual interaction between chains of different but well-defined molecular weights. This problem naturally calls for molecular simulation in which the constituent chain lengths can be precisely controlled.

The charm of polymer physics problems lies in the fact that detailed chemical structures are often secondary to generic features of

different polymers such as chain length and topology. For this reason, important behaviors can often be captured in highly simplified lattice models in Monte Carlo (MC) simulation. Baschnagel *et al.*¹⁴ used a bond-fluctuation model (BFM) to study bidisperse melts of short unentangled chains. It was found that mixing chains of different lengths does not affect their statics (chain conformation statistics), but dynamics are noticeably shifted with the shorter chains becoming accelerated and longer chains slowed down. This conclusion was corroborated by Lin, Mattice, and Von Meerwall¹⁵ where a more delicate lattice model was used. Unlike the BFM, which uses a cubic lattice, the newer model builds on a diamond lattice, and the potential energy considers torsion angle variations according to the rotational isomeric state (RIS) model.¹⁶ This setup allows for the modeling of chemically specific polymers. The study investigated the dynamics of polyethylene chains in bidisperse melts at high temperature (453 K) where the longer species is well within the entangled regime.

Molecular dynamics (MD) is the preferred method when realistic dynamics must be captured. Off-lattice models are typically used in MD simulation, among which the bead–spring chain model pioneered by Kremer and Grest¹⁷ has been particularly instrumental. However, most contributions focused on monodisperse polymer melts^{17–20} and only a very small number of studies investigated the effects of polydispersity.^{10,11,21–24} A bidisperse system provides the simplest case where interactions between different chain lengths can be investigated. Barsky¹⁰ studied chain diffusion dynamics in bidisperse mixtures of Kremer–Grest (KG) model chains and observed that mixing with longer chains reduces the mobility of the shorter chains, while mixing with shorter chains accelerates the motion of longer chains. The longest chain considered in that study had $N = 90$ (N is the number of monomeric units or “beads”), which is at most only marginally entangled and cannot capture most entanglement effects. In addition, limited by the computer power at the time, the study only probed the dynamics for a relatively short time period. Bidisperse systems of longer chains were studied later by Picu and Rakshit²² using a higher-level model which maps 40 KG beads into a single coarse-grained bead. Topological constraints due to entanglement are modeled by forcing the middle beads to move along the backbone (i.e., reptation) and only allowing three-dimensional motion in end beads. By construction, the model can only simulate well-entangled chains. They also found that the presence of surrounding shorter chains speeds up the dynamics of the longer chains. Because the model does not consider constraint release, the effect, at least as far their results are concerned, can only be attributed to chain-end effects. Baig *et al.*²⁵ also reported that mixing with shorter chains speeds up the relaxation of longer chains (and vice versa). The study used a more realistic united-atom model for bidisperse *cis*-1,4-polybutadiene melts, which retains both CLF and CR effects, and used the tube and segmental survival probability functions as indicators of the relaxation of entangled chains. Despite the changing dynamics, it also reported that static properties of the constraining tubes, including their primitive path conformations, are not affected by varying the surrounding chain length. Polydisperse polymers with realistic, albeit very narrow, molecular weight distributions were simulated more recently using a coarse-grained model for polyethylene.^{23,24} It was found that keeping the weight-average molecular weight constant, chain dynamics accelerates with polydispersity. Mobility of the shortest chains increases much faster than the average mobility does with polydispersity, which leads to CR and faster terminal relaxation.

There has been a particular appetite for probe diffusion problems, which study the dynamics of a specific chain type, labeled as the probe species, in a matrix of (usually) another chain type. This is a special case of binary mixtures where the volume fraction of the probe type ϕ_{probe} is sufficiently low that probe–probe interactions are not important. Such a setup is designed for studying the effects of matrix chains on the probe. The example most relevant to our study is Wang and Larson²⁶ which used MD to investigate the dynamics of a long entangled chain species (primarily $N_L = 350$) in a matrix of a shorter chain species spanning both unentangled and entangled regimes ($N_S = 25$ to 160). Both types were semiflexible, and the long-chain volume fraction was kept at $\phi_L = 0.15$ to minimize the entanglement between long chains. The study focused on the CR effects, which leads to tube relaxation (described as the Rouse motion of the tube itself), with varying short-chain length N_S . More recently, Shanbhag and Wang²⁷ used a BFM, MD, and slip–spring model to simulate the diffusion of a probe chain in two types of matrices, one with the same chain type as the probe and the other with infinitely long chains, designed for studying the self-diffusion and tracer diffusion of the probe chain, respectively.

The general conclusion that mutual interactions in a binary mixture result in the acceleration and deceleration of the slower and faster chain species, respectively, not only applies to mixtures with different chain lengths, but also to those of different chemical types, which, for example, was also reported by Kopf, Dünweg, and Paul¹¹ where the two chain species differ in monomeric mass. Interestingly, varying chain topology can lead to more complex mixing behaviors. Using a BFM, Shanbhag²⁸ showed that the mobility of a ring probe polymer changes non-monotonically with increasing length of the linear matrix chains.

In this work, we investigated the dynamics and rheology of bidisperse polymer melts using the KG bead–spring chain model. MD simulation was performed for binary mixtures between an entangled chain species ($N_L = 350$) and a shorter, unentangled or marginally entangled, chain species ($N_S = 25, 50$, and 100—monodisperse melts of the first two are unentangled and the last one, as shown below, is marginally entangled) as we were particularly interested in the interplay between chains of different dynamical regimes. The chain lengths under our investigations fall into the same range as studied in Wang and Larson.²⁶ However, we studied compositions where neither component can be viewed as the probe, i.e., each chain interacts with other chains of both the same and the opposite type. Two concentration levels were considered for each N_L – N_S combination—one has the $N_L = 350$ species as the majority ($\phi_L = 0.7$) and the other as the minority ($\phi_L = 0.3$) component. Compared with previous studies on bidisperse melts with the KG model,^{10,26} our MD simulations were also substantially longer to cover the entire relaxation spectrum of all chains involved as well as to directly compute the full stress relaxation profile.

We started with the mean-squared displacement (MSD) as a direct measurement of individual chain dynamics (Sec. III A). It was followed by a Rouse mode analysis (RMA) which reveals departure (or the lack thereof) from the unentangled limit and onset of entanglement in different components of the mixture (Sec. III B). Finally, we examined the stress relaxation dynamics of the entire melt and evaluated mixing rules for predicting the relaxation modulus of the bidisperse system given that of the monodisperse melt of each component (Sec. III C).

II. MODELS AND NUMERICAL METHODS

The KG bead–spring model¹⁷ was used. Each chain consists of N beads bonded by finitely extensible non-linear elastic (FENE) springs.³ The potential between bonding beads is

$$U_{\text{FENE}}(r) = -\frac{1}{2}KR_0^2 \ln \left[1 - \left(\frac{r}{R_0} \right)^2 \right] + 4\epsilon \left[\left(\frac{\sigma}{r} \right)^{12} - \left(\frac{\sigma}{r} \right)^6 + \frac{1}{4} \right], \quad (1)$$

where r is the distance between the beads, and σ and ϵ are the standard Lennard-Jones (LJ) length and energy parameters. The first term of the equation represents an attractive potential which models FENE springs between nearest neighbors along the chain with a maximum bond length $R_0 = 1.5\sigma$, while the second term models the excluded-volume repulsion between beads and the term is only included at $r \leq 2^{1/6}\sigma$. The spring constant $K = 30\sigma/\epsilon$ is chosen to allow a reasonable integration time step while preventing chains from crossing each other.¹⁷ Note that compared with the semiflexible chains studied in Wang and Larson,²⁶ our model is fully flexible with no angle potential. This difference must be kept in mind for any comparison we make with that study below.

The interaction between non-bonding beads is modeled by the standard LJ potential

$$U_{\text{LJ}}(r) = 4\epsilon \left[\left(\frac{\sigma}{r} \right)^{12} - \left(\frac{\sigma}{r} \right)^6 \right]. \quad (2)$$

The potential is truncated at $r = 2.5\sigma$ and shifted by a constant to ensure continuity at the cutoff. Note that the original model by Kremer and Grest¹⁷ used a shorter cutoff of $r = 2^{1/6}\sigma$, making the interaction between non-bonding beads purely repulsive. This practice is still widely seen in the polymer dynamics literature although full LJ potential including the attraction well is used more often recently.^{12,29–31} Practically, comparison between the two approaches found no significant difference in both chain statics and dynamics when temperature is sufficiently high,^{12,29} such as $T = 1.0\epsilon/k_B$ used in this study (k_B is the Boltzmann constant). Hereinafter, all results will be reported in reduced LJ units in which length, energy, time, and temperature are scaled by σ , ϵ , $\tau = \sqrt{m\sigma^2/\epsilon}$, and ϵ/k_B , respectively. For example, the non-dimensional LJ energy and length parameters in Eqs. (1) and (2) are both unity. A constant time step of 0.01 (in LJ time units or TUs) is used for all simulations.

Each monodisperse system contains 50 000 beads, except the longest $N = 350$ case which contains 56 000 beads, and each bidisperse system contains 56 000 beads. The difference in size here is very small, and, for selected monodisperse cases, we have tested the larger size of 56 000 and found no noticeable size dependence. For both monodisperse and bidisperse systems, the beads were placed in a cubic box with periodic boundary conditions at a constant bead density of 0.85. The bidisperse systems mix a long-chain species ($N_L = 350$) with shorter chains of various lengths ($N_S = 25, 50$, or 100) at two levels of mass (or volume—the constituent beads are identical) fraction: $\phi_L = 0.7$ and 0.3. The longer chain is moderately entangled—for reference, the entanglement strand length N_e for the KG model is in the range of 30 to 80 depending on the method of determination.³² Detailed compositions are listed in Table I.

TABLE I. Compositions of bidisperse systems simulated: N , ϕ , and n_c denote the chain length, mass/volume fraction, and total number of chains of a given species, respectively; subscripts “L” and “S” denote the longer and shorter component in the mixture, respectively.

| N_L | ϕ_L | $n_{c,L}$ | N_S | ϕ_S | $n_{c,S}$ | Total beads |
|-------|----------|-----------|-------|----------|-----------|-------------|
| 350 | 0.7 | 112 | 25 | 0.3 | 672 | 56 000 |
| 350 | 0.7 | 112 | 50 | 0.3 | 336 | 56 000 |
| 350 | 0.7 | 112 | 100 | 0.3 | 168 | 56 000 |
| 350 | 0.3 | 48 | 25 | 0.7 | 1568 | 56 000 |
| 350 | 0.3 | 48 | 50 | 0.7 | 784 | 56 000 |
| 350 | 0.3 | 48 | 100 | 0.7 | 392 | 56 000 |

All the simulations were carried out using the large-scale atomic/molecular massively parallel simulator (LAMMPS) package.³³ The initial configuration was generated by randomly placing the specified number and types of chains in the simulation cell. Generation of individual chains follows a procedure that is analogous to a self-avoiding walk in a continuum space, which prevents backfolding of successive bonds but still leaves a large number of bead overlaps. A dissipative particle dynamics (DPD) push-off method,³¹ originally proposed by Siozberg and Andzelm,³⁴ was then used to obtain an equilibrated structure for production runs. During the DPD run, interaction between non-bonding beads was replaced by a repulsive potential in the form of

$$U_{\text{DPD}}(r) = \begin{cases} \frac{A_{\text{DPD}}}{2} r_c \left(1 - \frac{r}{r_c} \right), & r < r_c, \\ 0, & r \geq r_c. \end{cases} \quad (3)$$

Compared with the LJ potential [Eq. (2)], which has nearly hard-sphere repulsion at short range, the DPD potential is much softer. It allows for easier passing of chains and thus fast relaxation during the initial equilibration steps.

DPD simulation was run at $T = 1.0$ using a cutoff distance $r_c = 1.0$. The potential was initially low with $A_{\text{DPD}} = 25$. At the beginning, restriction was imposed on the maximum distance each bead can move within one time step which gradually increases from 0.001 to 0.1 over 15 TUs. The restriction was then removed and the simulation was run for another 100 TUs. This was subsequently followed by a gradual ramp of A_{DPD} to 1000 over 5.5 TUs. The DPD potential was then replaced with the standard LJ potential, and MD in a canonical (NVT—constant number of particles, volume, and temperature) ensemble was performed for additional 500 TUs during which a random velocity distribution was reassigned to all beads every 0.5 TU.

Equilibration quality was examined through the mean square internal displacement (MSID),

$$\langle R^2(n) \rangle \equiv \langle |\vec{r}_j - \vec{r}_i|^2 \rangle, \quad (4)$$

which measures the square distance between the i th and j th monomeric unit of the same chain, averaged over all ij -pairs with the same index separation $n \equiv |j - i|$. Auhl *et al.*³⁵ showed that, compared with the radial distribution function, end-to-end distance, and radius of gyration, MSID better captures chain deformation at intermediate scales which does not fully relax until the whole chain is equilibrated.

Figure 1 plots $\langle R^2(n) \rangle / (nr_b^2)$ ($r_b = 0.97$ is the equilibrium bond/spring length), which is the characteristic ratio of the KG chain, vs n for our equilibrated monodisperse systems. All curves increase monotonically at the beginning. For the longer chains ($N \geq 50$), the characteristic ratio converges to a constant value at the large n limit—i.e., C_∞ . The obtained $C_\infty = 1.75$ in our simulation is in excellent agreement with previous studies (e.g., 1.74 in Kremer and Grest¹⁷ and 1.75 in Auhl *et al.*³⁵).

For each cell composition, three random initial configurations were independently generated, and each underwent the above equilibration procedure before its production run. Production runs were performed in an NVT ensemble with $T = 1.0$ using Nose–Hoover chains for thermostating. The production run of each configuration lasted for a total of 5×10^5 TUs for the monodisperse $N = 25$ case, 1×10^6 TUs for the monodisperse $N = 50$ and $N = 100$ cases, and 3×10^6 TUs for all other cases (any system, monodisperse or bidisperse, containing $N = 350$ chains). Results reported in this study were averages over these three trajectories from independent initial configurations unless specified otherwise. Error bars, when provided, report the standard error between the independent runs.

III. RESULTS AND DISCUSSION

A. Mean square displacement (MSD)

We studied the dynamics of each component in the mixture using the monomer MSD $g_1(t)$, which describes the motion of individual monomers,

$$g_1(t) \equiv \frac{1}{n_c} \sum_{i=1}^{n_c} \left(\frac{1}{N_i} \sum_{j=1}^{N_i} [\vec{r}_{ij}(t) - \vec{r}_{ij}(0)]^2 \right), \quad (5)$$

and the MSD of the center of mass $g_3(t)$ which describes the overall motion of the center of mass of individual chains,

$$g_3(t) \equiv \frac{1}{n_c} \sum_{i=1}^{n_c} [\vec{r}_{i.c.m.}(t) - \vec{r}_{i.c.m.}(0)]^2, \quad (6)$$

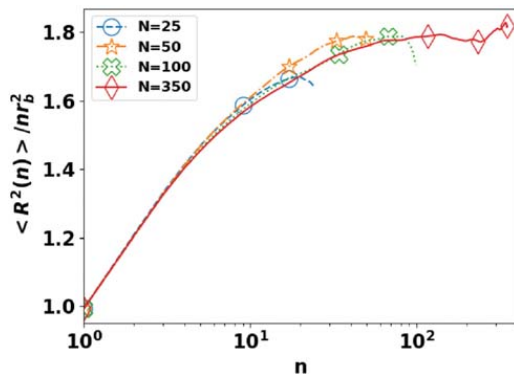


FIG. 1. Characteristic ratio calculated from the mean square internal displacement (MSID) for equilibrated monodisperse systems of different chain lengths.

where

$$\vec{r}_{i.c.m.}(t) \equiv \frac{1}{N_i} \sum_{j=1}^{N_i} \vec{r}_{ij}(t), \quad (7)$$

where n_c is the number of chains of each component, N_i is the length of the i th chain, $\vec{r}_{ij}(t)$ is the position of the j th monomer of the i th chain, and $\vec{r}_{i.c.m.}(t)$ is the position of the center of mass of the i th chain.^{36,37} An efficient method for MSD calculation based on fast Fourier transform (FFT), as detailed in Press *et al.*³⁸ and Calandrini *et al.*,³⁹ was used.

Theoretically, the monomeric MSD of an unentangled chain described by the Rouse model follows the following scaling behavior in different time regimes:^{4,37}

$$g_1(t) \sim \begin{cases} t^1, & t < \tau_0, \\ t^{1/2}, & \tau_0 < t < \tau_R, \\ t^1, & t > \tau_R, \end{cases} \quad (8)$$

where τ_0 signifies the characteristic relaxation time of a single monomer and τ_R is the Rouse time—the characteristic relaxation time of the whole chain (according to the Rouse model). For entangled systems, the simple tube model gives the following scalings:

$$g_1(t) \sim \begin{cases} t^1, & t < \tau_0, \\ t^{1/2}, & \tau_0 < t < \tau_e, \\ t^{1/4}, & \tau_e < t < \tau_R, \\ t^{1/2}, & \tau_R < t < \tau_d, \\ t^1, & t > \tau_d \end{cases} \quad (9)$$

and

$$g_3(t) \sim \begin{cases} t^1, & t < \tau_e, \\ t^{1/2}, & \tau_e < t < \tau_R, \\ t^1, & t > \tau_R, \end{cases} \quad (10)$$

where τ_e is the relaxation time of an entanglement strand and τ_d is the disentanglement time—the longest relaxation time of an entangled chain.

The monomer MSD of our monodisperse systems is presented in Fig. 2. Our calculation of $g_1(t)$ did not average over all monomers as indicated in Eq. (5). To minimize chain-end effects, only the middle monomer of each chain was included. At early times, all chains should start out with $g_1(t)$ scaling with t^1 . This regime is not captured in Fig. 2 because our sampling frequency was not high enough to capture the dynamics at such a small timescale. The next expected regime, for both unentangled and entangled chains, has a $t^{1/2}$ scaling which is indeed observed in all chain lengths studied. Dynamics of different chain lengths diverge thereafter. The $N = 25$ and 50 cases directly enter the diffusive regime (t^1), which is consistent with the Rouse model prediction [Eq. (8)]. Note that for $N = 50$, complete alignment with the t^1 scaling starts at $t \sim \mathcal{O}(10^4)$ which agrees with previous studies of monodisperse polymer dynamics.¹⁷ In comparison, the earlier bidisperse polymer study by Barsky¹⁰ only covered time scales up to $t \approx 4000$. Deviation from this pure Rouse dynamics is seen in longer chains. For $N = 100$, we observe a clear slow-down in the $t \sim \mathcal{O}(10^3)$ to $\mathcal{O}(10^4)$ regime, but it falls short of completely dropping

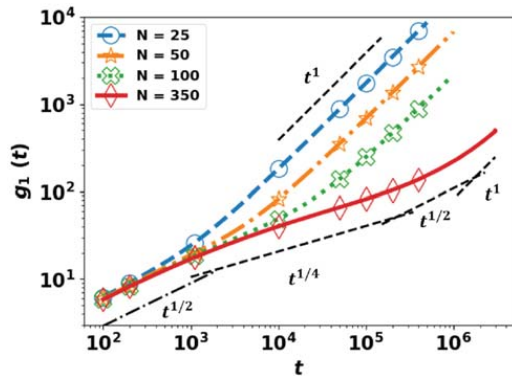


FIG. 2. Mean square displacement of internal monomers $g_1(t)$ of monodisperse systems.

to a $t^{1/4}$ scaling, which reflects weak entanglement and an insufficient separation between the entanglement strand length and the chain length (i.e., insufficient separation between τ_e and τ_R). A pronounced $\tau_e < t < \tau_R$ regime is found in the longest chain with $N=350$. A least-square regression analysis of the MSD data from $t \approx 3 \times 10^3$ to 2×10^5 gives a $t^{0.28 \pm 0.02}$ scaling, which is close to, but still slightly higher than, the theoretical $t^{1/4}$ prediction.

For comparison, the $g_1(t)$ profile for monodisperse $N=350$ semiflexible chains reported in Wang and Larson²⁶ was also visibly steeper than the $t^{1/4}$ scaling line. The increased slope could be attributed to CR and CLF, both of which were not considered in Eq. (9). CR leads to the relaxation of the constraining tubes, and the mobility of chain segments contains contributions from both chain reptation within tubes and the tube Rouse motion.⁴⁰ Meanwhile, even the longest $N=350$ chains studied here are still not significantly longer than the entanglement threshold. Therefore, CLF is felt over substantial portions of the chains (if not the entire chains), instead of just the chain ends (as in the case of well-entangled chains). Theories are typically constructed for much longer chains where the number of entanglement strands per chain $Z \equiv N/N_e \gg \mathcal{O}(1)$ [see N_e estimated in Eq. (11)]. Finally, we also note that slope estimation from regression is always subject to statistical error and can also be sensitive to the range of data points used. The increase seen in our $g_1(t)$ profile slope for $N=350$ is not large compared with uncertainty.

By fitting different segments of MSD data to the scaling laws with their corresponding theoretical exponents [Eq. (9)], we can identify the time scales for different dynamical regimes based on the intersections between the fitted lines. To obtain τ_0 , we ran an additional short 100 TU simulation with data stored at higher frequency for the $N=350$ case [to obtain the $g_1(t)$ profile for smaller time scales than those shown in Fig. 2]. The results are summarized in Table II. This approach, however, can be sensitive to the specific regression procedure and its uncertainty. From the obtained time scales, the entanglement strand length,

TABLE II. Time scales extracted from the pure $N=350$ melt MSD curve.

| τ_0 | τ_e | τ_R | τ_d |
|----------|--------------------|--------------------|--------------------|
| 3.20 | 3.43×10^3 | 1.66×10^5 | 1.74×10^6 |

$$N_e = \left(\frac{\tau_e}{\tau_0} \right)^{1/2} \approx 33, \quad (11)$$

can be estimated, which is consistent with literature values based on MSD.¹⁷

We next shift our focus to bidisperse systems, starting with the effects of a longer chain component ($N_L = 350$) on the mobility of the shorter chains. Figure 3(a) shows the center-of-mass MSD, $g_3(t)$, of pure $N=50$ chains and the same $N_S = 50$ chains when mixed with a

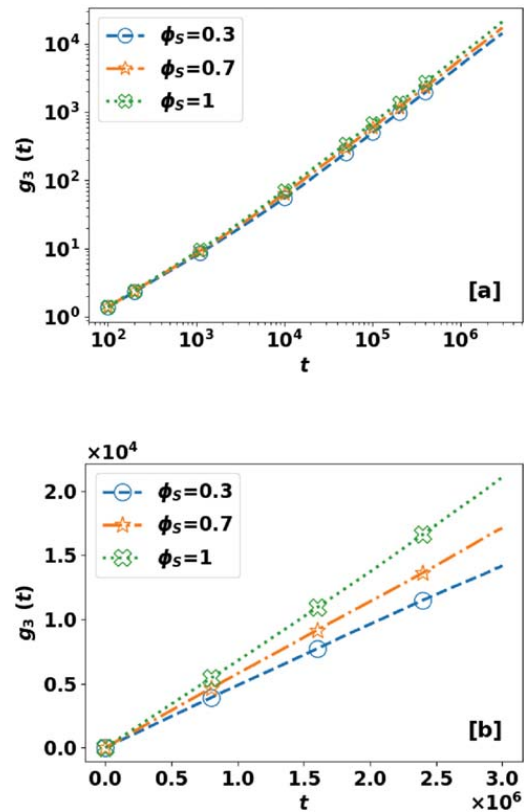


FIG. 3. Mean square displacement of the center of mass $g_3(t)$ for $N=50$ chains in its pure melt and in bidisperse mixtures with $N_L = 350$ chains as the minority and majority component: (a) log-log coordinates and (b) linear coordinates.

longer $N_L = 350$ component in log-log coordinates. At short time, MSD curves from monodisperse and bidisperse systems appear indistinguishable. However, the pure $N = 50$ case ($\phi_S = 1$) is the first to transition from the $t^{1/2}$ to t^1 scaling and shows higher chain mobility afterward. With increasing concentration of the longer chain (lowering ϕ_S), mobility of the $N = 50$ chains decreases. The difference appears small in Fig. 3(a), but when put in linear scales [Fig. 3(b)], it is clear that the diffusion rate of the $N = 50$ chains decreases. The same observation that the long-chain component impedes the motion of the shorter chains is also made when other shorter chains ($N_S = 25$ and 100) are mixed with $N_L = 350$ chains. It also agrees with the general observation made in a number of previous studies.^{10,14,22,25}

We further quantify chain mobility in the long-time limit by calculating its self-diffusion coefficient D using the Einstein relation,

$$\lim_{t \rightarrow \infty} g_3(t) \sim 6Dt, \quad (12)$$

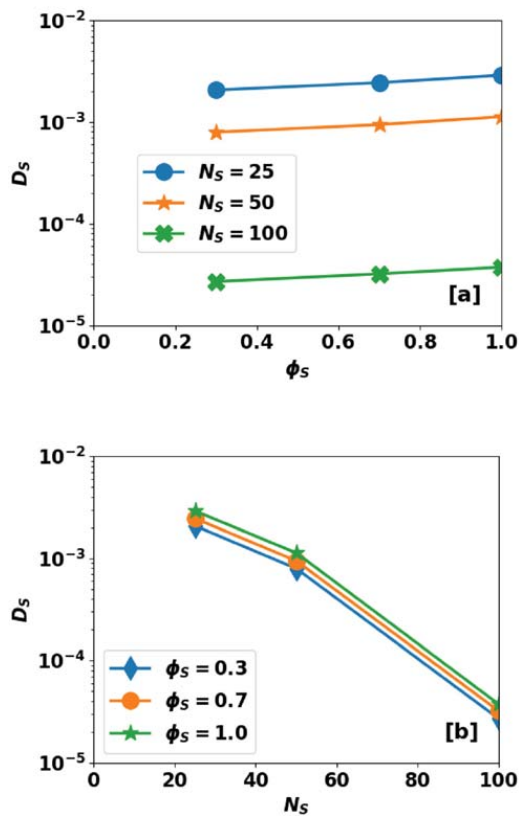


FIG. 4. Diffusion coefficient of the short-chain component in bidisperse mixtures with $N_L = 350$ chains (compared with that of pure short chain) as functions of (a) short chain mass/volume fraction ϕ_S and (b) short chain length N_S .

which allows the extraction of D from the slope of the MSD curve. Figure 4 shows the diffusion coefficient of the shorter component in bidisperse mixtures as well as that of pure short-chain melts. As shown in Fig. 4(a), the presence of the longer chains ($N_L = 350$) substantially reduces the diffusion rate of the shorter chains regardless of the length of the latter, and the effect is stronger as the fraction of the longer component increases. The change in D_S may not appear large in the logarithmic scale used in the figure, but for $\phi_S = 0.7$ and 0.3, D_S drops by $\approx 15\%$ and 30% , respectively, for all three short chain length N_S levels.

Figure 4(b) re-plots the same set of data using N_S as the independent variable. It highlights that for the three composition levels (including the pure short-chain limit) studied, the chain-length dependence follows the same pattern, i.e., lines for different ϕ_S stay parallel to one another. The trend extends at least up to $N_S = 100$ where weak entanglement has already kicked in, as reflected by the steeper slope between $N_S = 50$ and 100. This means that, e.g., $D_S(N_S = 50)/D_S(N_S = 25)$ stays nearly the same for different ϕ_S levels (note, again, the logarithmic scale in D_S), at least in the range tested, suggesting that the increasing resistance brought by the long chain can be lumped into a monomeric friction factor that increases with the long-chain fraction but remains independent of N_S , i.e., $\zeta(\phi_L)$. This observation can be rationalized considering that the relaxation of the longer species is a much slower process and, within the relaxation time of the shorter component, the long chains can be approximated as an invariant matrix.

We turn now to the effects of the shorter component on the long chains. Figure 5 shows the center-of-mass MSD of $N_L = 350$ chains in bidisperse mixtures with the $N_S = 25$ species as the diluent. It is observed that the presence of the shorter component speeds up the relaxation of the longer chains and the effect increases with the short-chain fraction $\phi_S = 1 - \phi_L$. Since $N = 350 \gg N_e$, entanglement effects are clearly shown in the $g_3(t)$ curve of the pure $N = 350$ case—a $t^{-0.6}$ scaling regime is found around $t \sim O(10^4)$. The exponent is slightly higher than the theoretical prediction of $1/2$ in the $\tau_e < t < \tau_R$ regime [Eq. (10)]. Again, we note that the $N = 350$ semiflexible chains reported in Wang and Larson²⁶ also showed a steeper $g_3(t)$ profile

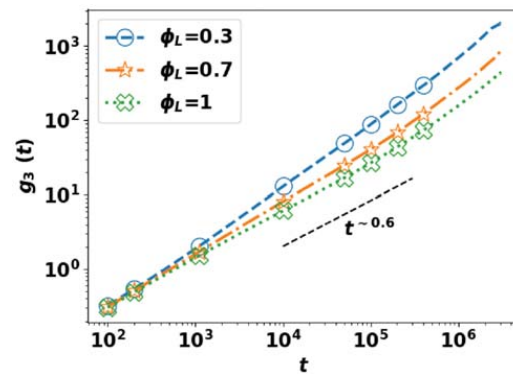


FIG. 5. MSD of the center of mass $g_3(t)$ of $N_L = 350$ chains in bidisperse mixtures with $N_S = 25$ chains (both as the minority and as the majority component). MSD of pure $N = 350$ chains is also included for comparison.

than the theoretical $t^{1/2}$ prediction. The discrepancy, as discussed above, may still be attributed to CLF and CR which are not considered in the theory. Transition to the t^1 diffusive regime occurs at $t \approx 2 \times 10^5 \sim \tau_R$. With increasing fraction of the short chains, the exponent (slope in log-log coordinates) of the same time range, $t \sim O(10^4)$, greatly increases, reaching 0.82 at $\phi_L = 0.3$. This intermediate regime becomes less differentiable from the long-time diffusive limit, suggesting a weakening of entanglement effects by short chain addition.

Effects of varying the short-chain length ($N_S = 25, 50$, and 100) on the mobility of the longer chain ($N_L = 350$) are shown in Figs. 6(a) (long-chain majority with $\phi_L = 0.7$) and 7(a) (long-chain minority with $\phi_L = 0.3$). Panel (b) of both figures replot the data in linear coordinates to highlight the changes in diffusion rate. At short time, dynamics of the $N = 350$ chains stays close to its pure melt limit, but

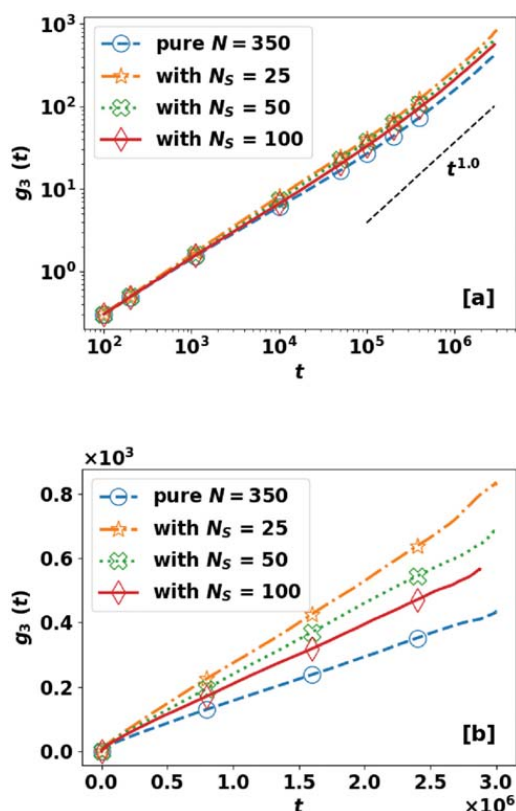


FIG. 6. MSD of the center of mass $g_3(t)$ of $N_L = 350$ chains in bidisperse mixtures as the majority component ($\phi_L = 0.7$), with $N_S = 25, 50$, and 100 chains as the minority component: (a) log-log coordinates; (b) linear coordinates. The MSD of pure $N = 350$ chains is also included for comparison.

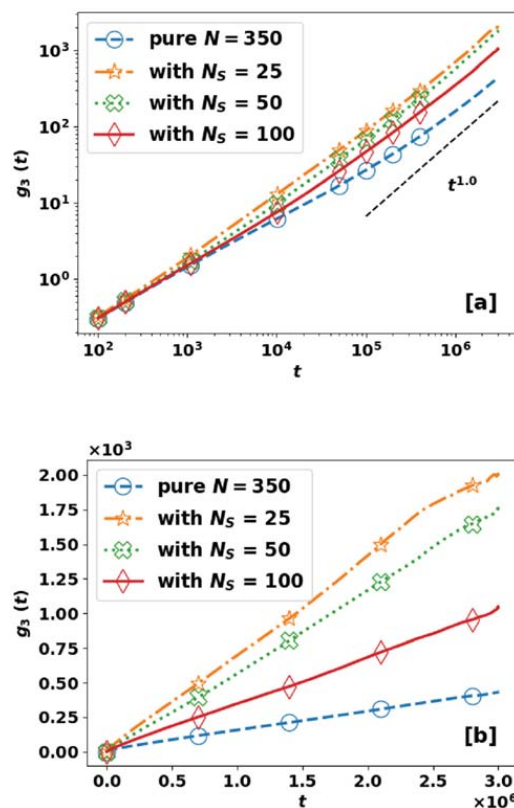


FIG. 7. MSD of the center of mass $g_3(t)$ of $N_L = 350$ chains in bidisperse mixtures as the minority component ($\phi_L = 0.3$), with $N_S = 25, 50$, and 100 chains as the majority component: (a) log-log coordinates; (b) linear coordinates. The MSD of pure $N = 350$ chains is also included for comparison.

after $t \sim O(10^3)$ ($\sim \tau_e$), it becomes clear that mixing with shorter chains increases the mobility of the longer chains and the effect is stronger as N_S decreases. Around $t \sim O(10^4)$ —i.e., the original $t^{1/2}$ scaling regime in pure entangled melts—the slope is again raised by the addition of the short chains, which is more clearly observed when the long chains become the minority component [Fig. 7(a)]. The onset of this intermediate regime of slower dynamics, which marks τ_e , is reduced. Overall, the introduction of short chains speeds up the dynamics of the entangled chain species and lessens the extent of entanglement.

Increasing slope in the $\tau_e < t < \tau_R$ segment, with decreasing matrix chain length N_S , was also previously reported by Wang and Larson²⁶ in both the $g_1(t)$ and $g_3(t)$ profiles of their long probe chain. For example, in their binary mixtures of $N_L = 350$ and $N_S = 25$ (both semiflexible) chains with $\phi_L = 0.15$, the slope of $g_3(t)$ reached 0.84,

whereas their $N_S = 160$ (and $N_L = 350$) case had a slope of 0.58. The latter is close to our monodisperse $N = 350$ case because $N_S = 160$ is already substantially entangled (specifically considering their higher chain rigidity which gives lower N_e than our flexible chains). With more short chains in the surrounding (higher ϕ_S) or faster relaxation of those chains (lower N_S), CR is stronger, which leads to faster tube relaxation and, eventually, the higher mobility in the longer entangled chains.

The diffusion coefficient of the $N_L = 350$ chains, D_L , is again calculated from the MSD data at the long-time limit. The result is plotted in Fig. 8. D_L increases with the short-chain fraction $\phi_S = 1 - \phi_L$, and the effect becomes stronger as N_S decreases. With 30% short chains in the mixture (i.e., $N_L = 350$ remains the majority), the speed-up is 87%, 52%, and 34% for $N_S = 25, 50$, and 100, respectively, while when short chains reach 70% (i.e., $N_L = 350$ becomes the minority), the speed-up reaches 455%, 320%, and 151% for the same three N_S levels.

Speed-up of long chain dynamics upon introducing the short chain component again agrees with various previous simulation studies.^{10,15,22,25,26} The results above have also been confirmed experimentally. Wang *et al.*⁴¹ studied the effects of short chains on the dynamics of long chains and vice versa using a binary mixture of 1,4-polybutadiene at different weight concentrations of the long chains. The diffusion coefficients of the different chains were measured using pulsed-gradient nuclear magnetic resonance (NMR) spin echo measurements. Their results showed that the dynamics of the longer chains were sped up by the shorter chains and the effects were stronger with decreasing weight fraction of the longer chains.

B. Rouse mode analysis (RMA)

The MSD analysis above suggests the following: (1) dynamics of the short-chain species is impeded by the long chains but still follows similar patterns as the corresponding pure short-chain melt; (2) dynamics of the long-chain species is accelerated by the short chains, and features of entanglement become weakened. Here, we apply Rouse mode analysis to directly examine the extent of entanglement effects in different species. We start with a quick review of the Rouse

model. It treats the probe chain as a Gaussian chain and considers all its surrounding chains to form a continuous viscous medium, i.e., a mean-field approach. Dynamics of each bead on the probe chain is described by the inertia-less Langevin equation.⁸ For example, the equation of motion for the i th bead is written as

$$\zeta \frac{d\vec{r}_i}{dt} = H_s [(\vec{r}_{i+1} - \vec{r}_i) - (\vec{r}_i - \vec{r}_{i-1})] + \vec{f}_i^r, \quad (13)$$

where ζ is the monomeric friction coefficient, H_s is the spring constant, \vec{r}_i is the position of the i th bead, and \vec{f}_i^r is the random force exerted on the i th bead, satisfying

$$\langle \vec{f}_i^r(t) \vec{f}_j^r(t') \rangle = 2\zeta k_B T \delta_{ij} \delta(t - t') \vec{\delta}, \quad (14)$$

where $\delta(t)$ is the Dirac delta function, δ_{ij} is the Kronecker delta, and $\vec{\delta}$ is the identity tensor. Equation (13) shows that position coordinates of neighboring beads are coupled in their dynamics through spring forces. The RMA projects the original bead coordinates \vec{r}_i to a set of mutually orthogonal coordinates known as Rouse modes or normal coordinates \vec{X}_p ($p = 0, 1, \dots, N-1$). We adopt the original form of projection by Rouse,²

$$\vec{X}_p \equiv \sqrt{\frac{2}{N}} \sum_{i=1}^N \vec{r}_i(t) \cos\left(\frac{(i-1/2)p\pi}{N}\right), \quad (15)$$

$(p = 0, 1, 2, \dots, N-1),$

which is widely used in the literature.^{11,13,42-44} The $p=0$ mode describes the motion of the center of mass of the chain, and the other modes ($1 \leq p \leq N-1$) describe the internal relaxations of sub-chains, or “blobs,” of the size of N/p beads. Each of the transformed coordinate or Rouse mode \vec{X}_p follows Langevin dynamics with its own friction coefficient and random force. Importantly, relaxation of different modes is mutually independent. The autocorrelation function (ACF) of each $p > 1$ mode decays exponentially,

$$\langle \vec{X}_p(t) \vec{X}_p(0) \rangle = \langle \vec{X}_p^2 \rangle \exp\left(-\frac{t}{\tau_p}\right), \quad (16)$$

with its own relaxation time τ_p given by

$$\tau_p^{-1} = \frac{12k_B T}{\zeta b^2} \sin^2\left(\frac{p\pi}{2N}\right), \quad (17)$$

where b^2 is the mean square bond (spring) length. For leading modes with $p \lesssim N/5$, which describes the motions of larger segments with $N/p \gtrsim 5$ beads, Eq. (17) can be approximated by²

$$\tau_p = \frac{\zeta b^2}{3\pi^2 k_B T} \left(\frac{N}{p}\right)^2. \quad (18)$$

Rouse model is commonly used to describe the dynamics of unentangled polymer melts. With increasing chain length, topological constraints set in and relaxation dynamics changes. For entangled chains, we may still project the coordinates to \vec{X}_p using Eq. (15), but the ACFs no longer follow simple exponential decay. A stretched exponential is often used instead,^{41-43,44,45}

$$\langle \vec{X}_p(t) \vec{X}_p(0) \rangle = \langle \vec{X}_p^2 \rangle \exp\left[-\left(\frac{t}{\tau_p}\right)^{\beta_p}\right], \quad (19)$$

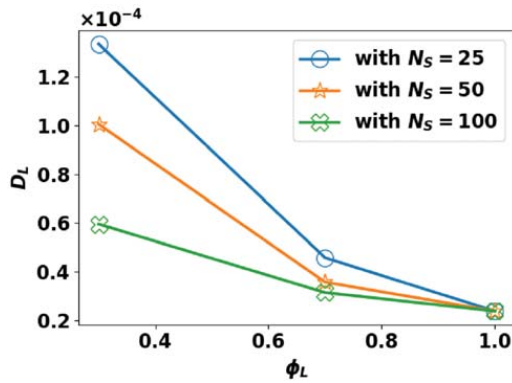


FIG. 8. Diffusion coefficient of the long chain ($N_L = 350$) in bidisperse mixtures with shorter chains of different lengths N_S .

where τ_p^* and β_p are the time scale and exponent (stretching parameter) for the p th mode. The relaxation time of a stretched exponential can be defined as

$$\tau_p \equiv \int_0^\infty \exp \left[- \left(\frac{t}{\tau_p^*} \right)^{\beta_p} \right] dt = \left(\frac{\tau_p^*}{\beta_p} \right) \Gamma \left(\frac{1}{\beta_p} \right), \quad (20)$$

where $\Gamma(x)$ is the gamma function. Note that at the simple exponential limit, i.e., $\beta_p \rightarrow 1$, the two time scales are the same $\tau_p = \tau_p^*$.

We start with the relaxation of $N_S = 25$ chains in its pure melt ($\phi_S = 1.0$) and in mixtures with $N_L = 350$ chains. Figure 9 shows the time ACF of the $p=1$ mode at different mass fractions. In all cases, the logarithm of the ACF follows a straight line for nearly the whole time range, i.e., the simple exponential decay as given in Eq. (16) accurately describes the relaxation dynamics of short chains. Relaxation dynamics of unentangled monodisperse melts of KG chains is known to be well approximated by the Rouse model despite its many simplifications.¹⁷ However, we find that even in mixtures with a long-chain species well beyond the entanglement threshold, the nature of the short-chain dynamics is not changed at least for ϕ_S down to 30%. (At very low ϕ_S , we do expect the dynamic pattern to differ—indeed, diffusion of small molecules, at extremely low concentration, in a matrix of long-chain polymers is known to display jerky “hop”-like movements.⁴⁷) The presence of longer chains seemingly do not have any effect other than to increase the relaxation time of the shorter chains—note in Fig. 9 that the pure $N_S = 25$ melt has the steepest slope and the relaxation slows down with increasing long chain fraction (ϕ_S decreases). This is consistent with the earlier discussion that having longer chains in the background medium increases the effective friction coefficient of the short chains. The results for $N_S = 50$ are similar and thus not shown here.

Fitting the ACF to the single exponential of Eq. (16) provides the relaxation time, which is plotted against $1/p^2$ in Figs. 10 and 11 for $N_S = 25$ and 50 chains, respectively. From Eq. (18), for the Rouse model, τ_p vs $1/p^2$ should give a straight line, at least for small p , whose

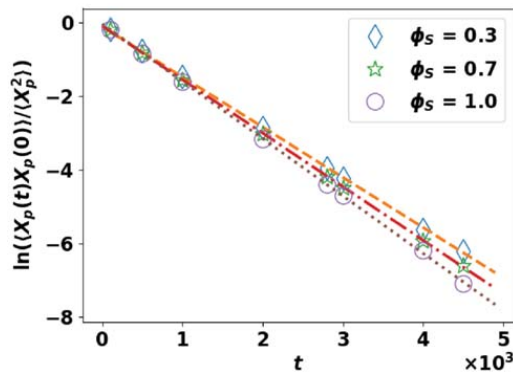


FIG. 9. Relaxation of the $p=1$ Rouse mode of $N_S = 25$ chains in its pure melt and in bidisperse mixtures with $N_L = 350$ chains. Lines represent linear regression corresponding to the simple exponential relaxation of Eq. (16).

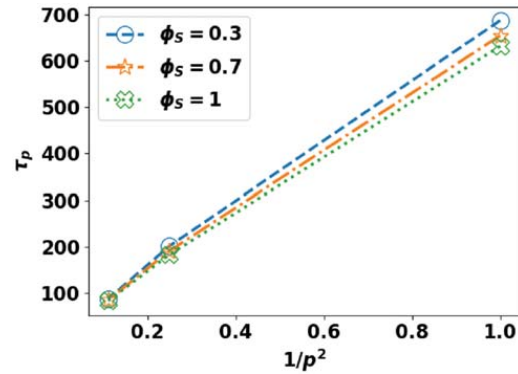


FIG. 10. Single-exponential relaxation time τ_p of $N_S = 25$ chains in its pure melt ($\phi_S = 1.0$) and in bidisperse mixtures with $N_L = 350$ chains ($p=1$ to $p=3$).

slope equals the longest relaxation time τ_1 . For $N_S = 25$ (Fig. 10), this Rouse behavior is clearly demonstrated, whereas some small deviations are observed in $N_S = 50$ case (Fig. 11). Introducing a longer $N_L = 350$ species does not change the nature of the dynamics, but the relaxation time of the shorter chains increases with increasing long-chain content. In both figures, the highest p mode available is limited by the sampling frequency—the frequency at which coordinates were stored—used in our simulation.

Slow-down of short-chain dynamics in the presence of longer chains in its surroundings is intuitively predictable and well established in the literature.^{10,25,26} Nevertheless, our finding, from results here as well as back in Fig. 4(b), that the reduced mobility can be fully described by an increased friction factor, which is only a function of composition ϕ_L and does not vary with N_S , has never been reported before to the best of our knowledge. Kopf, Dünweg, and Paul¹¹ found

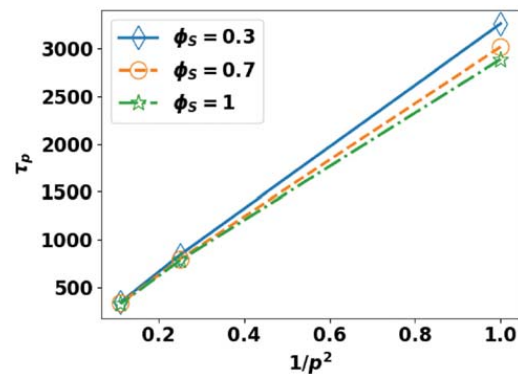


FIG. 11. Single-exponential relaxation time τ_p of $N_S = 50$ chains in its pure melt ($\phi_S = 1.0$) and in bidisperse mixtures with $N_L = 350$ chains ($p=1$ to $p=3$).

that when two unentangled isotope chain species with identical chain length but different monomeric mass are mixed, they retain the same Rouse dynamics as their pure melts but with different effective monomeric friction factors—the light and heavy components see their friction factor to increase and decrease, respectively. The effective friction factor depends on both the volume fraction of heavy chains and the mass ratio between the components. However, at least for $10 \leq N \leq 30$ investigated in that study, it does not depend on the chain length N . What we find here is that, for a short unentangled chain species, mixing with a longer species, which is well within the entangled regime, does not change its own dynamical patterns, even when, e.g., in the case of $N_S = 50$, its own length already exceeds N_e .

Departure from Rouse dynamics is observed as chain length gets longer and entanglement effects set in. Rouse mode projection [Eq. (15)] may still be applied to longer chains, but relaxation of each mode is no longer independent. As a result, its ACF does not follow the simple exponential decay as given in Eq. (16). Figure 12 shows stretched exponential [Eq. (19)] fits to the ACFs of leading Rouse modes of the monodisperse $N = 350$ system as well as its mixture with short $N_S = 25$ chains as the diluent. In both cases, it appears that the $p = 1$ mode may still be reasonably approximated by a simple exponential (i.e., close to straight lines in the figure). However, at $p = 3$, the curvature in the profile is too strong to be ignored, and a stretched exponential is required. The same behavior is observed in higher modes such as $p = 5$ and 7 (not shown here). Coupling between different modes is attributed to the topological constraints imposed by entanglements. Indeed, using a simple lattice model, Shaffer¹³ showed that allowing chains to cross one another would recover the Rouse dynamics in otherwise entangled chains. For bidisperse mixtures, we observe that introducing short $N_S = 25$ chains as a diluent, at least for ϕ_S up to 70% shown in Fig. 12, does not eliminate this non-Rouse behavior even though the relaxation dynamics of the $N_L = 350$ chains is significantly accelerated (compared with its pure melt).

Curvature in the $\ln(\langle \vec{X}_p(t) \vec{X}_p(0) \rangle / \langle \vec{X}_p^2 \rangle)$ vs t plot is measured by the stretching parameter β_p , which can thus be viewed as an

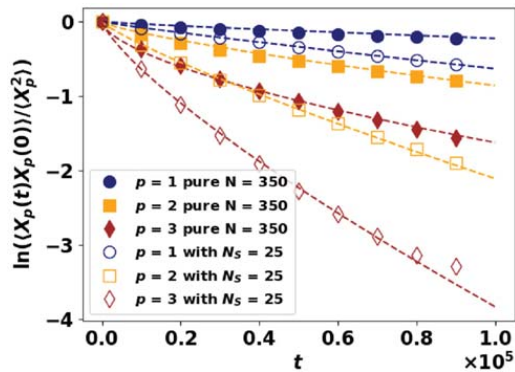


FIG. 12. Relaxation of the leading Rouse modes of $N = 350$ chains in its pure melt (filled symbols) and as the minority component in a bidisperse mixture with $N_S = 25$ (empty symbols; $\phi_L = 0.3$). Lines represent stretched exponential fits [Eq. (19)].

indicator of non-Rouse behaviors ($\beta_p = 1$ in the purely Rouse limit). Figure 13(a) shows β_p as a function of N/p (which measures the number of beads in each segment or sub-chain described by the p th mode) for monodisperse melts of different chain lengths. At the high- p (small N/p) end, all curves approximately overlap regardless of the chain length (entangled or not), indicating that relaxation of small segments is independent of the overall chain length. This terminal β_p value of $0.5 - 0.6$ is significantly lower than 1—departure of small-scale segmental relaxation from the Rouse model is obvious even for the shortest chains. This is likely due to the differences between the KG chain used in our simulation and the Gaussian chain in the Rouse model. In particular, the latter does not consider the excluded-volume effect between beads, which is more important in dynamics at small scales. Indeed, strong departure of β_p from 1 at small scales was noted in several earlier studies.^{12,15,19} At $N/p \approx 3$, β_p starts to rise steeply, reaching nearly 0.8 at $N/p \approx 5$ (segment size of five beads), after which curves of different N separate. For $N = 25$ (where $N/p = 5$ corresponds to the $p = 5$ mode), β_p continues to increase with lowering p , ending well above 0.9 for the $p = 1$ mode. For $N = 50$, β_p plateaus around 0.8 until $p = 3$ mode after which it again quickly rises above 0.9.

Entanglement effects are most clearly seen in the $N = 350$ case where, after the plateau at $5 \lesssim N/p \lesssim 10$, β_p quickly declines and reaches its minimum at $N/p \sim 70$. This minimum β_p is around 0.6. Strong departure from the Rouse model at this length scale is attributed to the topological constraints between entangled chains: each chain is now constrained to its surrounding tube (the chain follows reptation motion) and can no longer meander freely in the three-dimensional space. The size of segments N/p strongly affected by this effect also coincides with the entanglement strand size N_e of the KG model (30 – 80). Interestingly, leading modes ($p = 4$ to 1) again show a rapid surge of β_p —relaxation of largest segments returns to the Rouse-like single exponential behavior, which is consistent with the observation in Fig. 12 that a simple exponential adequately captures the relaxation behavior of the $p = 1$ mode. One can rationalize this considering that at length scales $\gg N_e$, the conformation of the constraining tube itself (or, more accurately, the primitive path) undergoes multiple turns. In addition, over the time scale of τ_d (the longest relaxation time of entangled chains), surrounding chains all have sufficient time to relax, which causes significant CR, and the tube (primitive path) conformation changes substantially through its own Rouse motion.⁴⁰ Chain motion at the largest scales is thus again described by a three-dimensional random walk. The $N = 100$ case is similar to $N = 50$, but a small dip in β_p is found near $N/p \approx 30$ as a sign of weak entanglement.

Dependence of relaxation time τ_p as calculated from Eq. (20), on the segment size N/p is shown in Fig. 13(b) (again for monodisperse melts). Rouse model predicts [Eq. (18)] $\tau_p / (N/p)^2$ to be a constant for $N/p \gtrsim 5$ which is indeed observed in the $N = 25$ and 50 cases in our simulation. Departure from the plateau is found at smaller scales ($N/p \lesssim 5$), where the relaxation times of all chain lengths again overlap. Entanglement causes a sudden slow-down in the dynamics, which shows as a surge in $\tau_p / (N/p)^2$ starting at $N/p \sim \mathcal{O}(10)$. At the long-segment (small- p) limit, another, much higher, plateau is reached. This conforms to the tube model prediction⁴ of

$$\tau_p \sim \left(\frac{N}{N_e} \right) \left(\frac{N}{p} \right)^2. \quad (21)$$

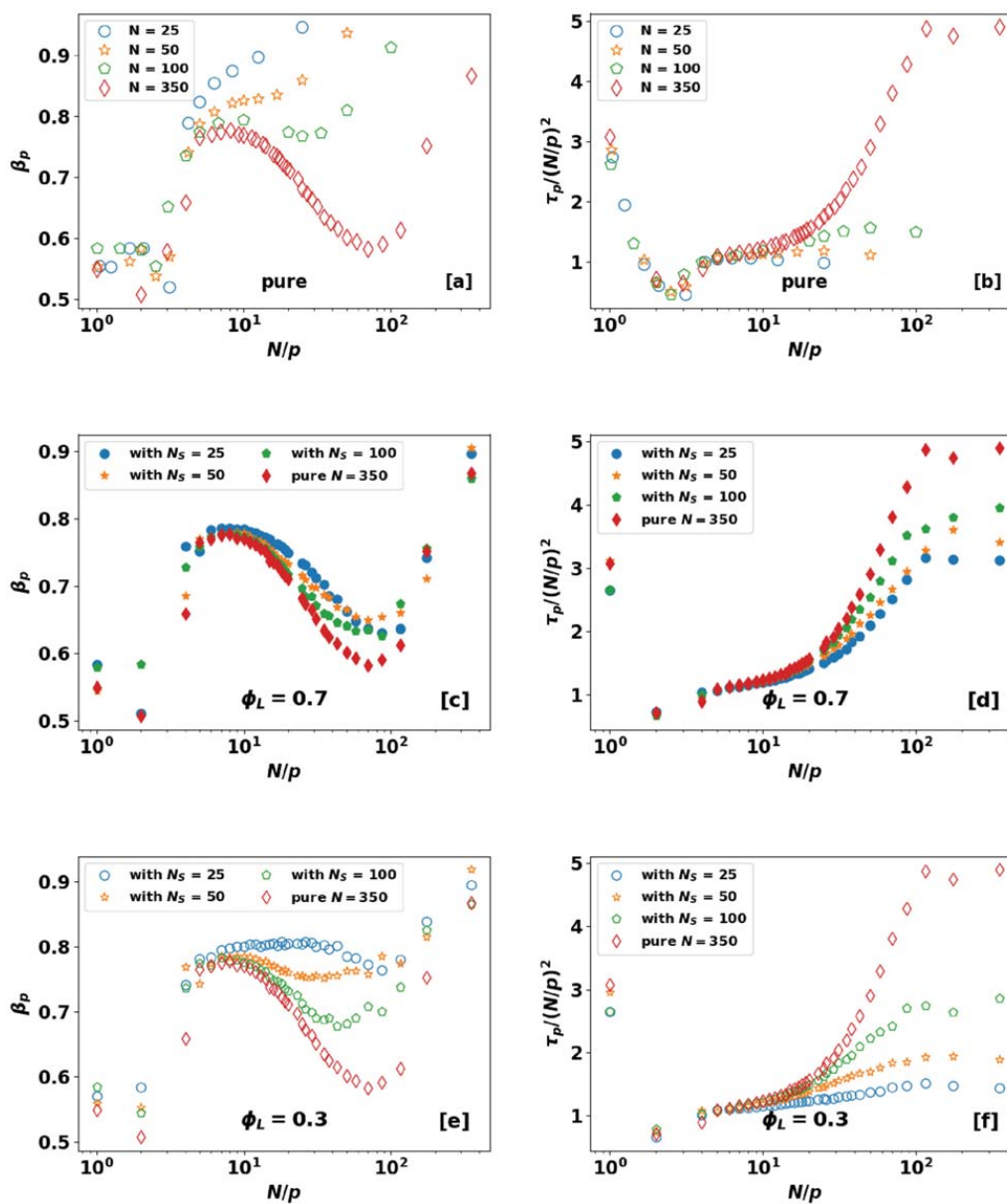


FIG. 13. Rouse mode analysis with stretched exponential fitting—stretching parameter β_p [(a), (c), and (e)] and relaxation time τ_p [scaled by $(N/p)^2$; (b), (d), and (f)]—of monodisperse melts of varying chain length [(a) and (b)] and the $N_L = 350$ component in bidisperse mixtures with the longer chains as the majority [$\phi_L = 0.7$; (c) and (d)] and minority [$\phi_L = 0.3$; (e) and (f)] component.

A raised right-end plateau is also discernible in the $N=100$ case, although the level of elevation (from the Rouse plateau) is small, indicating that $N=100$ is close to the onset of entanglement.

For monodisperse melts, stretched exponential analysis of Rouse modes has been performed in a number of previous studies using various models. Shaffer's¹³ BFM, despite its many differences in model construction with the KG model used in our study, showed strikingly similar results. Their β_p profile started with a plateau value between 0.7 and 0.8, which agrees with our plateau at $5 \lesssim N/p \lesssim 10$. They did not report a lower β_p level for smallest N/p , but such discrepancy at smallest scales is expected, given the differences between the models. For entangled chains, they also showed a deep dip at higher N/p , occurring also at $N/p \approx 60\text{--}70$ for their longest chains ($N=300$ and 500). For reference, their model reported $N_e \approx 32$ based on the self-diffusion coefficient of chains, i.e., their dip also occurred at $N/p \approx 2N_e$, which was quantitatively consistent with our observation. Their $N=160$ chains, similar to our $N=100$ case, showed a shallower dip occurring at smaller N/p , which is a sign of weak entanglement expected in the transitional regime. Their $\tau_p/(N/p)^2$ profiles also showed a raised plateau at the high- N/p end for entangled chains. Interestingly, both hallmarks of entanglement [dip in β_p and raised plateau in $\tau_p/(N/p)^2$] disappeared if chains were allowed to cross. More recent studies based on the KG model, for $N=500$ to 2000 , also showed an "entanglement dip" at $N/p \approx 70\text{--}100$ with β_p dropping down to ~ 0.5 .^{12,46,48} On the other hand, the diamond lattice model by Lin, Mattice, and Von Meerwall¹⁵ showed β_p to increase monotonically from ~ 0.4 to a plateau of ~ 0.7 at the high- N/p end without the entanglement dip. Similarly, Padding and Briels¹⁹ performed MD using a coarse-grained polyethylene model and also only reported a plateau at the high- N/p end for highly entangled chains. Note that unlike the KG model, in which the LJ potential of tightly-bonded beads is sufficient to prevent chain crossing, non-crossability had to be explicitly enforced in the above two models. For Padding and Briels,¹⁹ the coarse-grained non-bonded interactions were too soft to prevent chain crossing and an additional bond-crossing potential was imposed (the so-called TWENTANGLEMENT algorithm⁴⁵). Thus, whether or not an entanglement dip would occur seems to depend on the specific treatment of non-crossability.

In binary mixtures with shorter chains where the $N_L = 350$ species remains the majority component [Figs. 13(c) and 13(d)], the same hallmarks of entanglement—i.e., dip in β_p at $\mathcal{O}(10) \lesssim N/p \lesssim \mathcal{O}(10^2)$ and raised plateau in $\tau_p/(N/p)^2$ at $N/p \gtrsim \mathcal{O}(10^2)$ —are preserved. Introduction of the short chain diluent lessens the extent of entanglement, as reflected by the shallowing of the β_p dip and reduction in the raised $\tau_p/(N/p)^2$ plateau magnitude. At its core, this is still a CR effect—faster relaxation of the shorter chains in its surroundings emancipates the long chain from topological constraints earlier. This can be described as faster tube Rouse motion,⁴⁰ but as the diluent chains get shorter, tube dilation⁸ also plays a role. Indeed, Baig *et al.*²⁵ showed that tube dilation only occurs when $N_S < N_e$, whereas for larger N_S , the diluent accelerates tube relaxation without changing its diameter.

The effect strengthens as the diluent chain length decreases. Increasing the short-chain mass fraction to 70% [Figs. 13(e) and 13(f)] significantly alleviates entanglement and, with $N_S = 25$ as the diluent, dynamics of $N_L = 350$ chains is pushed to the marginally entangled limit [similar to the pure $N=100$ case in Figs. 13(a) and 13(b)].

Increasing CR with increasing ϕ_S and with decreasing N_S are both expected and well established.^{15,25,26}

C. Stress relaxation

Sections III A and III B focused on the dynamics of individual chains—in the case of bidisperse mixtures, discussion of MSD and RMA shows how the relaxation of one chain type is affected by the dynamics of the other. We turn now to the stress relaxation dynamics of the melt in its entirety. Stress relaxation modulus $G(t)$ is defined as the ratio of the time-dependent shear stress following a small step strain to the strain magnitude. $G(t)$ contains the full spectrum of information about the material linear viscoelasticity and is sensitive to the MWD of the polydisperse mixture. A bidisperse mixture offers a simple model for studying the effects of chain-length disparity on $G(t)$, which will further contribute to the general understanding of MWD effects on polymer rheology.

In equilibrium molecular dynamics, the Green–Kubo relation relates $G(t)$ to the ACF of shear stress fluctuations

$$G(t) = \frac{V}{k_B T} \langle \sigma_{xy}(t_0) \sigma_{xy}(t_0 + t) \rangle, \quad (22)$$

where V is the volume of the system, T is the temperature, and σ_{xy} is the instantaneous shear stress. The stress relaxation modulus is rather difficult to calculate due to intense stress fluctuations that are intrinsic to small-scale systems, which has a particularly strong impact on the stress ACF at the terminal (long-time) regime. In isotropic fluids, stress ACFs in multiple directions can be averaged in an attempt to reduce fluctuations.⁴⁹ We use the particular form of

$$G(t) = \frac{V}{5k_B T} [\langle \sigma_{xy}(t) \sigma_{xy}(0) \rangle + \langle \sigma_{yz}(t) \sigma_{yz}(0) \rangle + \langle \sigma_{zx}(t) \sigma_{zx}(0) \rangle] + \frac{V}{30k_B T} [\langle N_{xy}(t) N_{xy}(0) \rangle + \langle N_{xz}(t) N_{xz}(0) \rangle + \langle N_{yz}(t) N_{yz}(0) \rangle], \quad (23)$$

where

$$N_{z\beta} = \sigma_{zz} - \sigma_{\beta\beta}. \quad (24)$$

The same expression was also used in Ramírez *et al.*⁵⁰ The number of different components for averaging is nevertheless still too small to significantly reduce the noise in the signal.⁵² We further used the multi-tau correlator method developed by Ramírez *et al.*⁵⁰ which uses a hierarchical multi-level data structure to store and filter time series and calculate correlation functions on the fly. In its data structure, level 0 stores the most recent p data points in the time series. At level 1, the first entry stores the average value of the most recent m ($m < p$) points, the second entry stores the average of the next m points, and so on. Similarly, each entry at level l is the average of m entries at level $l-1$. As such, stored data represent local averages of the original time series, and the averaging window size (m^l for level l) increases with the level, so does the time lag it covers (the range of previous time where information is retained at the current level). For the smallest time lags (up to $p-1$ sampling intervals), the unfiltered time series is used, whereas for increasing time lag (higher levels), averages over larger window sizes are used. In this study, we use the same default parameters $p=16$ and $m=2$ as recommended in Ramírez *et al.*⁵⁰

Relaxation modulus is calculated for both monodisperse and bidisperse samples in our simulations. In Fig. 14, $G(t)$ is scaled by a factor of $t^{1/2}$, as the Rouse model predicts a $t^{-1/2}$ scaling in stress relaxation

$$G^{\text{Rouse}}(t) = \frac{\sqrt{\pi}}{2\sqrt{2}} \nu_{\text{chain}} k_B T \left(\frac{t}{\tau_R} \right)^{-1/2} \quad (t \lesssim \tau_R), \quad (25)$$

where ν_{chain} is the number density of chains, related to the bead number density ν_{bead} by

$$\nu_{\text{chain}} = \frac{\nu_{\text{bead}}}{N}. \quad (26)$$

Since τ_R scales with N^2 , for given monomer species and bead density, $G(t)$ magnitude does not depend on the chain length—chain length

only affects τ_R , i.e., when terminal relaxation [departure from Eq. (25)] kicks in. Using $\nu_{\text{bead}} = 0.85$ and $\tau_R = 1.66 \times 10^5$ based on the MSD of the pure $N=350$ case from our simulation (Table II), the Rouse prediction of $t^{1/2}G^{\text{Rouse}}(t) = 0.62$ (in LJ reduced units with G nondimensionalized by $k_B T$) is shown as a flat dashed line in Fig. 14.

It is observed that pure melts of the shorter ($N=25$ and 50) chains completely relax before a pronounced Rouse plateau can be formed. For the pure $N=350$ melt, a Rouse plateau is clearly identified from $t \sim \mathcal{O}(10)$ up to $t \approx 2000$. For comparison, $\tau_e = 3428$ according to Table II. Departure from the Rouse plateau at the small t limit is also consistent with the earlier conclusion from RMA that the Rouse model does not accurately capture the dynamics at small scales. Entanglement manifests as a strong spike above the Rouse plateau at longer time. For $N=100$, entanglement is not strong enough to cause substantially raised stress than the pure rouse level. For mixtures between $N_L = 350$ chains with a shorter component, if the long chains remain the majority [Fig. 14(a)], a spike is still clearly observable for different diluent chain lengths (down to $N_S = 25$). If the long chains become the minority [Fig. 14(b)], $t^{1/2}G(t)$ no longer rises above the Rouse plateau. However, compared with the short-chain cases, in bidisperse mixtures, a second lower (~ 0.2) plateau regime is found, indicating that even the weak entanglement present in those mixtures can appreciably hinder relaxation at longer time scales.

In practice, contributions of different components of a polydisperse mixture are usually accounted for through mixing rules that relate the MWD of the polydisperse mixture to its $G(t)$. A generalized form of the mixing rule is given as^{51–53}

$$G(t) = G_N^0 \left(\int_{\log N_L}^{\infty} F^{1/\beta}(t, N) w(N) d(\log N) \right)^\beta, \quad (27)$$

where G_N^0 is the plateau modulus and $F(t, N)$ is a kernel function accounting for the contribution from chains of length N . The $w(M)$ function is given by

$$w(N) \equiv \frac{dW(N)}{d \log N}, \quad (28)$$

where $W(N)$ is the cumulative weight fraction of chains with the degree of polymerization lower than N , and β is a parameter describing the mixing behavior. Different β values have been used in the literature. A β value of 1 gives linear combination derived from the simple tube model. The double reptation model by Des Cloizeaux⁹ leads to a β value of 2. Van Ruymbeke *et al.*⁷ adjusted the value to 2.25 to obtain better fits for the linear viscoelastic properties evaluated in their study. Higher β values have also been proposed in the literature to describe higher order entanglements.^{7,54,55} Several kernel functions have also been reported. The simplest choice is a step function⁵⁶ which assumes steep transition between strained and relaxed conformations. Tsenoglou⁵⁷ described the relaxation using a more realistic single exponential function which gives better qualitative prediction. More accurate quantitative description is possible with more sophisticated forms such as the relaxation function of Doi and Edwards,⁴ along with its derived form that accounts for the effects of contour length fluctuations,⁴ and the time-dependent diffusion model of Des Cloizeaux.⁵⁸

In a bidisperse mixture,

$$w(N) = \phi_S \delta(\log N - \log N_S) + \phi_L \delta(\log N - \log N_L). \quad (29)$$

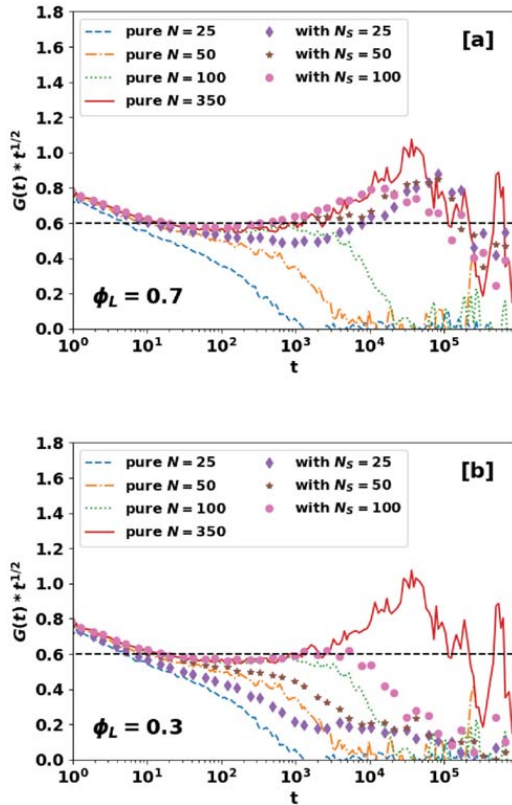


FIG. 14. Stress relaxation modulus $G(t)$ (scaled by $t^{1/2}$) of pure polymer melts of different chain length N (lines) and bidisperse melts with $N_L = 350$ and various N_S (symbols): (a) $\phi_L = 0.7$; (b) $\phi_L = 0.3$. Each profile is averaged over three independent configurations. Horizontal dashed line shows the Rouse model prediction.

Using the property

$$\int_{a-\epsilon}^{a+\epsilon} f(x)\delta(x-a)dx = f(a) \quad (\epsilon > 0) \quad (30)$$

of the Dirac delta function, Eq. (27) becomes

$$G_{S+L}(t) = G_N^0 \left(\phi_S F_S^{1/\beta}(t) + \phi_L F_L^{1/\beta}(t) \right)^\beta, \quad (31)$$

where

$$F_S(t) \equiv F(t, N_S) \quad (32)$$

and

$$F_L(t) \equiv F(t, N_L) \quad (33)$$

are the kernel functions of the short- and long-chain species, respectively.

Our focus here is not on the analytical theory of the relaxation of individual chain species itself, but on predicting mixture rheology based on the relaxation behaviors of individual components. Therefore, we circumvent the analytical expression of the kernel function and extract it directly from MD simulation of corresponding monodisperse melts. Note that at the $\phi_S \rightarrow 1$ limit, Eq. (31) becomes

$$G_S = G_N^0 F_S(t) \quad (34)$$

and at the $\phi_L \rightarrow 1$ limit,

$$G_L = G_N^0 F_L(t). \quad (35)$$

Combining Eqs. (34) and (35) with Eq. (31) leads to

$$G_{S+L} = \left(\phi_S G_S^{1/\beta}(t) + \phi_L G_L^{1/\beta}(t) \right)^\beta, \quad (36)$$

where $G_S(t)$ and $G_L(t)$ are obtained from the corresponding monodisperse simulation results.

Predictions from Eq. (36) are shown in Fig. 15 in comparison with direct MD results of bidisperse mixtures. Since the mixing rule of Eq. (27) is only applicable to entangled melts, binary mixtures between $N_S = 100$ and $N_L = 350$ are selected here. Corresponding monodisperse MD results are also displayed. At early times, a regime dominated by Rouse relaxation, all the curves overlap as expected. As per the above discussion, $G(t)$ from the Rouse model is independent of chain length at $t < \tau_R$. At longer times, dynamics of different cases separate with the pure $N = 100$ case being the first to decay and $N = 350$ being the last. Relaxation dynamics of bidisperse mixtures is sandwiched between the two monodisperse limits.

Comparing the mixing rule results with MD of bidisperse cases, $\beta = 2$ gives strikingly accurate prediction at $\phi_L = 0.7$ as shown in Fig. 15(a), showing that the double reptation model predicts the relaxation of the system reasonably well. Note that for t up to at least $\mathcal{O}(10^4)$, error bars in the MD data are smaller than the symbol size and thus the comparison is statistically significant. For $\phi_L = 0.3$, $\beta = 1$ seems to be more accurate for $t \lesssim 2 \times 10^4$ shown in the inset of Fig. 15(b), but as we examine $t > 2 \times 10^4$, we spot a kink in the MD profile, which brings the curve closer to the $\beta = 2$ line right before terminal relaxation. Admittedly, fluctuations (and statistical uncertainty) also grow in that regime as we move closer to terminal relaxation, making the observation less statistically conclusive than the earlier agreement

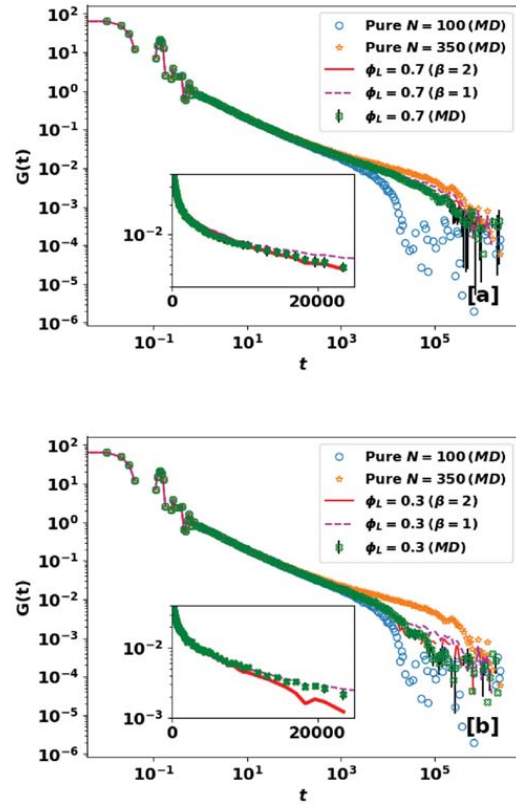


FIG. 15. Test of the mixing rule [Eq. (27)] in bidisperse mixtures of $N_S = 100$ and $N_L = 350$ at (a) $\phi_L = 0.7$ and (b) $\phi_L = 0.3$. Insets show enlarged views of the comparison between the mixing rule and MD before terminal relaxation in a linear time scale. Error bars are shown for bidisperse MD cases only, which are no larger than the symbol size except in the terminal-relaxation (large- t) regime. Uncertainties in pure-melt MD cases are similar.

with $\beta = 1$ at smaller t . We have also tested $\beta = 2.25$ which gave worse results and is thus not shown here. At this point, we are not ready to interpret these observations, including (i) the concentration-dependence of the β value and (ii) possible switch from $\beta = 1$ to $\beta = 2$ at later time in the $\phi_L = 0.3$ case. Definitive answers will require expansive simulations including multiple concentration levels and a wider range of chain lengths.

IV. CONCLUSIONS

We have studied the chain dynamics and stress relaxation of bidisperse polymer melts using MD simulation. For each bidisperse system, we mixed a long $N_L = 350$ chain component, whose monodisperse melt is entangled, with a short-chain diluent (which is either unentangled—i.e., $N_S = 25$ and 50 , or marginally entangled

$N_S = 100$). Two different composition levels, one with the long chains as the majority component ($\phi_L = 0.7$) and the other as the minority ($\phi_L = 0.3$) component, were studied.

Compared with a pure short-chain melt, mixing with longer chains significantly reduces the mobility of short chains. However, dynamics of a short, unentangled, chain species remains well-described by the Rouse model, despite the presence of the longer, entangled, chain species in the mixture. At least for ϕ_S down to 30% studied, dynamics of a short chain in a slow-moving matrix containing entangled long chains shows the same qualitative pattern as its relaxation in a pure monodisperse melt. Slow-down in the dynamics can be well captured by a higher effective monomeric friction coefficient.

Likewise, adding a short-chain diluent can significantly accelerate the motion of the longer, entangled, chain species. The effect is stronger as the short-chain mass fraction increases and as its chain length decreases. Unlike the previous case, however, this speed-up effect cannot be fully described by a quantitatively lower friction coefficient, which is instead accompanied by an overall lessening of the extent of entanglement.

Rouse mode analysis revealed that for short, unentangled, chains, relaxation of Rouse modes displays simple exponential decay, except the highest modes corresponding to dynamics at smallest scales. Mixing with longer chains does not change this qualitative observation. Meanwhile, for longer, entangled, chains, strong departure from simple-exponential relaxation is seen at intermediate length scales of $\mathcal{O}(N_c)$. Relaxation times of intermediate and large scales also become significantly elevated compared with the Rouse model. Both these characteristics of entanglement become weakened with the introduction of short-chain diluents.

Despite the success of the Rouse model in describing the dynamics of short chains (in both monodisperse melts and bidisperse mixtures with longer chains), stress relaxation of monodisperse short chains does not strictly follow the Rouse scaling. For monodisperse entangled chains, a well-defined Rouse scaling regime is observed, followed by a positive deviation from the Rouse model at longer times (in the entanglement regime). Bidisperse mixtures display similar positive deviation when the longer species is the majority. When it becomes the minority, the relaxation modulus no longer surpasses the Rouse scaling. Entanglement is instead reflected as an elongated (compared with a pure short-chain melt) tail of residue modulus.

Mixing rules for predicting a mixture's relaxation modulus from that of monodisperse melts of its constituent components were tested. The double reptation model provides reasonably accurate prediction when the longer chains are the majority. However, when longer chains are the minority, the simple tube model can be more accurate in certain regimes.

ACKNOWLEDGMENTS

The authors acknowledge the financial support from the Natural Sciences and Engineering Research Council of Canada (NSERC) Discovery Grants program (Nos. RGPIN-2014-04903 and RGPIN-2020-06774) and the allocation of computing resources awarded by Compute/Calcul Canada. S.Z. thanks the Canada Research Chairs (CRC) program (No. 950-229035). This work was made possible by the facilities of the Shared Hierarchical Academic Research Computing Network (SHARCNET: www.sharcnet.ca).

DEDICATION

This paper is dedicated to Robert Byron Bird (1924–2020) whose extraordinary contributions to the research and education in the dynamics and rheology of polymers, kinetic theory of fluids, and transport phenomena were matched by very few. His love of cultures, sense of humor, and passion for life continue to inspire many.

DATA AVAILABILITY

The data that support the findings of this study are available from the corresponding author upon reasonable request.

REFERENCES

1. J. M. Dealy, D. J. Read, and R. G. Larson, *Structure and Rheology of Molten Polymers: From Structure to Flow Behavior and Back Again* (Carl Hanser Verlag GmbH and Co KG, 2018).
2. P. E. Rouse, Jr., "A theory of the linear viscoelastic properties of dilute solutions of coiling polymers," *J. Chem. Phys.* **21**, 1272–1280 (1953).
3. R. B. Bird, C. F. Curtiss, R. C. Armstrong, and O. Hassager, *Dynamics of Polymeric Liquids*, 2nd ed. (Wiley, New York, 1987), Vol. 2.
4. M. Doi and S. F. Edwards, *The Theory of Polymer Dynamics* (Oxford University Press, 1988), Vol. 73.
5. S. F. Edwards, "Statistical mechanics with topological constraints. I," *Proc. Phys. Soc.* (1958–1967) **91**, 513 (1967).
6. P.-G. de Gennes, "Reptation of a polymer chain in the presence of fixed obstacles," *J. Chem. Phys.* **55**, 572–579 (1971).
7. E. Van Ruymbeke, R. Keunings, V. Stéphenne, A. Hagenaars, and C. Bailly, "Evaluation of reptation models for predicting the linear viscoelastic properties of entangled linear polymers," *Macromolecules* **35**, 2689–2699 (2002).
8. M. Doi, W. Graessley, E. Helfand, and D. Pearson, "Dynamics of polymers in polydisperse melts," *Macromolecules* **20**, 1900–1906 (1987).
9. J. Des Cloizeaux, "Relaxation of entangled and partially entangled polymers in melts: Time-dependent reptation," *Macromolecules* **25**, 835–841 (1992).
10. S. Barsky, "Molecular dynamics study of diffusion in bidisperse polymer melts," *J. Chem. Phys.* **112**, 3450–3456 (2000).
11. A. Kopf, B. Dünweg, and W. Paul, "Dynamics of polymer 'isotope' mixtures: Molecular dynamics simulation and Rouse model analysis," *J. Chem. Phys.* **107**, 6945–6955 (1997).
12. J. T. Kalathi, S. K. Kumar, M. Rubinstein, and G. S. Grest, "Rouse mode analysis of chain relaxation in homopolymer melts," *Macromolecules* **47**, 6925–6931 (2014).
13. J. S. Shaffer, "Effects of chain topology on polymer dynamics: Configurational relaxation in polymer melts," *J. Chem. Phys.* **103**, 761–772 (1995).
14. J. Baschnagel, W. Paul, V. Tries, and K. Binder, "Statics and dynamics of bidisperse polymer melts: A Monte Carlo study of the bond-fluctuation model," *Macromolecules* **31**, 3856–3867 (1998).
15. H. Lin, W. L. Mattice, and E. D. Von Meerwall, "Chain dynamics of bidisperse polyethylene melts: A Monte Carlo study on a high-coordination lattice," *Macromolecules* **40**, 959–966 (2007).
16. M. Rubinstein, R. H. Colby *et al.*, *Polymer Physics* (Oxford University Press, New York, 2003), Vol. 23.
17. K. Kremer and G. S. Grest, "Dynamics of entangled linear polymer melts: A molecular-dynamics simulation," *J. Chem. Phys.* **92**, 5057–5086 (1990).
18. M. Kröger, W. Loose, and S. Hess, "Rheology and structural changes of polymer melts via nonequilibrium molecular dynamics," *J. Rheol.* **37**, 1057–1079 (1993).
19. J. Padding and W. J. Briels, "Time and length scales of polymer melts studied by coarse-grained molecular dynamics simulations," *J. Chem. Phys.* **117**, 925–943 (2002).
20. A. E. Likhtman, S. K. Sukumaran, and J. Ramirez, "Linear viscoelasticity from molecular dynamics simulation of entangled polymers," *Macromolecules* **40**, 6748–6757 (2007).
21. J. Cao and A. E. Likhtman, "Time-dependent orientation coupling in equilibrium polymer melts," *Phys. Rev. Lett.* **104**, 207801 (2010).

- ²²R. Picu and A. Rakshit, "Coarse grained model of diffusion in entangled bidisperse polymer melts," *J. Chem. Phys.* **127**, 144909 (2007).
- ²³B. L. Peters, K. M. Salerno, T. Ge, D. Perahia, and G. S. Grest, "Effect of chain length dispersity on the mobility of entangled polymers," *Phys. Rev. Lett.* **121**, 057802 (2018).
- ²⁴B. L. Peters, K. M. Salerno, T. Ge, D. Perahia, and G. S. Grest, "Viscoelastic response of dispersed entangled polymer melts," *Macromolecules* **53**, 8400–8405 (2020).
- ²⁵C. Baig, P. S. Stephanou, G. Tsolou, V. G. Mavrantzas, and M. Kröger, "Understanding dynamics in binary mixtures of entangled cis-1,4-polybutadiene melts at the level of primitive path segments by mapping atomistic simulation data onto the tube model," *Macromolecules* **43**, 8239–8250 (2010).
- ²⁶Z. Wang and R. G. Larson, "Constraint release in entangled binary blends of linear polymers: A molecular dynamics study," *Macromolecules* **41**, 4945–4960 (2008).
- ²⁷S. Shanbhag and Z. Wang, "Molecular simulation of tracer diffusion and self-diffusion in entangled polymers," *Macromolecules* **53**, 4649–4658 (2020).
- ²⁸S. Shanbhag, "Unusual dynamics of ring probes in linear matrices," *J. Polym. Sci., Part B: Polym. Phys.* **55**, 169–177 (2017).
- ²⁹G. S. Grest, "Communication: Polymer entanglement dynamics: Role of attractive interactions," *J. Chem. Phys.* **145**, 141101 (2016).
- ³⁰A. Makke, M. Perez, J. Rottler, O. Lame, and J.-L. Barrat, "Predictors of cavitation in glassy polymers under tensile strain: A coarse-grained molecular dynamics investigation," *Macromol. Theory Simul.* **20**, 826–836 (2011).
- ³¹S. Zhang and L. Xi, "Effects of precursor topology on polymer networks simulated with molecular dynamics," *Polymer* **116**, 143–152 (2017).
- ³²L. Xi, "Molecular simulation for predicting the rheological properties of polymer melts," *Mol. Simul.* **45**, 1242–1264 (2019).
- ³³S. Plimpton, "Fast parallel algorithms for short-range molecular dynamics," *J. Comput. Phys.* **117**, 1–19 (1995).
- ³⁴Y. R. Shiozberg and J. W. Andzelm, "Fast protocol for equilibration of entangled and branched polymer chains," *Chem. Phys. Lett.* **523**, 139–143 (2012).
- ³⁵R. Auhl, R. Everaers, G. S. Grest, K. Kremer, and S. J. Plimpton, "Equilibration of long chain polymer melts in computer simulations," *J. Chem. Phys.* **119**, 12718–12728 (2003).
- ³⁶K. Kremer and G. S. Grest, "Simulations for structural and dynamic properties of dense polymer systems," *J. Chem. Soc., Faraday Trans.* **88**, 1707–1717 (1992).
- ³⁷H. P. Hsu and K. Kremer, "Static and dynamic properties of large polymer melts in equilibrium," *J. Chem. Phys.* **144**, 154907 (2016).
- ³⁸W. H. Press, S. A. Teukolsky, B. P. Flannery, and W. T. Vetterling, *Numerical Recipes in Fortran 77: Volume 1 of Fortran Numerical Recipes: The Art of Scientific Computing* (Cambridge University Press, 1992).
- ³⁹V. Calandrini, E. Pellegrini, P. Calligaris, K. Hinsens, and G. R. Kneller, "nmoldyn-interfacing spectroscopic experiments, molecular dynamics simulations and models for time correlation functions," *Ecole Thém. Soc. Française Neutron.* **12**, 201–232 (2011).
- ⁴⁰J. L. Viovy, M. Rubinstein, and R. H. Colby, "Constraint release in polymer melts: Tube reorganization versus tube dilation," *Macromolecules* **24**, 3587–3596 (1991).
- ⁴¹S. Wang, E. D. von Meerwall, S.-Q. Wang, A. Halasa, W.-L. Hsu, J. Zhou, and R. Quirk, "Diffusion and rheology of binary polymer mixtures," *Macromolecules* **37**, 1641–1651 (2004).
- ⁴²P. H. Verdier, "Monte Carlo studies of lattice-model polymer chains. I. Correlation functions in the statistical-bead model," *J. Chem. Phys.* **45**, 2118–2121 (1966).
- ⁴³M. Vladkov and J.-L. Barrat, "Linear and nonlinear viscoelasticity of a model unentangled polymer melt: Molecular dynamics and rouse modes analysis," *Macromol. Theory Simul.* **15**, 252–262 (2006).
- ⁴⁴J. T. Kalathi, S. K. Kumar, M. Rubinstein, and G. S. Grest, "Rouse mode analysis of chain relaxation in polymer nanocomposites," *Soft Matter* **11**, 4123–4132 (2015).
- ⁴⁵J. Padding and W. J. Briels, "Uncrossability constraints in mesoscopic polymer melt simulations: Non-rouse behavior of $C_{120}H_{242}$," *J. Chem. Phys.* **115**, 2846–2859 (2001).
- ⁴⁶Y. Li, M. Kröger, and W. K. Liu, "Nanoparticle effect on the dynamics of polymer chains and their entanglement network," *Phys. Rev. Lett.* **109**, 118001 (2012).
- ⁴⁷L. Xi, M. Shah, and B. L. Trout, "Hopping of water in a glassy polymer studied via transition path sampling and likelihood maximization," *J. Phys. Chem. B* **117**, 3634–3647 (2013).
- ⁴⁸H. P. Hsu and K. Kremer, "Detailed analysis of Rouse mode and dynamic scattering function of highly entangled polymer melts in equilibrium," *Eur. Phys. J.: Spec. Top.* **226**, 693–703 (2017).
- ⁴⁹P. J. Davis and D. J. Evans, "Comparison of constant pressure and constant volume nonequilibrium simulations of sheared model decane," *J. Chem. Phys.* **100**, 541–547 (1994).
- ⁵⁰J. Ramirez, S. K. Sukumaran, B. Vorselaars, and A. E. Likhtman, "Efficient on the fly calculation of time correlation functions in computer simulations," *J. Chem. Phys.* **133**, 154103 (2010).
- ⁵¹R. Anderssen and D. Mead, "Theoretical derivation of molecular weight scaling for rheological parameters," *J. Non-Newtonian Fluid Mech.* **76**, 299–306 (1998).
- ⁵²D. Maier, A. Eckstein, C. Friedrich, and J. Honerkamp, "Evaluation of models combining rheological data with the molecular weight distribution," *J. Rheol.* **42**, 1153–1173 (1998).
- ⁵³W. H. Tuminello, "Determining molecular weight distributions from the rheological properties of polymer melts," in *Proceedings of the 71st Society of Rheology Meeting*, Madison, Wisconsin (1999).
- ⁵⁴G. Marrucci, "Relaxation by reptation and tube enlargement: A model for polydisperse polymers," *J. Polym. Sci.: Polym. Phys. Ed.* **23**, 159–177 (1985).
- ⁵⁵W. Thimm, C. Friedrich, M. Marth, and J. Honerkamp, "On the rouse spectrum and the determination of the molecular weight distribution from rheological data," *J. Rheol.* **44**, 429–438 (2000).
- ⁵⁶W. H. Tuminello, "Molecular weight and molecular weight distribution from dynamic measurements of polymer melts," *Polym. Eng. Sci.* **26**, 1339–1347 (1986).
- ⁵⁷C. Tsenoglou, "Molecular weight polydispersity effects on the viscoelasticity of entangled linear polymers," *Macromolecules* **24**, 1762–1767 (1991).
- ⁵⁸J. Des Cloizeaux, "Relaxation of entangled polymers in melts," *Macromolecules* **23**, 3992–4006 (1990).

Chapter 5

Viscoelastic and thermo-mechanical properties of polymer-additive mixtures

In this chapter, we investigate the molecular parameters affecting the design of polymer-plasticizer mixtures using a single-bead model for the plasticizers. We focused on the thermophysical properties, dynamics, and the rheological properties of the mixtures; examining plasticization markers such as glass transition temperature T_g , Young's modulus Y , and the linear viscoelasticity of the mixtures at different molecular sizes and concentrations of the plasticizer additives. We observe that these different metrics for plasticization are indeed not correlated; a reduction in one property, for example, T_g does not lead to a corresponding reduction in Y .

This chapter builds on the earlier master's thesis of Kushal Panchal,¹ where the decorrelation between plasticizer effects on T_g and Y was first reported. I

repeated that work and refined the results with better accuracy. I then further studied the effects of the additives on viscoelastic properties. I carried out all the simulations reported in this chapter. I also analyzed the results and wrote the draft. The research was conducted under the supervision of Li Xi and Shiping Zhu who also provided feedback on the draft.

This chapter is **under preparation** for future publication.

5.1 Introduction

The thermophysical properties of polymers can be significantly altered upon the addition of additives.² One of such additives is a plasticizer, which is used to modify properties like the elastic moduli, glass transition temperature T_g , and rheological properties such as viscosity.^{3,4} Plasticizers are used to soften the polymer, improve the flexibility, reduce the brittleness, and enhance the workability of the polymer in general. Despite how prevalent plasticizers are, there is still a significant dearth in our understanding of how exactly they modify polymers. Different theories used – free volume, lubricity, and gel theory have been found inadequate in explaining different aspects of the plasticization process.⁵

In molecular dynamics (MD) simulations, an all-atom simulation, which fully models the chemical structure of the material, can be used when material-specific properties are being studied and several studies⁶⁻⁸ have investigated various aspects of the polymer-plasticizer interaction. For example, Li et al.⁷ studied the plasticization efficiency of phthalates in polyvinylchloride (PVC). All-atom simulations however suffer from the prohibitive computational time required

to fully run the simulations, due to the wide range of length and time scales involved in polymer relaxation especially, when viscoelastic properties are being investigated. Generic bare-bone models of polymers and plasticizers which capture the essential physics of the system can be used which leads to significant savings in the computational time required. In addition, it allows for the generic aspects of the physics to be focused on, rather than material-specific properties. As we further discussed in chapter 6, it turns out that developing a basic multi-bead model that mimics real plasticizer is non-trivial either due to rapid phase separation that occurs when the *model* additives are added to the polymers or in cases where they are compatible, the plasticization effects are minimal.

Several authors have investigated the interaction between polymers and small molecular additives using coarse-grained (CG) models in MD simulations.^{9–12} A previous work by Riggleman et al.¹³ used a bare-bones CG model, where the additives are modeled as Lennard-Jones particles and the polymer represented as a bead-spring model, to examine the effect of molecular additives on polymer properties. Among other things, they found that at a low mass fraction of the additive ($\sim 5\%$ mass fraction), there is a reduction in the T_g of the polymer. On the other hand, there is also an increase in various mechanical properties, such as the Young's modulus Y and the shear modulus. A phenomenon referred to as anti-plasticization. It was further explained that the antiplasticization effect is due to improved packing efficiency in the glassy state, wherein the additives are able to pack themselves neatly between polymer chains. Riggleman

et al.'s study by design, was focused on exploring the broad factors responsible for antiplasticization. The free volume theory,^{14–17} loosely described as the space available for particles or chain segments to move freely as the temperature is reduced, has long been used to explain some of the observed dynamic and thermophysical properties such as T_g and viscosity. Riggleman et al.¹³ further argued that, while there are local-scale fluctuations in the elastic constants, there was no corresponding long-scale density fluctuations which is a complete antithesis of the free volume concept as being responsible for the observed variations. Their investigation was however limited to a molecular size and a single concentration where the antiplasticization effect has been shown to occur.

There is also a relatively large body of work on polymer-particle interaction wherein the additives are modeled as nanoparticles.^{18–22} Among other things, it was reported that small neutral NPs reduce the viscosity of the host polymer and there is a reduction in the monomeric relaxation rates when the mixtures are weakly interacting. Furthermore, if the NPs are larger than half the entanglement mesh size, there is an increase in the viscosity and a negligible influence on the monomer relaxation rate.^{20,23} We are however interested in studying the plasticization effects of single-bead additives.

Previous works have largely focused on the antiplasticization effect.^{9,13,24} Our goal in this work is two-fold: (i) to explore the possibility of applying the Kremer-Grest (KG) model²⁵ for studying plasticization effects and (ii) to explore the dependence of the T_g , Y , and linear viscoelasticity of polymer-particle systems on the molecular dimensions of a single-bead additive. The KG model has been successfully used to investigate different areas in polymer physics

such as the nature of entanglements,²⁵ influence of polydispersity on linear viscoelasticity,^{26,27} polymer networks,²⁸ glass transition,²⁹ and many other polymeric features. The main difference between this work and polymer-nanoparticles is on the dimension of the particles. Relative to the monomer (bead) sizes of model polymers, their additive sizes are usually much larger and the interaction potential different. In general, it has been observed that small molecule additive enhances the dynamics of the polymer chains in a manner similar to a mixture of short chains and long chains.³⁰ We investigate these properties over a wide range of concentration and size dimensions.

5.2 Model and Methods

Our model consists of a mixture of polymer chains (A) and additives (B). Although we have tried other models – as further discussed in chapter 6 where we attempt to model a more realistic representation of the plasticizer. In the model we describe here, each polymer chain is a KG chain, represented using a bead-spring chain model²⁵ where the beads are the monomers of the polymer chain and the springs represent the bonds between the monomers. The bonded beads interact using a finitely extensible non-linear elastic (FENE) potential

$$U_{\text{FENE}}(r) = -\frac{1}{2}KR_0^2 \ln \left[1 - \left(\frac{r}{R_0} \right)^2 \right] + 4\epsilon \left[\left(\frac{\sigma}{r} \right)^{12} - \left(\frac{\sigma}{r} \right)^6 + \frac{1}{4} \right] \quad (5.1)$$

where r is the distance between the beads and σ and ϵ are the standard Lennard-Jones (LJ) length and energy parameters. The first term of the equation represents an attractive potential, and models the FENE springs between the closest neighbors along the chain with a maximum bond length $R_0 = 1.5\sigma$, while the second term models the excluded-volume repulsion between beads and the term is only included at $r \leq 2^{1/6}\sigma$. The spring constant $K = 30\epsilon/\sigma^2$ is chosen to allow a reasonable integration time step while preventing chains from crossing each other.²⁵ For the non-bonded beads, the interaction is modeled by the standard LJ potential

$$U_{\text{LJ}}(r) = 4\epsilon \left[\left(\frac{\sigma}{r}\right)^{12} - \left(\frac{\sigma}{r}\right)^6 \right]. \quad (5.2)$$

The potential is truncated at $r = 2.5\sigma$ and shifted by a constant to ensure continuity at the cutoff. The non-bonded additives interact with one another using the standard LJ potential of eq. (6.2).

We report the results in reduced LJ units wherein the length, energy, time, and temperature are scaled by σ , ϵ , $\tau = \sqrt{m_A\sigma^2/\epsilon}$, and ϵ/k_B (k_B is the Boltzmann constant), respectively. For the polymer chain, the non-dimensional LJ energy and length parameters are set at $\epsilon_A = 1$ and $\sigma_A = 1$. We use a polymer chain length $N = 100$ for all the simulations and the mass of each of the polymer beads m_A was kept at 1. To capture a range of additive molecular sizes, we varied σ_B of the additives from 0.5 to 1.0. The mass of the additives was varied as the cube of the particle size ($m_B \propto \sigma_B^3$). Finally, the cross-interaction between the polymer and the additives are captured via the Lorentz-Berthelot mixing

rules given by

$$\epsilon_{AB} = \sqrt{\epsilon_A/\epsilon_B} \quad (5.3)$$

and

$$\sigma_{AB} = \frac{1}{2}(\sigma_A + \sigma_B) \quad (5.4)$$

ϵ_B was set to $1.0\epsilon_A$ to promote entropic mixing.¹³ The mass concentration ϕ_B of the additives was varied from 1% to 30%. The total number of polymer and additives was kept close to 10000 as much as possible. A detailed composition of the mixture is listed in Table I.

We performed all simulations using the Large-scale Atomic/Molecular Massively Parallel Simulator (LAMMPS) package.³¹ The equation of motion was integrated using the velocity-Verlet algorithm with a timestep of $\Delta t = 0.001$ (in LJ time units or TUs). For both polymer chains and the additives, we generated their initial structures by arbitrarily packing the specified number of chains and particles into a cubic simulation cell. The individual chains were generated using a procedure similar to self-avoiding walk in a continuum space. This approach while preventing back-folding of the chains, still results in substantial overlaps of the chain beads. The mass of the chain beads and particles were set to 1 initially. We then equilibrate the mixture using a dissipative particle dynamics (DPD) push-off method of Sliozberg et al..³² For the duration of the DPD run, we replaced the interaction between non-bonding beads with a soft

repulsive potential of the form of

$$U_{\text{DPD}}(r) = \begin{cases} \frac{A_{\text{DPD}}}{2} r_c \left(1 - \frac{r}{r_c}\right) & r < r_c \\ 0 & r \geq r_c \end{cases}. \quad (5.5)$$

This potential allows the chains to pass through each other and therefore enhances a quicker relaxation during the initial equilibration steps. We ran the DPD simulation at $T = 1.0$ using a cut-off distance $r_c = 1.0$. The potential was initially low and set at $A_{\text{DPD}} = 25$. At the beginning, restriction was imposed on the maximum distance each bead can move within one time step which gradually increases from 0.001 to 0.1 over 15 TUs. The restriction was then removed and the simulation was run for another 100 TUs. This was subsequently followed by a gradual ramp of A_{DPD} to 1000 over 5.5 TUs. The DPD potential was then replaced with the standard LJ potential and MD in an NVE ensemble was performed for additional 500 TUs during which a random velocity distribution was reassigned to all beads every 0.5 TUs. Finally, we changed the masses of the additives from 1 to the specified masses and further ran MD in an NVT ensemble for an additional 20 000 TUs. Since the relaxation of the system is dependent on the relaxation time scale of the polymer chains, running the simulation long enough to ensure the polymer chains have relaxed guarantees that our system is well equilibrated. Our earlier paper³⁰ shows the mean square internal displacement (MSID) results for the polymer chains studied, where the MSID saturates to the characteristic ratio of the chain. While the model we have described above is similar to that used by Riggleman et al.,⁹ they however used a harmonic potential between the bonds with a much stiffer chain with $k = 2000\epsilon/\sigma^2$.

TABLE 5.1: Detailed compositions of polymer-plasticizer systems simulated at various plasticizer mass fractions. σ_B , m_B , M_B , and M_A are the plasticizer size, mass of each plasticizer particle, total mass of the plasticizer, and total mass of the polymer chains respectively. The length of the polymer chain was kept constant at $N = 100$

| $\phi_B(\%)$ | σ_B | m_B | M_B | M_A | $\phi_B(\%)$ | σ_B | m_B | M_B | M_A |
|--------------|------------|-------|--------|---------|--------------|------------|-------|---------|---------|
| 1 | 0.5 | 0.125 | 93.46 | 9252.34 | 10 | 0.5 | 0.125 | 588.24 | 5294.12 |
| 1 | 0.6 | 0.216 | 96.50 | 9553.25 | 10 | 0.6 | 0.216 | 733.70 | 6603.26 |
| 1 | 0.7 | 0.343 | 98.12 | 9713.93 | 10 | 0.7 | 0.343 | 839.25 | 7553.22 |
| 1 | 0.8 | 0.512 | 99.06 | 9806.53 | 10 | 0.8 | 0.512 | 912.98 | 8216.83 |
| 1 | 0.9 | 0.729 | 99.63 | 9863.33 | 10 | 0.9 | 0.729 | 964.16 | 8677.42 |
| 1 | 1.0 | 1.00 | 100.00 | 9900.00 | 10 | 1.0 | 1.0 | 1000.00 | 9000.00 |
| 2 | 0.5 | 0.125 | 175.44 | 8596.49 | 15 | 0.5 | 0.125 | 731.71 | 4146.34 |
| 2 | 0.6 | 0.216 | 186.45 | 9136.74 | 15 | 0.6 | 0.216 | 971.22 | 5503.60 |
| 2 | 0.7 | 0.343 | 192.62 | 9438.42 | 15 | 0.7 | 0.343 | 1165.21 | 6602.88 |
| 2 | 0.8 | 0.512 | 196.26 | 9616.68 | 15 | 0.8 | 0.512 | 1312.37 | 7436.77 |
| 2 | 0.9 | 0.729 | 198.52 | 9727.68 | 15 | 0.9 | 0.729 | 1420.76 | 8051.06 |
| 2 | 1.0 | 1.00 | 200.00 | 9800.00 | 15 | 1.0 | 1.0 | 1500.00 | 8500.00 |
| 3 | 0.5 | 0.125 | 247.93 | 8016.53 | 20 | 0.5 | 0.125 | 833.33 | 3333.33 |
| 3 | 0.6 | 0.216 | 270.54 | 8747.50 | 20 | 0.6 | 0.216 | 1158.80 | 4635.19 |
| 3 | 0.7 | 0.343 | 283.70 | 9172.89 | 20 | 0.7 | 0.343 | 1446.04 | 5784.15 |
| 3 | 0.8 | 0.512 | 291.66 | 9430.35 | 20 | 0.8 | 0.512 | 1679.79 | 6719.16 |
| 3 | 0.9 | 0.729 | 296.69 | 9593.02 | 20 | 0.9 | 0.729 | 1861.59 | 7446.34 |
| 3 | 1.0 | 1.00 | 300.00 | 9700.00 | 20 | 1.0 | 1.0 | 2000.00 | 8000.00 |
| 4 | 0.5 | 0.125 | 312.5 | 7500 | 25 | 0.5 | 0.125 | 909.09 | 2727.27 |
| 4 | 0.6 | 0.216 | 349.29 | 8382.92 | 25 | 0.6 | 0.216 | 1310.68 | 3932.04 |
| 4 | 0.7 | 0.343 | 371.53 | 8916.81 | 25 | 0.7 | 0.343 | 1690.49 | 5071.46 |
| 4 | 0.8 | 0.512 | 385.31 | 9247.44 | 25 | 0.8 | 0.512 | 2018.93 | 6056.78 |
| 4 | 0.9 | 0.729 | 394.14 | 9459.34 | 25 | 0.9 | 0.729 | 2287.42 | 6862.25 |
| 4 | 1.0 | 1.00 | 400.00 | 9600.00 | 25 | 1.0 | 1.0 | 2500.00 | 7500.00 |
| 5 | 0.5 | 0.125 | 370.37 | 7037.04 | 30 | 0.5 | 0.125 | 967.74 | 2258.06 |
| 5 | 0.6 | 0.216 | 423.20 | 8040.75 | 30 | 0.6 | 0.216 | 1436.17 | 3351.06 |
| 5 | 0.7 | 0.343 | 456.30 | 8669.68 | 30 | 0.7 | 0.343 | 1905.20 | 4445.47 |
| 5 | 0.8 | 0.512 | 477.26 | 9067.86 | 30 | 0.8 | 0.512 | 2332.93 | 5443.50 |
| 5 | 0.9 | 0.729 | 490.88 | 9326.64 | 30 | 0.9 | 0.729 | 2699.00 | 6297.67 |
| 5 | 1.0 | 1.00 | 500.00 | 9500 | 30 | 1.0 | 1.0 | 3000.00 | 7000.00 |

5.3 Results and Discussion

5.3.1 Glass Transition Temperature T_g

Although plasticization effects are vaguely defined, it is customary to use a reduction in T_g and other mechanical properties such as the elastic moduli as markers.^{7,33} We consequently start our discussion with the glass transition results. As the temperature is lowered and at a sufficiently fast cooling rate, amorphous polymer melt (applies to other materials such as organic liquids and metals as well) would solidify into a glassy state without crystallization.^{2,16,34,35} This transition from liquid to the glassy state occurs at T_g and involves an apparent discontinuity in thermodynamic quantities, such as the specific volume or heat capacity.^{29,36–38} Both experimental and MD simulation methods exploit this discontinuity for calculating T_g .

As shown in previous studies,^{7,28} determining T_g in MD simulations requires a proper equilibration procedure to obtain reliable results. After the equilibration steps described in section 5.2 to remove overlaps and fully relax the system, we further subject our system to several heating and cooling cycles to completely erase the thermal history. We ran MD simulation in NPT ensemble for 1000 TUs, then followed by 6 heating-cooling cycles – each with a 1000 TUs run at $1\epsilon/k_B$ and $0.6\epsilon/k_B$ at zero pressure maintained by Nosé-Hoover barostat. The production runs for the glass transition temperature simulations were also performed in an NPT ensemble. Starting from an initial temperature of $1\epsilon/k_B$, the system was cooled down at a rate of $1 \times 10^{-7}\epsilon/k_B\tau$ at zero pressure using a Nosé-Hoover thermostat and barostat – i.e. temperature drops by 0.01

over 100 TUs using an MD timestep of 0.001. We average the system volume every 1 TU over the 100 TUs used at each temperature. We then determine T_g by the intersection of the fitting lines of the specific volume delineated by a slope change. Before discussing the results for our polymer-particle systems,

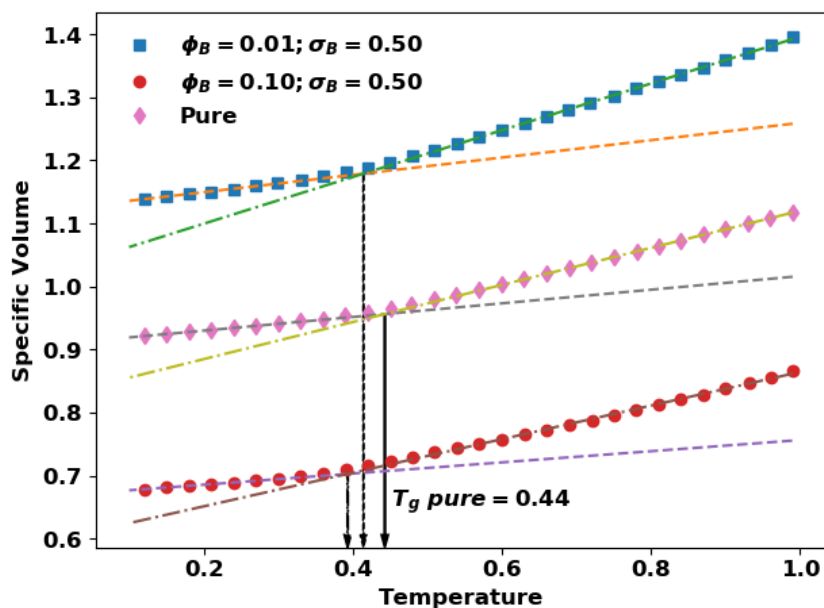


FIGURE 5.1: Glass transition temperature T_g of pure and additive polymer melt $N = 100$ determined from the dependence of the specific volume on temperature. Vertical offsets are added to the $\phi = 0.01$ and 0.1 curves by a factor of 1.25 and 0.77 respectively to make the plot clearer.

we determine the T_g for the pure melt of $N = 100$. For the pure melt case shown in fig. 5.1, we observe a dependence of the specific volume on temperature marked by a sudden change of slope around T_g . The slopes were calculated using at least 25 points on either side of the slope change. The intersection of the fitting lines to the slopes yielded a value of 0.44 which falls within the range of 0.41 – 0.45 commonly reported in the literature.^{28,29} For the same model but a bigger system size (500 chains of $N = 500$), Grest²⁹ used a cooling rate of

$1 \times 10^{-6} \epsilon / (k_B \tau)$ and obtained a value of 0.43. We also show the specific volume of two sample mixtures ($\sigma_B = 0.5$ at $\phi_B = 0.01$ and $\sigma_B = 0.5$ at $\phi_B = 0.10$) against temperature in fig. 5.1 where a similar dependence as with the pure polymer melt is observed. The T_g for both mixtures are lower than the pure polymer.

Figure 5.2 shows the dependence of the difference in T_g between the mixture and pure system, ΔT_g on the additive mass fraction ϕ_B . A negative value reflects the extent to which the T_g of the mixture is reduced relative to the pure polymer. Firstly, we note that the smaller-sized particles are better at reducing T_g at all concentrations considered. However, as the additive concentration increases to $\sim 10\%$, we observe a decrease in T_g for sizes $\sigma_B \leq 0.8$. For bigger sizes $\sigma_B > 0.8$ and up to $\phi_B = 10\%$, there is a plateau and there is not a noticeable dependence on ϕ_B . However, starting at around $\phi_B = 0.20$, there is again, an increase in ΔT_g

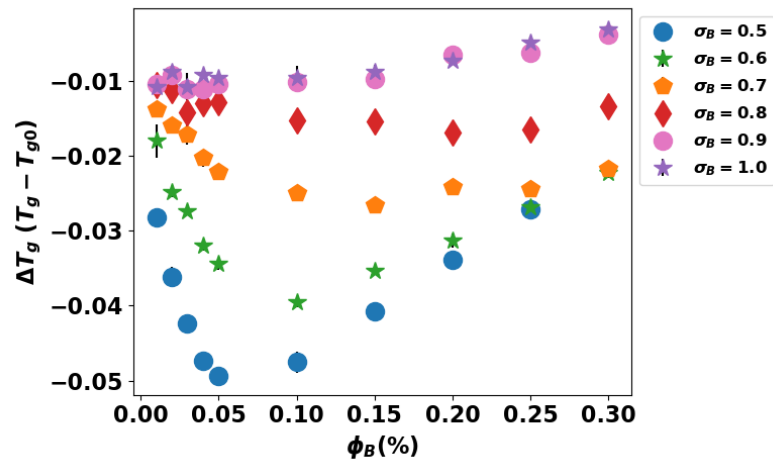


FIGURE 5.2: Change in glass transition temperature ΔT_g for additive concentration from 1% to 30% of various additive sizes. Error bars represent standard error over 3 independent samples and are smaller than marker sizes.

for all the sizes. Riggleman et al.¹³ reported a similar reduction in T_g for $\sigma_B = 0.5$ and $\phi_B = 0.05$ compared with the pure polymer. They argued that the observed changes in T_g and other antiplasticization markers are a reflection of changes in the packing efficiency, which modifies the process of glass formation itself rather than merely changing T_g . Essentially, the smaller beads pack themselves nicely in between the holes of the polymer melt³³ and makes the polymer melt a stronger glass former. We believe this is certainly the case for the mixtures we have studied here, at least for the smaller molecules ($0.5 \leq \sigma_B \leq 0.8$), with the effects becoming stronger as σ_B decreases. When the additive sizes are closer

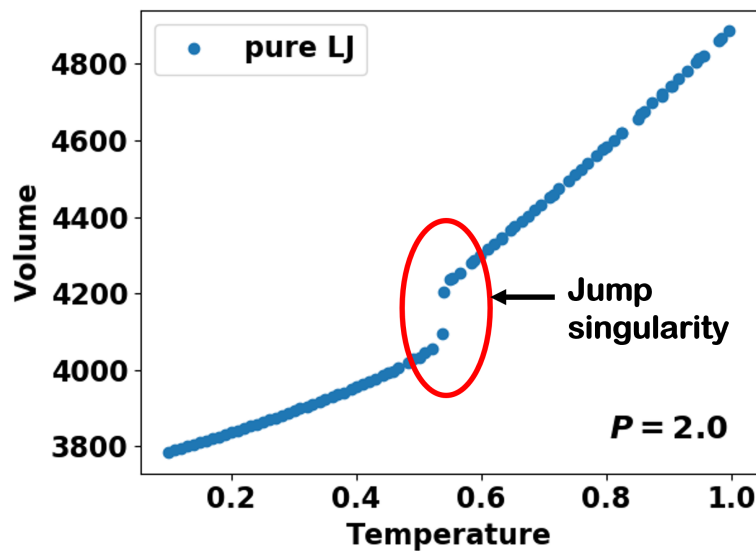


FIGURE 5.3: Temperature dependence of the specific volume for a Lennard-Jones liquid at a pressure of 2.0 showing a jump singularity.

to the size of the polymer bead ($\sigma_B > 0.8$) however, there is a reduction in the packing efficiency leading to an increase in ΔT_g . This effect of increasing ΔT_g becomes more pronounced at $\phi_B > 10\%$.

With the increase in T_g with concentration, extrapolating this trend will eventually lead to higher T_g in pure LJ liquid than pure polymer, which is counter-intuitive. Exploring the limit of pure LJ particles, it is well known that pure LJ particles are poor glass formers which crystallize when cooled to a lower temperature, and as such have no defined T_g . Depending on the pressure imposed during the simulation, the system is either unstable, wherein the volume of the simulation box keeps expanding during an NPT run at zero pressure, or a jump singularity is observed in the plot of the specific volume against temperature at the freezing temperature at higher pressures.³⁶ A plot of this discontinuity is shown in fig. 5.3 for the LJ particles at a pressure of 2.0. Since the pure LJ particles are poor glass formers, the strategy employed to prevent crystallization is to use a bidisperse model containing two different particle sizes and tune their interaction parameters. Additionally, the density of these bidisperse mixtures is usually much higher (~ 1.2 compared to our own 0.85) than the density of the systems we have investigated and usually simulated at constant volume conditions.³⁹ This makes it somewhat difficult to properly situate our results within the extremes of pure polymer and pure LJ particles. The Kob-Anderson model⁴⁰ is a notable example consisting of bidisperse LJ particles. In this model, large LJ spheres are mixed with smaller spheres at an 80-20 number fraction. Using a 3d model, a number density of 1.0 and a pressure of 1.0, Li et al.⁴¹ reported a glass transition temperature of 0.41. The two ends (polymer and additive) have similar T_g so it is not entirely strange that T_g does not decrease with ϕ_B .

5.3.2 Young's Modulus

The second property we investigate is the Young's modulus. We simulate tensile elongation by deforming the simulation box along the z dimension. The length of the box along this dimension changes as a function of time as

$$L_z(t) = L_{z,0} \exp(\dot{\epsilon}t) \quad (5.6)$$

where $L_{z,0}$ is the length before deformation, $\dot{\epsilon} = \frac{de}{dt}$ is the strain rate. We used $\dot{\epsilon} = 0.03271/\tau$ as used by previous studies.^{21,28} The lateral dimensions x and y were maintained at a temperature of $0.1\epsilon/k_B$ and zero pressure using the Nosé-Hoover barostat. The tensile stress is determined from the pressure difference between the elongated dimension (P_z) and the average of the transverse dimension (P_x and P_y)

$$s = -P_z + \frac{1}{2}(P_x + P_y) \quad (5.7)$$

and plotted against the engineering strain

$$e \equiv \frac{L_z - L_{z,0}}{L_{z,0}} \quad (5.8)$$

In the limit of small deformation, the relationship between the stress and strain is linear. The Young's modulus of the material is defined in this limit

$$Y \equiv \lim_{e \rightarrow 0} \frac{ds}{de} \quad (5.9)$$

The stress-strain curves for the pure polymer melt and some selected mixtures are shown in fig. 5.4. All the curves show the typical features of a polymer

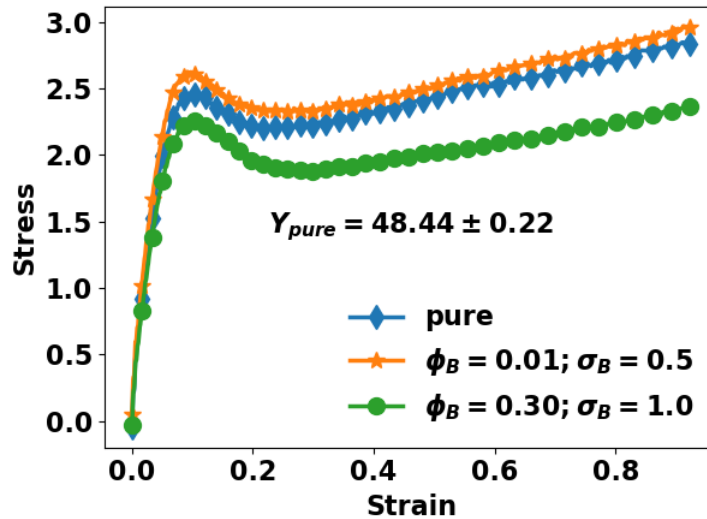


FIGURE 5.4: Young’s modulus Y for pure polymer and some selected mixtures. The linear portion of the strain used for the calculation was 2% of the overall strain.

undergoing tensile deformation: an elastic region at small strain; a yield point right after the elastic region where there is an upturn at the top of the curve; a strain softening region where the sample cross-sectional area reduces, resulting in a decrease in stress; and a strain hardening region showing an increase in stress before fracturing. Similar behaviors have been reported by several other researchers using MD simulation.^{42,43} These curves are also the typical profiles for pure, plasticized, and antiplasticized polymers. Compared to the pure polymer curve, the antiplasticized polymers show an increased slope in the elastic region – indicating the stiffening effect of the antiplasticizers; an increase in the maximum yield stress reached; a short softening region at intermediate strains; and a greater increase in stress in the strain-hardening regime at larger strains. On the contrary, plasticizers resulted in a decrease in the elastic region, a smaller yield stress, a more pronounced softening region and a much smaller increase

in stress in the strain-hardening regime. Now focusing on the linear regime and Young’s modulus, we only used ϵ up to 2% similar to previous works in the literature,^{13,28} to ensure the deformation is still in the linear regime. We obtained a value of 48.44 for the pure melt. The Y for the polymer-additive system tells a different story as shown in fig. 5.5. Again, we have plotted the difference between the mixture and pure system ΔY , against ϕ_B . Although the additives of all sizes lessened the T_g at all concentrations, this is not quite the case for Y . For the smaller additives ($\sigma_B \leq 0.8$) the Y is higher than the pure polymer –

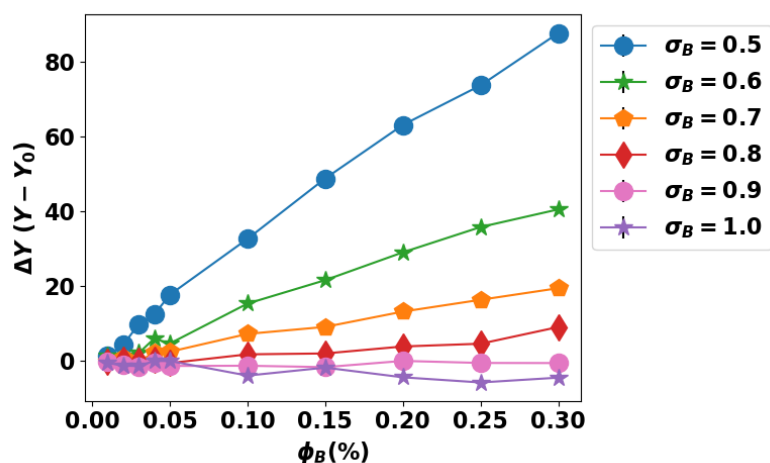


FIGURE 5.5: Change in Young’s Modulus $\Delta Y(Y - Y_0)$ for plasticizer concentration from 1% to 30% of various additive sizes. The error bars represent standard error over 100 independent configurations and are smaller than the markers.

indicating that these additives behave as antiplasticizers – broadly defined as a reduction in T_g and a simultaneous stiffening of the material. At 5% mass fraction of the $\sigma_B = 0.5$ additive, there was a $\sim 36\%$ increase in Y . This is also consistent with the earlier work of Riggleman et al.¹³ where at a 5% mass fraction of the additives and temperature of 0.1, (although the potential between

their connected beads was harmonic, we have used FENE in this work. In the limit of small deformation, the calculated values should be equal) they reported a similar increase in Y ($\sim 40\%$) and a decrease in T_g . For $\sigma_B \geq 0.9$ however, the Y values are lower than the pure melt at all the concentrations we have investigated and can consequently be regarded as plasticizers – which loosely defines additives that lower the T_g and Y simultaneously. The level of Y increase in these antiplasticizers (smaller additives) is much higher than the largest Y reduction at the larger additive size limit. For example, the maximum reduction in Y was merely 12% at $\phi_B = 25\%$ and $\sigma_B = 1$. On the contrary, there was over a $\sim 150\%$ increase in Y at the 30% mass fraction of the $\sigma_B = 0.5$ additive. An interesting observation was the decorrelation of the plasticization markers, T_g with Y – where a reduction in one property does not translate into a decrease in another. We show this trend in fig. 5.6 where we have plotted the change in T_g and Y for various bead sizes at $\phi_B = 1\%$. Indeed, there is a reduction in T_g and Y at $\sigma_B = 1.0$, however, as σ_B decreases, while the T_g continues to decrease, there is an increased stiffening of the polymer as reflected in the increase in Y . This finding reveals the hidden complexity behind the concept of plasticization: although plasticizers are used to label any material "softener", the "softening" effect in different properties (markers) are independent from each other and likely follow separate mechanisms. As such plasticization can be considered a loosely defined collective description of many different effects.

5.3.3 Linear Viscoelasticity

We now turn to the effects of the molecular additive on the overall rheological properties of the mixture. To do this, we calculate the linear viscoelastic (LVE)

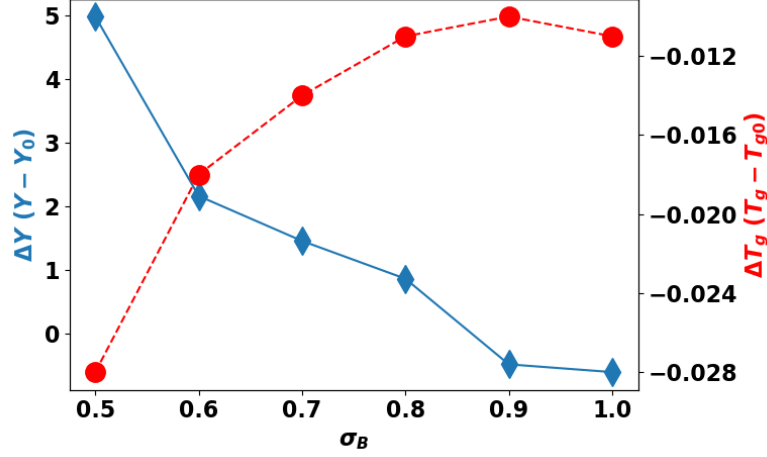


FIGURE 5.6: Young's modulus and glass transition temperature for various bead sizes at an additive concentration $\phi_B = 0.01$.

properties of the mixture at a temperature of $1.0\epsilon/k_B$. We ran MD in the NVT ensemble for 1×10^7 TUs. We use equilibrium molecular dynamics (EMD) for the calculation and explore different LVE properties such as the stress relaxation modulus $G(t)$ and the storage and loss moduli, G' and G'' respectively. Calculating G' and G'' is a 2-stage process that requires the determination of $G(t)$ of the mixture followed by its Fourier-integral.^{30,44–47} The Green-Kubo relation gives the relationship between $G(t)$ and the autocorrelation function (ACF) of the shear stress fluctuations

$$G(t) = \frac{V}{k_B T} \langle \sigma_{xy}(t_0) \sigma_{xy}(t_0 + t) \rangle \quad (5.10)$$

where V is the volume of the system, T is the temperature, and σ_{xy} is the instantaneous shear stress. To improve the signal to noise ratio of the stress signal in the system, we average the stress ACF over multiple directions. This results in

the form

$$\begin{aligned} G(t) = & \frac{V}{5k_B T} [\langle \sigma_{xy}(t)\sigma_{xy}(0) \rangle + \langle \sigma_{yz}(t)\sigma_{yz}(0) \rangle \\ & + \langle \sigma_{zx}(t)\sigma_{zx}(0) \rangle] + \frac{V}{30k_B T} [\langle N_{xy}(t)N_{xy}(0) \rangle \\ & + \langle N_{xz}(t)N_{xz}(0) \rangle + \langle N_{yz}(t)N_{yz}(0) \rangle] \end{aligned} \quad (5.11)$$

where

$$N_{\alpha\beta} = \sigma_{\alpha\alpha} - \sigma_{\beta\beta}. \quad (5.12)$$

Furthermore we used the multi-tau correlator method developed by Ramirez et al.⁴⁸ which uses a hierarchical multi-level data structure to store and filter time series and calculate correlation functions on the fly. In its data structure, level 0 stores the most recent p data points in the time series. At level 1, the first entry stores the average value of the most recent m ($m < p$) points, the second entry stores the average of the next m points, and so on. Similarly, each entry at level l is the average of m entries at level $l - 1$. As such, stored data represent local averages of the original time series and the averaging window size (m^l for level l) increases with the level, so does the time lag it covers (the range of previous time where information is retained at the current level). For the smallest time lags (up to $p - 1$ sampling intervals), the unfiltered time series is used, whereas for increasing time lag (higher levels), averages over larger window sizes are used. In this study, we use the same default parameters $p = 16$ and $m = 2$ as recommended in Ramirez et al.⁴⁸ The G' and G'' are then directly determined

by taking the Fourier integral of the $G(t)$

$$G' = \omega \int_0^{\infty} G(t) \sin(\omega t) \quad (5.13)$$

$$G'' = \omega \int_0^{\infty} G(t) \cos(\omega t) \quad (5.14)$$

The $G(t)$ is very sensitive to the molecular structure of the polymeric materials⁴⁹ and can give insight into the nature of the relaxation mechanism. At very short times in unentangled and entangled polymers, the $G(t)$ value is large due to the twisting and stretching of bonds. After a sufficient time, there is a significant relaxation of stress and the unentangled melt decays. The topological constraints in an entangled polymer however results in a plateau that is independent of the length of the chain before the chains are finally able to *reptate* out of their constraints.⁵⁰

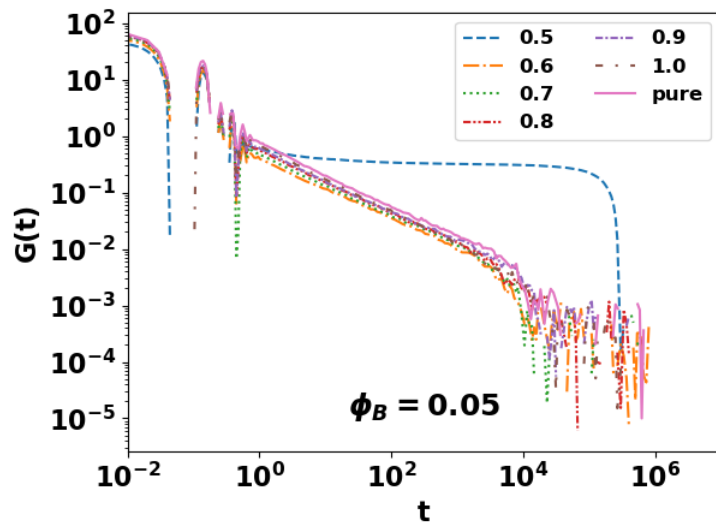


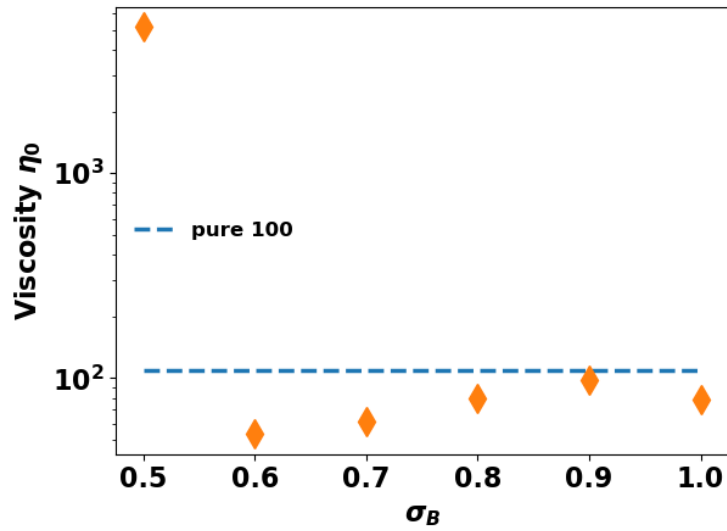
FIGURE 5.7: Stress relaxation modulus $G(t)$ at $\phi_B = 0.05$

Figure 5.7 shows the $G(t)$ of polymer-additive mixtures at $\phi_B = 0.05$ and

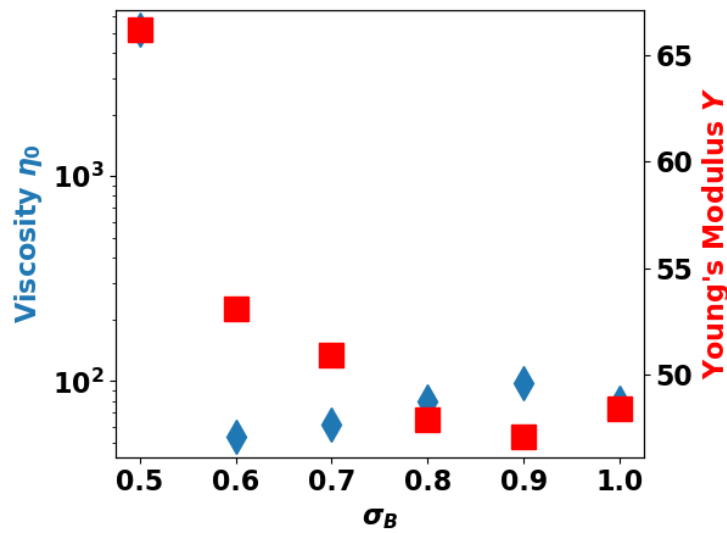
that of the pure melt, $N = 100$. The results are rather surprising especially for the smallest additive $\sigma_B = 0.5$. We repeated the simulation to ensure it was not due to an error in the simulation. There is an extended plateau that persisted even much further in time which is atypical for an uncrosslinked, unentangled polymer melt. Even in entangled polymers, the plateau region in the $G(t)$ curve is more gradual and does not decay abruptly as seen for the $\sigma_B = 0.5$ case at $t \sim \mathcal{O}(10^5)$. Several works and our earlier results^{30,46,47} have also shown that for the KG model we have used, a plateau in the $G(t)$ is not observed until $N \geq 350$. For the other bead sizes ($\sigma_B > 0.5$) however, the relaxation is typical and $\sigma_B = 0.6$ resulted in the lowest profile. However, the pure melt still has a much higher profile than all the other σ_B sizes except 0.5 – which indicates that the additives have effectively *plasticized* the polymer. To better quantify the plasticization effect we calculate the zero-shear viscosity η_0 of the mixtures which is a cumulative representation of $G(t)$. We calculate η_0 using⁵¹

$$\eta_0 \equiv \lim_{\dot{\gamma} \rightarrow 0} \eta(\dot{\gamma}) = \int_0^{\infty} G(t) dt \quad (5.15)$$

where $G(t)$ is the relaxation modulus and $\eta(\dot{\gamma})$ is the shear rate dependent viscosity. We show the viscosity results for the mixture in fig. 5.8a and have included the pure polymer melt for reference. η_0 for the pure polymer is 108.72 which compares favorably with the 129 from Maxwell's mode fitting result of Likhtman et al.⁴⁶ and the non-equilibrium MD result of ~ 107 reported by Kröger et al.⁵² The plot shows a spike in η_0 at $\sigma_B = 0.5$. At higher bead sizes ($\sigma_B > 0.5$), all the bead sizes reduced η_0 compared to the pure melt. As the bead size increases, η_0 also increases up until $\sigma_B = 0.9$ and then dropped at $\sigma = 1.0$.



(a) η_0 for the various mixtures at $\phi_B = 0.05$



(b) η_0 and Young's modulus Y at $\phi_B = 0.05$

FIGURE 5.8: Zero-shear viscosity η_0 and Young's modulus Y for various bead sizes at an additive concentration $\phi_B = 0.05$.

This shows that, the smaller the beads the better the plasticization effect of the additives. Again, we compare the viscosity plots with the Y results at the same $\phi_B = 0.05$ in fig. 5.8b. The figure also shows a decorrelation of η_0 with Y , where Y decreases with increase in σ_B while η_0 increases. There is also a slight dip in Y similar to the small rise in η_0 at $\sigma_B = 0.9$. Indeed, if we examine closely the T_g , Y , and η_0 of the mixture at $\sigma_B = 0.6$ of the additive and $\phi_B = 0.05$, we see that, as T_g decreases, Y increases, and η_0 decreases. If we had only measured T_g and η_0 , $\sigma_B = 0.6$ would be called a plasticizer. On the other hand, calculating T_g and Y alone would have made it an antiplasticizer. Figure 5.9 and fig. 5.10 show the G' and G'' for the same mixture. The extended plateau observed for $\sigma_B = 0.5$ carries over to the G' results where it is essentially a flat line. Since the G' is mainly the energy stored in the system, we again observe that the G' decreases with with decreasing additive size at all frequencies. Similar trends are observed in the G'' profiles.

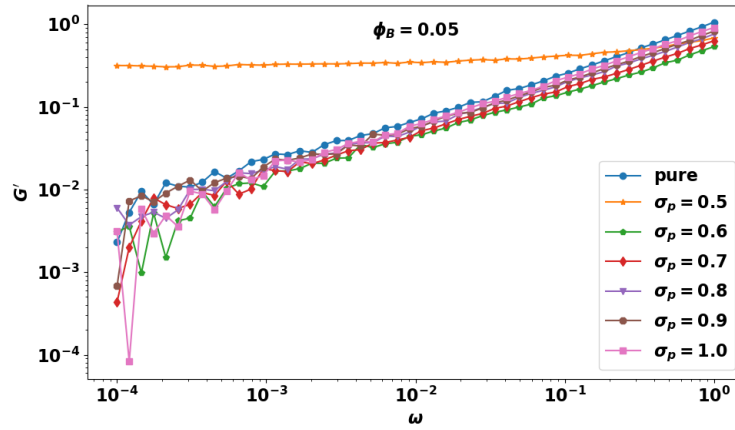


FIGURE 5.9: G' for polymer-additive mixture at an additive concentration of $\phi_B = 0.05$.

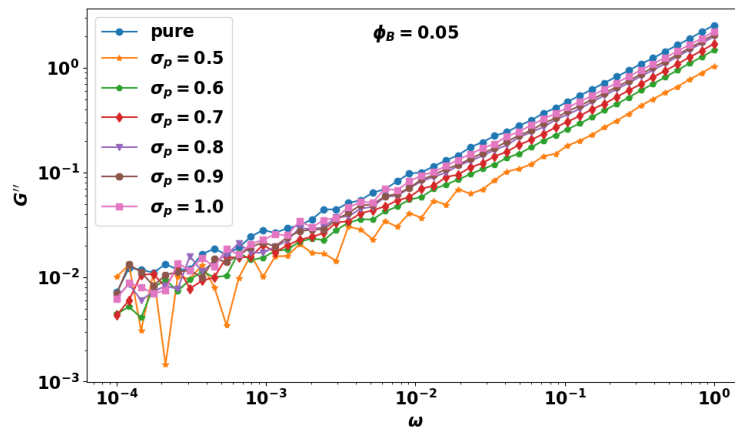


FIGURE 5.10: G'' for polymer-additive mixture at an additive concentration of $\phi_B = 0.05$.

5.3.4 Voronoi Analysis

One important theory used in the explanation of the glass transition phenomenon is the free volume theory.^{16,53} It is based on the idea that there are local pockets of space surrounding the beads of polymer chains that allows for some degree of mobility. The larger the space, the lower the T_g . Small molecule additives lower the T_g by making it easier for the chains to slide past each other and consequently increasing the free volume. Voronoi decomposition is the go-to approach for determining the free spaces around particles.^{54,55} Given the coordinates of the atomic centers of the particles – referred to as sites, the Voronoi cell determines a set of points in the plane that is closest to the given site.⁹

We show the probability density function (PDF) of the Voronoi volume of the polymer and additive in fig. 5.11 at a temperature of 0.1 for $\sigma_B = 0.5$ and 1.0. Our T_g results had earlier indicated that for $\sigma_B = 0.5$, the T_g decreases with increasing concentration, goes through a minimum around $\phi_B = 0.1$ and increases again at the highest concentration, $\phi_B = 0.30$ that we have studied. Figure 5.11a shows the PDF of the *free volume* around the polymer, normalized by the volume of the polymer bead. The results show that the free volume increases as ϕ_B decreases. Of course, this makes intuitive sense. However, unlike our T_g results, we do not see a corresponding transition in the mean value of the PDF. Similarly, fig. 5.11b shows the PDF of the free volume surrounding the additive, again normalized by volume of the particle. Again, we also see that there is more free volume surrounding the particles at a lower ϕ_B . On the other hand, when $\sigma_B = 1.0$, the PDF shown in fig. 5.11c and fig. 5.11d collapses on

one another. The concentration has very little effect because the additive particles are indistinguishable from the polymer beads. Comparing the Voronoi volume at $\phi_B = 0.05$ for different bead sizes in fig. 5.12, we see that the mean value of the free volume increases with increasing σ_B . Going by the free volume theory, it is expected that the increase in free volume will lead to a lower T_g . Our results however show an opposite trend – negating the idea of free volume as an explanation for T_g . Several authors have also shown the concept of free volume inadequate in explaining the different aspects of the glass transition phenomena.^{9,13,56} For example, Riggleman et al.¹³ showed that the increased particle mobility that is expected with increase in free volume does not hold.

On the other hand, the available free volume correlates with our results for the Young's modulus. An improvement in packing efficiency, which is as a result of increase in density (smaller volume occupied by polymer and additives) is responsible for the enhanced stiffness observed in mixtures containing the smaller additives. Figure 5.12 shows that the mean free volume increases with increasing additive size, resulting in a larger total volume occupied by the polymer and additives. This leads to a decrease in density, thereby leading to a reduction in the packing efficiency as the additive size increases. The smaller beads are however able to pack themselves more efficiently around the polymer beads and is responsible for the increase in Y shown in fig. 5.5. Indeed, Young's modulus is a measure of the stiffness at small strain limit, where particles are only displaced by a small distance on average. An increase in the local wiggle room surrounding each particle is bound to make such dislocation easier. This observation of enhanced stiffness with decrease in free volume is consistent

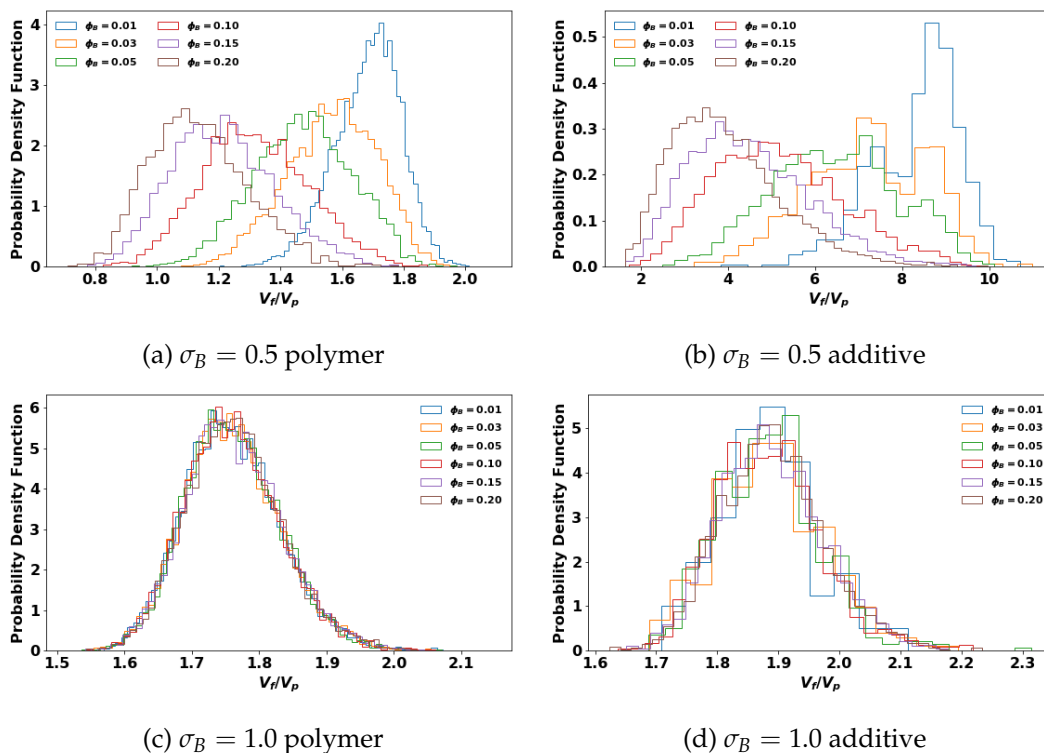


FIGURE 5.11: Probability density function of normalized Voronoi volume of (a) polymer beads at $\sigma_B = 0.5$ (b) additive beads at $\sigma_B = 0.5$ (c) polymer beads at $\sigma_B = 1.0$ (d) additive beads at $\sigma_B = 1.0$ for selected concentration. Each Voronoi volume (V_f) is normalized by that of its enclosed particle (V_p)

with other experimental and MD simulations studies.^{9,57} Using both all-atom MD simulation and experimental methods, Zhang et al.⁵⁷ studied the dependence of the Young's modulus on the fractional free volume in three kinds of epoxy matrices – diethylene toluene diamine (DETDA)/4,5-epoxycyclohexyl-1,2diglycidylidiformate(TDE85), single-walled carbon nanotube fortified with DETDA/TDE85, and m-phenylenediamine (MPD)/TDE85, with fractional free volume (FFV) of 15.64%, 14.45%, and 14.18% respectively. Both experimental and simulated results consistently showed that the Young's modulus increased with a reduction in FFV.

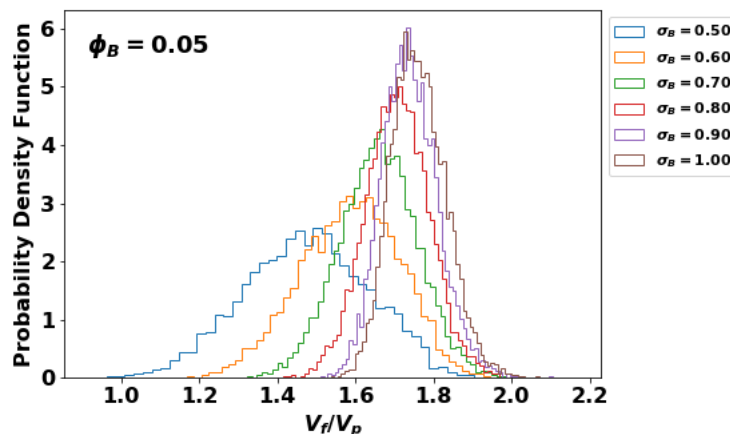


FIGURE 5.12: Probability density function of Voronoi volume at $\phi_B = 0.05$ for various bead sizes.

5.3.5 Rouse Mode Analysis

To gain insights into the phenomenological results reported in the section 5.3.1 to section 5.3.3, we carry out a Rouse mode analysis (RMA) on the chains. More specifically, we wanted to understand how the additives affect the segmental relaxation dynamics. Below, we give a short and non-exhaustive summary of the main conclusions of the RMA. The Rouse model treats the probe chain as a Gaussian chain and considers all its surrounding chains as a continuous viscous medium – i.e., a mean-field approach. Dynamics of each bead on the probe chain is described by the inertia-less Langevin equation.⁵⁸ For example, the equation of motion for the i -th bead is written as

$$\zeta \frac{d\vec{r}_i}{dt} = H_s [(\vec{r}_{i+1} - \vec{r}_i) - (\vec{r}_i - \vec{r}_{i-1})] + \vec{f}_i^r \quad (5.16)$$

where ζ is the monomeric friction coefficient, H_s is the spring constant, \vec{r}_i is the position of the i -th bead, and \vec{f}_i^r is the random force exerted on the i -th bead satisfying

$$\langle \vec{f}_i^r(t) \vec{f}_j^r(t') \rangle = 2\zeta k_B T \delta_{ij} \delta(t - t') \vec{\delta} \quad (5.17)$$

where $\delta(t)$ is the Dirac delta function, δ_{ij} is the Kronecker delta, and $\vec{\delta}$ is the identity tensor. Equation (5.16) shows that position coordinates of neighboring beads are coupled in their dynamics through spring forces. The RMA projects the original bead coordinates \vec{r}_i to a set of mutually orthogonal coordinates known as Rouse modes or normal coordinates \vec{X}_p ($p = 0, 1, \dots, N - 1$). We adopt the original form of projection by Rouse⁵⁹

$$\vec{X}_p \equiv \sqrt{\frac{2}{N}} \sum_{n=1}^N \vec{r}_n(t) \cos\left(\frac{(i - 1/2)p\pi}{N}\right) \quad (5.18)$$

$(p = 0, 1, 2, \dots, N - 1)$

which is widely used in the literature.^{20,45,60–62} The $p = 0$ mode describes the motion of the center of mass of the chain and the other modes ($1 \leq p \leq N - 1$) describe the internal relaxations of sub-chains, or "blobs", of the size of N/p beads. Each of the transformed coordinate or Rouse mode \vec{X}_p follows Langevin dynamics with its own friction coefficient and random force. Importantly, relaxation of different modes is mutually independent. The autocorrelation function (ACF) of each $p > 1$ mode decays exponentially

$$\langle \vec{X}_p(t) \vec{X}_p(0) \rangle = \langle \vec{X}_p^2 \rangle \exp\left(-\frac{t}{\tau_p}\right) \quad (5.19)$$

with its own relaxation time τ_p given by

$$\tau_{p,Rouse}^{-1} = \frac{12k_B T}{\zeta b^2} \sin^2 \left(\frac{p\pi}{2N} \right) \quad (5.20)$$

where b^2 is the mean-square bond (spring) length. For leading modes with $p \lesssim N/5$, which describes the motions of larger segments with $N/p \gtrsim 5$ beads, eq. (5.20) can be approximated by⁵⁹

$$\tau_{p,Rouse} = \frac{\zeta b^2}{3\pi^2 k_B T} \left(\frac{N}{p} \right)^2. \quad (5.21)$$

The Rouse model is commonly used to describe the dynamics of unentangled polymer melts. With increasing chain length, topological constraints set in and relaxation dynamics changes. For entangled chains, we may still project the coordinates to \vec{X}_p using eq. (5.18) but the ACFs no longer follow simple exponential decay. A stretched exponential is often used instead^{18,61–64}

$$\langle \vec{X}_p(t) \vec{X}_p(0) \rangle = \langle \vec{X}_p^2 \rangle \exp \left[- \left(\frac{t}{\tau_p^*} \right)^{\beta_p} \right] \quad (5.22)$$

where τ_p^* and β_p are the time scale and exponent (stretching parameter) for the p -th mode. The relaxation time of a stretched exponential can be defined as

$$\tau_p \equiv \int_0^\infty \exp \left[- \left(\frac{t}{\tau_p^*} \right)^{\beta_p} \right] dt = \left(\frac{\tau_p^*}{\beta_p} \right) \Gamma \left(\frac{1}{\beta_p} \right) \quad (5.23)$$

where $\Gamma(x)$ is the gamma function. Note that at the simple exponential limit, i.e., $\beta_p \rightarrow 1$, the two time scales are the same $\tau_p = \tau_p^*$. In the reptation model,

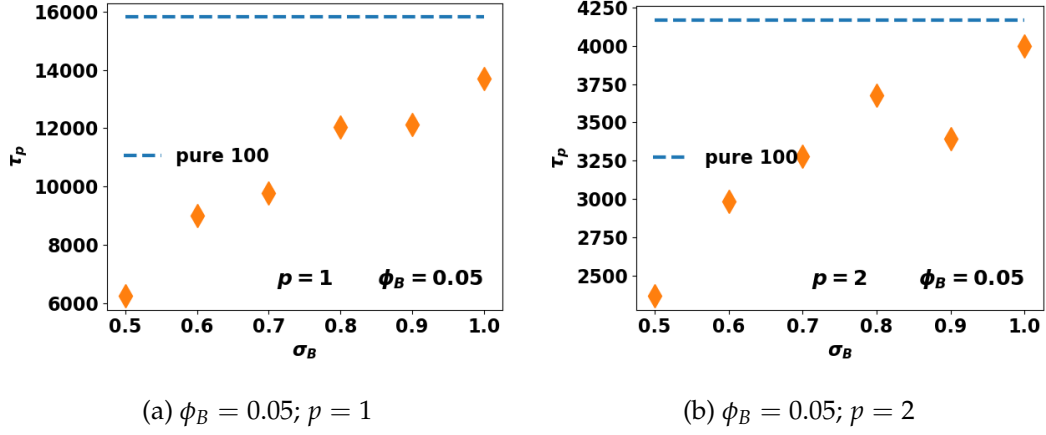


FIGURE 5.13: Rouse Mode Analysis of the polymer-additive mixture at $\phi_B = 0.05$ for various bead sizes.

the longest relaxation time is

$$\tau_{p, rept} = \frac{N^2 b^2}{p^2} \frac{\zeta}{\pi^2 k_B T} \frac{N}{N_e} \quad (5.24)$$

Our earlier work³⁰ on the dynamics and stress relaxation of polymer melts have shown that chain lengths $N \geq 100$ are much better described by the stretched exponential of eq. (5.22). We therefore used eq. (5.23) to determine the sub-segment relaxation time of the chains upon the addition of the additives. We show the relaxation time of the first two modes against the bead size at $\phi_B = 0.05$ in fig. 5.13. The relaxation time of the pure polymer is also included for comparison. It can be readily seen in fig. 5.13a for the $p = 1$ mode that the additives lower the relaxation time τ_p of the polymer. The smaller the bead size, the stronger the reduction in τ_p . Viscosity is strongly related to the relaxation time in polymers⁵³ and we note that viscosity follows a similar trend to τ_p . For the $p = 2$ mode, which signifies the relaxation of half-segments of the chain, the trend is also similar to the $p = 1$ mode.

The increase in relaxation time with additive size is also consistent with our observations for T_g even though our RMA was done at a temperature of 1.0. The glass transition phenomenon is observed when the characteristic timescale that defines the relaxation of the molecules with respect to each other far exceeds the observation timescale.¹⁶ According to the empirical Vogel-Fulcher law,^{16,65} it is expected that the relaxation time will continue to increase as the temperature is lowered. This suggests that the dynamics governing the glass transition phenomenon is similar to viscoelasticity.

As stated earlier on the decorrelation of Young's modulus with viscosity, it also follows that the nature of the dynamics in the viscoelastic measurements is rather different from that of the Young's modulus given the decrease in Y with increasing additive size. Temperature dependence of these measures could also be a factor in this decorrelation. Riggleman et al.¹³ had earlier reported a surprising dependence of the Young's modulus on temperature where antiplastitized and pure polymer had similar Y values close to the T_g despite a ~ 1.6 -factor difference at a lower temperature of 0.1. The relaxation times of higher p-modes may shed some light on the relationship between τ_p of the smaller segments of the chain and Y since Young's modulus is defined in the limit of small deformation and at short times. However, our previous work³⁰ on the relaxation times at higher p-modes indicate a departure of small-scale segmental relaxation from Rouse model due to differences between the KG chain and the Gaussian chain model of the Rouse model, specifically, the neglect of excluded volume interactions in the Rouse model which is important at smaller length scales. Furthermore, at intermediate p-modes of 5–10, if eq. (5.24) – (τ_1/p^2) is

used, we would obtain the same dependence where the relaxation time still increases with additive size.

5.3.6 Mean Square Displacement

We studied the mobility of the polymer chains and in the mixtures by calculating the mean square displacement of the center of mass of the chains

$$g_3(t) \equiv \langle [\vec{r}_{i,c.m.}(t) - \vec{r}_{i,c.m.}(0)]^2 \rangle \quad (5.25)$$

where

$$\vec{r}_{i,c.m.}(t) = \frac{1}{N} \sum_1^N \vec{r}_{i,j}(t) \quad (5.26)$$

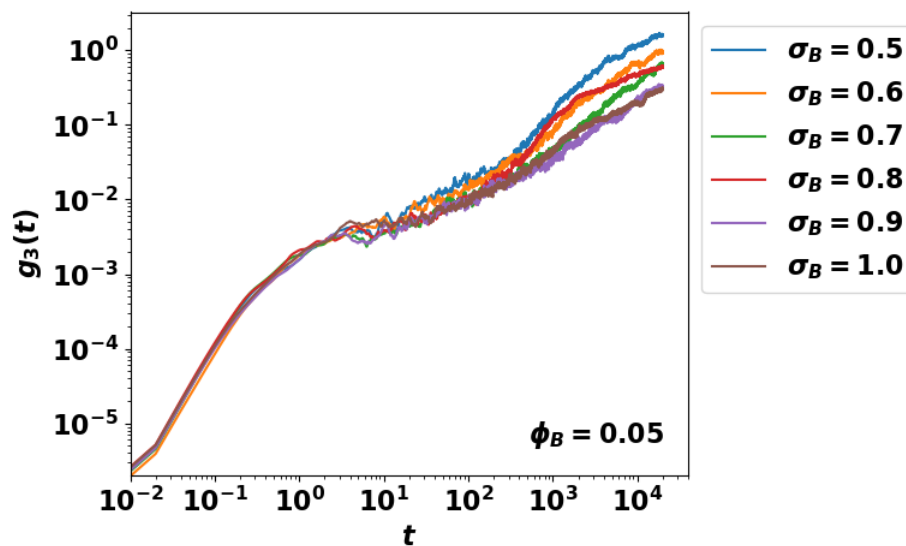
N is the length of the chain, $\vec{r}_{i,j}(t)$ is the position of each monomer and $\vec{r}_{i,c.m.}(t)$ is the position of the center of mass for each chain.^{47,66} The dynamics of the plasticizer additives was calculated using

$$g_p(t) \equiv \langle [\vec{r}_i(t) - \vec{r}_i(0)]^2 \rangle \quad (5.27)$$

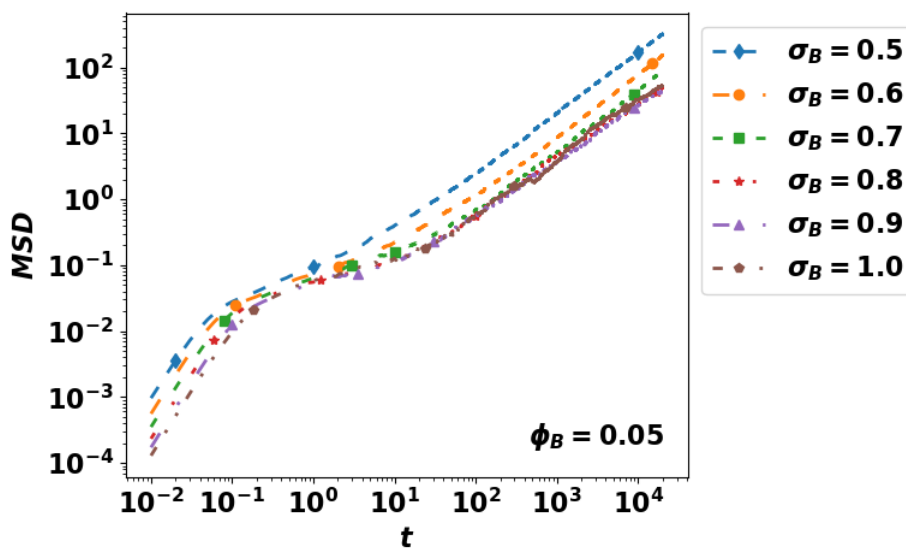
where $\vec{r}_i(t)$ is the coordinate of each additive. For the results presented here, we ran MD in NVT ensemble for a total time 2×10^5 TUs at $T = 0.4$ and 1×10^7 TUs at $T = 1.0$. At a low temperature of 0.4, lower than the T_g of the pure polymer, the $g_3(t)$ curve shows dynamics that are typical in the glassy regime. At early times, all the curves start out strongly overlapping one another. The dynamics here is superdiffusive and the slope of $\log g_3(t)$ vs $\log t$ is greater than 1. At intermediate times around $\mathcal{O}(10^1)$, there is a plateau region, where neighboring

atoms dynamically arrest other atoms and only localized segmental motion is permitted (caging effect).^{7,67} At later times, the curves again start to separate. Amid the fluctuations, we notice a general trend of the curves going down with increasing additive size, indicating the relaxation time is faster as the additive size decreases. This is also consistent with the results from RMA where the relaxation time increases with increasing additive size. It then suggests that the nature of the dynamics in T_g and $G(t)$ are similar. As also noted by Li et al.⁷ when comparing the dynamics of pure PVC and plasticized PVC near the glass transition zone, we observe that the dynamics of the different curves are practically indistinguishable in the caging zone which again challenges the free volume theory that the additives create more space between the chains.

Figure 5.14b shows the MSD for the plasticizer additives at the different sizes. There is a clear dependence of the dynamics on the additive size even at the early times. The dynamics of the different additives slows down with increasing additive size. The time spent in the plateau region (caging zone) by the additives before escaping and transitioning into the diffusive zone decreases with increasing additive size. It should be noted that the temperature used here is 0.4. Since the smallest additives are better at depressing the T_g , therefore it is not surprising that they have higher mobility. The dynamics are different at higher temperatures. Figure 5.15a shows the $g_3(t)$ of the polymer chains in the mixtures with the different additive bead sizes at $\phi_B = 0.05$ and temperature $T = 1.0$. All the curves strongly overlap and are practically indistinguishable from one another. The differences in the mobility of the chains appears small and are subsumed in the log scale plots. Plotting the same results on a linear scale tells



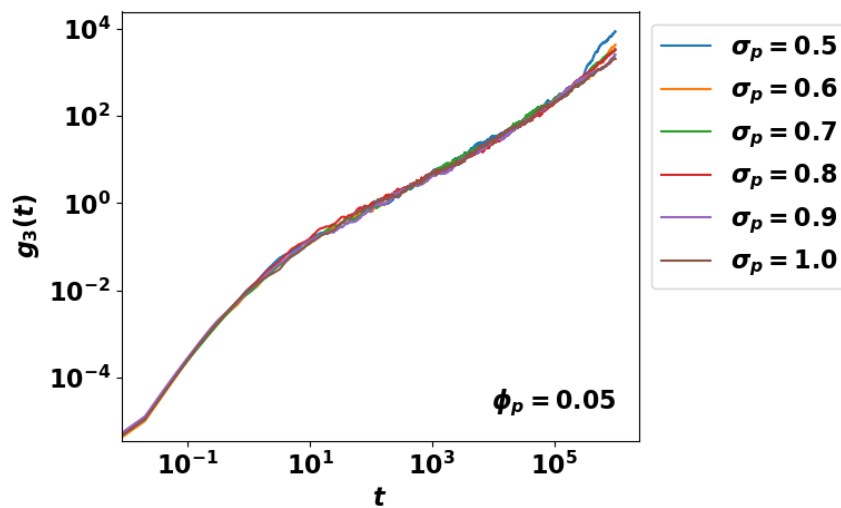
(a) Polymer MSD.



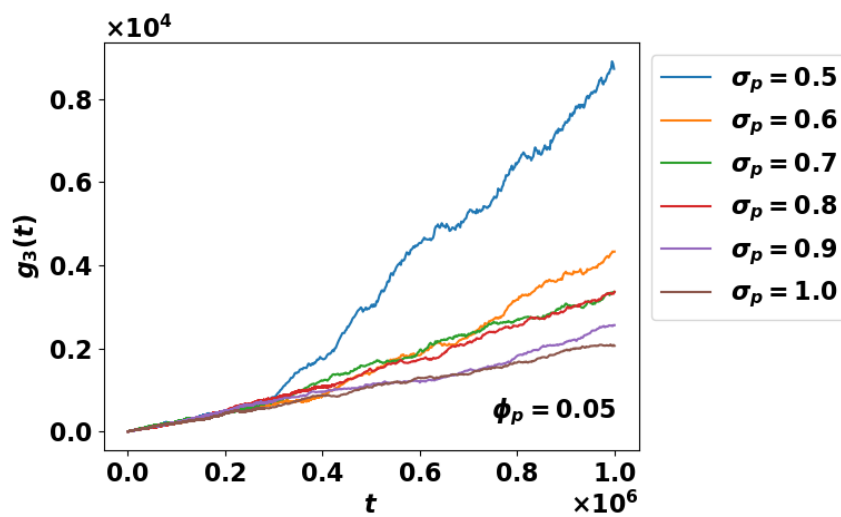
(b) Plasticizer MSD.

FIGURE 5.14: Mean square displacement of (a) the polymer chains, (b) the plasticizer additives at $T = 0.4$

a different story as shown in fig. 5.15b. At early to intermediate times, the plots again are indistinguishable from one another. However, at $t \sim \mathcal{O}(3 \times 10^5)$, all the curves begin to separate, with $\sigma_B = 0.5$ having the highest mobility and the largest bead size, $\sigma_B = 1.0$ the least. In general, the dynamics increase with decreasing bead sizes. There is however an overlap between $\sigma_B = 0.7$ and $\sigma_B = 0.8$ at these later times. This general trend is consistent with our earlier RMA results where the relaxation time of the chains decrease with decreasing bead size of the additives. This is also similar to our earlier work³⁰ comparing the effect of short chain lengths on the dynamics of long entangled chains. In that work we observed that the shorter chains sped up the dynamics of the longer chains and the effect became stronger with decreasing chain length of the shorter chains.



(a) $g_3(t)$ at $T = 1.0$ (log-log coordinates)



(b) $g_3(t)$ at $T = 1.0$ (linear coordinates)

FIGURE 5.15: Mean square displacement $g_3(t)$ of the polymer in the polymer-additive mixture at $T = 1.0$.

5.4 Conclusion

In this work, we have explored the effects of molecular structure of a polymer additive on key plasticization markers such as the glass transition temperature, Young's modulus, and on the linear viscoelasticity of the polymer mixture. We used LJ particles as the additive and varied the size σ_B from 0.5 to 1.0. The mass of each bead m_B varied as the cube of the size of the bead.

Compared with the pure polymer, our glass transition results show that the smaller-sized particles ($\sigma_B \leq 0.8$) are better at reducing the T_g of the pure polymers. The effect is stronger with increasing concentration until it gets to a critical concentration at $\sim 10\%$ mass fraction of the additive where there is a decrease in the efficiency of the smaller-sized particles at reducing T_g . The larger-sized additives however, are only marginally able to reduce the T_g at all the concentration studied. Calculation of the Young's modulus Y of the system also shows that the smaller-sized particles ($\sigma \leq 0.8$) increased the stiffness of the pure polymer – meaning that they serve as strong anti-plasticizing agents while the larger-sized particles led to a decrease in Y . The magnitude of the increase in Y for the antiplasticizers is a lot much higher than the reduction due to the larger-sized additive. Our viscoelasticity results revealed that the lowest bead size $\sigma_B = 0.5$ that we have studied showed atypical relaxation profile similar to a cross-linked polymer. While the other bead sizes $\sigma_B > 0.6$ lowered the viscosity relative to the pure polymer.

Our Rouse mode analysis revealed that the relaxation time of polymer chain decreases as the bead size decreases. We further explored the concept of free

volume available to the polymer beads by determining the Voronoi volume around each particle. Our results showed that the free volume is inadequate in explaining some observed features. For example, despite the increased free volume available to the larger-sized particles, they are worse at reducing T_g , which is contrary to the predictions. One of the most important takeaways from this study is the decorrelation of the various plasticization markers. We observe that a reduction in one property, for example, γ does not guarantee a decrease in the other property, like T_g or the zero-shear viscosity, η_0 .

References

- [1] K. Panchal. The Effects of Molecular Structure and Design on the Plasticizer Performance Through Coarse-Grained Molecular Simulation. Master's thesis. 2018.
- [2] K. F. Freed. The descent into glass formation in polymer fluids. *Accounts of chemical research* 44(3) (2011), 194–203.
- [3] G. Wypych. *Handbook of plasticizers*. ChemTec Publishing, 2004.
- [4] M. Kutz. *Applied plastics engineering handbook: processing and materials*. William Andrew, 2011.
- [5] P. H. Daniels. A brief overview of theories of PVC plasticization and methods used to evaluate PVC-plasticizer interaction. *Journal of vinyl and additive technology* 15(4) (2009), 219–223.
- [6] J. Gupta, C. Nunes, and S. Jonnalagadda. A molecular dynamics approach for predicting the glass transition temperature and plasticization effect in amorphous pharmaceuticals. *Molecular pharmaceutics* 10(11) (2013), 4136–4145.
- [7] D. Li et al. An atomistic evaluation of the compatibility and plasticization efficacy of phthalates in poly (vinyl chloride). *Macromolecules* 51(18) (2018), 6997–7012.
- [8] D. Li et al. Effects of molecular design parameters on plasticizer performance in poly (vinyl chloride): a comprehensive molecular simulation study (2021).

- [9] R. A. Riggleman, J. F. Douglas, and J. J. de Pablo. Tuning polymer melt fragility with antiplasticizer additives. *The Journal of chemical physics* 126(23) (2007), 234903.
- [10] J. H. Mangalara and D. S. Simmons. Tuning polymer glass formation behavior and mechanical properties with oligomeric diluents of varying stiffness. *ACS Macro Letters* 4(10) (2015), 1134–1138.
- [11] E. M. Zirdehi and F. Varnik. Non-monotonic effect of additive particle size on the glass transition in polymers. *The Journal of chemical physics* 150(2) (2019), 024903.
- [12] J. DeFelice and J. E. Lipson. The influence of additives on polymer matrix mobility and the glass transition. *Soft Matter* 17(2) (2021), 376–387.
- [13] R. A. Riggleman, J. F. Douglas, and J. J. de Pablo. Antiplasticization and the elastic properties of glass-forming polymer liquids. *Soft Matter* 6(2) (2010), 292–304.
- [14] M. H. Cohen and D. Turnbull. Molecular transport in liquids and glasses. *The Journal of Chemical Physics* 31(5) (1959), 1164–1169.
- [15] J. Jackle. Models of the glass transition. *Reports on Progress in Physics* 49(2) (1986), 171.
- [16] R. A. L. Jones. *Soft condensed matter*. Vol. 6. Oxford University Press, 2002.
- [17] R. P. White and J. E. Lipson. Polymer free volume and its connection to the glass transition. *Macromolecules* 49(11) (2016), 3987–4007.

- [18] Y. Li, M. Kröger, and W. K. Liu. Nanoparticle effect on the dynamics of polymer chains and their entanglement network. *Physical review letters* 109(11) (2012), 118001.
- [19] J. T. Kalathi, G. S. Grest, and S. K. Kumar. Universal viscosity behavior of polymer nanocomposites. *Physical review letters* 109(19) (2012), 198301.
- [20] J. T. Kalathi et al. Rouse mode analysis of chain relaxation in polymer nanocomposites. *Soft matter* 11(20) (2015), 4123–4132.
- [21] J. Shen et al. Revisiting stress–strain behavior and mechanical reinforcement of polymer nanocomposites from molecular dynamics simulations. *Physical Chemistry Chemical Physics* 22(29) (2020), 16760–16771.
- [22] R. A. A. Khan et al. A novel shift in the glass transition temperature of polymer nanocomposites: a molecular dynamics simulation study. *Physical Chemistry Chemical Physics* 23(21) (2021), 12216–12225.
- [23] J. T. Kalathi et al. Nanoparticle diffusion in polymer nanocomposites. *Physical review letters* 112(10) (2014), 108301.
- [24] R. A. Riggleman et al. Influence of confinement on the fragility of antiplasticized and pure polymer films. *Physical review letters* 97(4) (2006), 045502.
- [25] K. Kremer and G. S. Grest. Dynamics of entangled linear polymer melts: A molecular-dynamics simulation. *The Journal of Chemical Physics* 92(8) (1990), 5057–5086.
- [26] S. Barsky. Molecular dynamics study of diffusion in bidisperse polymer melts. *The Journal of Chemical Physics* 112(7) (Feb. 2000), 3450–3456. ISSN: 0021-9606.

- [27] S. Shanbhag and Z. Wang. Molecular Simulation of Tracer Diffusion and Self-Diffusion in Entangled Polymers. *Macromolecules* 53(12) (2020), 4649–4658.
- [28] S. Zhang and L. Xi. Effects of precursor topology on polymer networks simulated with molecular dynamics. *Polymer* 116 (2017), 143–152.
- [29] G. S. Grest. *Communication: Polymer entanglement dynamics: Role of attractive interactions*. 2016.
- [30] O. Adeyemi, S. Zhu, and L. Xi. Dynamics and stress relaxation of bidisperse polymer melts with unentangled and moderately entangled chains. *Physics of Fluids* 33(6) (2021), 063105.
- [31] S. Plimpton. *Fast parallel algorithms for short-range molecular dynamics*. Tech. rep. Sandia National Labs., Albuquerque, NM (United States), 1993.
- [32] Y. R. Sliozberg and J. W. Andzelm. Fast protocol for equilibration of entangled and branched polymer chains. *Chemical Physics Letters* 523 (2012), 139–143.
- [33] J.-L. Barrat, J. Baschnagel, and A. Lyulin. Molecular dynamics simulations of glassy polymers. *Soft Matter* 6(15) (2010), 3430–3446.
- [34] J.-L. Barrat and M. L. Klein. Molecular dynamics simulations of supercooled liquids near the glass transition. *Annual Review of Physical Chemistry* 42(1) (1991), 23–53.
- [35] K. Binder. *Monte Carlo and molecular dynamics simulations in polymer science*. Oxford University Press, 1995.

- [36] S. Nosé and F. Yonezawa. Isobaric-isothermal molecular dynamics study on the glass transition of a Lennard-Jones system. *Solid state communications* 56(12) (1985), 1005–1008.
- [37] S. Nosé and F. Yonezawa. Isothermal–isobaric computer simulations of melting and crystallization of a Lennard-Jones system. *The Journal of chemical physics* 84(3) (1986), 1803–1814.
- [38] J. A. Forrest and K. Dalnoki-Veress. The glass transition in thin polymer films. *Advances in Colloid and Interface Science* 94(1-3) (2001), 167–195.
- [39] L. Berthier and G. Tarjus. Critical test of the mode-coupling theory of the glass transition. *Physical Review E* 82(3) (2010), 031502.
- [40] W. Kob and H. C. Andersen. Testing mode-coupling theory for a supercooled binary Lennard-Jones mixture. II. Intermediate scattering function and dynamic susceptibility. *Physical Review E* 52(4) (1995), 4134.
- [41] D. Li, H. Xu, and J. Wittmer. Glass transition of two-dimensional 80–20 Kob–Andersen model at constant pressure. *Journal of Physics: Condensed Matter* 28(4) (2016), 045101.
- [42] F. M. Capaldi, M. C. Boyce, and G. C. Rutledge. Enhanced mobility accompanies the active deformation of a glassy amorphous polymer. *Physical review letters* 89(17) (2002), 175505.
- [43] D. Hossain et al. Molecular dynamics simulations of deformation mechanisms of amorphous polyethylene. *Polymer* 51(25) (2010), 6071–6083.
- [44] S. Sen, S. K. Kumar, and P. Koblinski. Viscoelastic properties of polymer melts from equilibrium molecular dynamics simulations. *Macromolecules* 38(3) (2005), 650–653.

- [45] M. Vladkov and J.-L. Barrat. Linear and nonlinear viscoelasticity of a model unentangled polymer melt: molecular dynamics and rouse modes analysis. *Macromolecular theory and simulations* 15(3) (2006), 252–262.
- [46] A. E. Likhtman, S. K. Sukumaran, and J. Ramirez. Linear viscoelasticity from molecular dynamics simulation of entangled polymers. *Macromolecules* 40(18) (2007), 6748–6757. ISSN: 00249297.
- [47] H. P. Hsu and K. Kremer. Static and dynamic properties of large polymer melts in equilibrium. *Journal of Chemical Physics* 144(15) (2016), 154907. ISSN: 00219606.
- [48] J. Ramirez et al. Efficient on the fly calculation of time correlation functions in computer simulations. *The Journal of chemical physics* 133(15) (2010), 154103.
- [49] J. M. Dealy, D. J. Read, and R. G. Larson. *Structure and rheology of molten polymers: from structure to flow behavior and back again*. Carl Hanser Verlag GmbH Co KG, 2018.
- [50] M. Doi and S. F. Edwards. *The theory of polymer dynamics*. Vol. 73. oxford university press, 1988.
- [51] L. Xi. Molecular simulation for predicting the rheological properties of polymer melts. *Molecular Simulation* 45(14-15) (2019), 1242–1264.
- [52] M. Kröger and S. Hess. Rheological evidence for a dynamical crossover in polymer melts via nonequilibrium molecular dynamics. *Physical review letters* 85(5) (2000), 1128.
- [53] M. Rubinstein, R. H. Colby, et al. *Polymer physics*. Vol. 23. Oxford university press New York, 2003.

- [54] G. Voronoi. Nouvelles applications des paramètres continus à la théorie des formes quadratiques. Deuxième mémoire. Recherches sur les paralléloèdres primitifs. *Journal für die reine und angewandte Mathematik (Crelles Journal)* 1908(134) (1908), 198–287.
- [55] C. Rycroft. *Voro++: A three-dimensional Voronoi cell library in C++*. Tech. rep. Lawrence Berkeley National Lab.(LBNL), Berkeley, CA (United States), 2009.
- [56] F. W. Starr et al. What do we learn from the local geometry of glass-forming liquids? *Physical review letters* 89(12) (2002), 125501.
- [57] W. Zhang et al. Mechanism of modulus improvement for epoxy resin matrices: A molecular dynamics simulation. *Reactive and Functional Polymers* 111 (2017), 60–67.
- [58] M. Doi et al. Dynamics of polymers in polydisperse melts. *Macromolecules* 20(8) (1987), 1900–1906.
- [59] P. E. Rouse Jr. A theory of the linear viscoelastic properties of dilute solutions of coiling polymers. *The Journal of Chemical Physics* 21(7) (1953), 1272–1280.
- [60] P. H. Verdier. Monte Carlo Studies of Lattice-Model Polymer Chains. I. Correlation Functions in the Statistical-Bead Model. *The Journal of Chemical Physics* 45(6) (1966), 2118–2121.
- [61] J. S. Shaffer. Effects of chain topology on polymer dynamics: Configurational relaxation in polymer melts. *The Journal of chemical physics* 103(2) (1995), 761–772.

- [62] A. Kopf, B. Dünweg, and W. Paul. Dynamics of polymer "isotope" mixtures: Molecular dynamics simulation and Rouse model analysis. *Journal of Chemical Physics* 107(17) (1997), 6945–6955. ISSN: 00219606.
- [63] J. Padding and W. J. Briels. Uncrossability constraints in mesoscopic polymer melt simulations: non-Rouse behavior of C₁₂₀H₂₄₂. *The Journal of Chemical Physics* 115(6) (2001), 2846–2859.
- [64] J. T. Kalathi et al. Rouse mode analysis of chain relaxation in homopolymer melts. *Macromolecules* 47(19) (2014), 6925–6931. ISSN: 15205835.
- [65] J. D. Ferry. *Viscoelastic properties of polymers*. John Wiley & Sons, 1980.
- [66] K. Kremer and G. S. Grest. Simulations for structural and dynamic properties of dense polymer systems. *Journal of the Chemical Society, Faraday Transactions* 88(13) (1992), 1707–1717.
- [67] G. D. Smith and D. Bedrov. Relationship between the α - and β -relaxation processes in amorphous polymers: Insight from atomistic molecular dynamics simulations of 1, 4-polybutadiene melts and blends. *Journal of Polymer Science Part B: Polymer Physics* 45(6) (2007), 627–643.

Chapter 6

Polymer-plasticizer mixtures with more realistic plasticizer models

This chapter is a continuation of Chapter 5. We expand our discussion on the single-bead molecular models of plasticizers to multi-bead models that mimic real plasticizers. Our goal is to develop model plasticizers that are fully miscible with the polymer and also have plasticization effects. It turned out that this attempt is non-trivial. We tuned these multi-bead models by exploring different parameters such as the energy interaction parameter between the host polymer and plasticizers, positions of attractive anchor beads within the plasticizers to prevent phase separation, and the length of the non-polar legs. Most of the models we tried are not compatible with the polymers – resulting in separation of the mixture into different phases while a few were compatible at high interaction energy between the polymers and plasticizers. We further quantified phase separation by determining the radial distribution function of the polymer-plasticizer mixtures and examined the temperature dependence of the

phase separation tendency of some select models. In continuation of the overall theme of this thesis, we explored the linear viscoelasticity of the miscible mixtures. By calculating the viscosity of the model systems, our simulations showed that the models we have tried show limited plasticization effects.

I developed the models, set up the simulations, analyzed the results, and wrote the draft. Li Xi made comprehensive recommendations, edited the draft, and supervised the whole research.

This chapter is **under preparation** for future publication.

6.1 Introduction

Plasticizers play a huge role in the polymer industry. Among other things, they are used to soften the polymeric material, impart flexibility and pliability, and improve the rheological properties of the polymer during processing.^{1,2} Indeed, their uses are numerous and the *plasticizer* term can mean different things – which often depends on the thermophysical properties (e.g. glass transition temperature T_g , Young's modulus Y_m) the plasticizers are being used to modify. Loosely speaking, any substance capable of softening any material can be regarded as plasticizers. For example, adding water to clay to make it more pliable. However, the bulk of industrial plasticizers used in the polymer industry are more *restrictive* in their molecular make-up. Most notably, phthalates, which are the most popular class of plasticizers in the poly(vinylchloride) (PVC) market, and accounting for over 90% of the market share,³ are dialkyl esters of phthalic acid, containing a strong polar core with non-polar alkyl chain legs.

Despite how ubiquitous plasticizer usage is in the polymer industry, there is a significant gap in our understanding of the plasticization mechanisms, especially their structure-property relationships. Many of the theories that have been put forward – gel, lubricity, and free volume theories are mostly phenomenological and are somewhat insufficient in linking the molecular structure of the plasticizers to their plasticization capabilities.^{1,4} Experimentally, it is rather challenging to isolate the microscopic origin of the observed macroscopic plasticization effects, partly due to the disordered nature of polymers. This makes computer simulations an attractive alternative.

In molecular dynamics (MD) simulations, very few all-atom simulations – where all the atoms are explicitly modeled, have been used to study different aspects of the plasticization phenomena.⁵⁻⁷ One such investigation was carried out by Li et al.⁶ using an all-atom simulation where they compared the plasticization effects of some common phthalates on PVC. Their studies revealed that, compatibility with PVC worsened with an increase in the side chain length of phthalates having identical alkyl side chain configuration. Since plasticization is a multi-property attribute, which includes the rheological properties, exploring the viscoelastic response of plasticized polymers using an all-atom simulation would take several years using the fastest supercomputers due to the extensive time and length scales in polymer relaxation.^{8,9} There is also a significant effort being deployed in targeted molecular design of plasticizers¹⁰ especially so-called green plasticizers due to the toxicological and environmental concerns of short chain phthalates, thus underscoring the need for robust models capable of offering insights into the exact nature of the plasticization process.^{11,12}

In studying the plasticization phenomenon, the vast array of possible plasticizer choices makes experimentally iterating through the likely alternatives very daunting. Coarse-grained (CG) simulations where multiple atoms can be coarsened into a single bead are helpful in side-stepping the long relaxation times that are inherent in polymer dynamics, especially when the rheological properties which depends on the relaxation time are being studied. Few studies^{13–15} have used the CG approach to study the interaction between plasticizers and polymers. The plasticizers are usually modeled as single-bead molecular additives, and have provided unique insights into several aspects of the plasticization process – including the role of molecular packing and density variation in some observed properties like Y_m and T_g . Our studies on single-bead plasticizers reported in chapter 5 also showed a decorrelation of T_g and Y_m – where small-sized additives are better at reducing T_g but not Y_m while the larger-sized beads are better at lowering Y_m but not as effective at reducing T_g .

While the single-bead models are valuable for studying and understanding the phenomenology and fundamental physics of plasticization, they however are not realistic and can offer only limited insights into how the molecular structure of the plasticizer – including the chain length, stiffness, etc. contributes to the plasticization mechanism. The single-bead model is a very basic model devoid of some of the other relevant attributes of a plasticizer. Most industrial plasticizers such as Bis(2-ethylhexyl)phthalate (DEHP), Diisobutylphthalate (DIOP), Diisononylphthalate (DINP), and Diisodecylphthalate (DIDP) have long nonpolar alkyl legs with a strong repulsive behavior and an attractive polar core. The repulsive parts serve to isolate the interactions between polymer

segments and loosen their dynamics while the attractive parts slow down the interaction to help in the formation of a mixture.

Studies using multi-bead models that attempt to mimic the real structures of plasticizers are rather few. Most notably, Mangalara et al.¹⁶ used multi-bead oligomers to study the mechanical properties and glass formation behavior of polymers. The beads of the oligomers are half the size of the host polymer beads and the interaction between the beads of the oligomers are purely repulsive. While this is a much better improvement over the single-bead, it is still different from a real plasticizer especially accounting for the polarities of the different parts intrinsic to most plasticizers.

Lattice and off-lattice models are routinely employed in computer simulations to study different areas of polymer physics. For example, the bond fluctuation model^{9,17–20} is a noteworthy lattice algorithm used in Monte-Carlo simulations that have been used to study glass transition in polymers,²¹ bidisperse polymers,²² etc. When studying realistic dynamics however, MD simulations are preferred. Our intention here is similar in spirit to the famed off-lattice Kremer-Grest (KG) model²³ used in studying the generic dynamics of polymers. Among other things, the KG model has further aided our understanding of different aspects of polymer physics such as entanglement effects in dense polymer melts^{24–26} and the viscoelastic properties^{27–29} in polymers using MD simulations.

In this work, our goal is to develop a robust multi-bead model that is similar to real plasticizers to aid our understanding of the plasticization mechanism. Real plasticizers contain polar and non-polar groups for different purposes: non-polar groups break the polar-polar interactions between polymer segments while polar groups help maintain its compatibility with the polymer. We attempt to find a sweet spot that maximizes plasticization efficiency while maintaining compatibility. Firstly, we attempt to construct such model that remains compatible with polymer, after which the plasticization effects will be tested as done for the single-bead additive in chapter 5. As we show in the later sections, it turns out this process is non-trivial, especially due to compatibility issues between the plasticizers and polymers. This chapter is still work in progress and the remainder is structured as follows: we describe the polymer and plasticizer models in section 6.2.1. We then discuss the compatibility of the polymer-plasticizer mixture in section 6.3.1, the temperature dependency in section 6.3.2, and the linear viscoelasticity properties of the mixtures in section 6.3.3.

6.2 Models and Methods

6.2.1 Polymer Model and Simulation Procedure

Each polymer chain is represented using a bead-spring chain model²³ where the beads B , are the monomers of the polymer chain and the springs represent the bonds between the monomers. The bonded beads interact using a finitely

extensible non-linear elastic (FENE) potential

$$U_{\text{FENE}}(r) = -\frac{1}{2}KR_0^2 \ln \left[1 - \left(\frac{r}{R_0} \right)^2 \right] + 4\epsilon \left[\left(\frac{\sigma}{r} \right)^{12} - \left(\frac{\sigma}{r} \right)^6 + \frac{1}{4} \right] \quad (6.1)$$

where r is the distance between the beads and σ and ϵ are the standard Lennard-Jones (LJ) length and energy parameters. The first term of the equation represents an attractive potential, and models the FENE springs between the closest neighbors along the chain with a maximum bond length $R_0 = 1.5\sigma$, while the second term models the excluded-volume repulsion between beads and the term is only included at $r \leq 2^{1/6}\sigma$. The spring constant $K = 30\epsilon/\sigma^2$ is chosen to allow a reasonable integration time step while preventing chains from crossing each other.²³ For the non-bonded beads, the interaction is modeled by the standard LJ potential

$$U_{\text{LJ}}(r) = 4\epsilon \left[\left(\frac{\sigma}{r} \right)^{12} - \left(\frac{\sigma}{r} \right)^6 \right]. \quad (6.2)$$

The potential is truncated at $r = 2.5\sigma$ and shifted by a constant to ensure continuity at the cutoff. The non-dimensional LJ energy and length parameters are set at $\epsilon = 1$ and $\sigma = 1$. We use a polymer chain length $N = 25$ for all the simulations and the mass of each of the polymer beads was kept at 1.

The plasticizer models we have tested consist of purely repulsive beads, R with an attractive middle torso, Y beads. To some degree, this is similar to nearly all plasticizers used in the PVC industry.¹⁰ For example, DEHP consists of a strong polar core in between a pair of nonpolar alkyl legs as shown in

fig. 6.1. The polar core of the DEHP is strongly attracted to the polar parts of the PVC chain. The nonpolar alkyl legs also interpose in between the strong polar-polar interactions of a PVC chain thereby weakening the strongly attractive PVC-PVC interactions. We similarly model this behavior using a model

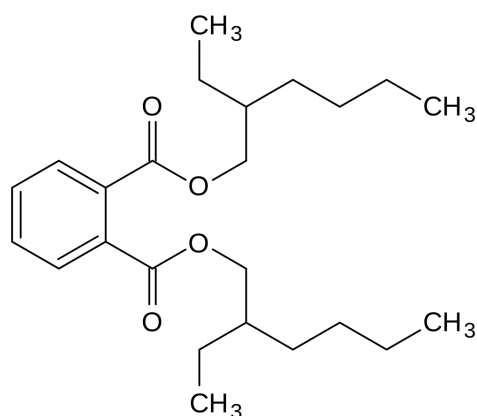


FIGURE 6.1: Chemical structure of Bis(2-ethylhexylphthalate) DEHP

with an attractive core sandwiched between two repulsive tails. A more general configuration of the models has the form given in fig. 6.2. The leg length is n , k is the length of the attractive "anchor" beads to enhance compatibility, and



FIGURE 6.2: Generic Plasticizer Model

m is the torso length. Bead Y has the same size dimension as the polymer B bead i.e. $\sigma_Y = 1$ and has a cutoff $r_c = 2.5$. We varied the interaction between the $B - Y$ beads by tuning ϵ_Y using 0.1, 0.3, 0.5, 1.0, 1.2, 1.5, 2.0, 3.0, 4.0, and 5.0. These ϵ values represent the range from weakly attractive to strongly attractive. We kept the r_c for the $B - R$ and $R - Y$ interaction at $2^{1/6}$ to ensure it is purely repulsive. As with the polymer beads, the bonded beads of the plasticizers also

interact using eq. (6.1) and the non-bonded beads with eq. (6.2). The interaction between the polymer and plasticizer beads are also governed by eq. (6.2). A summary of the plasticizer model configurations is given in table 6.1.

All the results are reported in reduced LJ units wherein the length, energy, time, and temperature are scaled by σ , ϵ , $\tau = \sqrt{m\sigma^2/\epsilon}$, and ϵ/k_B (k_B is the Boltzmann constant), respectively. The mass concentration ϕ_B of the model particles was kept at 15%. The total number of polymer and plasticizer particles was kept close to 10000 as much as possible. We performed all simulations us-

TABLE 6.1: Multi-bead model configuration of the form (R) n –(Y) k –(R) m –(Y) k –(R) n where n and m are the leg and torso length respectively

| Model | n | k | m | model structure |
|-------|---|---|---|-----------------------|
| A | 1 | 0 | 1 | R-Y-R-Y-R |
| B | 2 | 0 | 1 | R-R-Y-R-Y-R-R |
| C | 3 | 0 | 1 | R-R-R-Y-R-Y-R-R-R |
| D | 1 | 0 | 2 | R-Y-R-R-Y-R |
| E | 2 | 0 | 2 | R-R-Y-R-R-Y-R-R |
| F | 3 | 0 | 2 | R-R-R-Y-R-R-Y-R-R-R |
| G | 1 | 0 | 3 | R-Y-R-R-R-Y-R |
| H | 2 | 0 | 3 | R-R-Y-R-R-R-Y-R-R |
| I | 3 | 0 | 3 | R-R-R-Y-R-R-R-Y-R-R-R |
| J | 2 | 2 | 1 | R-R-Y-Y-R-Y-Y-R-R |

ing the Large-scale Atomic/Molecular Massively Parallel Simulator (LAMMPS) package.³⁰ We integrated the equation of motion using the velocity-Verlet algorithm with a timestep of $\Delta t = 0.01$ (in LJ units of TUs). For both polymer chains and the plasticizer chains, we generated their initial structures by arbitrarily packing the specified number of chains and particles into a cubic simulation cell. At this stage there was no distinction between the polymer chains and the

plasticizer chains. The individual chains were generated using a procedure similar to self-avoiding walk in a continuum space. This approach while preventing back-folding of the chains, still results in substantial overlaps of the chain beads. The mass of the chain beads and particles were set to 1 initially. We then equilibrate the mixture using a dissipative particle dynamics (DPD) push-off method of Sliozberg et al.³¹ For the duration of the DPD run, we replaced the interaction between non-bonding beads with a soft repulsive potential of the form of

$$U_{\text{DPD}}(r) = \begin{cases} \frac{A_{\text{DPD}}}{2} r_c \left(1 - \frac{r}{r_c}\right) & r < r_c \\ 0 & r \geq r_c \end{cases}. \quad (6.3)$$

This potential allows the chains to pass through each other and therefore enhances a quicker relaxation during the initial equilibration steps. We ran the DPD simulation at $T = 1.0$ using a cut-off distance $r_c = 1.0$. The potential was initially low and set at $A_{\text{DPD}} = 25$. At the beginning, restriction was imposed on the maximum distance each bead can move within one time step which gradually increases from 0.001 to 0.1 over 15 TUs. The restriction was then removed and the simulation was run for another 100 TUs. This was subsequently followed by a gradual ramp of A_{DPD} to 1000 over 5.5 TUs. The DPD potential was then replaced with the standard LJ potential and MD in an NVE ensemble was performed for additional 500 TUs during which a random velocity distribution was reassigned to all beads every 0.5 TUs. Finally, we further ran MD in an NVT ensemble for an additional 20 000 TUs to fully relax the system. Since the relaxation of the system is dependent on the relaxation time scale of the polymer

chains, running the simulation long enough to ensure the polymer chains have relaxed guarantees that our system is well equilibrated. Our earlier paper²⁹ shows the mean square internal displacement (MSID) results for the polymer chains studied where the MSID saturates to the characteristic ratio of the chain. After the relaxation, we flipped the plasticizer beads as desired to either R or Y beads, tuned ϵ_Y as desired, and ran MD in an NVT ensemble for 1000 TUs.

6.3 Results

Before the plasticization efficiency can be reliably determined, the compatibility of the plasticizers need to be tested to ensure the mixtures do not phase separate. Although the compatibility requirement between the components are driven primarily by processing needs i.e. the need to ensure the components are well blended together prior to processing, there is also the renewed concern of plasticizer loss from migration. Short-chain phthalates are particularly infamous for this migration. Indeed, trace amounts of plasticizers have been found in human blood due to plasticizer loss from packages into food products.³²⁻³⁴ We discuss two main aspects of compatibility here – (i) the phase separation: at the minimum the plasticizer should not separate from the polymer on the timescale of the simulation or experiment. We examined this by visual inspection³⁵ and by determining the radial distribution function $g(r)$ of the mixtures, (ii) and we also investigated the temperature dependence of the phase separation between the plasticizers and polymers.

6.3.1 Phase Separation

Given the molecular structures of the plasticizer and the interaction parameters between the polymer and the plasticizer, only a few of the plasticizer models we have tested are compatible with the polymer. Granted that given sufficient time, most plasticizers will eventually migrate out of the host polymer, it should be kept in mind that even with phthalates, the timescale of the migration is rather long. We ran a short MD simulation of 1000 TUs to test the compatibility of our plasticizers with the polymer. Viscoelastic measurements are typically done over a much longer timescale $\mathcal{O}(10^6 TU)$.²⁹ Therefore, at the minimum, the plasticizers should not separate until past the timescale for viscoelastic measurements. We examine the phase separation visually and analyze the structure of the mixture by computing the radial distribution function $g(r)$. The $g(r)$ gives the probability of finding a particle at a distance r from a reference particle.^{36,37} To begin, we show the visualization of a well-mixed polymer-plasticizer system in fig. 6.3. The well-mixed system was obtained prior to tuning the interaction between the plasticizers and polymers – at the stage when both of them were indistinguishable in their interaction. The plasticizers are well-dispersed within the host polymer without any apparent clustering of the plasticizer particles. We start with the models $A - C$ given in table 6.1. The models only differ in the length of the repulsive R legs while having another R bead sandwiched between two attractive Y beads. We varied the ϵ interaction between the B and Y beads. It should be noted that ϵ is a measure of how strongly the particles are attracted to each other. We tracked the evolution of the microstructure to

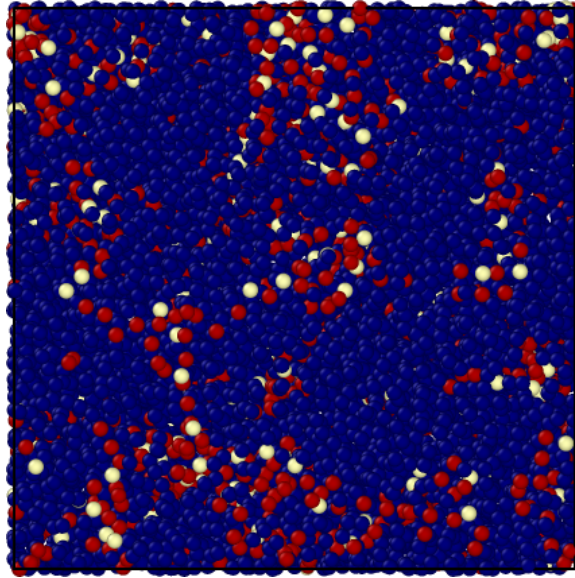


FIGURE 6.3: Visualization of a well-mixed polymer-plasticizer mixture prior to phase separation. The blue beads the polymer beads. The red and yellow beads make up the plasticizer beads. The yellow beads serve as attractive anchor points to enhance miscibility with the blue polymer beads.

ensure the system is at steady state by calculating the time-dependent coordination number (CN) using

$$CN_{BR} \equiv 4\pi\nu_R \int_0^{r_{min}} g_{BR}(r)r^2 dr \quad (6.4)$$

where ν_R is the domain-average number density of type R ; g_{BR} is the radial distribution function of the R beads around a reference particle B , and r_{min} delineates the edge of the first solvation shell and is the minimum position between the first two neighboring peaks in the $g_{BR}(r)$ profile. Representative plots of the CN are shown in fig. 6.4 for $\epsilon = 0.3, 1.2,$ and 4.0 . At a low ϵ value of 0.3 , the CN starts from a high value and instantaneously drops and fluctuates around a mean value – which indicates the evolution of the structure has reached a steady

state. At an intermediate ϵ value of 1.2 however, CN decays over a longer time period before eventually fluctuating around the mean. Finally, when ϵ is 4.0, the structure of the system is not changing as much. The CN indicates the average number of particles of type R around a central B atom. A high CN decaying to low CN shows that there is a reduction in the number of R beads surrounding the B beads and is a precursor for phase separation. These figures are typical for all the models and indicate all our systems have attained steady state. Representative snapshots at different ϵ for models A and C at the final time are shown in fig. 6.5 and fig. 6.6 respectively. For model A , we observe phase separation for ϵ up to 1.2, microphase separation at $\epsilon = 1.5$; where there are growing clusters of the plasticizer beads dispersed within the polymer beads, and miscibility for $\epsilon > 2$. For model C however, phase separation was observed at all values except at $\epsilon = 3.0 - 5.0$. The corresponding polymer-plasticizer $g(r)$ for the representative systems i.e. the probability of finding a plasticizer particle (either the R or Y beads) at a given distance r from a polymer particle are shown in fig. 6.7 and fig. 6.8 respectively. At low ϵ and 0 TU, fig. 6.7a shows that the $B - Y$ and the $B - R$ beads are rather uniformly distributed within the system. At 1000 TU however, the mixture has completely separated into two different phases as shown by the low peak of the $B - R$ and $B - Y$ curves compared to the start time. Due to the weak attraction between the $B - Y$ beads, the $B - Y$ curve is very similar to the $B - R$ curve, indicating that there is no obvious preference for the Y beads. Similarly, at $\epsilon = 1.2$ as shown in fig. 6.7b, although the $B - Y$ curve is slightly higher at 1000 TU, the attraction is still not sufficient to prevent a phase separation. On the other hand, at a higher ϵ value of 4.0, there is a distinct and much higher peak in the $B - Y$ curve in fig. 6.7c, showing that there

are more Y beads in the neighborhood of the B particles which prevents a phase separation of the mixture. Indeed, the $B - R$ line shows there are more plasticizer particles surrounding the polymer particles on average. Increasing the chain length of the repulsive legs in model C does not fundamentally change the nature of the system structure at low ϵ as fig. 6.8a and fig. 6.8b show. At higher ϵ however, there is a higher tendency for the plasticizers to stay away from the polymer beads due to the increasing R -leg length as can be seen in the reduced $B - R$ line in fig. 6.8c. The increased attraction between the B and Y beads also promotes their contact at the interface and forces the additional R legs inwards. A closer look at fig. 6.6c shows that there are more Y beads at the $B - Y$ interface resulting in a microphase separation where there are pockets of plasticizer clusters distributed within the polymer phase. The plasticizer chains are still somewhat dispersed within the mixture but the $R - Y$ cluster is increasing in size. It appears the Y beads create an outer covering for the R beads thus reducing their $B - R$ contact in what looks like an apparent micelle formation – where hydrophilic groups concentrate at the surface and the hydrophobic groups move inwards.³⁸

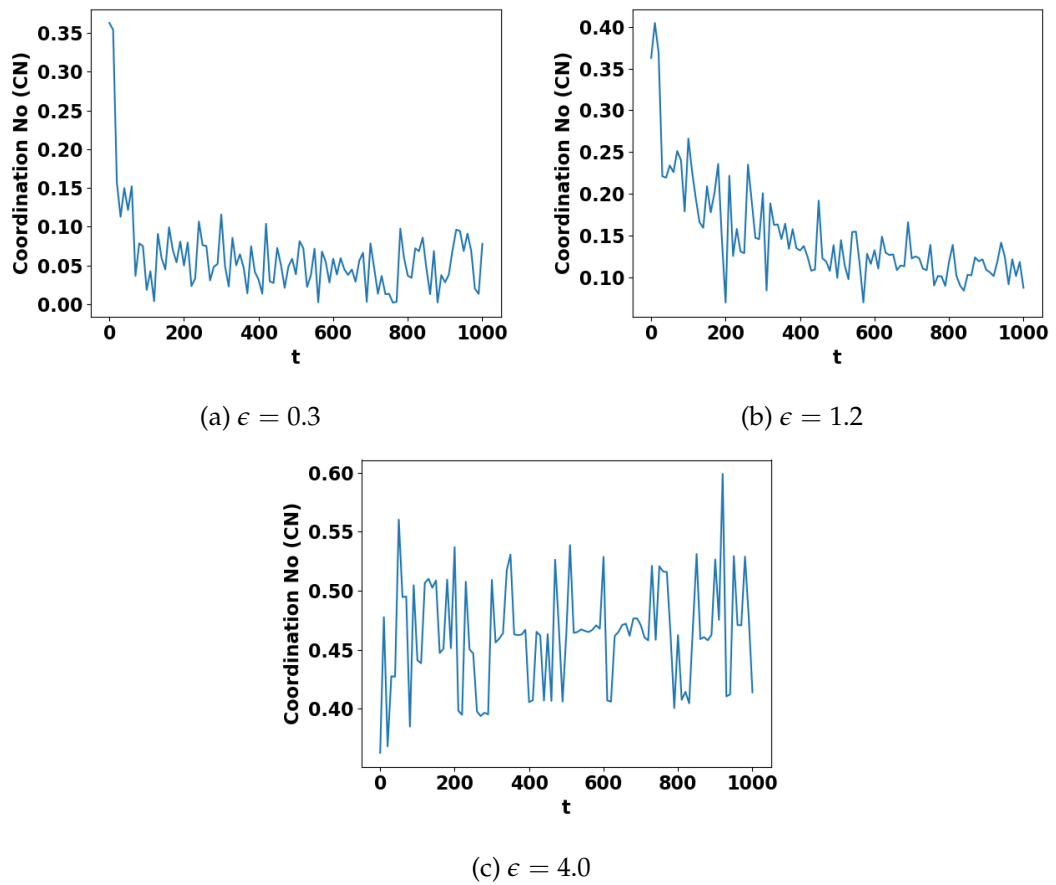


FIGURE 6.4: Time-dependent coordination number showing the evolution of the microstructure at $\epsilon = 0.3, 1.2,$ and 4.0 . These plots are typical for our systems and indicate the structure has reached a steady state.

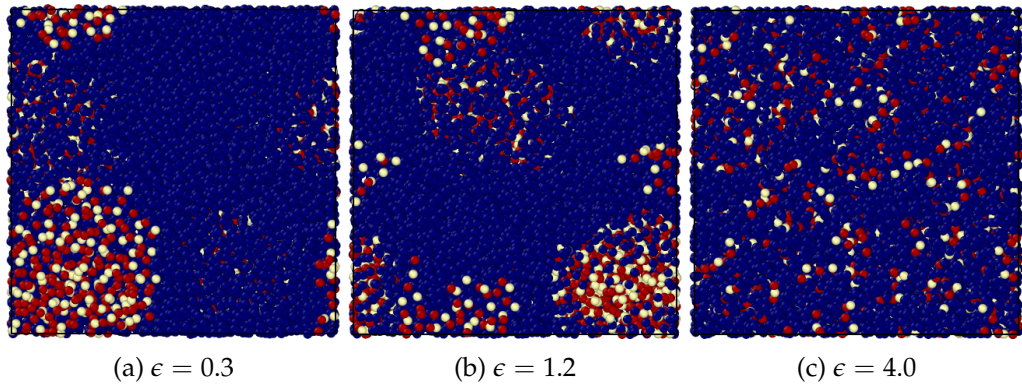


FIGURE 6.5: Model A. Phase separation and compatibility between the polymer and plasticizer beads at 100 TUs. The blue B and red R beads are the polymer and plasticizer beads respectively. The yellow beads (Y) are part of plasticizer beads and are tuned to make the plasticizer chain more attractive to the polymer chain. The figures are the ϵ interaction between the B and Y beads (a) $\epsilon = 0.3$ (phase separation), (b) $\epsilon = 1.2$ (phase separation), and (c) $\epsilon = 4.0$ (compatibility).

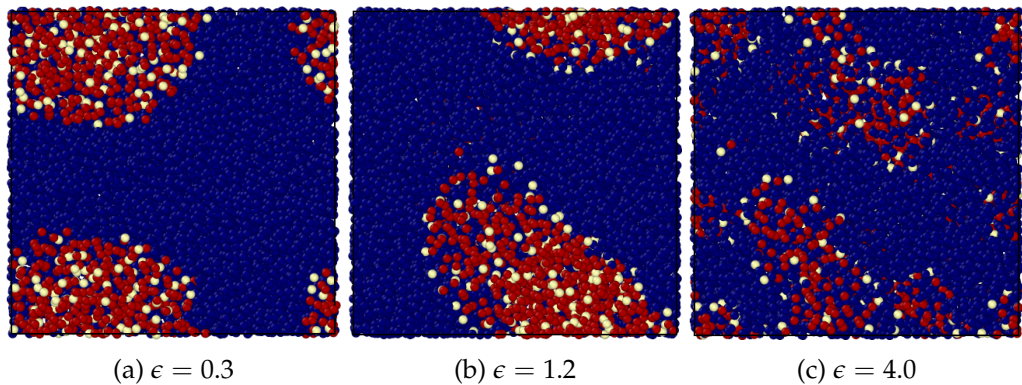


FIGURE 6.6: Model C. Phase separation and microphase separation between the polymer and plasticizer beads at 100 TUs. The blue B and red R beads are the polymer and plasticizer beads respectively. The yellow beads Y are part of plasticizer beads and are tuned to make the plasticizer chain more attractive to the polymer chain. The figures are the ϵ interaction between the B and Y beads (a) $\epsilon = 0.3$ (phase separation), (b) $\epsilon = 1.2$ (phase separation), and (c) $\epsilon = 4.0$ (microphase separation).

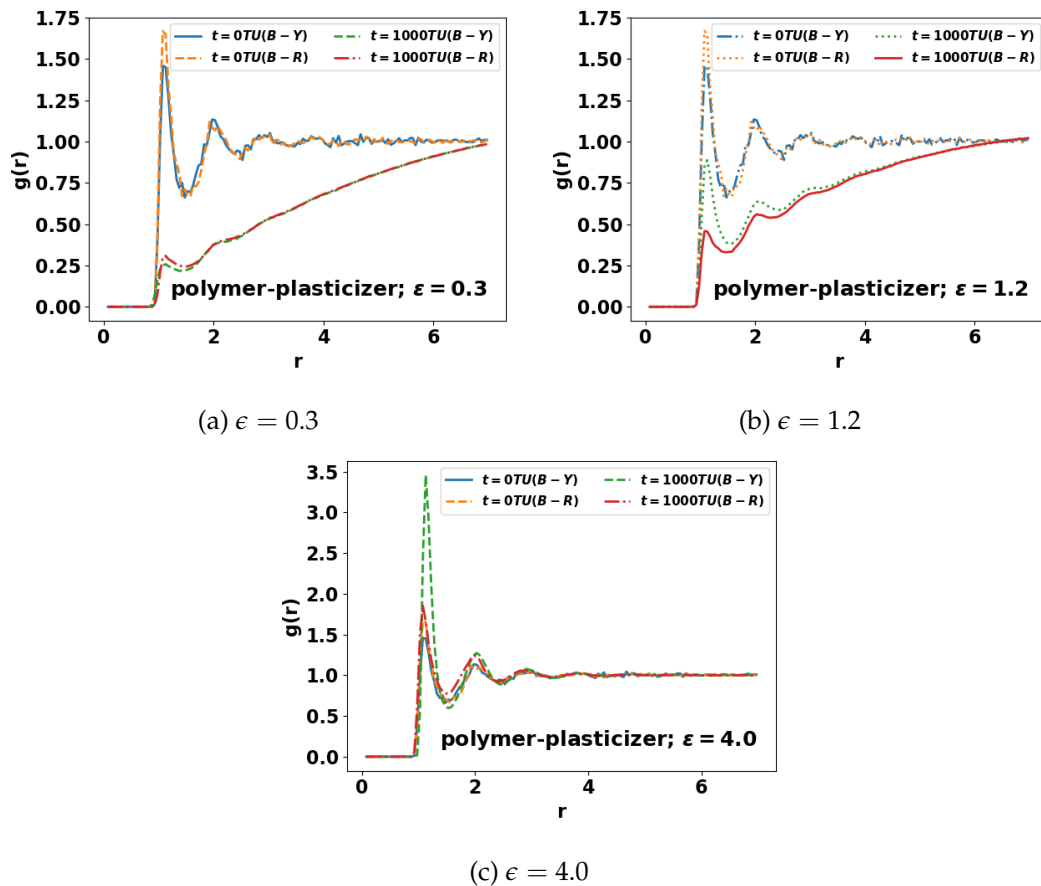


FIGURE 6.7: Radial distribution function $g(r)$ of model A, $R - Y - R - Y - R$. The figures are the ϵ interaction between the B and Y beads at (a) $\epsilon = 0.3$ (phase separation), (b) $\epsilon = 1.2$ (phase separation), and (c) $\epsilon = 4.0$ (compatibility)

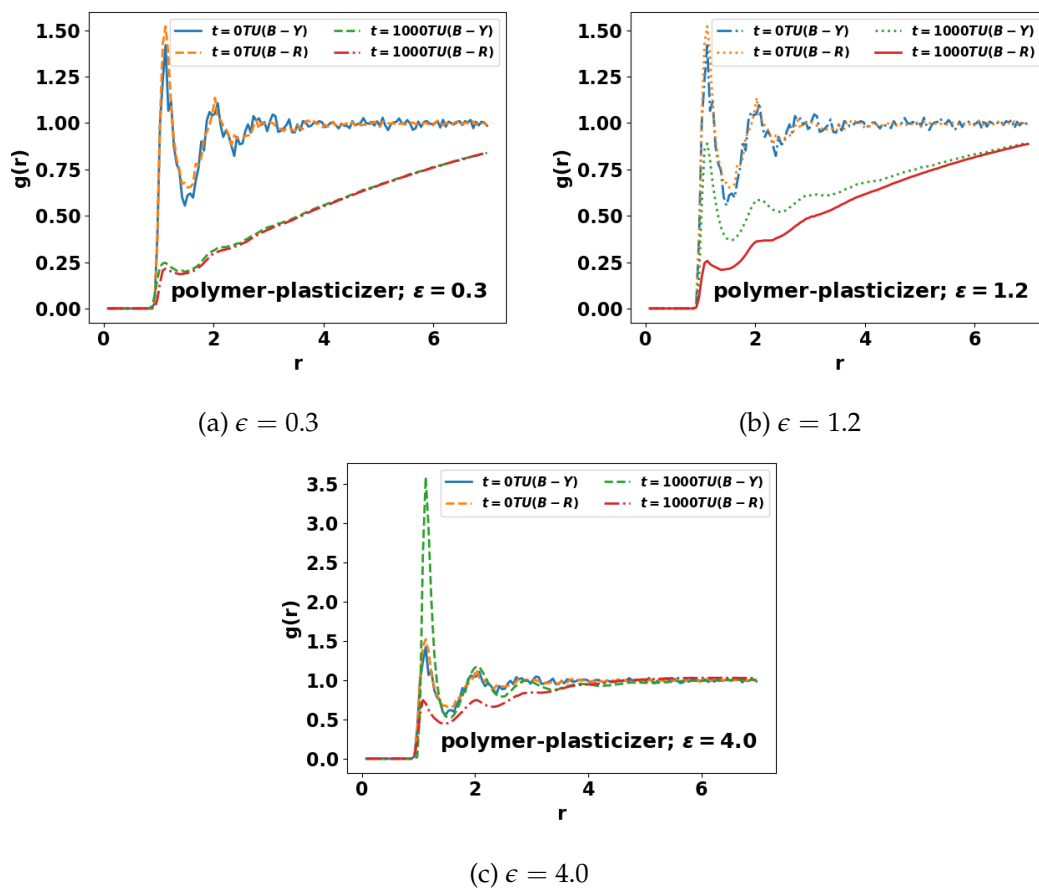


FIGURE 6.8: Radial distribution function $g(r)$ of model C, $R - R - R - Y - R - Y - R - R - R$. The figures are the ϵ interaction between the B and Y beads at (a) $\epsilon = 0.3$ (phase separation), (b) $\epsilon = 1.2$ (phase separation), and (c) $\epsilon = 4.0$ (microphase separation).

Models D – F wherein we have increased the middle R beads compared to models A – C tell a similar story as shown in fig. 6.9 and fig. 6.10. Here as well, the outer chain length of the R beads increases from D to F. At low ϵ values there is a distinct separation of the mixture into different phases which can be readily seen in fig. 6.11a and fig. 6.12a by the difference in the $B - R$ and $B - Y$ peaks at the start and end times. On increasing the ϵ to 3.0 however for model D, fig. 6.11b shows that there is a sizable number of both R and Y beads surrounding the B beads. In this case, the Y beads successfully act as anchors of attraction to prevent phase separation. Increasing the ϵ to a higher value of 5.0 in fig. 6.11c also results in a compatible system. In fig. 6.12b and fig. 6.12c, increasing the chain length also results in clustering of the plasticizer beads and a tendency towards a microphase separation. There is a distinct $B - Y$ peak, which is again due to the higher attraction between the $B - Y$ beads.

Further increasing the middle R beads in models G – I does not change the phase separation narrative at low ϵ value as shown in fig. 6.13a and fig. 6.14a. A low ϵ value of 0.1 shown in fig. 6.15a is consistent with earlier results showing phase separation at similar values. At an intermediate ϵ value of 2.0, fig. 6.15b shows a strong $B - Y$ attachment and a much lower $B - R$ peak, suggesting a microphase separation i.e., each plasticizer molecule still has to stay close to the interface with the polymer phase to enhance the $B - Y$ contact. A further increase in ϵ to 5.0 again in fig. 6.15c shows a well-mixed polymer-plasticizer mixture with Y beads serving as an anchor point of attraction between the B and Y beads as reflected in the $g(r)$ peak. Yet again, fig. 6.16a shows phase separation while fig. 6.16b and fig. 6.16c show that an increase in the outer R

legs results in poorer compatibility even at higher ϵ values.

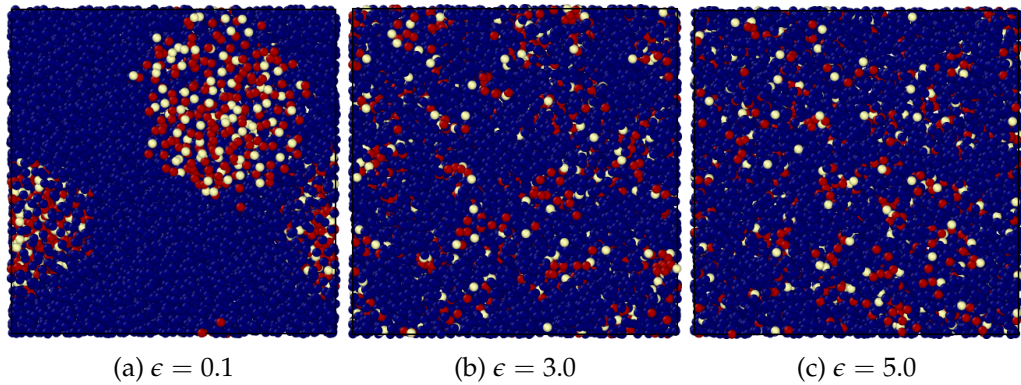


FIGURE 6.9: Model D. Phase separation and compatibility between the polymer and plasticizer beads at 100 TUs. The blue B and red R beads are the polymer and plasticizer beads respectively. The yellow beads (Y) are part of plasticizer beads and are tuned to make the plasticizer chain more attractive to the polymer chain. The figures are the ϵ interaction between the B and Y beads showing (a) $\epsilon = 0.1$ (phase separation), (b) $\epsilon = 3.0$ (compatibility), and (c) $\epsilon = 5.0$ (compatibility).

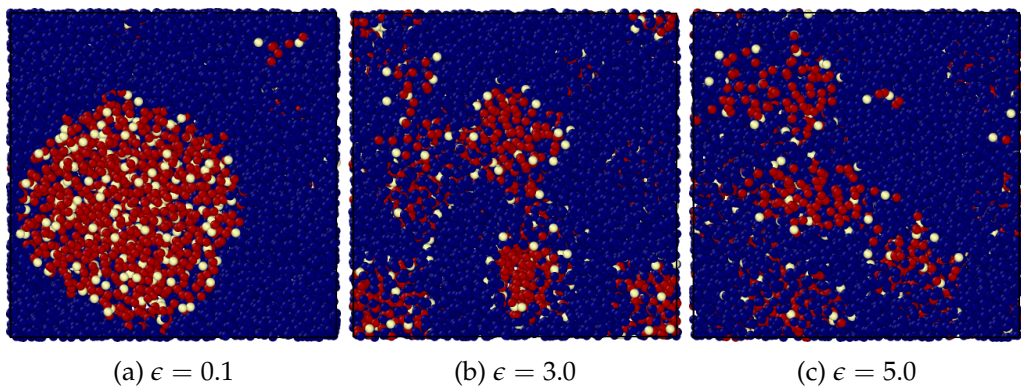


FIGURE 6.10: Model F. Phase separation and microphase separation between the polymer and plasticizer beads at 100 TUs. The blue B and red R beads are the polymer and plasticizer beads respectively. The yellow beads Y are part of plasticizer beads and are tuned to make the plasticizer chain more attractive to the polymer chain. The figures are the ϵ interaction between the B and Y beads (a) $\epsilon = 0.1$ (phase separation), (b) $\epsilon = 3.0$ (microphase separation), and (c) $\epsilon = 5.0$ (microphase separation).

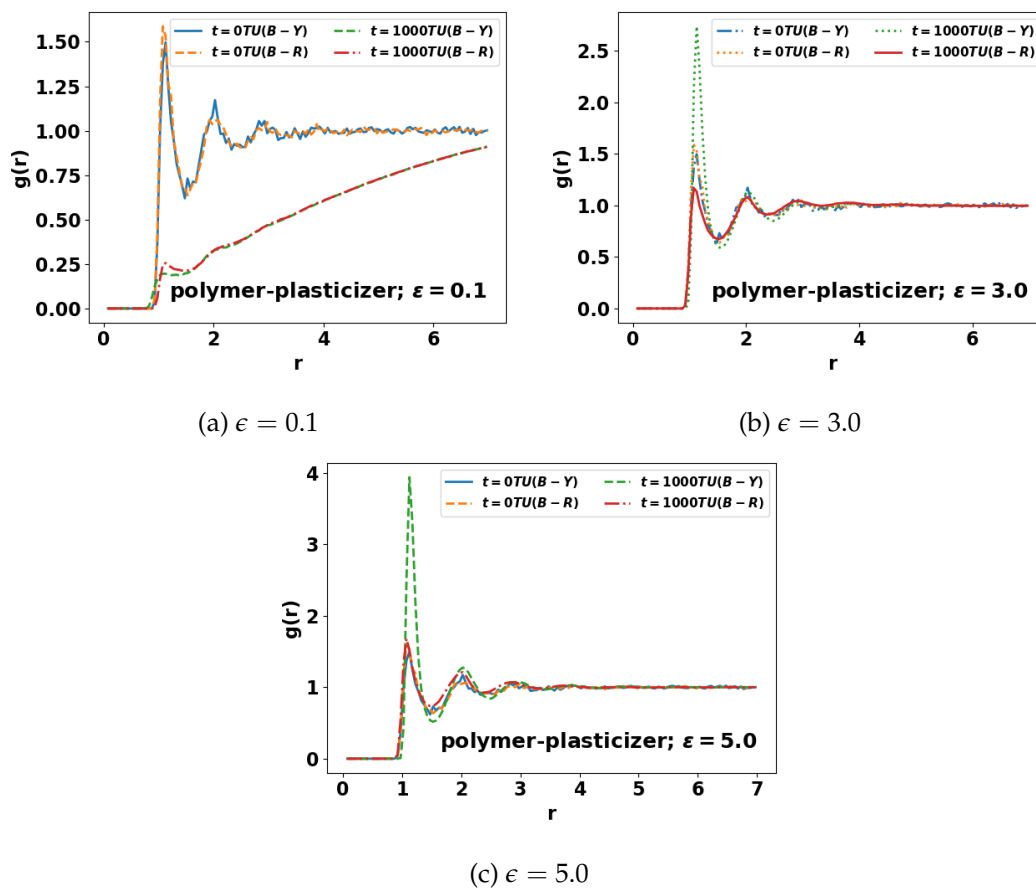


FIGURE 6.11: Radial distribution function for model D. The figures are the ϵ interaction between the B and Y beads (a) $\epsilon = 0.1$ (phase separation), (b) $\epsilon = 3.0$ (compatibility), and (c) $\epsilon = 5.0$ (compatibility)

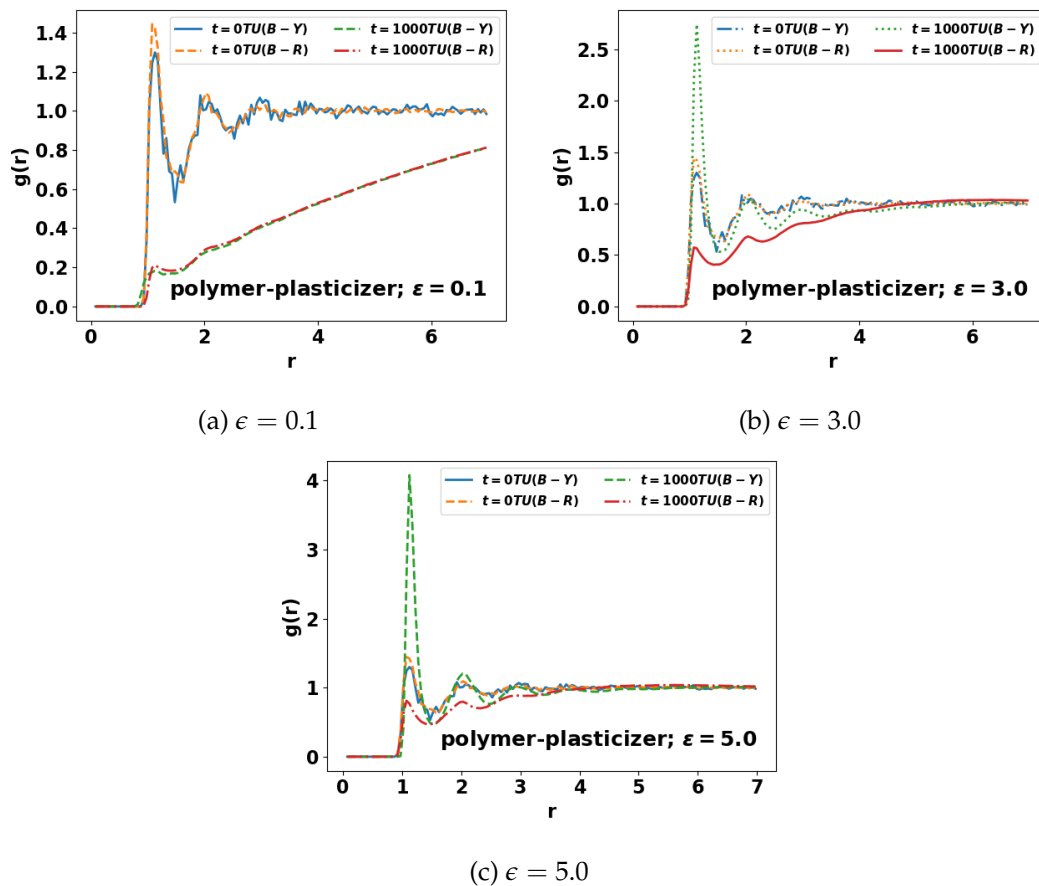


FIGURE 6.12: Radial distribution function for model F. The figures are the ϵ interaction between the (B) and (Y) beads (a) $\epsilon = 0.1$ (phase separation), (b) $\epsilon = 3.0$ (microphase separation), and (c) $\epsilon = 5.0$ (microphase separation)

Finally, we increase the anchor Y beads in model I and the $g(r)$ at different ϵ values are shown in fig. 6.17 where the phase separation at low ϵ is apparent. Increasing the Y beads does not improve the compatibility at $\epsilon = 1.0$ as shown in fig. 6.18b. When the ϵ increases to 5.0, fig. 6.18c shows a well-dispersed plasticizer in the polymer phase enhanced by the increased $B - Y$ attraction.

Summarily, in all the models we have studied, shorter R legs and higher ϵ values favor the compatibility between the polymer and the plasticizer. On the other hand, low ϵ values and an increase in the repulsive R legs reduces the compatibility – also resulting in complete phase separation. At higher ϵ and longer R beads, it mostly results in a microphase separation. This is summarized in fig. 6.19 This is to a certain degree consistent with the earlier full-atom simulation of Li et al.⁶ where they compared the compatibility and plasticization efficiency of phthalates with the same alkyl side chain configuration with PVC. Specifically, it was reported that increasing the length of the side chain results in worse compatibility and plasticization efficiency.

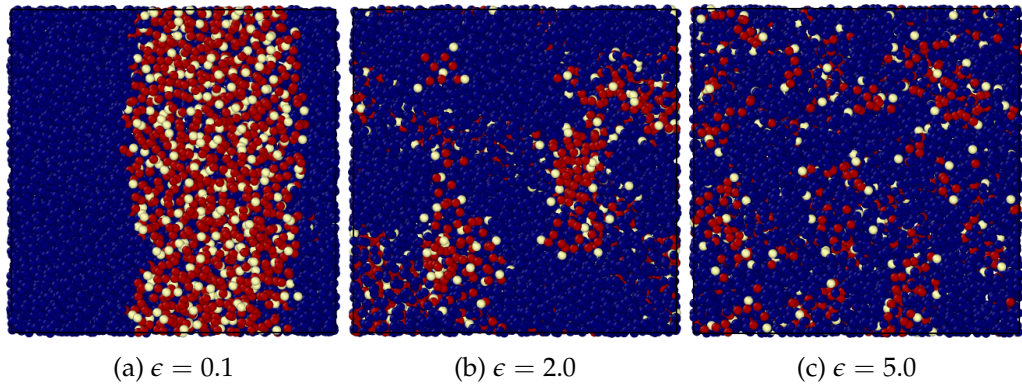


FIGURE 6.13: Model G. Phase separation, microphase separation, and compatibility between the polymer and plasticizer beads. The blue B and red R beads are the polymer and plasticizer beads respectively. The yellow beads (Y) are part of plasticizer beads and are tuned to make the plasticizer chain more attractive to the polymer chain. The figures are the ϵ interaction between the B and Y beads (a) $\epsilon = 0.1$ (phase separation), (b) $\epsilon = 2.0$ (microphase separation), and (c) $\epsilon = 5.0$ (compatibility).

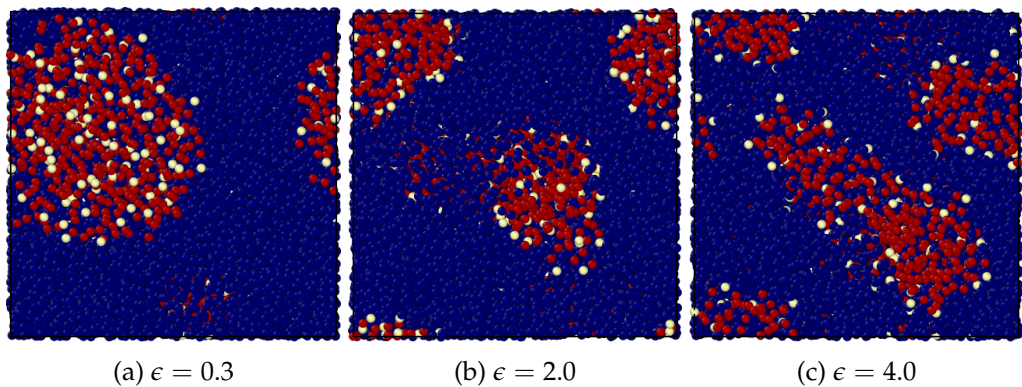


FIGURE 6.14: Model I. Phase separation and microphase separation between the polymer and plasticizer beads. The blue B and red R beads are the polymer and plasticizer beads respectively. The yellow beads (Y) are part of plasticizer beads and are tuned to make the plasticizer chain more attractive to the polymer chain. The figures are the ϵ interaction between the B and Y beads (a) $\epsilon = 0.3$ (phase separation), (b) $\epsilon = 2.0$ (microphase separation), and (c) $\epsilon = 4.0$ (microphase separation).

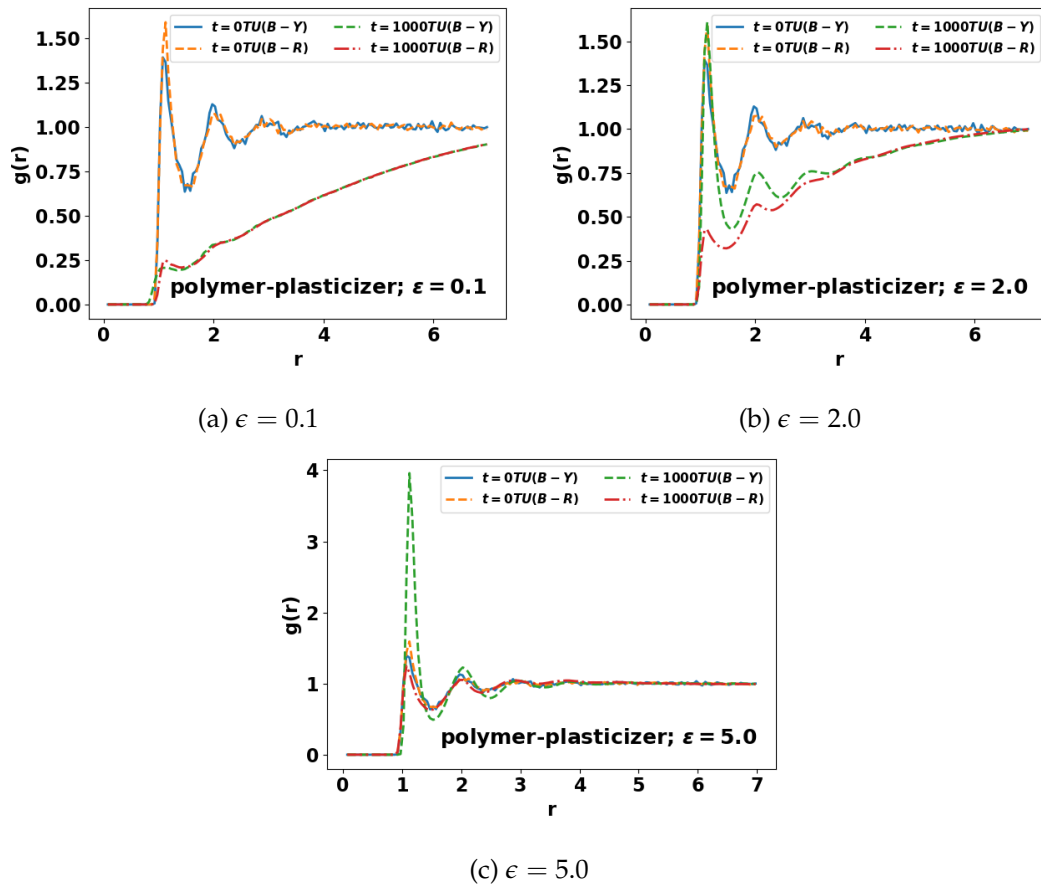


FIGURE 6.15: Radial distribution function for model G. The figures are the ϵ interaction between the B and Y beads (a) $\epsilon = 0.1$ (phase separation), (b) $\epsilon = 2.0$ (microphase separation), and (c) $\epsilon = 5.0$ (compatibility)

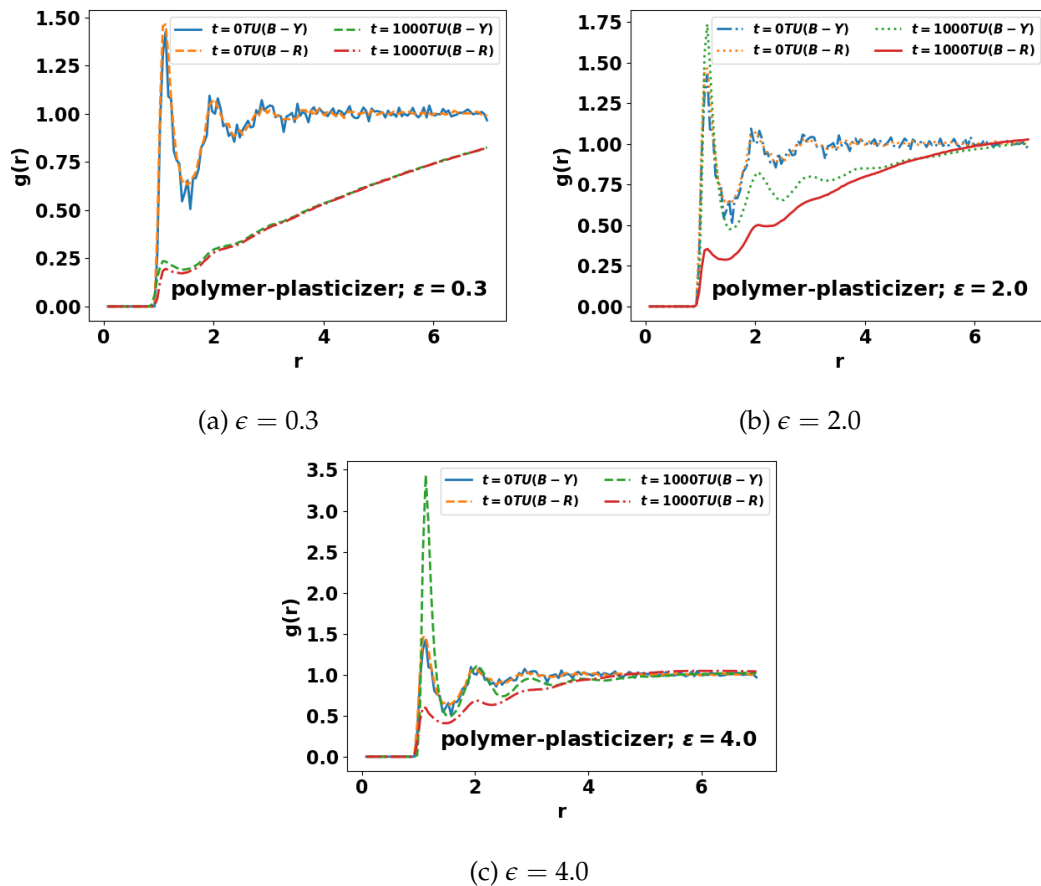


FIGURE 6.16: Radial distribution function for model I. The figures are the ϵ interaction between the (B) and (Y) beads (a) $\epsilon = 0.3$ (phase separation) (b) $\epsilon = 2.0$ (microphase separation), and (c) $\epsilon = 4.0$ (microphase separation)

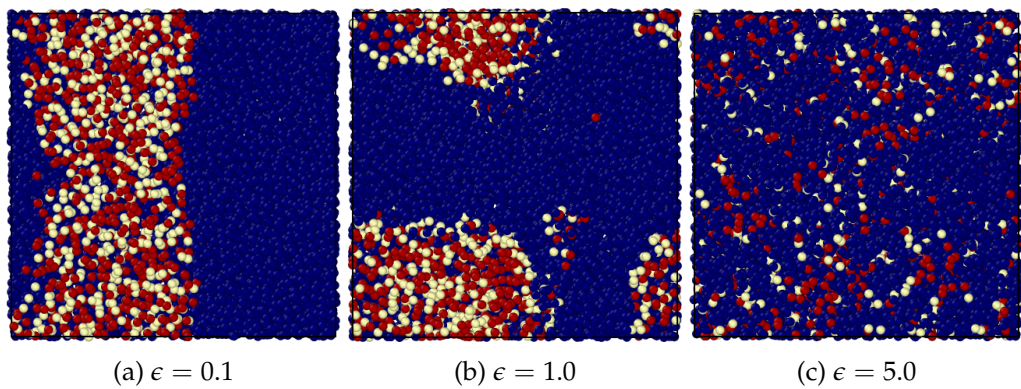


FIGURE 6.17: Phase separation and compatibility between the polymer and plasticizer beads of model J. The blue B and red R beads are the polymer and plasticizer beads respectively. The yellow beads Y are part of plasticizer beads and are tuned to make the plasticizer chain more attractive to the polymer chain. The figures are the ϵ interaction between the B and Y beads (a) $\epsilon = 0.1$ (phase separation), (b) $\epsilon = 1.0$ (phase separation), and (c) $\epsilon = 5.0$ (compatibility).

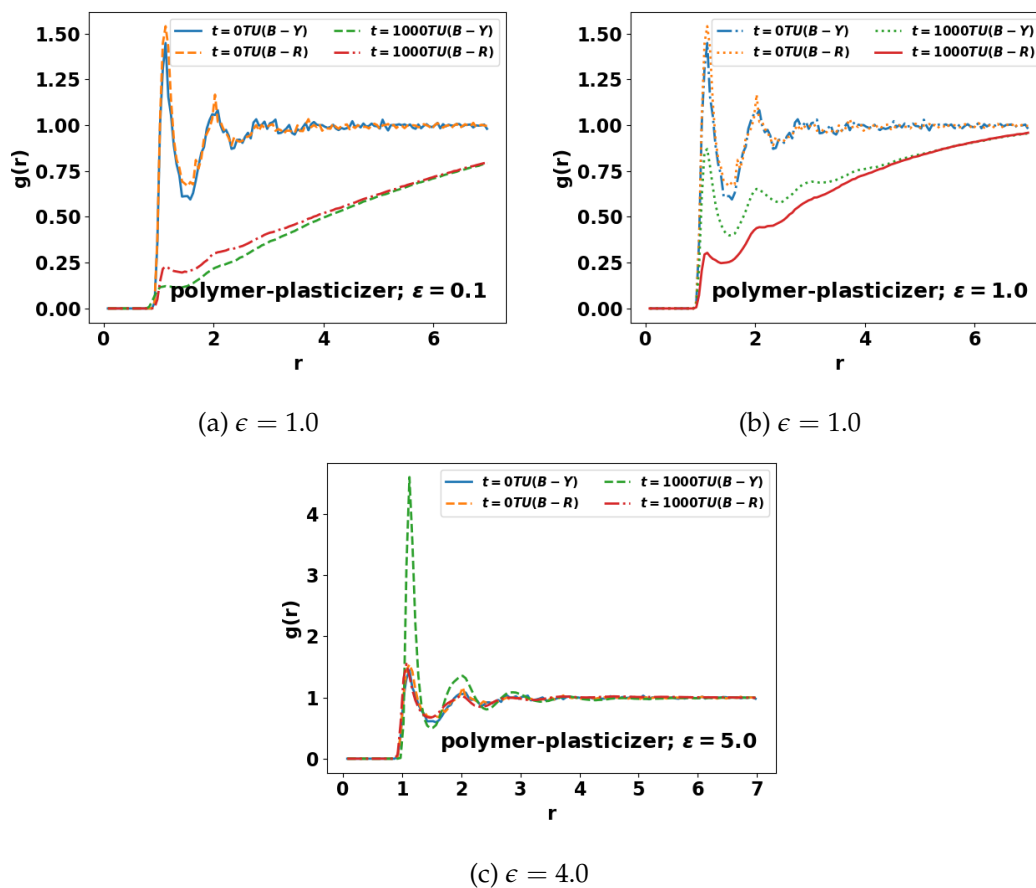


FIGURE 6.18: Radial distribution function for model J. The figures are the ϵ interaction between the (B) and (Y) beads (a) $\epsilon = 0.1$ (phase separation), (b) $\epsilon = 1.0$ (phase separation), and (c) $\epsilon = 5.0$ (compatibility)

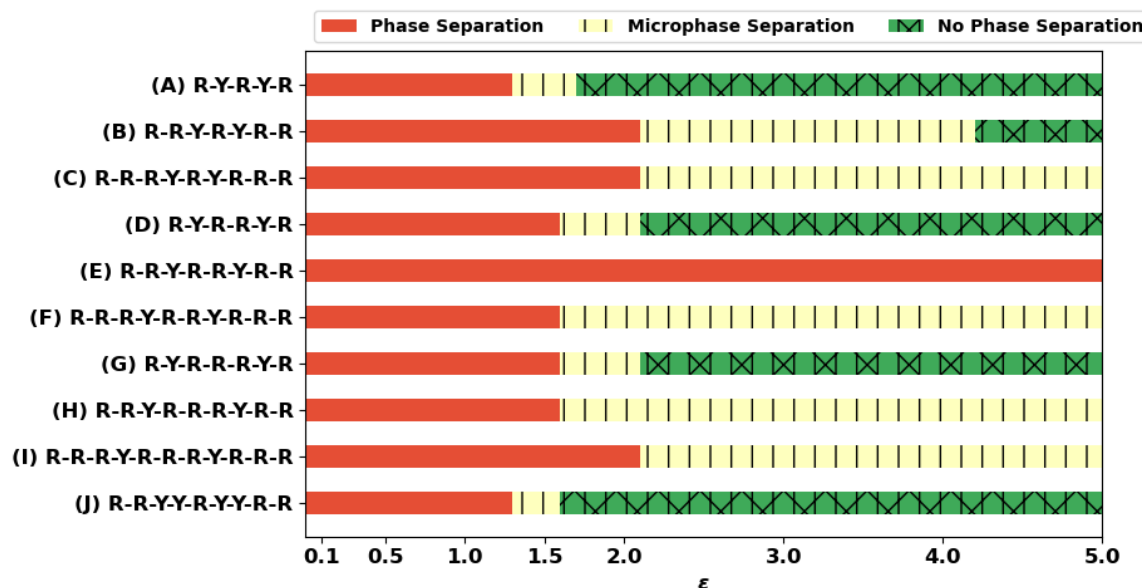


FIGURE 6.19: Summary of the phase separation of the various models. We used ϵ values of 0.1, 0.3, 0.5, 1.0, 1.2, 1.5, 2.0, 3.0, 4.0, and 5.0. Red represents the phase separation region, yellow the microphase separation, and green represents regions where the plasticizer and polymer are compatible.

6.3.2 Temperature Effects

In order to understand how temperature affects compatibility, we further examined model A that showed the greatest compatibility, and varied the temperature while varying the energy interaction parameter the same as with the previous models. We showed the results for $\epsilon = 1.5$ in fig. 6.20. At a low temperature, $T = 0.4$, lower than the T_g for the KG model (T_g for the KG model is $\sim 0.42^{26,39}$), fig. 6.20a shows that there is no phase separation. The system is more or less frozen in place. Although there is a drop in the number of R particles surrounding the B particles, there is a significant number of Y beads surrounding the B beads. Obviously, this is due to the reduced dynamics of the system at the lower temperature. While the thermo-mechanical measurements can be done at such low temperatures, the viscoelastic properties are almost impossible to be measured due to the increase in relaxation times at such reduced temperature. Once the temperature increased as shown in fig. 6.20b to fig. 6.20d, the microphase separation was strongest at $T = 0.8$ where the number of R beads of the plasticizer surrounding the polymer blue B beads have reduced significantly. Increasing the temperature also ensures the particles stay closer together as observed in the $B - R$ curves.

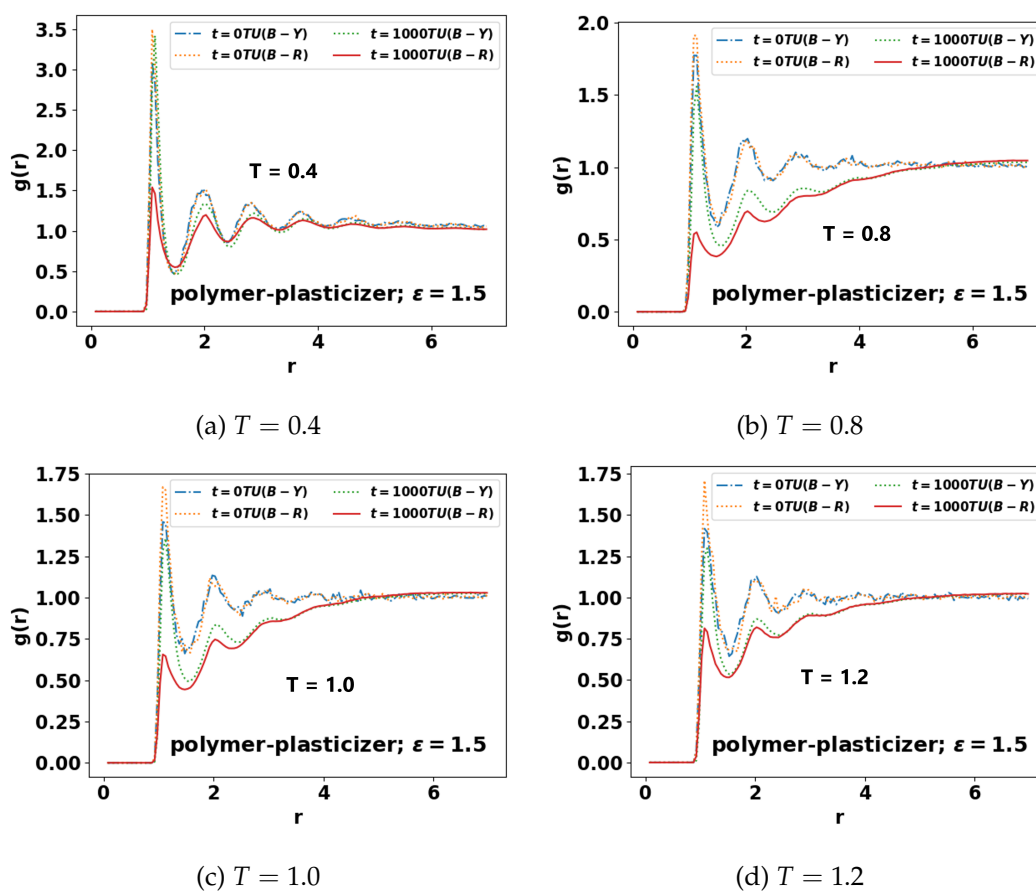


FIGURE 6.20: Radial distribution function $g(r)$ for model A at different temperatures. The ϵ interaction was kept at 1.5 between the B and Y beads (a) $T = 0.4$, (b) $T = 0.8$ (c) $T = 1.0$, and (d) $T = 1.2$

6.3.3 Linear Viscoelasticity

To check plasticization effects, we investigate the linear viscoelasticity of some select models that have shown miscibility with the host polymer. Specifically, we determine the stress relaxation modulus $G(t)$ of the various systems using equilibrium molecular dynamics simulation. The Green-Kubo relation gives the relationship between the $G(t)$ and the autocorrelation function (ACF) of the shear stress fluctuations as

$$G(t) = \frac{V}{k_B T} \langle \sigma_{xy}(t_0) \sigma_{xy}(t_0 + t) \rangle \quad (6.5)$$

where V is the volume of the system, T is the temperature, and σ_{xy} is the instantaneous shear stress. To improve the signal to noise ratio of the stress signal in the system, we average the stress ACF over multiple directions. This results in the form

$$\begin{aligned} G(t) = & \frac{V}{5k_B T} [\langle \sigma_{xy}(t) \sigma_{xy}(0) \rangle + \langle \sigma_{yz}(t) \sigma_{yz}(0) \rangle \\ & + \langle \sigma_{zx}(t) \sigma_{zx}(0) \rangle] + \frac{V}{30k_B T} [\langle N_{xy}(t) N_{xy}(0) \rangle \quad (6.6) \\ & + \langle N_{xz}(t) N_{xz}(0) \rangle + \langle N_{yz}(t) N_{yz}(0) \rangle] \end{aligned}$$

where

$$N_{\alpha\beta} = \sigma_{\alpha\alpha} - \sigma_{\beta\beta}. \quad (6.7)$$

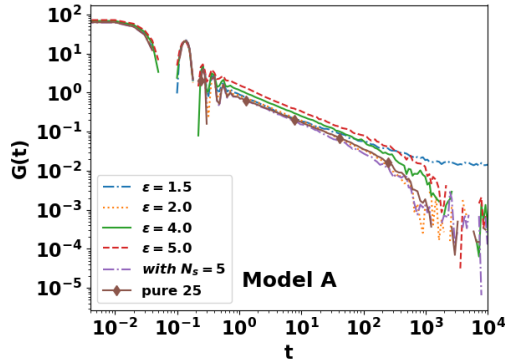
We used the multi-tau correlator method developed by Ramirez et al.⁴⁰ which uses a hierarchical multi-level data structure to store and filter time series and calculate correlation functions on the fly. In its data structure, level 0 stores the

most recent p data points in the time series. At level 1, the first entry stores the average value of the most recent m ($m < p$) points, the second entry stores the average of the next m points, and so on. Similarly, each entry at level l is the average of m entries at level $l - 1$. As such, stored data represent local averages of the original time series and the averaging window size (m^l for level l) increases with the level, so does the time lag it covers (the range of previous time where information is retained at the current level). For the smallest time lags (up to $p - 1$ sampling intervals), the unfiltered time series is used, whereas for increasing time lag (higher levels), averages over larger window sizes are used. In this study, we use the same default parameters $p = 16$ and $m = 2$ as recommended in Ramirez et al.⁴⁰ Furthermore, to effectively compare between the different systems, we calculate the zero-shear viscosity η_0 from⁴¹

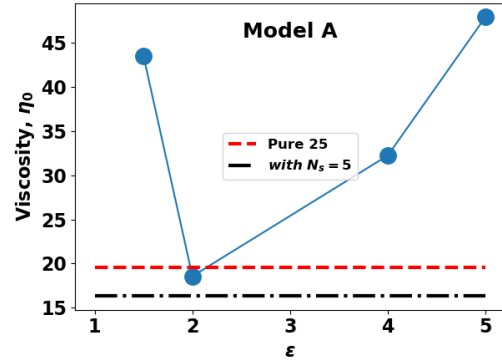
$$\eta_0 \equiv \lim_{\dot{\gamma} \rightarrow 0} \eta(\dot{\gamma}) = \int_0^{\infty} G(t) dt \quad (6.8)$$

where $G(t)$ is the relaxation modulus and $\eta(\dot{\gamma})$ is the shear rate dependent viscosity. Figure 6.21 shows the $G(t)$ and η_0 for models A, G, and J. These are plasticizer models that have shown limited compatibility with the polymer at high ϵ values. The $G(t)$ for the polymer mixtures, the pure polymer, and the polymer mixed with "dummy" plasticizers N_s – shorter chains with equal length to the plasticizers but having all B beads is given in fig. 6.21a – spanning over five decades. These $G(t)$ profile are typical for a short polymeric material, with very high modulus at the early times and intense fluctuations at $t \sim \mathcal{O}(10^{-1})$ due to bond oscillations.²⁸ The customary plateau in entangled polymers at intermediate times are absent due to the short chain length ($N = 25$) we have used.

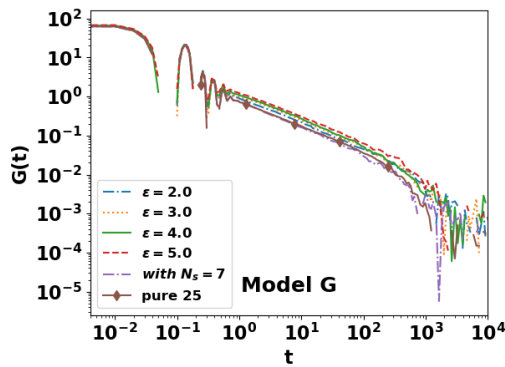
The entanglement length N_e for the KG model^{42,43} is ~ 85 . At early times, all the curves overlap and are indistinguishable from one another. At intermediate times $t \sim \mathcal{O}(10^{-1})$, all the curves separate into distinct lines and the curve for the polymer mixed with dummy plasticizers is lower than the pure polymer and the plasticized polymers with various ϵ values. However, at much later times $t \sim \mathcal{O}(10^1)$, there is an overlap between the profiles of the pure polymer and when $\epsilon = 2$. In general, the profiles are higher with increasing ϵ with the exception at $\epsilon = 1.5$ where there is a microphase separation and the curve does not decay (at least on the timescale of our simulations) which is reminiscent of a gel or cross-linked polymers.⁴⁴ The corresponding viscosity for model A is shown in fig. 6.21b. The polymer mixed with the dummy plasticizers resulted in the lowest viscosity followed by the pure polymer. For the plasticized polymers, the viscosity increases with ϵ except at $\epsilon = 1.5$ where there is a dramatic increase in viscosity. If plasticization is defined as a reduction in viscosity, then only $\epsilon = 2$ has shown the tendency of being an effective plasticizer. Similarly for models G and J, larger ϵ values, although enhanced miscibility, resulted in curves with higher $G(t)$ profiles especially up to $t \sim \mathcal{O}(10^1)$ due to the stronger intermolecular attraction between the polymer and plasticizer beads. At later times, it is harder to distinguish between the different lines. Again, the viscosity plot fig. 6.21d and fig. 6.21f show that the polymer mixed with the dummy additives has a much lower viscosity than at the various ϵ values, with the viscosity increasing as ϵ increases. Compared to the pure polymer, the viscosity at $\epsilon = 5.0$ increased by $\sim 92\%$ and $\sim 480\%$ for models G and J respectively. Summarily, the models that have large enough ϵ to ensure miscibility showed little or no plasticization effect.



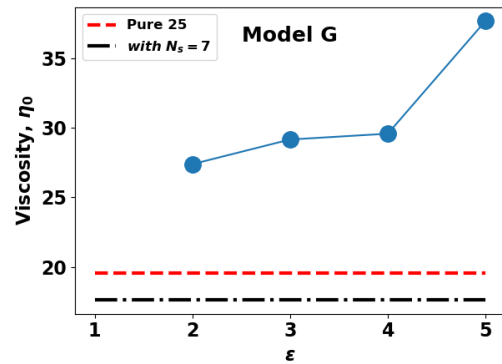
(a) R – Y – R – Y – R



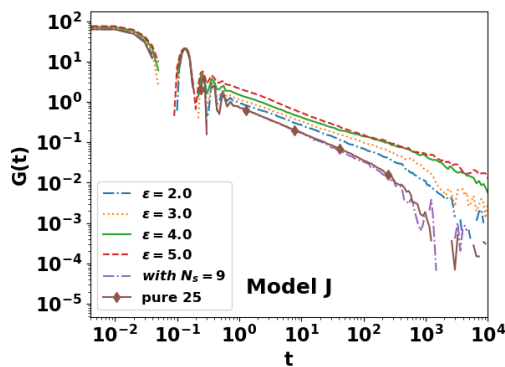
(b) R – Y – R – Y – R



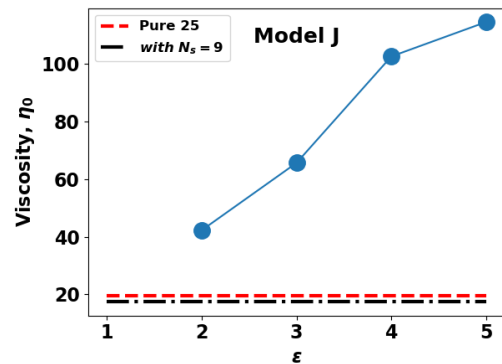
(c) R – Y – R – R – R – Y – R



(d) R – Y – R – R – R – Y – R



(e) R – R – Y – Y – R – Y – Y – R – R



(f) R – R – Y – Y – R – Y – Y – R – R

FIGURE 6.21: Stress relaxation modulus $G(t)$ and zero-shear viscosity η_0 for models A, G, and J at a temperature of 1.0. The pure polymer and polymer mixed with a short chain additive N_s equal in length to the plasticizer length are included as references.

6.4 Discussion

Most of the plasticizer models we have explored resulted in phase separation. The few models that are compatible with the polymer showed little or no plasticization tendency when we examined the linear viscoelasticity. Nevertheless, a few other directions can still be explored. As mentioned earlier, phthalates are one of the most popular class of plasticizers. They are however mostly used with a polar polymer, PVC. We have accounted for polarity using a rather crude method of tuning the relative attraction between the polymers and plasticizers. As such, an additional way to further check the viability of these models would be to better tune the polymer chains to account for polarity, for example by including partial charges on the polymers. Additionally, the pair potential we have used for both our plasticizer models and polymers has been the LJ potential – which is mostly used to describe the interaction between non-polar molecules.⁴⁵ Indeed, the benzene ring in the middle of phthalates is not strictly non-polar. It is polarizable. Explicitly incorporating polarization effects using, for example, fluctuating-charge models^{46,47} that accounts for polarization by determining the charge distribution as a result of geometrical or external perturbations may significantly improve the modeling predictions.

Indeed, instead of the random trials-and-errors approach we have used here for modeling the plasticizers, a more efficient method may be some systematic coarse graining to get CG forcefields that map to realistic atomic models for example, DEHP. This approach can provide insight into the features that are critical to proper plasticization behaviors. We have also used fully flexible models for the plasticizers. On the contrary, real plasticizers have nearly fixed angles

between the legs which are generally long, although not long enough to entangle with the polymers, but the increased chain length causes additional friction. Furthermore, it is also possible that real plasticizers are not completely miscible with the host polymer in a thermodynamic sense. They may just temporarily stay blended for long enough time. Additional simulations would be needed to properly investigate this. The length of the polymer chains we have used are also rather short at $N = 25$. Industrial polymers are usually much longer and entanglement effects typically play a role. It will be interesting to see the effects of entanglements, if any, on the observed properties.

6.5 Conclusion

In this chapter, we have described our various attempts at developing plasticizer models that mimic real plasticizers. We developed models that have a strong attractive polar core and a repulsive non-polar legs – which are the typical attributes of a real plasticizer such as DEHP. By tuning the interaction parameter ϵ between the polymer and the plasticizer, we explore the evolution of the structure of the system. The mixtures mostly separate into different components for the parameters we have explored. There are a few intermediate cases where the phase separation is not complete – resulting in microphase separation. Finally, there were also a few systems where both the plasticizers and polymers were completely miscible, especially at high ϵ values and short leg length of the plasticizer. Our simulations show that models with longer legs showed worse compatibility with the polymer. In the miscible systems, our linear viscoelastic results show that the models do not lower the viscosity of the

polymer. This underscores the fact that the interaction between the plasticizers and polymers are non-trivial.

References

- [1] G. Wypych. *Handbook of plasticizers*. ChemTec Publishing, 2004.
- [2] M. Kutz. *Applied plastics engineering handbook: processing and materials*. William Andrew, 2011.
- [3] J. Murphy. *Additives for plastics handbook*. Elsevier, 2001.
- [4] P. H. Daniels. A brief overview of theories of PVC plasticization and methods used to evaluate PVC-plasticizer interaction. *Journal of vinyl and additive technology* 15(4) (2009), 219–223.
- [5] K. G. Wagner et al. Glass transition temperature of a cationic polymethacrylate dependent on the plasticizer content–Simulation vs. experiment. *Chemical physics letters* 406(1-3) (2005), 90–94.
- [6] D. Li et al. An atomistic evaluation of the compatibility and plasticization efficacy of phthalates in poly (vinyl chloride). *Macromolecules* 51(18) (2018), 6997–7012.
- [7] D. Li et al. Effects of molecular design parameters on plasticizer performance in poly(vinyl chloride): a comprehensive molecular simulation study. *Chem. Eng. Sci.*, in press (2021).
- [8] R. L. Andrew. *Molecular modeling principles and applications*. Prentice Hall, London (2001).
- [9] K. Binder. *Monte Carlo and molecular dynamics simulations in polymer science*. Oxford University Press, 1995.

- [10] D. Li et al. Effects of molecular design parameters on plasticizer performance in poly (vinyl chloride): a comprehensive molecular simulation study (2021).
- [11] H. C. Erythropel, M. Maric, and D. G. Cooper. Designing green plasticizers: influence of molecular geometry on biodegradation and plasticization properties. *Chemosphere* 86(8) (2012), 759–766.
- [12] R. Jamarani et al. How green is your plasticizer? *Polymers* 10(8) (2018), 834.
- [13] R. A. Riggleman et al. Influence of confinement on the fragility of antiplasticized and pure polymer films. *Physical review letters* 97(4) (2006), 045502.
- [14] R. A. Riggleman, J. F. Douglas, and J. J. de Pablo. Tuning polymer melt fragility with antiplasticizer additives. *The Journal of chemical physics* 126(23) (2007), 234903.
- [15] R. A. Riggleman, J. F. Douglas, and J. J. de Pablo. Antiplasticization and the elastic properties of glass-forming polymer liquids. *Soft Matter* 6(2) (2010), 292–304.
- [16] J. H. Mangalara and D. S. Simmons. Tuning polymer glass formation behavior and mechanical properties with oligomeric diluents of varying stiffness. *ACS Macro Letters* 4(10) (2015), 1134–1138.
- [17] I. Carmesin and K. Kremer. The bond fluctuation method: a new effective algorithm for the dynamics of polymers in all spatial dimensions. *Macromolecules* 21(9) (1988), 2819–2823.
- [18] I. Carmesin and K. Kremer. Static and dynamic properties of two-dimensional polymer melts. *Journal de Physique* 51(10) (1990), 915–932.

- [19] W. Paul et al. Crossover scaling in semidilute polymer solutions: a Monte Carlo test. *Journal De Physique Ii* 1(1) (1991), 37–60.
- [20] W. Paul et al. Dynamics of polymer solutions and melts. Reptation predictions and scaling of relaxation times. *The Journal of chemical physics* 95(10) (1991), 7726–7740.
- [21] J. Baschnagel, K. Binder, and H.-P. Wittmann. The influence of the cooling rate on the glass transition and the glassy state in three-dimensional dense polymer melts: a Monte Carlo study. *Journal of Physics: Condensed Matter* 5(11) (1993), 1597.
- [22] J. Baschnagel et al. Statics and dynamics of bidisperse polymer melts: A Monte Carlo study of the bond-fluctuation model. *Macromolecules* 31(12) (1998), 3856–3867.
- [23] K. Kremer and G. S. Grest. Dynamics of entangled linear polymer melts: A molecular-dynamics simulation. *The Journal of Chemical Physics* 92(8) (1990), 5057–5086.
- [24] M. Pütz, K. Kremer, and G. S. Grest. What is the entanglement length in a polymer melt? *Europhysics Letters* 49(6) (Mar. 2000), 735–741. ISSN: 02955075.
- [25] H. P. Hsu and K. Kremer. Static and dynamic properties of large polymer melts in equilibrium. *Journal of Chemical Physics* 144(15) (2016), 154907. ISSN: 00219606.
- [26] G. S. Grest. *Communication: Polymer entanglement dynamics: Role of attractive interactions*. 2016.

- [27] M. Kröger, W. Loose, and S. Hess. Rheology and structural changes of polymer melts via nonequilibrium molecular dynamics. *Journal of rheology* 37(6) (1993), 1057–1079.
- [28] A. E. Likhtman, S. K. Sukumaran, and J. Ramirez. Linear viscoelasticity from molecular dynamics simulation of entangled polymers. *Macromolecules* 40(18) (2007), 6748–6757. ISSN: 00249297.
- [29] O. Adeyemi, S. Zhu, and L. Xi. Dynamics and stress relaxation of bidisperse polymer melts with unentangled and moderately entangled chains. *Physics of Fluids* 33(6) (2021), 063105.
- [30] S. Plimpton. *Fast parallel algorithms for short-range molecular dynamics*. Tech. rep. Sandia National Labs., Albuquerque, NM (United States), 1993.
- [31] Y. R. Sliozberg and J. W. Andzelm. Fast protocol for equilibration of entangled and branched polymer chains. *Chemical Physics Letters* 523 (2012), 139–143.
- [32] M. Rahman and C. S. Brazel. The plasticizer market: an assessment of traditional plasticizers and research trends to meet new challenges. *Progress in polymer science* 29(12) (2004), 1223–1248.
- [33] M. Hakkarainen. Migration of monomeric and polymeric PVC plasticizers. *Chromatography for sustainable polymeric materials* (2008), 159–185.
- [34] M. A. Babich, C. Bevington, and M. A. Dreyfus. Plasticizer migration from children’s toys, child care articles, art materials, and school supplies. *Regulatory Toxicology and Pharmacology* 111 (2020), 104574.

- [35] A. Stukowski. Visualization and analysis of atomistic simulation data with OVITO–the Open Visualization Tool. *Modelling and Simulation in Materials Science and Engineering* 18(1) (2009), 015012.
- [36] M. P. Allen and D. J. Tildesley. *Computer simulation of liquids*. Oxford university press, 2017.
- [37] V. Garcia-Negron et al. Evaluation of nano-and mesoscale structural features in composite materials through hierarchical decomposition of the radial distribution function. *Journal of Applied Crystallography* 51(1) (2018), 76–86.
- [38] R. A. L. Jones. *Soft condensed matter*. Vol. 6. Oxford University Press, 2002.
- [39] J.-L. Barrat, J. Baschnagel, and A. Lyulin. Molecular dynamics simulations of glassy polymers. *Soft Matter* 6(15) (2010), 3430–3446.
- [40] J. Ramirez et al. Efficient on the fly calculation of time correlation functions in computer simulations. *The Journal of chemical physics* 133(15) (2010), 154103.
- [41] L. Xi. Molecular simulation for predicting the rheological properties of polymer melts. *Molecular Simulation* 45(14-15) (2019), 1242–1264.
- [42] J.-X. Hou et al. Stress relaxation in entangled polymer melts. *Physical review letters* 105(6) (2010), 068301.
- [43] J.-X. Hou. Determine mesh size through monomer mean-square displacement. *Polymers* 11(9) (2019), 1405.

- [44] J. M. Dealy, D. J. Read, and R. G. Larson. *Structure and rheology of molten polymers: from structure to flow behavior and back again*. Carl Hanser Verlag GmbH Co KG, 2018.
- [45] R. B. Bird, W. E. Stewart, and E. N. Lightfoot. *Transport phenomena*. Vol. 1. John Wiley & Sons, 2006.
- [46] S. W. Rick and B. Berne. Dynamical fluctuating charge force fields: the aqueous solvation of amides. *Journal of the American Chemical Society* 118(3) (1996), 672–679.
- [47] S. Patel and C. L. Brooks III. Fluctuating charge force fields: recent developments and applications from small molecules to macromolecular biological systems. *Molecular Simulation* 32(3-4) (2006), 231–249.

Chapter 7

Conclusions and Contributions

In this thesis, we have focused on the dynamics and linear viscoelastic properties of pure polymers, polydisperse polymers, and polymer blends using coarse-grained molecular dynamics (MD) simulation. We dwelt on two prominent theories of polymer dynamics – the Rouse model that describes the dynamics of short unentangled chains and the tube and reptation model describing that of long, entangled chains. We used the well-known Kremer-Grest (KG) model for our polymer chains and the length of the polymer chains we have studied straddled these two theoretical regimes.

Our first two contributions are to the methodology development for the computational estimation of key quantities and properties in polymer dynamics and rheology. Those efforts focused on pure polymer melts. Chapter 2 focuses on the extraction of the entanglement strand length N_e from molecular dynamics simulation. The reptation model predicts four distinct characteristic timescales; τ_0 – the monomer characteristic time, τ_e – the entanglement time, τ_R – the Rouse

relaxation time, and τ_d – the disentanglement time. Additionally, one of the important parameters of the reptation model was the definition of a length scale – the entanglement length, N_e where the topological interactions between a test chain and matrix chains become significant. In MD simulations, the N_e is usually determined from the intersections of the timescales associated with different segments of the chain. However, there is a considerable variability in the values of the timescales obtained and moreover, the calculated N_e depends on the chosen timescales. This underscores the need for a proper definition of the reported N_e . Here, we devised a protocol for the reliable estimation of the power law time scales from the monomer mean square displacement. Among other things, the calculated N_e strongly depends on the timescales used – with the longer timescales τ_R and τ_d giving the largest value while the earlier timescales τ_0 and τ_e gave a much smaller value. This is due to the time dependent widening of the "tube" containing the test chain. Additionally, and for the first time, to the best of our knowledge, we also used Rouse mode analysis (RMA) to also extract N_e . The RMA offers a more robust and less sensitive method for calculating N_e . This yielded a value closer to that determined from τ_R and τ_d .

Chapter 3 focuses on the methods for calculating linear viscoelastic properties of polymer melts. We compared three different methods for predicting the linear viscoelastic properties (G' and G'') of polymers in MD simulations – equilibrium molecular dynamics (EMD), non-equilibrium molecular dynamics (NEMD), and Rouse mode analysis (RMA), given a fixed amount of computational resource. Besides the intense stress fluctuations peculiar to the EMD approach, the Fourier transformation of the $G(t)$ to G' and G'' is also non-trivial

due to the non-uniform sampling time in the $G(t)$. We used an interpolation scheme to overcome this hurdle. The NEMD method traditionally uses an excessive amount of computational resources to avoid potential statistical inaccuracy. Through careful error analysis, we identified the exact amount of computing time necessary for statistical accuracy. We presented results at much lower frequencies and longer chain length than previously reported in the literature. The RMA is only applicable to short chain lengths. Therefore, we compared the uncertainty of these three approaches for short chain lengths using the amount of computational resource as a constraint. Our results showed that RMA gave the lowest uncertainty.

The rest of the thesis focuses on viscoelastic properties of more realistic polymer systems, including polydisperse polymer melts and polymer-additive blends. In chapter 4, idealizing a polydisperse mixture using a bidisperse system consisting a short unentangled chain and another long enough to be considered entangled based on the Kremer-Grest (KG) model, we studied the effects of polydispersity on the dynamics of the polymer chains by calculating the monomer and center-of-mass mean square displacement. Our results showed that the dynamics of the longer chains are sped up by the shorter chains and the converse is true for the shorter chains wherein their dynamics are inhibited by the longer chains. However, the nature of the dynamics of the short chains is unaffected by the presence of the longer chains. By performing a RMA on the individual chains, we also showed that the shorter chains lessened the entanglement effects of the longer chains. We further tested a semi-empirical mixing rule for predicting the stress relaxation modulus of the system using the individual

stress relaxation $G(t)$ profiles of the constituent chains. This is a rather unique approach as we were able to see how the bidisperse components affect the bulk $G(t)$. Here, our results showed that the double reptation model better predicts the $G(t)$ when the longer chains are the majority. However, a simple mixing rule yields a much better result when the shorter chains are the majority.

In chapter 5, we explored the ability of small molecular additives to plasticize a polymer chain by varying the mass concentration and molecular dimensions of the additives. The markers for plasticization are typically indicated by a reduction in the glass transition temperature, Young's modulus, and the zero-shear viscosity η_0 . We found that T_g , Y , and η_0 are de-correlated. Furthermore, as the mass concentration of the additives increase, the smaller-sized particles effectively reduce the T_g . There is however a transition concentration where the efficiency of the reduction in T_g by the additives begin to reduce.

In chapter 6, we described our different attempts at modeling a multi-bead plasticizer model which mimic a real plasticizer. Detailed analysis of the microstructure showed that our models are either incompatible with the polymers or only marginally miscible with the polymers over a narrow range and do not give rise to plasticization.